M.Sc. Graduation Project

Flexible Composite Propeller Design for Optimized Performance in Propulsive and Regenerative Operating Conditions

C. D. Rotundo

Technische Universiteit Delft

Delft University of Technology

Challenge the future

M.Sc. Graduation Project

Flexible Composite Propeller Design for Optimized Performance in Propulsive and Regenerative Operating Conditions

by

C. D. Rotundo

in partial fulfilment of the requirements for the degree of

Master of Science
in Aerospace Engineering

at the Delft University of Technology,

Student number:	5479118
Project duration:	February 6, 2023 – November 16, 2023
Department:	Flight Performance and Propulsion
Chairman:	Prof. Dr. ing. G. Eitelberg
Examiner:	Dr. ir. R. De Breuker
Supervisors:	Dr. ir. T. Sinnige
	Dr. J. Sodja

Delft University of Technology

Preface

This project marks the end of my graduate studies at TU Delft in Flight Performance and Propulsion. My studies at TU Delft have been both challenging and rewarding, and I believe that completing this thesis has forced me to step outside my comfort zone. This was difficult at times, although at this point I am glad that I made the decision to choose a topic that I knew would challenge me, as I believe that it has enabled me to grow, both as a student and as an engineer. Furthermore, living approximately seven hours away by plane from where I would consider to be home for the last two years has certainly not been easy either sometimes, although my experience being abroad was mostly fun, and I got to learn something new on most days. I know that I am incredibly fortunate to have had this opportunity during my life. Lastly, there are several people whom I am grateful to have received support from while I embarked on this journey.

First, I would like to thank my supervisors, Dr. Jurij Sodja and Dr. Tomas Sinnige, for being great mentors to me while I completed my thesis and literature study. I am especially thankful for the critical and insightful feedback that I received whenever necessary, and I believe that their support in helping me navigate a topic that I initially had quite limited exposure to has enabled me to do my best while learning as much as I could. I am also grateful for being given as much freedom as possible to explore a topic that has been fascinating to me over the past eleven months or so. I also appreciated their suggestion to present my work at a conference, and I am thankful to have received all the advice and support that I needed in putting the contents together for this. Moreover, I appreciated the additional time that Jurij spent helping me modify PROTEUS to be suitable for my project, particularly regarding steps involving the derivation of sensitivities for aerodynamic loads as well as the setup of the optimization procedure. Without his help, I believe that these steps would have been much more difficult and time-consuming to complete. I am also grateful to Tomas for helping me set up the BEM model and optimization framework. I would additionally like to express my gratitude toward Dr. Georg Eitelberg and Dr. Roeland De Breuker for their willingness to participate in my assessment committee, respectively as the chair and examiner. I worked diligently to complete this project and am excited to have the opportunity to defend my thesis.

Second, I would like to express my sincere appreciation to my parents, who have made large sacrifices to enable me to choose what I want to do and where I want to go during my life, all while being endlessly supportive of all the choices that I make. I believe that this is something that I am not owed in life, and it is through their hard work that I have the freedom to pursue my own lifelong goals. I am grateful for the moral support and advice that I received during this time, as it has enabled me to maintain my motivation, even at times when the tasks in front of me seemed insurmountable. I am also grateful to my sister, who has always been there to hang out with me when I am back in Toronto, or to video call when I am away.

Third, I am grateful to my housemates current and past, whom I have shared a living space with during the time that I spent in Delft: Anne, Burak, Lucas, Miki, Sam, Sid, and TQ. I enjoyed always having someone to play games with when I had free time. I even came to appreciate the dinners that we shared on most nights, despite not being fully on board with this idea at the start of my studies.

I am also thankful for all the people I met and worked with during my studies, including Frederick, Octavian, Andrea, and Gabriel, who chose to work with me on group projects during the first year of our graduate studies and ended up being people who I would consider friends by now. I am also grateful to my friends and colleagues from the now former FPP study room, NB 1.01, especially Jeffrey, Ludovico, Thimo, and Yoram, as I saw them almost every day during the time that I spent working on my thesis. Having people to share a common goal with helped me maintain my motivation throughout this process. I am lastly thankful to the rest of my friends and colleagues in Delft for the memories that we shared.

C. D. Rotundo
Delft, November 2023

Abstract

The ever-growing aerospace industry's urgent need to reduce greenhouse gas emissions has ignited a surge of interest in hybrid or fully electric propulsion systems. The electrification of aircraft introduces the possibility for energy to be recovered during phases of flight where no power input is required, and previous research has demonstrated the potential for small energy balance enhancements using dual role propellers. The design and operation of dual-role propellers involves considering two opposing load cases: positive thrust and torque during propulsive operation, and negative thrust and torque in regenerative operation. Thus, the ideal blade shape for maximizing performance in each opposing operating condition will be very different. Structural tailoring of the composite blades may be an effective approach for reducing energy consumption during operation in both regimes. Accordingly, the primary objective of this research is to determine the extent of dual-role propeller performance improvements that may be obtained through the application of aeroelastic tailoring. Sensitivity studies were conducted to convey an understanding of how dual-role propeller performance is affected through variations in structural designs (ply orientations and thicknesses). Optimization studies were subsequently performed to identify the extent of performance enhancements yielded solely through aeroelastic tailoring for flexible constant- and variable-pitch propellers of fixed geometry, assuming installation on a reference aircraft, and evaluated over multiple cruise distances for a climb-cruise-descent mission.

The thesis objectives were achieved through the development and application of an aeroelastic analysis and optimization framework. Blade element momentum (BEM) theory was used for the aerodynamic model with engineering corrections for compressibility, effects of rotation, root- and tip-losses, and the turbulent wake state. Excellent agreement was obtained from comparisons with a previous BEM code, and reasonable agreement in performance trends was observed through comparisons with experimental data during verification and validation. A modified version of PROTEUS, an aeroelastic tailoring code that was developed at the TU Delft, was used for the structural model. The aerodynamic analysis routine of PROTEUS was modified to instead use the developed BEM code for the evaluation of loads, sensitivities, and performance. The structural model of PROTEUS was modified to feature centrifugal forces and different input structures that are more conducive to the analysis of rotor blades. The structural model implemented during this project accounts for geometric nonlinearities, as well as nonlinear loads through the application of a corotational framework, and it is capable of accurately representing the detailed 3D blade as a reduced-order Timoshenko beam element mesh through its use of a cross-sectional modeller. Finally, a tightly coupled aeroelastic analysis procedure was developed and applied, which ensures convergence through the minimization of a residual vector using Newton's method, and analytical sensitivities for all loads were included in the analysis. Excellent agreement was obtained during verification studies for both the structural and aeroelastic analyses.

Results from the optimization and sensitivity studies indicate that the flexible blades constructed out of symmetric-unbalanced laminates yield a significant variation in thrust and power through the presence of bend-twist and extension-shear coupling, which results in an increasing change in twist distribution with increasing deflection or elongation. Only small variations in performance were observed from symmetric-balanced laminates, as the minimal amount of coupling resulted in negligible twist deformations, which confirms that the presence of bend-twist and extension-shear coupling drives variations in performance obtained through aeroelastic tailoring. Furthermore, it was found that the presence of an aerodynamic wash-out effect augments the range of advance ratio values corresponding to high-efficiency operation during both propulsive and regenerative modes. An opposite trend was observed in the presence of a wash-in effect. Lastly, due to the significantly decreased loading in descent, combined with its small contribution towards the total mission energy consumption, effects of aeroelastic tailoring are significantly greater in propulsive conditions (climb and cruise) in comparison to regenerative conditions.

From optimization, it was found that the flexible constant-pitch propeller features an energy consumption that is between 0.7% and 1.5% lower than the energy consumption of the rigid propellers. Despite this consistent decrease in energy consumption, all optimal flexible constant-pitch propellers were found to regenerate between 3% and 25% less energy than the rigid variable-pitch propeller, and between 3% and 10% less energy than the rigid constant-pitch propeller. This further suggests that the application of aeroelastic tailoring is most-suitable for improving performance in propulsive mode, as the enhanced performance yielded in propulsive mode outweighs the degraded performance in descent by a significant enough margin to enable the flexible constant-pitch propeller to outperform all rigid propellers. Moreover, the flexible variable-pitch propeller naturally yielded an even better performance than the constant-pitch propeller, with a total mission energy consumption that is between 1.5% and 2.0% less than the energy consumption of the rigid propellers. It has thus been shown that aeroelastic tailoring can yield noticeable improvements in propeller performance, at least for the fixed mission profile and reference aircraft that was studied.

Nomenclature

Symbols

Symbol	Context	Definition	Dimensions
$\boldsymbol{A}$	Structures	In-plane stiffness tensor in $(\tilde{x}, \tilde{y}, \tilde{z})$ frame	$[\mathrm{M}][\mathrm{T}]^{-2}$
$\boldsymbol{B}$	Structures	Coupling stiffness tensor in $(\tilde{x}, \tilde{y}, \tilde{z})$ frame	$[\mathrm{M}][\mathrm{L}][\mathrm{T}]^{-2}$
$\boldsymbol{C}$	Structures	Timoshenko cross-sectional stiffness matrix	
C_P	Aerodynamics	Total power coefficient	$[-]$
C_Q	Aerodynamics	Total torque coefficient	$[-]$
C_T	Aerodynamics	Total thrust coefficient	$[-]$
C_d	Aerodynamics	Sectional drag coefficient	$[-]$
C_l	Aerodynamics	Sectional lift coefficient	$[-]$
C_m	Aerodynamics	Sectional moment coefficient	$[-]$
C_p	Aerodynamics	Sectional power coefficient	$[-]$
C_q	Aerodynamics	Sectional torque coefficient (blade-design level)	$[-]$
C_t	Aerodynamics	Sectional thrust coefficient (blade-design level)	$[-]$
C_x	Aerodynamics	Sectional axial force coefficient	$[-]$
C_θ	Aerodynamics	Sectional tangential force coefficient	$[-]$
$\boldsymbol{D}$	Structures	Out-of-plane stiffness tensor in $(\tilde{x}, \tilde{y}, \tilde{z})$ frame	$[\mathrm{M}][\mathrm{L}]^2[\mathrm{T}]^{-2}$
D	Aerodynamics	Drag	$[\mathrm{M}][\mathrm{L}][\mathrm{T}]^{-2}$
E	Optimization	Mission energy consumption	$[\mathrm{M}][\mathrm{L}]^2[\mathrm{T}]^{-2}$
$E_{\mathrm{min}}^{\mathrm{CP}}$	Optimization	Min. energy consumption of rigid constant-pitch propeller	$[\mathrm{M}][\mathrm{L}]^2[\mathrm{T}]^{-2}$
$E_{\mathrm{min}}^{\mathrm{VP}}$	Optimization	Min. energy consumption of rigid variable-pitch propeller	$[\mathrm{M}][\mathrm{L}]^2[\mathrm{T}]^{-2}$
E_{rigid}	Optimization	Minimum energy consumption of the rigid propeller	$[\mathrm{M}][\mathrm{L}]^2[\mathrm{T}]^{-2}$
E_{11}	Structures	Elastic modulus of unidirectional ply along $\hat{x}_1$ axis	$[\mathrm{M}][\mathrm{L}]^{-1}[\mathrm{T}]^{-2}$
E_{22}	Structures	Elastic modulus of unidirectional ply along $\hat{x}_2$ axis	$[\mathrm{M}][\mathrm{L}]^{-1}[\mathrm{T}]^{-2}$
EA	Structures	Extensional stiffness of beam element	$[\mathrm{M}][\mathrm{L}][\mathrm{T}]^{-2}$
EI_s	Structures	Bending stiffness of beam element ($s \in \{2,3\}$)	$[\mathrm{M}][\mathrm{L}]^3[\mathrm{T}]^{-2}$
F	Aerodynamics	Prandtl root- and tip-loss factor	$[-]$
G_{12}	Structures	Shear modulus of unidirectional ply in $\hat{x}_1$-$\hat{x}_2$ plane	$[\mathrm{M}][\mathrm{L}]^{-1}[\mathrm{T}]^{-2}$
GA_s	Structures	Shear stiffness of beam element ($s \in \{2,3\}$)	$[\mathrm{M}][\mathrm{L}]^2[\mathrm{T}]^{-2}$
GJ	Structures	Torsional stiffness of beam element	$[\mathrm{M}][\mathrm{L}]^3[\mathrm{T}]^{-2}$
J	Aerodynamics	Advance ratio ($J = nD/V_\infty$)	$[-]$
$\boldsymbol{J}$	Structures	Jacobian matrix for aeroelastic analysis	
$\boldsymbol{K}$	Structures	Stiffness matrix in global coordinates	
L	Aerodynamics	Lift	$[\mathrm{M}][\mathrm{L}][\mathrm{T}]^{-2}$
$\boldsymbol{M}$	Structures	Mass matrix of beam element in global coordinates	
M	Structures	Internal structural moment resultant in $(\tilde{x}, \tilde{y}, \tilde{z})$ frame	$[\mathrm{M}][\mathrm{L}][\mathrm{T}]^{-2}$
$\boldsymbol{M}^{\mathrm{L}}$	Structures	Mass matrix of beam element in local coordinates	
Ma	Aerodynamics	Mach number	$[-]$
$\boldsymbol{N}$	Optimization	Normalization matrix for design variables	
$\boldsymbol{N}$	Structures	Matrix of shape functions for the beam element	

Symbol	Context	Definition	Dimensions
N	Structures	Internal structural force resultant in $(\tilde{x}, \tilde{y}, \tilde{z})$ frame	$[\mathrm{M}][\mathrm{T}]^{-2}$
N_{b}	Aerodynamics	Number of blades	$[-]$
N_{trim}	Optimization	Number of applicable propeller operating conditions	$[-]$
P	Aerodynamics	Power	$[\mathrm{M}][\mathrm{L}]^{2}[\mathrm{T}]^{-3}$
P	Optimization	Power consumption in each mission segment	$[\mathrm{M}][\mathrm{L}]^{2}[\mathrm{T}]^{-3}$
P_{max}	Optimization	Maximum power consumption	$[L]$
P_C	Aerodynamics	Integral power coefficient ($P_C = C_P\, J^{-3}$)	$[-]$
$\boldsymbol{Q}$	Structures	Plane stress constitutive matrix in $(\hat{x}_1, \hat{x}_2, \hat{x}_3)$ frame	$[\mathrm{M}][\mathrm{L}]^{-1}[\mathrm{T}]^{-2}$
$\tilde{\boldsymbol{Q}}$	Structures	Plane stress constitutive matrix in $(\tilde{x}, \tilde{y}, \tilde{z})$ frame	$[\mathrm{M}][\mathrm{L}]^{-1}[\mathrm{T}]^{-2}$
Q	Aerodynamics	Torque	$[\mathrm{M}][\mathrm{L}]^{2}[\mathrm{T}]^{-2}$
Q_C	Aerodynamics	Integral torque coefficient (($Q_C = C_Q\, J^{-2}$))	$[-]$
$\underset{\sim}{R}$		Residual vector for aeroelastic and BEM calculations	
R	Aerodynamics	Rotor tip radius	$[\mathrm{L}]$
$\mathcal{R}$	Structures	Rotation matrix	$[-]$
Re	Aerodynamics	Reynolds number	$[-]$
T	Aerodynamics	Thrust	$[\mathrm{M}][\mathrm{L}][\mathrm{T}]^{-2}$
$\boldsymbol{T_1}$	Structures	Stress transformation matrix $(\hat{x}_1, \hat{x}_2, \hat{x}_3) \to (\tilde{x}, \tilde{y}, \tilde{z})$	$[-]$
$\boldsymbol{T_2}$	Structures	Strain transformation matrix $(\hat{x}_1, \hat{x}_2, \hat{x}_3) \to (\tilde{x}, \tilde{y}, \tilde{z})$	$[-]$
T	Aerodynamics	Total thrust coefficient ($T_C = C_T\, J^{-2}$)	$[-]$
$\mathcal{U}$	Structures	Strain energy of beam element	$[\mathrm{M}][\mathrm{L}]^{2}[\mathrm{T}]^{-2}$
U	Structures	Material stiffness invariant	$[\mathrm{M}][\mathrm{L}]^{-1}[\mathrm{T}]^{-2}$
$\mathcal{V}$	Structures	Kinetic energy of beam element	$[\mathrm{M}][\mathrm{L}]^{2}[\mathrm{T}]^{-2}$
V	Aerodynamics	Resultant local velocity (with induced velocity)	$[\mathrm{L}][\mathrm{T}]^{-1}$
V_∞	Aerodynamics	Freestream velocity (in axial direction)	$[\mathrm{L}][\mathrm{T}]^{-1}$
a	Aerodynamics	Axial induction factor in propeller plane	$[-]$
a'	Aerodynamics	Tangential induction factor in propeller plane	$[-]$
c	Aerodynamics	Local chord length	$[\mathrm{L}]$
$\left(e_1^{\mathrm{b}}, e_2^{\mathrm{b}}, e_3^{\mathrm{b}}\right)$	Structures	Global coordinate system of blade structure	$[-]$
$\left(e_1^{0}, e_2^{0}, e_3^{0}\right)$	Structures	Local coordinate system of beam element	$[-]$
$\underset{\sim}{f}$	Aeroelasticity	Forces acting at structural degrees of freedom	$[\mathrm{M}][\mathrm{L}][\mathrm{T}]^{-2}$
f	Optimization	Normalized objective function	$[-]$
$\underset{\sim}{\tilde{f}}$	Structures	Force acting on structure at eccentric node	$[\mathrm{M}][\mathrm{L}]^{2}[\mathrm{T}]^{-2}$
g	Optimization	Normalized inequality constraint	$[-]$
h	Optimization	Normalized equality constraint	$[-]$
l_0	Structures	Beam element length	$[\mathrm{L}]$
$\underset{\sim}{\tilde{m}}$	Structures	Moment acting on structure at eccentric node	$[\mathrm{M}][\mathrm{L}]^{2}[\mathrm{T}]^{-2}$
$\bar{m}$	Structures	Beam element mass per unit length	$[\mathrm{M}][\mathrm{L}]^{-1}$
n	Aerodynamics	Rotor speed (revolutions-per-second)	$[\mathrm{T}]^{-1}$
$\underset{\sim}{p}$	Structures	Full degree of freedom deformation vector	$[\mathrm{L}]$, $[-]$
$\underset{\sim}{p}_{\mathrm{e}}$	Structures	Element degree of freedom deformation vector	$[\mathrm{L}]$, $[-]$
p_i	Optimization	Blade tip degree of freedom deformation ($i \in \{1, 2, \ldots, 6\}$)	$[L]$
p_{max}	Optimization	Maximum tip displacement	$[L]$
q_∞	Aerodynamics	Freestream dynamic pressure	$[\mathrm{M}][\mathrm{L}]^{-3}$
$\underset{\sim}{r}$	Structures	Vectorized undeformed radial position along blade	$[\mathrm{L}]$, $[-]$
r	Aerodynamics	Local propeller blade radial location	$[\mathrm{L}]$
t	Optimization	Time spent in each mission segment	$[\mathrm{T}]$

Symbol	Context	Definition	Dimensions
u	Structures	Beam element deformation along e_1^0 axis	[L]
v	Structures	Beam element deformation along e_2^0 axis	[L]
v_i	Aerodynamics	Axial induced velocity in propeller plane	$[\mathrm{L}][\mathrm{T}]^{-1}$
v_w	Aerodynamics	Axial induced velocity far downstream of propeller	$[\mathrm{L}][\mathrm{T}]^{-1}$
w	Structures	Beam element deformation along e_3^0 axis	[L]
x_l	Structures	Beam element length coordinate	[L]
ΔS	Aerodynamics	Surface area of blade element	$[\mathrm{L}]^2$
$\boldsymbol{\Gamma}_i$	Structures	Material stiffness invariant matrices ($i \in \{0,\dots,4\}$)	$[\mathrm{M}][\mathrm{L}]^{-1}[\mathrm{T}]^{-2}$
Ω	Aerodynamics	Rotor speed (revolutions-per-second)	$[\mathrm{T}]^{-1}$
$\underline{\Omega}$	Aerodynamics	Vectorized rotor speed (revolutions-per-second)	$[\mathrm{T}]^{-1}$
Φ	Optimization	Design variable	
$\underline{\Phi}$	Optimization	Design vector	
$\underline{\Phi}_0$	Optimization	Midpoint between lower and upper bound of design vector	
Φ^L	Optimization	Lower bound of design variable	
$\underline{\Phi}^\mathrm{L}$	Optimization	Lower bound of design vector	
Φ^U	Optimization	Upper bound of design variable	
$\underline{\Phi}^\mathrm{U}$	Optimization	Upper bound of design vector	
$\hat{\underline{\Phi}}$	Optimization	Normalized design vector	[−]
Θ	Optimization	Ply orientation used to define stacking sequences	[−]
α	Aerodynamics	Local static angle of attack	[−]
β	Aerodynamics	Blade twist angle	[−]
$\beta_{0.7}$	Aerodynamics	Blade twist angle at a reference span location of $r/R = 0.7$	[−]
ε	Structures	Direct strain	[−]
$\varepsilon_\mathrm{max}^\mathrm{T}$	Optimization	Maximum normal strain (tensile)	[−]
$\varepsilon_\mathrm{min}^\mathrm{C}$	Optimization	Minimum normal strain (compressive)	[−]
η_eh	Aerodynamics	Energy-harvesting efficiency	[−]
η_P	Aerodynamics	Propulsive efficiency	[−]
η_T	Aerodynamics	Turbine efficiency	[−]
γ	Structures	Shear strain	[−]
κ	Structures	Curvature	$[L]^{-1}$
ν	Structures	Poisson ratio	[−]
ω	Aerodynamics	Rotor speed (radians-per-second)	$[\mathrm{T}]^{-1}$
ϕ	Structures	Beam element rotation around e_1^0 axis	[−]
φ	Aerodynamics	Local resultant flow angle (with induced velocity)	[−]
ψ	Structures	Beam element rotation around e_3^0 axis	[−]
ρ_∞	Aerodynamics	Freestream flow density	$[\mathrm{M}][\mathrm{L}]^{-3}$
ρ_s	Structures	Material density	$[\mathrm{M}][\mathrm{L}]^{-3}$
σ	Structures	Normal stress	$[\mathrm{M}][\mathrm{L}]^{-1}[\mathrm{T}]^{-2}$
σ^UC	Structures	Ultimate compressive strength	$[\mathrm{M}][\mathrm{L}]^{-1}[\mathrm{T}]^{-2}$
σ^UT	Structures	Ultimate tensile strength	$[\mathrm{M}][\mathrm{L}]^{-1}[\mathrm{T}]^{-2}$
τ	Structures	Shear stress	$[\mathrm{M}][\mathrm{L}]^{-1}[\mathrm{T}]^{-2}$
τ_max	Optimization	Maximum shear strain	[−]
τ_{12}^U	Structures	Ultimate in-plane shear stress	$[\mathrm{M}][\mathrm{L}]^{-1}[\mathrm{T}]^{-2}$
θ	Structures	Beam element rotation around e_2^0 axis	[−]
ξ_i^k	Structures	Lamination parameters ($k \in \{\mathrm{A,B,D}\}$, $i \in \{1,\dots,4\}$)	[−]

SUBSCRIPTS

Subscript	Definition
0	Quantity evaluated far downstream of propeller
11	Structural quantity of ply aligned with $\hat{x}_1$ axis (aligned with fibres)
1	Flow quantity evaluated directly behind propeller plane
12	Structural quantity of ply within $\hat{x}_1$-$\hat{x}_2$ plane
2	Flow quantity evaluated directly in front of propeller plane
22	Structural quantity of ply aligned with $\hat{x}_2$ axis (orthogonal to fibres and in-plane)
∞	Flow quantity evaluated far upstream of propeller
a	Load or stiffness contribution due to external aerodynamics
c	Load or stiffness contribution due to rotation (centrifugal)
e	Load or stiffness contribution due to external eccentric loads
root	Quantity observed at blade root
s	Force or stiffness contribution due to internal structure
tip	Quantity observed at blade tip

SUPERSCRIPTS

Superscript	Definition
BE	Quantity evaluated using blade element theory
CP	Quantity evaluated for constant-pitch propellers
M	Quantity evaluated using momentum theory
VP	Quantity evaluated for variable-pitch propellers

ABBREVIATIONS

Abbreviation	Definition
BEM	Blade Element Momentum
CFD	Computational Fluid Dynamics
CPVR	Constant-pitch and variable-RPM propeller configuration
LLFVW	Lifting-Line Free-Vortex Wake
NVLM	Nonlinear Vortex Lattice Method
RANS	Reynolds-Averaged Navier-Stokes
TE	Trailing Edge
UML	Unified Modelling Language
VLM	Vortex Lattice Method
VPCR	Variable-pitch and constant-RPM propeller configuration
VPVR	Variable-pitch and variable-RPM propeller configuration

CONTENTS

LIST OF FIGURES

List of Tables

1
Introduction

The need to reduce greenhouse gas emissions within the rapidly expanding aerospace industry has resulted in recent interest in the development of hybrid- or fully electric propulsion systems. This recent interest in electrified propulsion systems has resulted in a renewed interest in propeller-based propulsion systems. Furthermore, with batteries being used for energy storage and electric motors for supplying power, the electrification of aircraft enables the possibility for energy to be recovered during phases of flight where no power input is otherwise required, such as during descending flight.

The design and operation of dual-role propellers involves considering two opposing load cases: positive thrust and torque during propulsive operation, and negative thrust and torque in regenerative operation. This suggests that a propeller that is designed exclusively for propulsive operation will perform poorly in energy harvesting conditions. Indeed, Sinnige *et al.* [1] have shown that a propeller that is designed exclusively for propulsive operation will have a maximum energy harvesting efficiency of approximately 10% [1]. Conversely, Erzen *et al.* [2] saw a 19% decrease in energy consumption during the ascend/descend flight pattern and a 27% increase in the number of traffic pattern circuits performed with a dual-role propeller in comparison to a conventional propeller design when used during flight patterns that are conducive to regeneration during descent [2]. These results indicate that considering both propulsive and regenerative operation during the design of propellers has the potential to yield at least a small decrease in energy consumption due to energy balance improvements that may be attained in descending flight.

The objective of this thesis is to determine whether it is possible to yield further increases in performance of dual-role propellers through the application of aeroelastic tailoring. By including bend-twist or extension-shear coupling through the strategic design of the laminates used in the construction of each propeller blade, it may be possible to broaden the range of advance ratio values where the propeller operates with high efficiency. There has not been any work to-date that involves the application of this approach towards dual-role propellers, although work has been done to optimize flexible propellers for maximum efficiency during the propulsive case. For example, Sodja *et al.* [3] considered exclusively applying geometry modifications for this purpose, and Khan [4] applied different ply stacking sequences to a propeller with a fixed geometry. To build upon this work, an aeroelastic analysis and optimization framework has been developed and applied to maximize the performance of dual-role propellers.

This chapter is organized as follows: Section 1.1 contains an overview of the previous research and state-of-the-art on dual-role propeller design and analysis, and Section 1.2 contains a discussion on previous applications of aeroelastic tailoring towards the design of propellers. Using the discussion from the two preceding sections as a guide, Section 1.3 contains an overview of gaps in current research and a list of research objectives to address these gaps. Finally, the scope of this thesis has been outlined in Section 1.4, including the research questions and boundaries of the project.

1.1. Dual-Role Propeller Design and Analysis

The use of propellers as wind turbines to harvest energy on an aircraft was first suggested by the well-known aerodynamicist Glauert [5] in 1926, although there were no feasible implementations of this technology at the time of his research. This concept was subsequently revisited over 70 years later by

MacCready [6] in 1999, who provided an initial application of the concept towards a battery-electric and self-launching sailplane, which operates its propellers as onboard energy harvesters during descending flight, thereby using its potential energy to recharge its battery. The energy-harvesting performance of the so-called *Regenosoar* concept that was developed by MacCready was later studied in more depth by Barnes [7–9]. Through a detailed multidisciplinary analysis of the model provided by MacCready, Barnes found that the capability of regeneration can enhance range, steepen descent, and add thrust-reversal while landing [7]. Both MacCready and Barnes suggested that the propeller geometry yielding optimal performance during regenerative operation is vastly different from the geometry yielding optimal performance during propulsive operation. This is because the flow and loading encountered by each blade section is notably different between the two cases, as indicated by the velocity triangles in Figure 1.1.

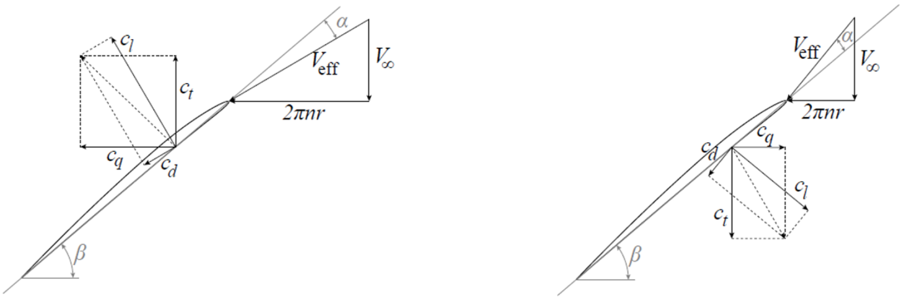

(a) Propulsive operation.

(b) Regenerative operation.

Figure 1.1: Velocity triangles for a propeller operating in propulsive and regenerative modes [1].

MacCready [6] and Barnes [7] suggested several ways to mitigate this problem, such as including two sets of propellers, with one set operating in propulsive conditions and the other set operating in regenerative conditions, and either of the two propeller rotors being capable of folding when not in use [6, 7]. This propeller design was implemented into an aircraft configuration by Barnes in [7, 9], where a rotor of low solidity was used in propulsive conditions and one with a high solidity was used in regenerative conditions. Another suggestion was to have a design that is a compromise between the two, otherwise yielding “good, but not ideal, effectiveness in both charging and power delivery modes”, or to design a propeller with an even number of blades, with half optimized for maximum regenerative performance and the other half optimized for propulsive performance [6]. Designing propeller blades that fold inward or outward mid-flight introduces an undesirable level of complexity, especially for general aviation applications, which is the primary interest of this work. The work of this project is mainly targeted towards finding an acceptable compromise between performance in propulsive and regenerative operating conditions, as suggested by the preceding authors. Allowing the propeller to passively deform during its operation was not suggested, although it may enable a suitable compromise in performance.

More recently, Erzen *et al.* [2] presented a propeller design for exploiting the capability of the *Pipistrel Alpha Electro* for in-flight power recuperation. The propeller design approach involved considering three disciplines: aerodynamics, electronics, and operations. For the aerodynamic design, low-fidelity computational tools were used such as XFOIL to optimize the airfoil shape and blade design. RANS simulations were later used for verification purposes. The design of the electrical system involved allowing the capability of a hardware-enabled bidirectional power flow, with the ability to optimize the angular velocity and torque combination for maximized energy-harvesting at given descent rates [2]. This was accomplished by the power control unit and main computer, which allowed the aircraft to switch between propulsive and regenerative operation without additional pilot inputs [2]. Finally, the strategic design included a design of the mission profile to minimize overall energy consumption, the flight pattern was designed to exploit the benefits of reverse thrust, including the requirement of a steeper descent. As a result, the propeller that was designed for both propulsive and regenerative operation yielded a 19% decrease in energy consumption and a 27% increase in the number of traffic pattern circuits [2]. The observed improvement in performance is heavily dependent on the selected flight pattern, and thus a consistent mission must be considered to realistically estimate potential decreases in consumption.

The results obtained by Erzen *et al.* in [2] present a positive outlook on benefits that may be realized through the use of dual-role propellers, although the performance in energy-harvesting conditions is generally very limited for propellers that are designed for propulsive operation only. For example, in 2019, Sinnige *et al.* [1] investigated the interaction effects between wing and propeller of a wingtip-mounted tractor propeller in propulsive and energy-harvesting conditions. Although most of the results obtained cover the interaction effects between wing and propeller, experimental and numerical results on the blade loading, slipstream characteristics, and energy-harvesting performance of an isolated propeller were also collected. As shown in Figure 1.2, the authors were first to observe that the thrust and power coefficient curves flatten considerably in regenerative conditions, since the TUD-PROWIM propeller under investigation is not designed to operate in these conditions. As a result, the energy-harvesting mode caused the blades to encounter separation and a distorted loading (and induced velocity) distribution that did not resemble the usual distributions of a minimum-induced-loss propeller. Accordingly, the peak energy-harvesting efficiency obtained by the authors was approximately 10%, which is low in comparison to small conventional wind turbines [1]. The qualitative results from this work were again obtained by Goyal *et al.* [10], where a detailed study was performed on isolated energy-harvesting propellers.

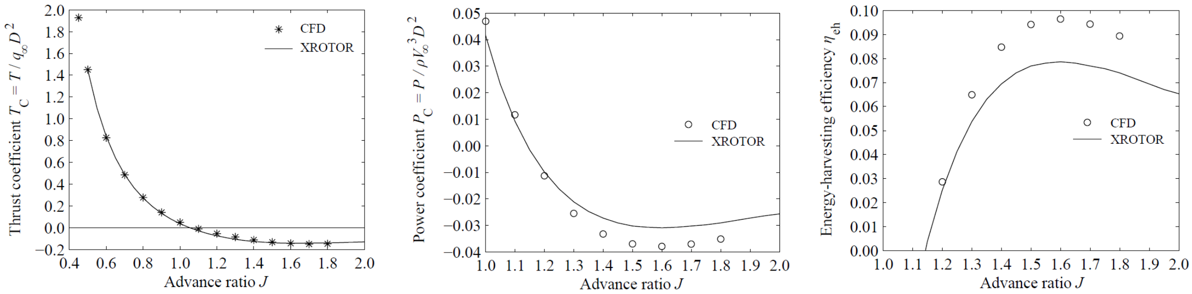

(a) Thrust. **(b)** Power. **(c)** Efficiency.

Figure 1.2: Propeller performance data that was obtained by Sinnige *et al.* [1].

Goyal *et al.* [10] investigated the performance of an isolated propeller in propulsive and regenerative conditions, both experimentally and with a multi-fidelity numerical approach. The propeller considered by Goyal *et al.* has a similar design to the propeller that was analysed by Sinnige *et al.* in [1] and the size and number of blades is different. Low-fidelity simulations were performed using a BEM code that accounted for effects of rotation using RFOIL (see [11] for the underlying theory). High-fidelity simulations were performed using experimentally validated RANS simulations. The observations made by the authors were similar to that of Sinnige *et al.*: the flow field is dominated by separation and viscous losses in energy-harvesting conditions and the blade loading distribution is considerably distorted, thus leading to a significantly degraded performance and a relatively low maximum energy-harvesting efficiency. This presence of separation means that it is crucial to account for effects of rotation in the prediction of blade loading, as the Coriolis and centrifugal forces encountered by the blades have a profound influence on viscous effects such as separation and transition. It is clear that RANS simulations tended to always yield acceptable results, whereas the BEM code tended to yield noticeable discrepancies in the presence of separated flow. The authors' BEM code noticeably overpredicted the power coefficient at high advance ratios, and errors were equivalently observed in the predicted energy-harvesting efficiency despite a reasonable agreement in the predicted thrust coefficient. This is shown in Figure 1.3. The authors suggest that this is due to an overprediction of separation and an underprediction of the drag [10]. Nevertheless, the general trends are reasonably predicted up to around the peak energy-harvesting efficiency.

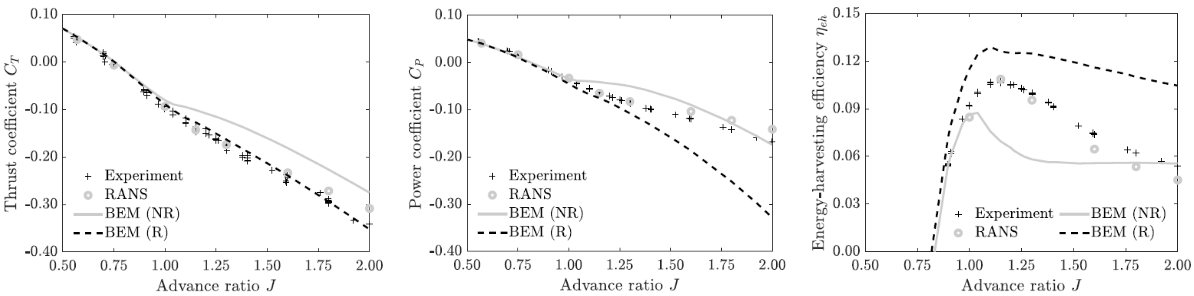

(a) Thrust. **(b)** Power. **(c)** Efficiency.

Figure 1.3: Performance data for the TUD-XPROP-3 propeller obtained by Goyal *et al.* [10].

Plots of the streamlines at various blade sections are provided in Figure 1.4, as computed by Goyal *et al.* to indicate locations where the flow is separated. The qualitative trends regarding the presence of flow separation in energy-harvesting conditions were also reported by other researchers, such as Binder *et al.* [12] for a ducted fan, which encountered separation originating at the tips of the blade with decreasing rotational speed and constant freestream velocity. Binder *et al.* hypothesized that when operating a fan in energy-harvesting conditions, there will always be a region of separated flow originating from the tips, as shown in Figure 1.5. However, the model used by Binder *et al.* is of a ducted fan with both a rotor and a stator [12]. Compared to the single-row unducted propellers that are of interest to this project, the presence of the stator and duct alters the flow conditions near the blade tips in addition to the mass flow rate. The results presented in [12] are thus not entirely applicable, although their predictions of generic flow conditions at different operating points were also reported by Sinnige *et al.*, Goyal *et al.* [1, 10].

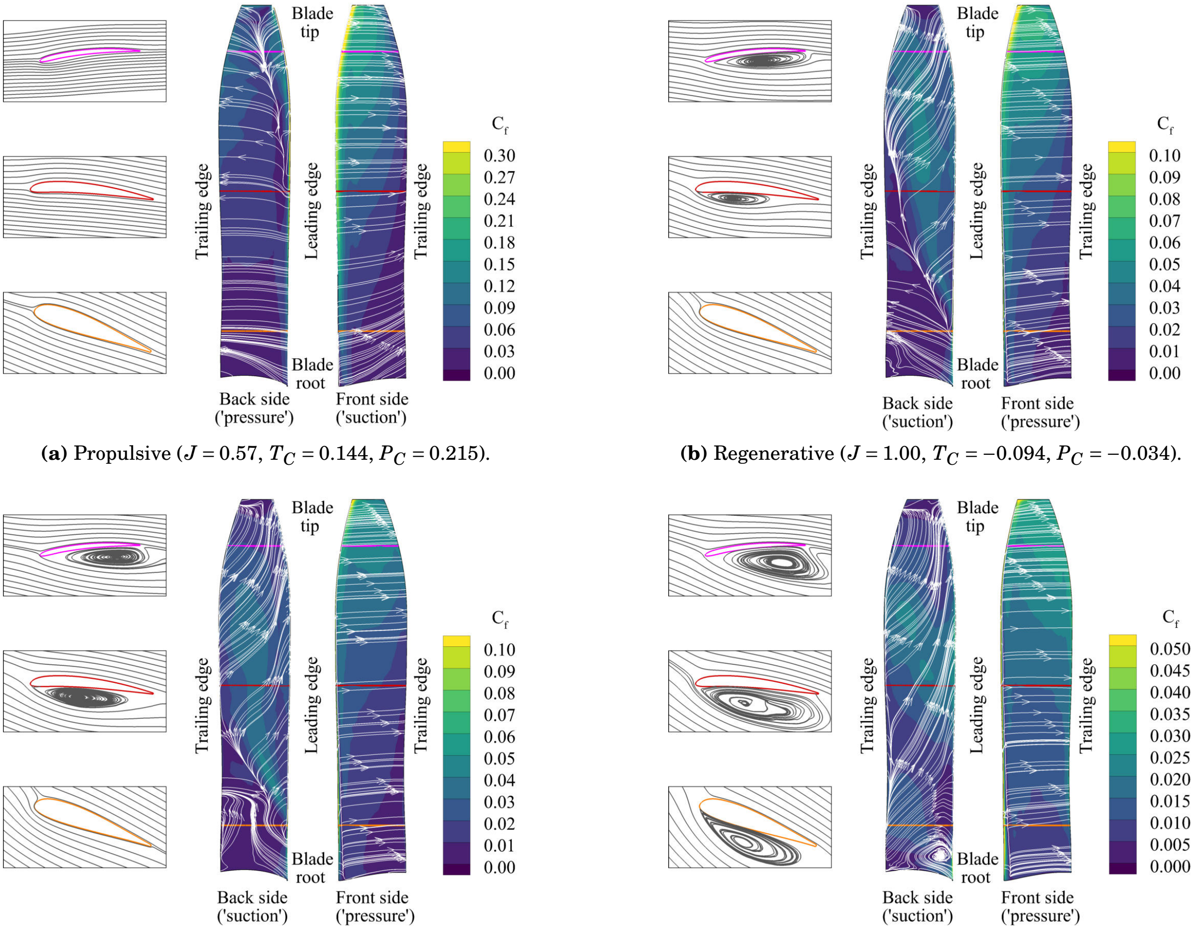

(a) Propulsive ($J = 0.57$, $T_C = 0.144$, $P_C = 0.215$).

(b) Regenerative ($J = 1.00$, $T_C = -0.094$, $P_C = -0.034$).

(c) Regenerative ($J = 1.15$, $T_C = -0.108$, $P_C = -0.043$).

(d) Regenerative ($J = 1.60$, $T_C = -0.093$, $P_C = -0.025$).

Figure 1.4: Friction coefficient and streamline plots for the TUD-XPROP propeller at propulsive and regenerative modes, showing flow separation originating at the tips with increasing advance ratio [10].

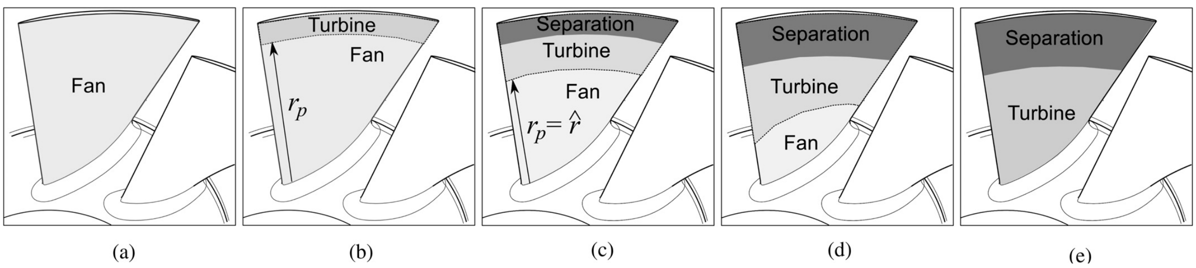

Figure 1.5: Trends hypothesized by Binder et al. for an increasing flow coefficient from (a) to (e) [12].

Lastly, Nederlof *et al.* [13] identified important effects on performance associated with variations in blade collective pitch angle. First, it has been shown that the peak energy-harvesting efficiency increases with decreasing pitch setting, while the propulsive efficiency increases with increasing pitch setting [13]. Additionally, because the advance ratio of maximum energy-harvesting efficiency tends to decrease with decreasing pitch setting, the rotational speed is proportionally higher, which allows more power to be recovered. Nederlof *et al.* also identified that the thrust coefficient decreases proportionally faster than the power coefficient with decreasing pitch setting, which causes the maximum turbine efficiency to decrease with decreasing pitch setting. Additionally, the diagram shown in Figure 1.6 shows that the negative lift vector already points largely in the direction of negative torque for higher pitch settings, and therefore the negative blade sectional angle of attack does not need to be as high as it otherwise needs to be at low pitch settings for the propeller to operate in energy-harvesting conditions. For this reason, the peak turbine efficiency tends to occur at lower advance ratios with decreasing pitch setting, and more negative thrust is required to reach energy harvesting conditions with decreasing pitch setting. Plots of the various efficiencies in addition to the thrust and power coefficient as a function of advance ratio are shown in Figure 1.7 and Figure 1.8 to support this discussion.

(a) Low pitch setting. **(b)** High pitch setting.

Figure 1.6: A comparison of relevant blade forces and flow velocity components acting on a propeller blade section with either a low- or a high-pitch setting during energy-harvesting conditions [13].

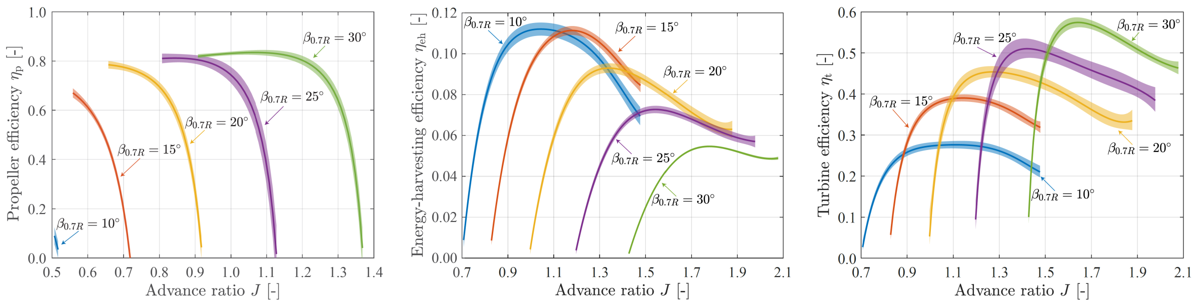

(a) Propulsive efficiency. **(b)** Energy-harvesting efficiency. **(c)** Turbine efficiency.

Figure 1.7: Efficiency plots for the TUD-XPROP-3 propeller at varying blade pitch settings [13].

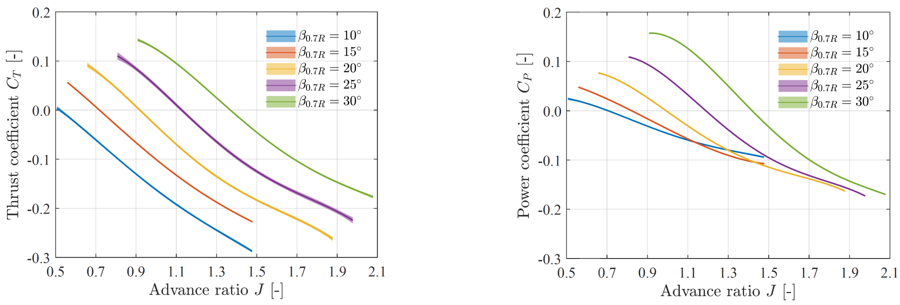

(a) Thrust coefficient. **(b)** Power coefficient.

Figure 1.8: Performance plots for the TUD-XPROP-3 propeller at varying blade pitch settings [13].

To conclude, it has first been shown that blade loads encountered during regenerative and propulsive conditions are directly opposite to each other. Since the pioneering work of MacCready [6], few designs have been proposed for a propeller that can also operate as a wind turbine during flight, and the research within this area is somewhat sparse in academic contexts despite its potential impact. Few promising examples have been presented, with the most notable resulting from the work of Erzen *et al.* [2], where improvements were observed over the otherwise conventional propeller. Conversely, it has been shown by Barnes [7–9], Sinnige *et al.* [1], Goyal *et al.* [10], and Binder *et al.* [12] that due to a vastly different loading on the blades between the two modes of operation, a conventional propeller design will encounter detrimental effects of separation and other losses during energy-harvesting, therefore implying that a new propeller design should be proposed. This also has been found to result in noticeable inaccuracies between the low-fidelity methods that are normally used to evaluate propeller performance in comparison to experimental data [10]. Finally, important trends associated with the blade collective pitch angle have also been identified by Nederlof *et al.* [13], indicating that blades of a dual-role propeller may benefit from being able to change their pitch setting during different flight phases.

1.2. PROPELLER AEROELASTICITY AND AEROELASTIC TAILORING

Shirk *et al.* [14] provided a historical background and motivation for the general use of aeroelastic tailoring for various applications. The authors also performed trend studies and discussed applications of this approach, both for yielding performance improvements and decreasing weight. Shirk *et al.* primarily discussed the advantages of this approach towards the design of aircraft wings, although they also highlighted the patent of Munk [15], involving the concept of a wooden propeller blade with diagonal plies that will twist favourably for improved performance with increasing load. A similar patent application was placed in 2015 by Wood and Ramakrishnan [16], with General Electric, for an open-rotor concept, which has composite blades that will deform favourably under increasing load to yield decreases in noise.

Several studies on the design of flexible propellers or wind turbines for improved performance in their normal operating modes were performed following the published works of Munk and Shirk *et al.*. For example, the earliest use of aeroelastic tailoring for the design of composite propellers appears to have been undertaken by Dwyer and Rogers [17], who used a BEM code to investigate differences in performance between rigid and flexible blades. The authors modified individual ply orientations to yield a coupling between the centrifugal force and shear strain, although they found that the blade mass was too small to yield large enough centrifugal forces to provide a desirable amount of twist. The authors solved this problem by including concentrated masses at several spanwise positions. A maximum improvement of 5% was found at on-design conditions, with a 20% gain at off-design conditions for a fixed-pitch propeller. For a variable-pitch propeller, the authors found an improvement of at-most 5%. Nevertheless, it is unclear whether Dwyer and Rogers made any attempt to improve efficiency without affecting the thrust coefficient, as was successfully attempted in other research that is presented in this section. Indeed, it is also necessary to prevent the thrust coefficient from deceasing when modifying a baseline propeller to maintain its original capabilities. Even if the authors did not consider this, their work demonstrates that propeller performance may be noticeably influenced by aeroelastic tailoring.

Years later, Yamamoto and August performed a two-way coupled structural and aerodynamic analysis of a large advanced propeller blade in [18] using the NASTRAN finite element analysis software for the structure and a 3D finite-difference Euler solver for the aerodynamics. The structure was discretized using shell elements, and a nonlinear finite-element solver was used to iteratively compute deformations, which affect aerodynamic loads. This process would be repeated until convergence. The authors demonstrated that the centrifugal loads will always untwist the blade, whereas the aerodynamic loads can either increase or decrease the amount of twist of each propeller blade. This was also observed by Sodja *et al.* [3]. Yamamoto and August also suggested that the centrifugal loads produced most of the total deformations affecting performance, although this may be configuration-dependent.

Chattopadhyay *et al.* later used blade element momentum theory and the finite element method (treating the blade as a composite box-beam) to optimize the design of a prop-rotor for maximum cruise efficiency and hover figure of merit [19]. They formulated a multi-level optimization problem, which used nonlinear programming for the continuous design variables (including the rotor geometry) to maximize aerodynamic performance, and integer programming for the discrete design variables (including ply orientations and thicknesses). This work is mostly not relevant to the current project, firstly because the authors focused on maximizing the hover figure of merit, which is of course not relevant to propellers. Additionally, they did not use aeroelastic tailoring to improve performance, and instead relied purely on aerodynamic optimization for this, with aeroelastic tailoring only being applied to minimize deformations. Thus, the optimization results cannot be used to indicate the potential for improvements to be made, and the optimization method that was applied in this work has not been considered anyway.

Around a decade after the work of Chattopadhyay *et al.*, a different methodology from theirs was applied by Sandak and Rosen [20] to design a flexible propeller with improved performance. Instead of using a fully flexible blade, the authors designed a rigid blade with a flexible element in the root section. The nonlinear torsion spring element reacts to varying loads at different operating conditions to change the collective pitch angle of the propeller. The authors mainly intended on using this to improve performance at problematic flight regimes (such as during take-off, initial climb, or low-speed flight). To accomplish this, a multi-objective optimization procedure was applied to maximize the weighted efficiency in different flight regimes, with design variables being the spring constants. It was found that straight blades exhibit a small torsional moment, and therefore the spring deformation depends primarily on bending deformations in these cases [20]. Additionally, the authors were successful in exploiting the geometric bend-twist coupling that results from a backward sweep angle. Overall, a potential improvement in efficiency between 7 and 17% was observed. Though, this is dependent on the propeller blade geometry as well as chosen weight functions. Moreover, the physical implementation of their root spring model was not investigated in this work, and therefore these numbers may not be realistic in practical applications. Nevertheless, it was suggested in the authors' conclusion that the non-physical torsion spring model may be physically realizable using anisotropic composite materials.

Sodja *et al.* [3] continued the work of Sandak and Rosen through the development of an optimization procedure for the geometric design of a flexible propeller made from an isotropic material, with design variables corresponding to the blade axis geometry. The work of Sodja *et al.* consisted of aerodynamic optimization, allowable stress design, and blade-axis optimization. The authors used a BEM model for the aerodynamics, and the finite element method based on *Euler-Bernoulli beam theory* and *Saint-Venant theory of torsion* for the structure. The authors' optimizer minimized the curvature of the efficiency vs. advance ratio curve and maximized efficiency at on-design conditions. This framework was selected to yield designs with maximum on- and off-design efficiency. It was found that the deformation of the blade is heavily affected by the sweep angle, as the aerodynamic loads tended to deform the forward-swept (FB) blade opposite to the direction of rotation and away from the propeller plane, with the opposite effect occurring for the blade with zero or backward sweep [3]. The inertial forces always deformed the blade towards the propeller plane. The result of this is that for propulsive operation, forward-swept blades exhibit an unfavourable wash-in effect that results in a relatively narrow range of advance ratios of high propulsive efficiency [3]. Backward-swept blades (BB) conversely have a favourable deformation with increasing freestream velocity and constant speed [3]. As the load increases, the bend-twist coupling results in a wash-out effect that maximizes off-design propulsive efficiency. Thus, Sodja *et al.* demonstrated the potential to increase on- and off-design efficiency of fixed-pitch propellers by introducing bend-twist coupling through blade-axis flexibility. The authors also successfully validated their findings through the collection of experimental data. The propeller blades under investigation are shown in Figure 1.9 to clarify the authors' valuable physical insights.

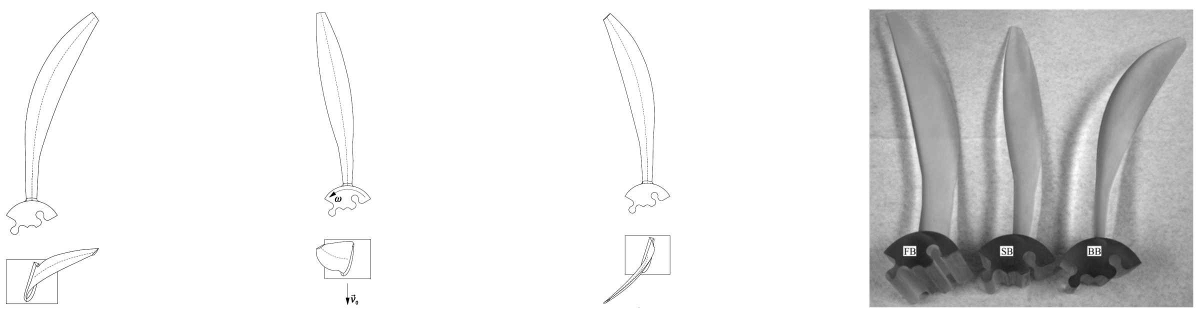

(a) BB. **(b)** SB. **(c)** FB. **(d)** Manufactured blades.

Figure 1.9: Pictures of the modelled and physical propeller blades analysed by Sodja *et al.* [3, 21].

A different approach toward the design of a propeller blade with the ability to passively deform under aerodynamic loads was applied by Heinzen *et al.* [22]. In this work, rather than using a flexible material, the propeller blades were allowed to pivot freely about their radial axis, and the aerodynamic design of the blades were conducted so that their pitching moments would be balanced at collective pitch angles that yield favourable performance. The authors used variations in blade pivot point and sweep angle to control the blade's static margin over a range of operating conditions. Flexible propeller blades have a fixed pitch angle, and their geometry or structure result in perturbations of the elastic axis or twist angle to yield improvements in performance at applicable operating conditions.

Most recently, Möhren *et al.* developed a static aeroelastic analysis procedure for propellers, which couples a finite element structural model to a blade-element momentum theory aerodynamic model. The authors used their model to evaluate the performance of flexible propellers during propulsive conditions, to characterize the importance of elastic effects on propeller performance. In particular, the thrust evaluated with rigid propellers was compared to the thrust evaluated with flexible propellers. Möhren *et al.* found that blade elasticity had the largest effect on performance in cases of low disk loading. Moreover, propellers with a large diameter or a high amount of sweep were found to be most impacted by aeroelastic effects.

In addition to the journal publications that have been previously presented, multiple PhD theses have also been produced on the aeroelastic tailoring of propeller or wind turbine blades for yielding performance improvements. The earliest work was done by Khan [4], who developed a coupled propeller aerodynamic and structural analysis framework and applied it towards the structural design of a flexible composite propeller in [4]. The aerodynamic model is an application of blade element momentum theory and the structural model is an application of the finite element method, where the propeller was represented by a single laminate of five plies. The ply orientations were adjusted to yield increases in the thrust coefficient, C_T, and propulsive efficiency, η_{P}, and decreases in the power coefficient, C_P. The same methodology was used to characterize the effect of bend-twist coupling on propeller performance in a subsequent paper published by Khan *et al.* [24]. In both works, it was shown that it is possible to yield noticeable increases or decreases in the thrust coefficient, power coefficient, and efficiency over a wide range of advance ratio values through modifications of only the ply orientations of a flexible composite propeller with a constant geometry. Moreover, Khan was notably successful in improving on-design efficiency while maintaining the baseline thrust coefficient, and generally was able to obtain significant changes in performance through the introduction of bend-twist coupling. In the work of Khan *et al.* [4, 24] and Chattopadhyay *et al.* [19], only symmetric stacking sequences were considered to simplify the calculation procedure and to eliminate any elongation coupling, unlike the previous work of Dwyer and Rogers [17].

Two notable PhD theses were produced at the TU Delft on aeroelastic tailoring of flexible wind turbine blades: first in 2016 by Ferede [25], and then in 2019 by Hegberg [26]. In the thesis of Ferede, an optimization procedure is developed to minimize the blade mass of stall-controlled wind turbines through modifications of the blade geometry and ply orientations. Lamination parameters were also used to ensure that all structural design variables are continuous. The aerodynamic loads are evaluated using blade element momentum theory and the deformations are evaluated using the nonlinear Timoshenko beam model. The purpose of this work was to present a stiffness optimization methodology, and this notably resulted in a considerable mass decrease. The work of Ferede also highlights the benefit of using unbalanced laminates, as the presence of extension-shear and bend-twist coupling was exploited to yield performance improvements. This finding was also demonstrated by Ferede *et al.* [27] in the following year. The more recent work of Hegberg concerns the design of pitch-regulated wind turbines. In this case, the aerodynamic loads were instead evaluated using an inviscid vortex lattice method with mutually interfering spanwise and chordwise vortex panels, and a prescribed cylindrical wake. The aerodynamic model is considered to have an equal fidelity to the structural model, which is similar to the model that was used by Ferede. Lamination parameters were again used to allow for a gradient-based optimization, and the objective function in this case is to minimize the blade mass when subjected to two separate load cases: one to represent typical wind loads and another to represent extreme wind shear. A noticeable decrease in blade mass was observed from the optimization procedure.

Static aeroelastic analysis procedures for propellers have been developed and applied by other researchers, including Möhren *et al.* [23] and Gur and Rosen [28]. At the TU Delft, the static aeroelastic analysis program, *PROTEUS*, was developed by Werter and De Breuker [29] and applied towards the conceptual design of aircraft wings in [30, 31] and wind turbine blades in [26, 27]. The structural model of PROTEUS is similar to the method applied in [23], as both models apply the finite-element method to solve deformations on a reduced-order Timoshenko beam element mesh, which is obtained from the 3D blade structural geometry using a cross-sectional modeller. During this project, PROTEUS has been modified to be applicable to propellers through the use of a BEM model for the aerodynamics and a change in the optimization problem to improve propeller performance rather than to minimize weight.

The presented state-of-the-art review shows several promising examples regarding the application of aeroelastic tailoring. It is apparent that aeroelastic tailoring has received attention from both industrial and academic parties. Moreover, when applied towards the design of propellers, aeroelastic tailoring has largely been used towards the improvement of performance in propulsive conditions (increasing efficiency or thrust over a range of applicable advance ratios). However, aeroelastic tailoring has not been applied towards improving the regenerative performance (increasing the energy-harvesting or turbine efficiency) of a propeller. This research gap has been addressed by this thesis through the development and application of a novel propeller design framework that considers effects of static aeroelasticity. This research builds upon the work of Sodja *et al.* [3, 21] and Khan *et al.* [4, 24] by providing physical insights into effects on regenerative or propulsive performance through variations in structural design variables and geometric parameters (including the blade axis geometry and blade stiffness properties). This has been accomplished using an analysis method that is similar to the method of [23] and an optimization procedure that is similar to [4, 26]. In this way, propeller performance in propulsive conditions is not being improved directly. Instead, the goal of this work is to address suggestions made in [6, 7, 32] to design a propeller that minimizes mission energy by providing a compromise between performance in propulsive and regenerative modes. This distinction is what separates this work from previous research.

1.3. RESEARCH OBJECTIVES AND QUESTIONS

From the discussion that was provided above, the following observations were made:

- Conventional aerodynamic models used to evaluate propeller performance should be modified to account for effects resulting from blade rotation and flow separation. These effects are known to cause conventional propellers to underperform significantly during energy-harvesting conditions.
- Loads encountered by the propeller during regenerative operation are opposite to the loads encountered during propulsive operation, and therefore the ideal aerodynamic design of a dual-role propeller may be profoundly different from that of a conventional propeller.
- Aeroelastic tailoring has the potential to yield noticeable changes in propeller performance, particularly due to effects of bend-twist or extension-shear coupling.
  - Most research concerning propeller aeroelastic tailoring aims at improving efficiency in propulsive mode, and aeroelastic tailoring has not been applied towards the design of dual-role propellers.
  - Propulsive efficiency of a propeller is generally improved through modifications in the structural design by introducing a wash-out effect, as this will primarily result in deformations that decrease the blade angle of attack with increasing blade loading (and vice versa). This might also delay separation.
  - It may be interesting to exploit synergies between geometric parameters and structural design variables, as effects of bend-twist coupling were notably amplified in cases involving propeller blades that have either large diameters or large amounts of sweep. The diameter and sweep have been held constant during this research to solely assess the influence of aeroelastic tailoring on performance.
  - It was found by Möhren *et al.* [23] that the effect of blade elasticity increases for a decreasing stiffness or increasing blade loading. This suggests that it may be possible to yield notable improvements in performance during the propulsive mode, which is characterized by a high blade loading (particularly during climb). Conversely, this suggests that the effect of aeroelastic tailoring may not be as noticeable during the descent, where the loading encountered by the blade is significantly lower.
  - Only one example has been found (from Dwyer and Rogers [17]) involving the application of extension-twist coupling, through the use of a non-zero $\boldsymbol{B}$-matrix, to yield twist deformations that are dependent on centrifugal loads. For this case, concentrated masses needed to be added near the middle and tip of the blade so that performance enhancements would be noticeable. For this reason, bend-twist and extension-shear coupling, which primarily couple twist deformations to aerodynamic forces, are expected to be the dominant mechanisms influencing propeller performance. Accordingly, balanced laminates (with $\boldsymbol{B} = \mathbf{0}$) have been exclusively considered during this project.

The above points have been applied during this research project to establish a reasonable project scope and to formulate relevant research questions and objectives. Particular emphasis has been placed on implementing an efficient aeroelastic analysis method that maintains a reasonable level of accuracy and precision, as well as on formulating an optimization problem that appropriately includes both the propulsive and regenerative operating conditions.

1.3.1. RESEARCH OBJECTIVES AND ASSOCIATED QUESTIONS

In previous research, comprehensive sensitivity studies involving variations in laminate properties have not been performed. Moreover, aeroelastic tailoring of dual-role propellers has not previously been considered, as all previous investigations focused on only the propulsive case. Thus, the first objective of this research project is to study the behaviour and structural design trends of a flexible dual-role propeller of constant geometry made from composite materials under static aerodynamic loads. A numerical aeroelastic analysis and optimization procedure has been developed to perform sensitivity studies and optimization of the flexible composite propeller. For the sensitivity studies, propeller performance quantities and deformations were evaluated at varying ply orientations and laminate thicknesses over a range of operating conditions characterizing propulsive and regenerative conditions. These results were used to identify important structural design trends, as well as to compare how performance in propulsive mode differs from performance in regenerative mode. During the optimization, a theoretical propeller structural design was obtained that minimizes power consumption while maintaining an approximately equivalent thrust across a fixed mission profile with a variable cruise distance. Both variable-pitch and constant-pitch propellers were considered for the full mission optimization studies. Optimization studies were also performed for each mission segment individually to compare with results from the full mission optimization. The results obtained from the optimization procedure have been used to show the effectiveness of aeroelastic tailoring when applied towards the design of propellers. Additionally, ideal structural design characteristics of dual-role propellers were obtained using the structural blade designs obtained from the optimization studies. Through these investigations, the extent that dual-role propeller performance may be enhanced through the application of aeroelastic tailoring has been explicitly shown and favourable structural design characteristics have been identified. Finally, off-design performance of each optimal blade design has been evaluated through the collection of performance maps over a range of operating conditions characterizing both the propulsive and the regenerative case. These results have been used to identify how the optimal propeller blades generally perform. Corresponding to the research objectives discussed in this section, the following research questions have been formulated and answered during this project.

(1) *To what extent can further enhancements in dual-role propeller performance be obtained solely through the application of aeroelastic tailoring?*
   - (a) *Which structural characteristics (i.e. material properties, ply orientations, and laminate thicknesses) have an important influence on dual-role propeller performance, and how are performance quantities and deformations affected by variations in these structural characteristics?*
   - (b) *How do structural modifications in favour of improving performance during propulsive operation affect performance during regenerative operation?*

(2) *How does the application of aeroelastic tailoring impact overall energy consumption over a generic climb-cruise-descent mission profile for constant-pitch or variable-pitch dual-role propellers?*
   - (a) *How does the blade structure that is optimized for each individual mission segment differ from the blade structure that is optimized for a mission with a variable cruise distance?*
   - (b) *How do energy consumption results from optimization studies involving each individual mission segment compare with results from optimization studies involving the full mission?*
   - (c) *How do the optimal propeller blade designs perform over a range of operating conditions that may otherwise not be considered during the optimization studies?*

This research project is expected to build upon the work of Sodja *et al.* [3, 21] and Khan *et al.* [4, 24] by providing physical insights into effects on regenerative or propulsive performance through variations in structural parameters, as previous work considered either only the structural design of propellers for propulsive operation or the geometric design of flexible propellers. Thus, the goal of this work is to address suggestions made in [6, 7, 32] to design a propeller that provides a compromise between performance in propulsive and regenerative modes through the implementation of the modern technique of aeroelastic tailoring. This distinction is what separates the work that is planned for this thesis from the existing body of knowledge. A similar investigation to the one that has been applied during this project was also applied by Ferede [25] and Hegberg [26] for the design of wind turbine blades.

The discussed objectives have been realized through the application of a similar structural analysis method to Möhren *et al.* [23] and Hegberg [26], integrated within a gradient-based optimization framework. The objective function of the optimization problem involves maximizing propeller performance during both propulsive and regenerative operation. Classical laminated plate theory has been used to represent the composite structure (like the work of [4, 17, 25, 26]) and a geometrically nonlinear beam model has been used to evaluate blade deformations (similar to the work of [3, 21, 25, 26]). Furthermore, structural properties of each laminate have been represented using lamination parameters, as was done in [25, 26], so all design variables remain continuous. Moreover, as indicated in [1, 10, 13], the aerodynamic loads are strongly affected by flow separation, and it is therefore necessary that the selected aerodynamic model can account for these effects. Thus, a blade-element momentum theory model with corrections for rotational effects has been used to evaluate loads, similar to the model that was applied by Goyal *et al.* [10].

1.4. THESIS SCOPE AND OUTLINE

A comprehensive review of literature on the relevant disciplines concerning this research project was completed as a separate project before beginning any work for this thesis. The contents of this literature study are provided in Appendix B for reference. The past research that was reviewed covered aerodynamic, structural, and aeroelastic analysis methods for propellers, as well as relevant optimization strategies. Some information provided in this literature study may extend beyond the scope of this thesis, although the research that was compiled and critically reviewed has been used to establish the scope for this work, as well as to motivate decisions made concerning the methodologies, assumptions, and formulations applied during this project. Decisions made using results from the literature study are summarized below.

The aeroelastic analysis and optimization procedure under consideration during this project is a modified version of PROTEUS, which was previously developed and applied at the TU Delft towards the conceptual design of aircraft wings in [30, 31] and wind turbine blades in [26, 27]. PROTEUS has been selected for this project because it already features many of the modelling characteristics of interest, including the capability to account for nonlinearities in geometry and loading, as well as a very low computational requirement despite providing a medium to high level of fidelity. The structural model of PROTEUS is similar to the method applied by Möhren *et al.* [23], as both models apply the finite-element method to solve deformations on a reduced-order 1D Timoshenko beam element mesh, which is obtained from the 3D blade structural geometry using a cross-sectional modeller. The difference between the two approaches is that PROTEUS accounts for geometric nonlinearities due to large beam deformations, as well as nonlinear structural responses to loads (such as the centrifugal-stiffening effect). Modifications to PROTEUS were made to account for the aerodynamics of propellers through the use of a BEM model, the inclusion of centrifugal forces in the structural model, and the implementation of a suitable optimization problem that features an appropriate objective and constraint function. Blade element momentum theory was selected because it provides a sufficient level of precision and has the lowest computational cost, making it ideal for optimization. The effect of rotation on fluid particles in the boundary layer has been accounted for through the use of the RFOIL during the collection of airfoil polar data because it is the only physics-informed stall-delay model that was identified from the literature. Finally, a two-way coupled aeroelastic solver is required to couple the aerodynamic and structural models from different tools, as the structural deformations must influence the aerodynamic loads to allow the optimization to proceed. For this, a tightly coupled approach has been applied, like the method implemented by Ferede [25] and Hegberg [26]. This method was selected because it is robust and guarantees fast convergence.

The TUD-XPROP-3 was used as the baseline propeller for both optimization and verification/validation out of convenience. This propeller was selected for verification and validation of the aerodynamic and aeroelastic analyses because numerical and experimental results for it exist in both propulsive and regenerative modes from Goyal *et al.* [10] and Nederlof *et al.* [13]. For the optimization problem, the power consumption was minimized whilst maintaining thrust requirements in both propulsive and regenerative conditions. Constraints have also been applied to ensure that strains, deformations, and power consumption values do not exceed the maximum allowable values, similar to the approach of Sodja *et al.* [3]. Finally, to account for both propulsive and regenerative operating conditions, a weighted multi-objective optimization procedure was applied through the evaluation of approximate total energy consumption in a generic climb-cruise-descent mission with a varying cruise distance, like the work of van Neerven [33], and Scholtens [34]. This ensures that the optimizer appropriately accounts for all relevant operating conditions of the propeller, with weighting factors that are assigned based on the mission profile of interest. Both constant-pitch and variable-pitch propellers were investigated to provide a complete picture of the effects of aeroelastic tailoring. For optimization, previous researchers have parametrized the propeller blade structure using a combination of discrete and continuous variables to represent the distribution of laminates, although more recent developments have been made towards the derivation of so-called *lamination parameters*, which enable the design space to be represented by a fixed number of continuous design variables. As a result, the use of lamination parameters enables the application of a gradient-based optimization procedure, and thus they have been selected as structural design variables.

When designing a dual-role propeller for an aircraft, it is ideal to consider structural and geometric design variables, the mission strategy, electrical system design, and overall aircraft design. For this project, only the uninstalled propeller has been considered and aerodynamic optimization of the propeller has not been applied before the structural optimization, as the propeller under consideration throughout most of this work represents the geometry of a previous-generation aircraft propeller. Nevertheless, applying an aerodynamic optimization before the structural optimization to yield a rigid blade geometry that maximizes performance may have yielded more realistic conclusions to the research objectives. It also would have been beneficial to consider the concurrent application of aerodynamic and structural optimization, considering both geometric and structural design variables, to yield an optimal flexible blade design with greater performance than what would otherwise be obtained through aeroelastic optimization alone. This investigation would even enable the direct comparison between performance enhancements obtained through aerodynamic optimization and aeroelastic optimization alone, which could provide insight into how the less-conventional approach of aeroelastic tailoring compares to the more traditional approach of aerodynamic optimization. The mission strategy under consideration during this project has also remained fixed, and the electrical system has not been considered. Thus, the mission profile and operating conditions considered in each segment have been held constant during the analysis. As discussed already, a generic climb-cruise-descent mission strategy has been assumed during the optimization, with varying cruise distances. In this way, coupling between aircraft design, aircraft mission, and propeller performance has been ignored during this thesis, as the mission analysis has only been used to quantify the relative importance of differing propeller operating conditions. Lastly, only structural design variables have been included during the optimization study, while the blade geometry has remained constant.

This thesis has six chapters, including its introduction. Details on the underlying theory and formulations used for the aerodynamic, structural, and aeroelastic analyses are first provided in Chapter 2. Chapter 3 subsequently contains the formulation used for the optimization problem under consideration, as well as an overview of the design study that was completed. Next, results from verification and validation of the aerodynamic, structural, and aeroelastic analysis methods that were applied during this project have been provided in Chapter 4. Chapter 5 then contains results and discussions from sensitivity studies and optimization cases, which were used to address the research objectives and answer the research questions for this thesis. Lastly, Chapter 6 contains conclusions from this work, answers to the research questions, and a list of future recommendations.

2

Propeller Analysis Methods

Underlying theory on the propeller analysis routines that were applied during this project are summarized in this chapter. Section 2.1 contains details on the aerodynamic analysis routine that was applied, Section 2.2 contains an overview of the structural model that was used, and Section 2.3 contains information on the nonlinear aeroelastic analysis procedure that was applied. An overall summary of the propeller analysis routine that was developed is lastly provided in Section 2.4.

2.1. Blade Element Momentum Theory

During this project, a blade element momentum (BEM) model has been used to evaluate propeller performance. The advantage of this approach is that it has a very low computational cost, while also being capable of accounting for all aerodynamic phenomena of interest when appropriate corrections are applied. Most BEM codes rely on the same assumptions and underlying theory, with a few minor differences in the engineering correction models that are included. With blade element momentum theory, the propeller blade aerodynamic loads are evaluated iteratively using both momentum theory and blade element theory, correcting the axial and tangential induced velocities until the loads evaluated with momentum theory are equal to the loads obtained from blade element theory. Thus, the 3D characteristic of the propeller flowfield is decomposed into a 1D conservation of momentum and 2D sectional aerodynamics. The BEM formulation that was applied during this research is based on the theory of Adkins and Liebeck [35].

2.1.1. Momentum Theory

With momentum theory, the thrust and torque distributions acting on each propeller blade are evaluated through a conservation of momentum. Diagrams of the control volume for a propeller in propulsive and regenerative conditions are shown in Figure 2.1. Momentum is added to the flow during positive thrust conditions, which causes the streamtube to contract in the direction of positive velocity, with the axial velocity at the propeller plane being $V_\infty + v_\mathrm{i}$ and the axial velocity far downstream being $V_\infty + v_\mathrm{w}$.

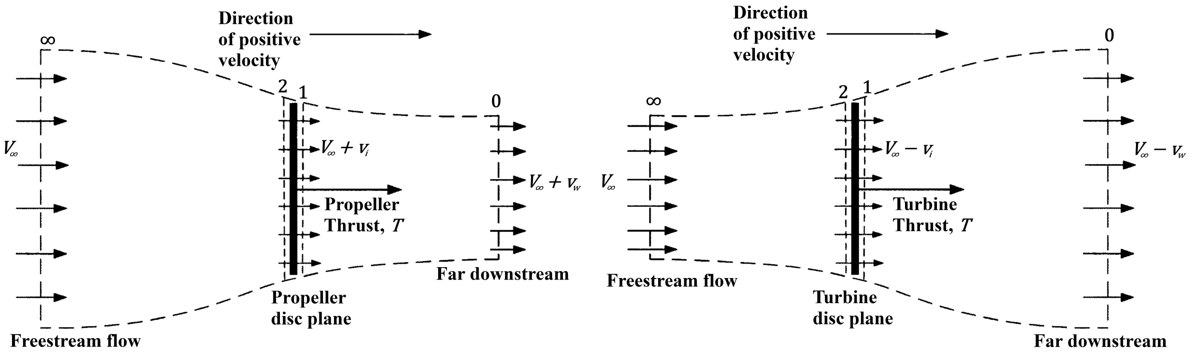

(a) Propulsive mode.

(b) Regenerative mode.

Figure 2.1: Control volumes used during the analysis with *actuator disk theory* (adapted from [36]).

Because the induced velocity components at each radial position of the propeller blade are different, the control volume pictured above is discretized into several annuli, with each annulus corresponding to a unique blade element. By applying a conservation of momentum through each annulus, the differential thrust and torque that is imparted onto the flow by the propeller can be evaluated. Diagrams of the annular control volumes at the rotor disk are shown in Figure 2.2.

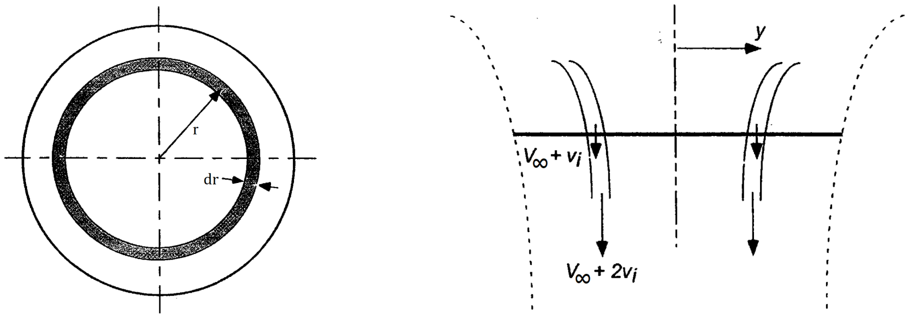

(a) Front view. **(b)** Sectional view.

Figure 2.2: Annulus of the propeller disk, which is used for the momentum analysis [37].

By evaluating the differential thrust and torque through each annulus of the control volume, the total thrust and torque has been evaluated using the following integral. The thrust and torque coefficients in this case are obtained through a normalization by the freestream dynamic pressure, q_∞. This normalization is not usually applied for the analysis of propellers, although this convention has been applied during this work because it yields a result that is more compatible with blade element theory.

$$T = \int_{r_{\text{root}}}^{r_{\text{tip}}} C_t \left(\frac{1}{2}\rho_\infty V_\infty^2\right) 2\pi r\, dr = \int_{r_{\text{root}}}^{r_{\text{tip}}} C_t\, q_\infty\, 2\pi r\, dr \tag{2.1}$$

$$Q = \int_{r_{\text{root}}}^{r_{\text{tip}}} C_q \cdot r \left(\frac{1}{2}\rho_\infty V_\infty^2\right) 2\pi r\, dr = \int_{r_{\text{root}}}^{r_{\text{tip}}} C_q\, q_\infty\, 2\pi r^2\, dr \tag{2.2}$$

One important drawback of this approach is that the mutual interference between blade elements and annular control volumes is not accounted for [38]. This means that 3D effects are generally not accounted for by BEM models unless engineering correction models are applied. In addition, it is assumed during this formulation that the flow encountered by the propeller is axisymmetric and steady, and the static pressure far upstream is approximately equal to the static pressure far downstream. With these assumptions, the thrust and torque coefficients are evaluated using Equation (2.3) and Equation (2.4), neglecting any losses in circulation due to effects associated with the propeller's finite number of blades [35].

$$C_t(r) = 4a(1+a) \tag{2.3}$$

$$C_q(r) = 4a'(1+a)\frac{\omega r}{V_\infty} \tag{2.4}$$

CORRECTIONS FOR ROOT- AND TIP-LOSSES

Equation (2.3) and Equation (2.4) both do not account for the fact that circulation decreases near the root and tip of each propeller blade. Indeed, when the chord at these locations is finite, blade element momentum theory will produce a non-zero lift when it should instead be zero. This loss of lift at the tip of the rotor is important and if it is neglected, then the thrust for a given amount of power will be noticeably overestimated [36, 37]. Various approaches to modelling this effect exist, although the simple analytical expression that was developed by Prandtl (see [39]) has been selected for this project.

$$F_{\text{root}} = \left(\frac{2}{\pi}\right)\cos^{-1}\left(\exp\left[-\frac{N_{\text{b}}}{2}\left(\frac{r - r_{\text{root}}}{r_{\text{root}}\left|\sin(\varphi)\right|}\right)\right]\right) \tag{2.5}$$

$$F_{\text{tip}} = \left(\frac{2}{\pi}\right)\cos^{-1}\left(\exp\left[-\frac{N_{\text{b}}}{2}\left(\frac{r_{\text{tip}} - r}{r\left|\sin(\varphi)\right|}\right)\right]\right) \tag{2.6}$$

$$F = F_{\text{root}} \cdot F_{\text{tip}} \tag{2.7}$$

A closed-form expression for the optimal circulation distribution over a lightly loaded propeller blade was developed by Goldstein [40]. The so-called Prandtl tip-loss factor, shown in Equation (2.7), provides a reasonable approximation to this exact solution, which improves as the number of blades increases, as indicated by sample plots of the circulation distribution shown in Figure 2.3. For this project, it is only important that the characteristic of losses near the blade tips is represented accurately, and therefore the Prandtl tip-loss factor was applied instead of the method of Goldstein.

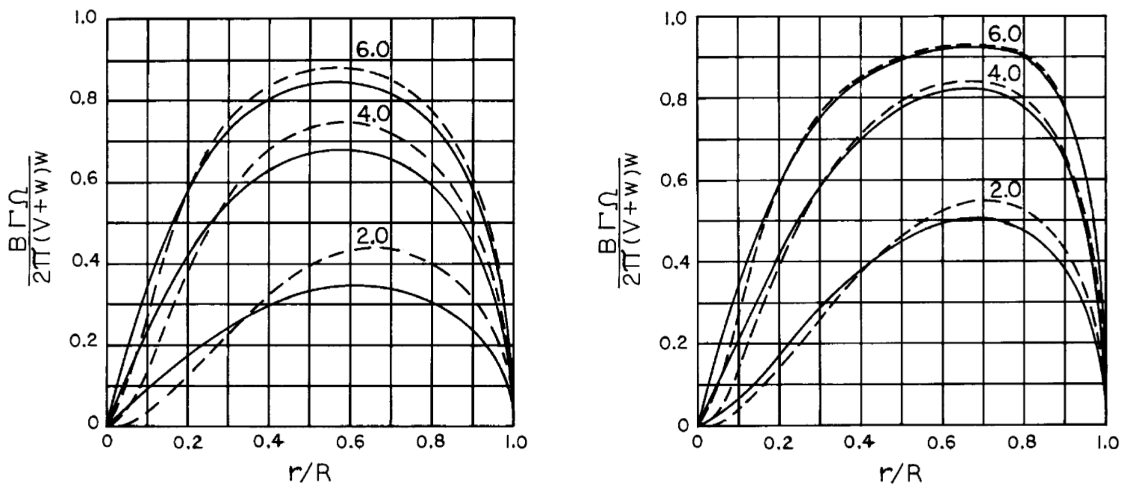

(a) Number of blades: 2

(b) Number of blades: 4

Figure 2.3: Ideal radial distributions of circulation for propellers with different tip-speed-ratios, λ_2 (dashed lines are the Prandtl approximation and solid lines are the exact solution of Goldstein) [41].

LARGE NEGATIVE INDUCTION FACTORS

Because the axial induction factor can either be positive (in propulsive conditions) or negative (in regenerative mode), it is important to consider circumstances where the value of the induction factor is large and negative. Because the velocity in the propeller wake is expressed by $V_\infty(1+2a)$, if a drops below -0.5, then the flow far downstream would reverse directions. This flow reversal is non-physical, as the actual flow entrains momentum from outside the wake and turbulence increases [42].

Several methods have been developed to correct for this, which are usually based on a quadratic fit to empirical results. For example, Glauert [5] defined a parabolic curve, given by Equation (2.8).

$$C_t = -0.889 + \frac{0.0203 - (0.143 + a)^2}{0.6427} \qquad -0.4 > a > -1.0 \tag{2.8}$$

Modifications to this expression have been proposed by several others, including Burton *et al.* [43] and Buhl [44]. These expressions are shown respectively in Equation (2.9) and Equation (2.10).

$$C_t = 1.39(1+a) - 1.816 \qquad -0.326 > a > -1.0 \tag{2.9}$$

$$C_t = \left(4F - \frac{50}{9}\right)a^2 + \left(4F - \frac{40}{9}\right)a - \frac{8}{9} \qquad -0.4 > a > -1.0 \tag{2.10}$$

All three of the above expressions were originally developed to correct the overall thrust coefficient through the propeller disk [5]. However, the thrust coefficient associated with each annulus of the rotor disk needs to be corrected for applications involving BEM. It is therefore possible that none of the three proposed expressions realistically represent the thrust coefficient distribution at large negative induction factors. However, because the axial induction factor typically only falls below −0.35 at the root and tip sections of each blade, this correction is expected to have a negligible influence on the overall loads and performance. During this work, this correction has therefore primarily been applied to maintain consistency (preventing a non-physical flow reversal). As shown in Figure 2.4, the expression that was proposed by Buhl [44] maintains continuity with the curve that is generated by momentum theory when corrections for root and tip losses are applied, while the other two equations yield a gap in the predicted thrust after applying the tip-loss factor to the original momentum equation because they do not explicitly account for losses in circulation near the root and tip of the blade.

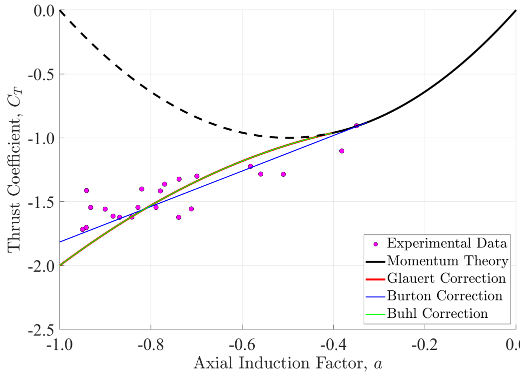

(a) $F = 1.00$

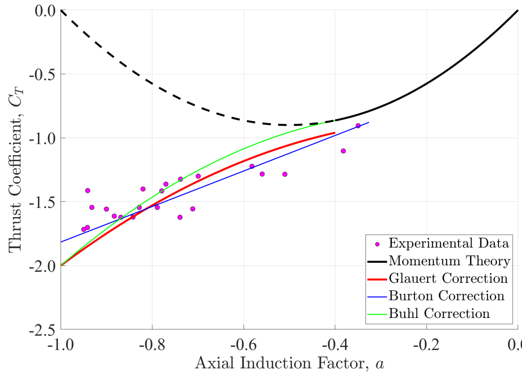

(b) $F = 0.90$

Figure 2.4: A comparison between theoretical thrust coefficient expressions at with and without the Prandtl tip-loss factor, also compared with experimental results (collected by Lock *et al.* [45]) for the total thrust coefficient produced by an airscrew in negative thrust conditions.

Because wake-mixing occurs at large negative induction factors, the helicoidal vortex structure does not exist, meaning that the Prandtl tip loss factor may no longer be valid. However, because the blades have a finite span, there must be zero circulation at the root and tip, and thus corrections for this loss in circulation are still required. Several authors continue to multiply the total thrust by the Prandtl tip loss factor in these conditions for convenience [43]. This method will be applied during this project (rather than applying the expression proposed by Buhl [44]), thus ensuring that the aerodynamic loads vanish around the root and tip of the blade. Accordingly, Equation (2.9), which was proposed by Burton *et al.* [43], has been applied throughout this project because it appears to fit the experimental data best.

COMPLETE MOMENTUM THEORY EQUATIONS

Combining everything shown above, the following assumptions have been applied for the momentum theory concerning this project. This is consistent with most implementations of BEM theory.

- The propeller rotor is represented as an actuator disk with a finite number of blades, and the entire control volume surrounding the streamtube of the propeller is divided into several annular control volumes, each corresponding to a unique rotor blade section
  - There is no aerodynamic interaction between neighbouring annular control volumes
  - The flow velocity and static pressure are uniform within each annulus
- The loss in circulation near the root and tip of each blade is represented by the Prandtl tip-loss factor
- The static pressure values far upstream and far downstream are both uniform and ambient
  - The swirl that is generated by the rotor negligibly influences the pressure distribution
- The flow through each annular control volume is inviscid, incompressible, and irrotational
- The flow that enters the propeller streamtube far upstream is purely axial and uniform
- The turbulent wake state is assumed to occur at axial induction factors below −0.326, and the Prandtl tip-loss factor is still applied in this condition

From these assumptions, expressions for the thrust and torque coefficients are shown below.

$$C_t^{\mathrm{M}} = \begin{cases} 4a(1+a)F & a \geq -0.326 \\ (1.39(1+a) - 1.816)F & a < -0.326 \end{cases} \tag{2.11}$$

$$C_q^{\mathrm{M}} = 4a'(1+a)\frac{\omega r}{V_\infty}F \tag{2.12}$$

Figure 2.5 contains notional diagrams of the thrust and torque coefficients for varying axial or tangential induction factor values. In both cases, the magnitude of the thrust and torque scales with the tip-loss factor, although this has only been indicated within the plot of the thrust coefficient. In the plot of the torque coefficient, $(\omega r/V_\infty)F$ was set equal to 1, as this term does not affect the general trends.

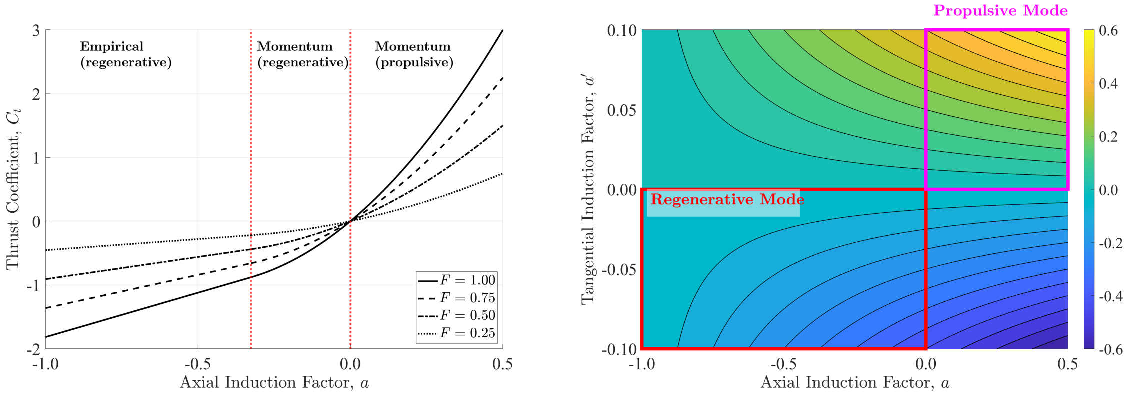

(a) C_t vs. a for varying tip loss factor values.

(b) C_q vs. (a, a'), with $(\omega r/V_\infty)F = 1$.

Figure 2.5: Plots of the thrust and torque coefficients as functions of the induction factors.

2.1.2. BLADE ELEMENT THEORY

The thrust and torque cannot be evaluated with momentum theory alone because the inductions factors are not known *a priori*. Thus, blade element theory must also be applied to allow for the induction factors to be iteratively evaluated. With blade element theory, the propeller blade is discretized into several blade elements, and the thrust and torque that acts on each blade element is evaluated using lift and drag polar plots. Figure 2.6 contains a schematic diagram of a propeller blade element, with the local flow velocity components, aerodynamic loads, and flow angles indicated.

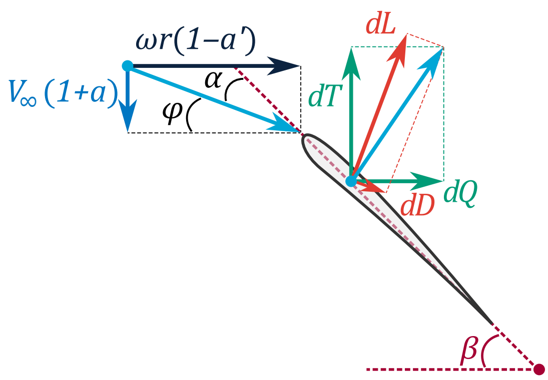

Figure 2.6: A diagram of a propeller blade element with associated aerodynamic loads.

The main assumptions concerning blade element theory are provided below.

- Each blade of the propeller is divided into several sections, with each section corresponding to an annular control volume from momentum theory
  - Each blade encounters identical aerodynamic loads (uniform inflow)
  - There is no aerodynamic interaction between neighbouring blade elements
- Two-dimensional forces are evaluated at each blade section using lift and drag polar plots
  - Lift and drag polar data is evaluated numerically using a modified version of XFOIL called RFOIL, which is capable of accounting for rotational effects that stabilize the boundary layer to delay the onset of flow separation and decrease drag
  - Compressibility effects are accounted for using the well-known *Prandtl-Glauert* transformation

The following equations are used to evaluate thrust and torque at each blade element.

$$dT = \frac{1}{2}\rho_\infty V^2 c\, C_z\, N_\mathrm{b}\, dr \tag{2.13}$$

$$dQ = \frac{1}{2}\rho_\infty V^2 c\, C_x\, N_\mathrm{b}\, r\, dr \tag{2.14}$$

The force coefficients, C_z and C_x, are evaluated using the transformation shown in Equation (2.15). Additionally, expressions for the resultant flow velocity, V, and angles (φ, α) are easily discerned from Figure 2.6 and provided in Equation (2.16). With these expressions, all terms required for calculating the differential thrust and torque acting on a blade element are known, except for the induction factors.

$$\begin{bmatrix} C_z \\ C_x \end{bmatrix} = \begin{bmatrix} \cos(\varphi) & -\sin(\varphi) \\ \sin(\varphi) & \cos(\varphi) \end{bmatrix} \begin{bmatrix} C_l(\alpha, Re, Ma) \\ C_d(\alpha, Re, Ma) \end{bmatrix} \tag{2.15}$$

$$V = \sqrt{(V_\infty(1+a))^2 + (\omega\, r\,(1-a'))^2} \qquad \tan(\varphi) = \frac{V_\infty(1+a)}{\omega\, r\,(1-a')} \qquad \alpha = \beta - \varphi \tag{2.16}$$

The thrust and torque coefficients for each blade element are provided below in Equation (2.17) and Equation (2.18) after normalizing by the freestream dynamic pressure and annular cross-section:

$$C_t^{\mathrm{BE}} = \frac{dT}{q_\infty\, 2\pi\, r\, dr} = C_z\, \sigma(r) \left(\frac{V}{V_\infty}\right)^2 \tag{2.17}$$

$$C_q^{\mathrm{BE}} = \frac{dQ}{q_\infty\, 2\pi\, r^2\, dr} = C_x\, \sigma(r) \left(\frac{V}{V_\infty}\right)^2 \tag{2.18}$$

where the local solidity is defined by $\sigma(r) = (N_b\, c)/(2\pi\, r)$.

2.1.3. CALCULATING PROPELLER PERFORMANCE

The BEM code that was used during this project was initially developed and applied by Goyal *et al.* for the results that were presented in [10]. A modification was made to the iterative scheme, although the underlying theory was not changed. In the present implementation, the induction factors are iteratively evaluated using Newton's method to minimize a residual vector, $\underset{\sim}{R}$, as shown below.

$$\underset{\sim}{R} = \begin{bmatrix} R_1 \\ R_2 \end{bmatrix} = \begin{bmatrix} C_t^{\mathrm{BE}} \\ C_q^{\mathrm{BE}} \end{bmatrix} - \begin{bmatrix} C_t^{\mathrm{M}} \\ C_q^{\mathrm{M}} \end{bmatrix} \implies \begin{bmatrix} a_{i+1} \\ a'_{i+1} \end{bmatrix} = \begin{bmatrix} a_i \\ a'_i \end{bmatrix} - \begin{bmatrix} {}^{\partial R_1}/_{\partial a} & {}^{\partial R_1}/_{\partial a'} \\ {}^{\partial R_2}/_{\partial a} & {}^{\partial R_2}/_{\partial a'} \end{bmatrix}^{-1} \cdot \underset{\sim}{R}$$

A UML activity diagram has been provided in Figure 2.7 to indicate the BEM solution procedure.

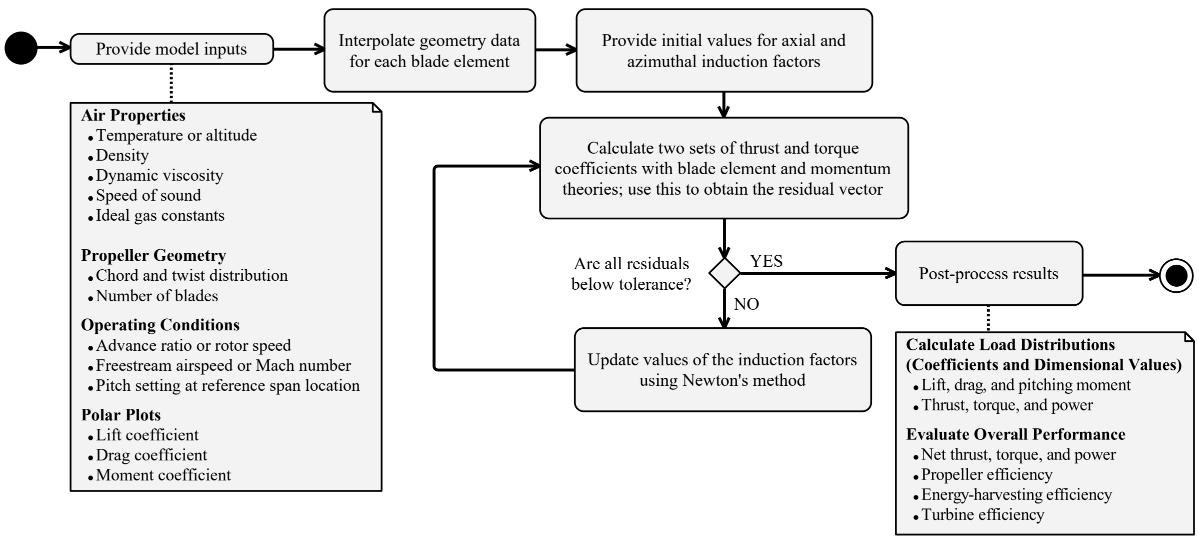

Figure 2.7: A UML activity diagram of the aerodynamic analysis procedure.

After solving the BEM equations, the total thrust and torque is evaluated by the solver using Equation (2.1) and Equation (2.2). It is then possible to evaluate the thrust, torque, and power coefficients using Equation (2.19) and Equation (2.20). Usually, the thrust and power coefficients are normalized using the freestream velocity and propeller disk area at the aircraft design level, as it is more convenient to use these terms in discussions regarding propeller installation effects. Discussions during this work are for isolated propellers only and thus remain at the blade-design level. For this reason, it is convenient to normalize the thrust and power by an effective dynamic pressure that is defined using the rotation rate of the propeller. The coefficients T_C, Q_C, and P_C are used to represent the performance of any type of rotor that provides a thrust (such as a wind turbine), whereas the coefficients C_T, C_Q, and C_P are exclusively used for the evaluation of propeller performance. While P_C represents the nondimensional shaft-power of the propeller, T_C represents the nondimensional thrust-power of the propeller. In this way, the thrust coefficient, T_C, accordingly represents the nondimensional average disc loading of the propeller.

$$T_C = \frac{T}{\rho_\infty V_\infty^2 (2R)^2} \qquad Q_C = \frac{Q}{\rho_\infty V_\infty^2 (2R)^3} \qquad P_C = \frac{P}{\rho_\infty V_\infty^3 (2R)^2} \tag{2.19}$$

$$C_T = \frac{T}{\rho_\infty n^2 (2R)^4} \qquad C_Q = \frac{Q}{\rho_\infty n^2 (2R)^5} \qquad C_P = \frac{P}{\rho_\infty n^3 (2R)^5} \tag{2.20}$$

Efficiencies in different operating conditions are evaluated using Equation (2.21). The usual propulsive efficiency, η_P, is defined as the ratio between the thrust power and the shaft power; this must be maximized to minimize fuel consumption in propulsive conditions. The energy-harvesting efficiency, η_eh, is defined to characterize performance during regenerative mode, since it represents the ratio between the total power extracted from the freestream and the total power available in the freestream. This efficiency is limited by the Betz upper-limit of 59.3% and is usually used for the analysis of wind turbines [46]. This metric will be used during this project to quantify the percentage of available power in the flow that is being recovered by the propeller during energy harvesting conditions. Lastly, the turbine efficiency, η_T, was defined by Glauert [39] as the inverse of the propeller efficiency [47]. This metric is useful for quantifying the ratio between the extracted power and the power that is used to provide negative thrust.

$$\eta_\mathrm{P} = \eta_\mathrm{T}^{-1} = \frac{V_\infty T}{P} = \frac{J\,C_T}{C_P} = \frac{T_C}{P_C}; \qquad \eta_\mathrm{eh} = \frac{-P}{\left(\frac{1}{2}\rho_\infty V_\infty^2\right)\left(\frac{1}{4}\pi(2R)^2\right)V_\infty} = \frac{-8P}{\rho_\infty \pi (2R)^2 V_\infty^3} = \frac{-8P_C}{\pi} \tag{2.21}$$

2.2. STRUCTURAL MODELLING

This section describes the main concepts that were applied to develop the structural model. A finite element model was developed to perform the structural analysis of each blade under consideration, this model receives inputs corresponding to the blade structural design (geometry, materials, laminate details) and outputs deformations, stresses, and strains. The properties of each laminate of the propeller blade are expressed in terms of lamination parameters, which are used to provide their corresponding $\{\boldsymbol{A},\boldsymbol{B},\boldsymbol{D}\}$ matrices. The cross-sectional modelling approach of Ferede [25] was used to define the blade structure with Timoshenko beam elements, while preserving the anisotropic properties of each laminate. The Timoshenko beam elements are defined within the corotational framework that was formulated by De Breuker [48] to account for nonlinearities that may be present due to large deformations or centrifugal forces. During this project, the finite element model has only been applied to determine blade deformations, stresses, and strains through a static structural analysis. Buckling was not analysed during this project, despite being required during the design of aircraft wings and wind turbines. This is because the centrifugal loads encountered by each blade are typically large enough to ensure that structural members are primarily subjected to tensile loads. The minimal presence of compressive loads prevents bucking from occurring. This assumption was proven to be valid for this project during the collection of results.

2.2.1. STRESS-STRAIN FORMULATION FOR COMPOSITE LAMINATES

Classical laminated plate theory is essential for providing a relationship between the stress resultants and the local strains. Details concerning classical laminated plate theory have therefore been provided within this section to indicate how the structural properties of each laminate are represented. The textbooks of Kassapoglou [49], Agarwal *et al.* [50], Daniel and Ishai [51], Whitney [52], and Jones [53] were consulted for general details concerning classical laminated plate theory, while the textbook of Tsai and Hahn [54] was referenced for details regarding lamination parameters.

It has been assumed that the blade structure is made entirely from pure fibre laminates, meaning that laminates do not include a core material. Additionally, each ply that is used to construct a given laminate is unidirectional and therefore orthotropic, and thus the stress-strain characteristics of the material are uniform across three planes of symmetry that are orthogonal to the principal axes, as shown in Figure 2.8a. Unidirectional laminae have one preferred axis. A laminated plate that is composed of several plies with this characteristic is reasonably approximated as monotropic (since its height is usually small enough to be neglected), which means that material properties are only invariant across the $\hat{x}_1$-$\hat{x}_2$ plane, as shown in Figure 2.8b [49]. Coordinate systems for plies will be denoted as shown in Figure 2.8, with $\hat{x}_1$ being aligned with the fibres, and the $(\tilde{x}, \tilde{y}, \tilde{z})$ axis being fixed for a given laminate, as shown in Figure 2.8b.

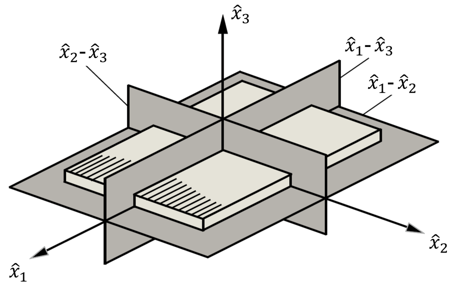

(a) Planes of symmetry for an orthotropic plate.

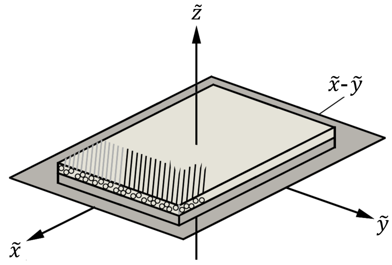

(b) Planes of symmetry for a monotropic plate.

Figure 2.8: Diagrams of the coordinate systems used for plies (adapted from [55]).

The stress-strain relationship of an orthotropic ply is shown in Equation (2.22) within the $(\hat{x}_1, \hat{x}_2, \hat{x}_3)$ coordinate system. This equation relies on the *plane stress* assumption. The stress-strain relationship of an orthotropic ply in the global $(\tilde{x}, \tilde{y}, \tilde{z})$ frame is given by Equation (2.23), where θ is the ply orientation angle (equivalent to the clockwise angle between the $\tilde{x}$ and $\hat{x}_1$ axes).

$$\begin{bmatrix}\sigma_1\\ \sigma_2\\ \tau_{12}\end{bmatrix} = \begin{bmatrix}\frac{E_{11}^2}{E_{11}-E_{22}\nu_{12}^2} & \frac{\nu_{12}E_{11}E_{22}}{E_{11}-E_{22}\nu_{12}^2} & 0\\ \frac{\nu_{12}E_{11}E_{22}}{E_{11}-E_{22}\nu_{12}^2} & \frac{E_{11}E_{22}}{E_{11}-E_{22}\nu_{12}^2} & 0\\ 0 & 0 & G_{12}\end{bmatrix}\begin{bmatrix}\varepsilon_1\\ \varepsilon_2\\ \gamma_{12}\end{bmatrix} = \boldsymbol{Q}\begin{bmatrix}\varepsilon_1\\ \varepsilon_2\\ \gamma_{12}\end{bmatrix}, \qquad \nu_{21} = \nu_{12}\frac{E_{22}}{E_{11}} \tag{2.22}$$

Subscripts 1, 2, and 3 are used to denote quantities in the local $(\hat{x}_1, \hat{x}_2, \hat{x}_3)$ frame, and subscripts x, y, and z are used to denote quantities in the global $(\tilde{x}, \tilde{y}, \tilde{z})$ frame.

$$\begin{bmatrix}\sigma_x\\ \sigma_y\\ \tau_{xy}\end{bmatrix} = \boldsymbol{T_1}^{-1}\begin{bmatrix}\frac{E_{11}^2}{E_{11}-E_{22}\nu_{12}^2} & \frac{\nu_{12}E_{11}E_{22}}{E_{11}-E_{22}\nu_{12}^2} & 0\\ \frac{\nu_{12}E_{11}E_{22}}{E_{11}-E_{22}\nu_{12}^2} & \frac{E_{11}E_{22}}{E_{11}-E_{22}\nu_{12}^2} & 0\\ 0 & 0 & G_{12}\end{bmatrix}\boldsymbol{T_2}\begin{bmatrix}\varepsilon_x\\ \varepsilon_y\\ \gamma_{xy}\end{bmatrix} = \bar{\boldsymbol{Q}}\begin{bmatrix}\varepsilon_x\\ \varepsilon_y\\ \gamma_{xy}\end{bmatrix} \tag{2.23}$$

The two transformation matrices, $\boldsymbol{T_1}$ and $\boldsymbol{T_2}$, are defined to compute the stress-strain relationship in coordinates that are rotated about the $\hat{x}_3$-axis by an angle of θ. The two transformation matrices are required here because engineering notation is being used instead of tensor notation, and the engineering shear strain is twice the tensor shear strain [49].

$$\boldsymbol{T_1} = \begin{bmatrix}\cos^2(\theta) & \sin^2(\theta) & 2\sin(\theta)\cos(\theta)\\ \sin^2(\theta) & \cos^2(\theta) & -2\sin(\theta)\cos(\theta)\\ -\sin(\theta)\cos(\theta) & \sin(\theta)\cos(\theta) & \cos^2(\theta)-\sin^2(\theta)\end{bmatrix}, \qquad \boldsymbol{T_2} = \begin{bmatrix}\cos^2(\theta) & \sin^2(\theta) & \sin(\theta)\cos(\theta)\\ \sin^2(\theta) & \cos^2(\theta) & -\sin(\theta)\cos(\theta)\\ -2\sin(\theta)\cos(\theta) & 2\sin(\theta)\cos(\theta) & \cos^2(\theta)-\sin^2(\theta)\end{bmatrix}$$

The unique stress-strain relationships of each ply within a given laminate are used to define the stiffness tensor that relates plane forces and moments to plane strains and curvatures, as shown below.

$$\begin{bmatrix}N_x\\ N_y\\ N_{xy}\\ M_x\\ M_y\\ M_{xy}\end{bmatrix} = \left[\begin{array}{ccc:ccc}A_{11} & A_{12} & A_{16} & B_{11} & B_{12} & B_{16}\\ A_{12} & A_{22} & A_{26} & B_{12} & B_{22} & B_{26}\\ A_{16} & A_{26} & A_{66} & B_{16} & B_{26} & B_{66}\\ \hdashline B_{11} & B_{12} & B_{16} & D_{11} & D_{12} & D_{16}\\ B_{12} & B_{22} & B_{26} & D_{12} & D_{22} & D_{26}\\ B_{16} & B_{26} & B_{66} & D_{16} & D_{26} & D_{66}\end{array}\right] \cdot \begin{bmatrix}\varepsilon_x\\ \varepsilon_y\\ \gamma_{xy}\\ \kappa_x\\ \kappa_y\\ \kappa_{xy}\end{bmatrix} = \begin{bmatrix}\boldsymbol{A} & \boldsymbol{B}\\ \boldsymbol{B} & \boldsymbol{D}\end{bmatrix}\cdot\begin{bmatrix}\underline{\varepsilon}\\ \underline{\kappa}\end{bmatrix} \tag{2.24}$$

The $(\boldsymbol{A}, \boldsymbol{B}, \boldsymbol{D})$ stiffness tensors are essential to classical laminated plate theory, as they couple stress resultants (expressed as a force or moment per unit length) to local strains. The $\boldsymbol{A}$ matrix describes the in-plane stiffness and the $\boldsymbol{D}$ matrix describes the out-of-plane stiffness. The $\boldsymbol{B}$ matrix is called the coupling matrix because it couples the plane curvatures to plane forces, while also coupling the plane strains to plane moments. Thus, a laminate with a non-zero $\boldsymbol{B}$ matrix can encounter curvatures due to extensional forces. Figure 2.9 depicts the internal sign convention for a monotropic plate and the coordinates used to index through plies of a laminate. Only symmetric laminates are considered, meaning that $\boldsymbol{B} = \boldsymbol{0}$.

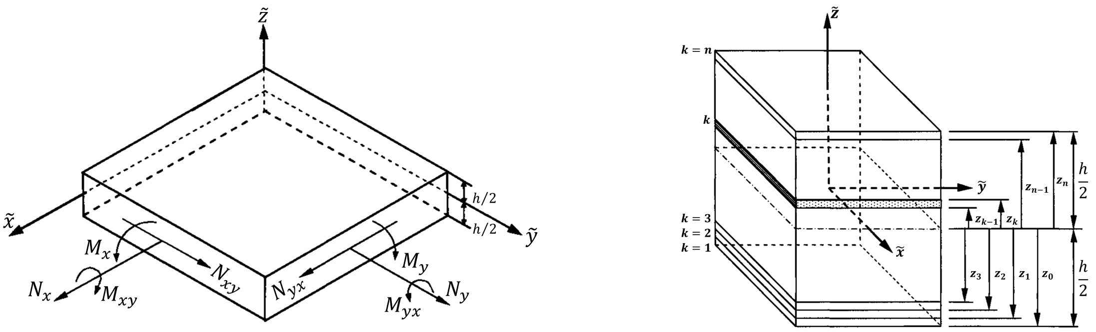

(a) Coordinates for internal forces and moments. **(b)** Variables denoting layers of a laminate.

Figure 2.9: Diagrams of variables and coordinates describing a laminated plate (adapted from [51]).

Entries of the $(\boldsymbol{A}, \boldsymbol{B}, \boldsymbol{D})$ stiffness tensors are given by the expressions shown in Equation (2.25).

$$A_{ij} = \sum_{k=1}^{k=n} \bar{Q}_{ij}(z_k - z_{k-1}), \qquad B_{ij} = \sum_{k=1}^{k=n} \frac{\bar{Q}_{ij}}{2}\left(z_k^2 - z_{k-1}^2\right), \qquad D_{ij} = \sum_{k=1}^{k=n} \frac{\bar{Q}_{ij}}{3}\left(z_k^3 - z_{k-1}^3\right) \tag{2.25}$$

2.2.2. LAMINATION PARAMETERS

As shown in the preceding section, the stiffness tensor for a laminated plate depends on the unique material properties, thickness, and orientation of each lamina. Optimization problems that are defined with these variables are usually highly nonlinear, non-convex, and prone to suffering from objective functions that can have several local optimum values [56]. The main advantages of using these variables to define the structure are that they all bear a straightforward physical meaning, and their use guarantees that the structure is always physically realizable. Nevertheless, the optimization problem must be formulated as an integer programming problem if the number of plies is not established *a priori*, as this is a discrete variable. To enable the use of a gradient-based optimization procedure without any loss of generality, lamination parameters were introduced by Tsai and Hahn [54] to allow the stiffness properties of a laminated plate to be represented using a fixed number of variables that are defined within convex feasible regions [57]. For any laminate with an arbitrary number of plies of differing orientations, only 12 variables, shown in Equation (2.26), are required to define its thickness-normalized stiffness properties completely. The main drawback of this approach is that the lamination parameters do not bear any physical meaning.

$$\left.\begin{aligned} \xi^{\mathrm{A}}_{[1,2,3,4]} &= \int_{-1/2}^{1/2} [\cos(2\theta), \sin(2\theta), \cos(4\theta), \sin(4\theta)]\,\mathrm{d}\bar{z} \\ \xi^{\mathrm{B}}_{[1,2,3,4]} &= \int_{-1/2}^{1/2} [\cos(2\theta), \sin(2\theta), \cos(4\theta), \sin(4\theta)]\,\bar{z}\,\mathrm{d}\bar{z} \\ \xi^{\mathrm{D}}_{[1,2,3,4]} &= \int_{-1/2}^{1/2} [\cos(2\theta), \sin(2\theta), \cos(4\theta), \sin(4\theta)]\,\bar{z}^2\,\mathrm{d}\bar{z} \end{aligned}\right\} \qquad \bar{z} = z/h \tag{2.26}$$

In this case, z refers to the continuous generalization of the discrete variable $\{z_k\}_{k=1}^{k=n}$ that is shown in Figure 2.9b, and thus θ is dependent on z or $\bar{z}$. The $(\boldsymbol{A}, \boldsymbol{B}, \boldsymbol{D})$ stiffness tensors are obtained from the lamination parameters using material stiffness invariants, which are defined using the $\boldsymbol{Q}$ matrix of each ply from Equation (2.22). This is shown in Equation (2.27). Only 8 lamination parameters remain for symmetric laminates. Research on the feasible regions for lamination parameters in addition to some expressions for the boundaries considered during this project are provided in Appendix B.

$$\boldsymbol{\Gamma_0} = \begin{bmatrix} U_1 & U_4 & 0 \\ U_4 & U_1 & 0 \\ 0 & 0 & U_5 \end{bmatrix}, \boldsymbol{\Gamma_1} = \begin{bmatrix} U_2 & 0 & 0 \\ 0 & -U_2 & 0 \\ 0 & 0 & 0 \end{bmatrix}, \boldsymbol{\Gamma_2} = \begin{bmatrix} 0 & 0 & U_2 \\ 0 & 0 & U_2 \\ U_2 & U_2 & 0 \end{bmatrix}, \boldsymbol{\Gamma_3} = \begin{bmatrix} U_3 & -U_3 & 0 \\ -U_3 & U_3 & 0 \\ 0 & 0 & -U_3 \end{bmatrix}, \boldsymbol{\Gamma_4} = \begin{bmatrix} 0 & 0 & 2U_3 \\ 0 & 0 & -2U_3 \\ 2U_3 & -2U_3 & 0 \end{bmatrix}$$

$$\left.\begin{aligned}
U_1 &= \frac{1}{8}(3Q_{11}+3Q_{22}+2Q_{12}+4Q_{66})\\
U_2 &= \frac{1}{2}(Q_{11}-Q_{22})\\
U_3 &= \frac{1}{8}(Q_{11}+Q_{22}-2Q_{12}-4Q_{66})\\
U_4 &= \frac{1}{8}(Q_{11}+Q_{22}+6Q_{12}-4Q_{66})\\
U_5 &= \frac{1}{8}(Q_{11}+Q_{22}-2Q_{12}+4Q_{66})
\end{aligned}\right\}$$

$$\left.\begin{aligned}
\boldsymbol{A} &= h\left(\boldsymbol{\Gamma_0}+\boldsymbol{\Gamma_1}\xi_1^A+\boldsymbol{\Gamma_2}\xi_2^A+\boldsymbol{\Gamma_3}\xi_3^A+\boldsymbol{\Gamma_4}\xi_4^A\right)\\
\boldsymbol{B} &= \frac{h^2}{4}\left(\boldsymbol{\Gamma_1}\xi_1^B+\boldsymbol{\Gamma_2}\xi_2^B+\boldsymbol{\Gamma_3}\xi_3^B+\boldsymbol{\Gamma_4}\xi_4^B\right)\\
\boldsymbol{D} &= \frac{h^3}{12}\left(\boldsymbol{\Gamma_0}+\boldsymbol{\Gamma_1}\xi_1^D+\boldsymbol{\Gamma_2}\xi_2^D+\boldsymbol{\Gamma_3}\xi_3^D+\boldsymbol{\Gamma_4}\xi_4^D\right)
\end{aligned}\right\} \tag{2.27}$$

2.2.3. CROSS-SECTIONAL MODELLING

A generic propeller structural design is shown in Figure 2.10, according to Lis [58]. However, within the research that was presented in Section 1.1, the structural design of a propeller blade has been represented in several ways. For example, Dwyer and Rogers [17] represented each blade as a hollow composite beam. On the other hand, the SR7L propeller blade that was analysed by Yamamoto and August [18] has an aluminium spar, with a fibreglass shell and foam fill. Additionally, Sodja *et al.* [3, 21] modelled a 3D-printed propeller with a solid cross-section, and Chattopadhyay *et al.* [19] represented their propeller blade as a composite box-beam with an aluminium honeycomb fill. Because only general design trends are of interest for this project, the structural design of the propeller blade does not need to be as detailed as the representations that were used in many of these preceding works. In the work of Khan [4, 24], the propeller blade is represented by a variable-thickness plate made from composite materials.

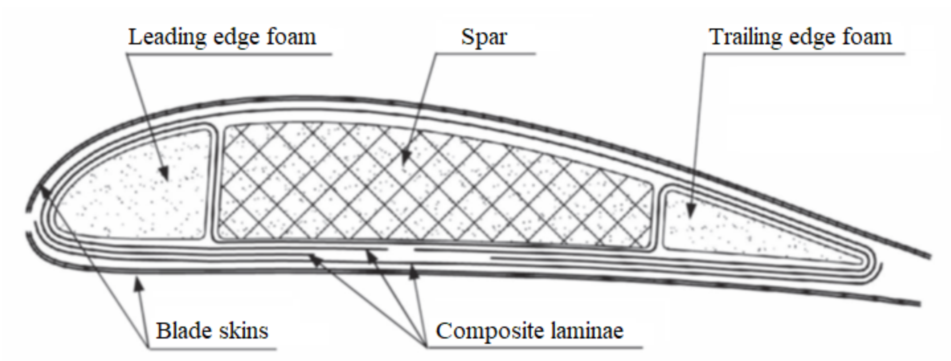

Figure 2.10: A notional diagram depicting the realistic cross-section of a generic blade structure featuring a spar, foam fill, and composite shell (adapted from [58]).

The structural representations of Khan [4] and Dwyer and Rogers [17] are the most convenient because they allow the qualitative effects of bend-twist coupling to be evaluated while remaining relatively simple in comparison to the other examples presented above.

It is reasonable to assume that only the outer composite shell and spar skins of the blade contribute to its torsional stiffness, similar to the methods presented in [17, 19]. Composite or aluminium spar caps can be included in the structural model to yield a more realistic result, similar to the model of Hegberg [26]. This will not noticeably influence general design trends. Furthermore, to reduce the number of design variables, only one laminate has been used to represent the structure in the chordwise direction on its upper and lower surfaces at each spanwise location, and the structure will consist of multiple evenly spaced laminates along its span, either with or without spars. Complexity may be increased as necessary, though this model is at least more detailed than the model used by Khan *et al.* and Dwyer and Rogers, which were at least useful for identifying general trends, as is the primary focus of this work. Thus, the blade cross-section shown within Figure 2.10 resembles the cross-section that was considered during this project, except foam was not included during this project. Lastly, the simplified cross-sectional geometry may not feature spar caps, if the blade is instead defined as a hollow shell.

By applying the cross-sectional modelling approach of Ferede [25], the three-dimensional properties of the blade structure, which are defined using classical laminated plate theory, are represented equivalently using one-dimensional Timoshenko beam elements. The advantage of this approach is that it preserves the strain energy and anisotropic properties of each laminate, while reducing the number of degrees of freedom. This is advantageous for applications involving aeroelasticity and optimization because it results in a decreased computational cost. The underlying theory concerning the cross-sectional modeller has been left out for brevity, as this theory was not changed from the work of Ferede and Abdalla [59].

The cross-sectional modeller is capable of representing any arbitrary open or closed and single- or multiple-celled thin-walled cross-section. Each cross-section is modelled in three-dimensions using linear shell elements of constant properties, and this shell-element representation is used by the cross-sectional modeller to approximate the mass and stiffness properties of the section. Figure 2.11 contains a notional diagram of the shell element discretization of a blade section that includes spar caps.

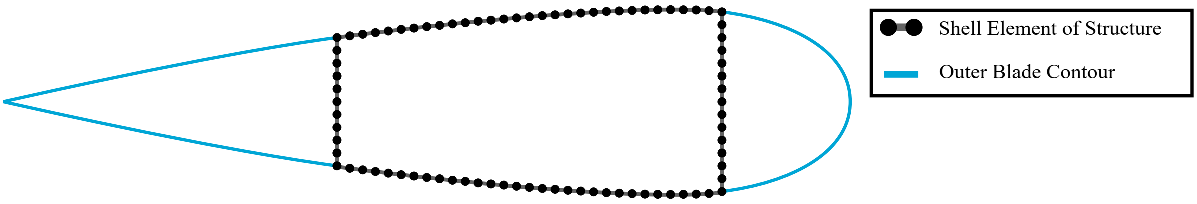

Figure 2.11: A notional diagram of the shell-element representation of a blade section with spar caps.

The $(\boldsymbol{A}, \boldsymbol{B}, \boldsymbol{D})$ matrices of each laminate of the cross-section are used to obtain the local stiffness matrix, $\boldsymbol{C}$, which relates forces and moments applied at a node of the beam element mesh to its strains and curvatures, as shown in Equation (2.28) from [26] and [30]. The first strain (ε_{11}) acts in the axial direction, while the remaining two strains (ε_{12} and ε_{13}) act in the shear direction. The first curvature (κ_1) corresponds to torsional deformations, while the remaining two curvatures (κ_2 and κ_3) refer to bending. The stiffness properties of the blade can be determined around any arbitrary reference location. The shell element representation is also used to approximate the mass properties of each element, including the mass per unit length, the first mass moment of inertia, and the second mass moment of inertia. All mass and stiffness quantities are considered to vary linearly over each beam element.

$$\begin{bmatrix} F_1 \\ F_2 \\ F_3 \\ M_1 \\ M_2 \\ M_3 \end{bmatrix} = \begin{bmatrix} EA & C_{12} & C_{13} & C_{14} & C_{15} & C_{16} \\ C_{12} & GA_2 & C_{23} & C_{24} & C_{25} & C_{26} \\ C_{13} & C_{23} & GA_3 & C_{34} & C_{35} & C_{36} \\ C_{14} & C_{24} & C_{34} & GJ & C_{45} & C_{46} \\ C_{15} & C_{25} & C_{35} & C_{45} & EI_2 & C_{56} \\ C_{16} & C_{26} & C_{36} & C_{46} & C_{56} & EI_3 \end{bmatrix} \cdot \begin{bmatrix} \varepsilon_{11} \\ \varepsilon_{12} \\ \varepsilon_{13} \\ \kappa_1 \\ \kappa_2 \\ \kappa_3 \end{bmatrix} = \boldsymbol{C} \cdot \begin{bmatrix} \underline{\varepsilon} \\ \underline{\kappa} \end{bmatrix} \tag{2.28}$$

After the aeroelastic analysis has been completed, the cross-sectional modeller is used again to recover the skin strains using the computed deformations and the three-dimensional shell-element discretization. This may be used to evaluate stresses to ensure that they are below the maximum stress.

2.2.4. GEOMETRICALLY NONLINEAR BEAM MODEL

The static structural model is defined after the cross-sectional properties of the blade have been calculated. The static structural analysis is largely based on the work of De Breuker [48], and this section includes a brief summary of the model that was implemented during this project based on their work. A more complete overview of this model may be found within [30, 48].

As mentioned previously, the linear Timoshenko beam elements that have been used during this project each have constant properties, and therefore also a constant cross-section. Thus, changes in geometry or structure along the span of each blade must be represented by a sufficient number of elements to accurately represent any gradual changes. Each local Timoshenko beam element has 20 degrees of freedom and is shear-deformable. The strain energy of the beam is given by $\mathcal{U}$.

$$\mathcal{U} = \frac{l_0}{2}\int_0^1 \begin{bmatrix} \underline{\varepsilon}^{\mathrm{T}} & \underline{\kappa}^{\mathrm{T}} \end{bmatrix} \boldsymbol{C} \begin{bmatrix} \underline{\varepsilon} \\ \underline{\kappa} \end{bmatrix} d\xi \qquad \xi = \frac{x_l}{l_0} \tag{2.29}$$

The length of the beam element that connects nodes 1 and 2 is computed using the following expression, where (x_i, y_i, z_i) denotes the spatial coordinates of the i^{th} beam node.

$$l_0 = \sqrt{(x_2 - x_1)^2 + (y_2 - y_1)^2 + (z_2 - z_1)^2} \tag{2.30}$$

Figure 2.12 indicates the definition of the 20 degrees of freedom of each element. The only degrees of freedom that are considered in the local stiffness matrix correspond to the two end nodes, and the remaining eight degrees of freedom located strictly between the two nodes are treated as parameters that enrich the displacement and rotation shape functions, to prevent the shear locking effect [48].

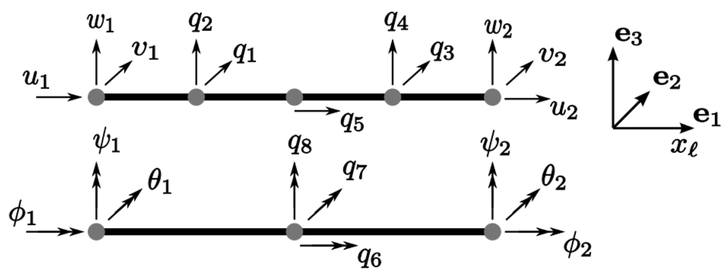

Figure 2.12: A diagram indicating the element degrees of freedom [48].

Corresponding to Figure 2.12, the following shape functions are used to describe deformations at any point along the element, based on deformations in the 20 degrees of freedom.

$$u(\xi) = u_1(1.0-\xi) + u_2\xi + q_5\xi(1.0-\xi) \tag{2.31}$$
$$v(\xi) = v_1(1.0-\xi) + v_2\xi + q_1\xi(1.0-\xi) + q_3\xi(1.0-\xi)(0.5-\xi) \tag{2.32}$$
$$w(\xi) = w_1(1.0-\xi) + w_2\xi + q_2\xi(1.0-\xi) + q_4\xi(1.0-\xi)(0.5-\xi) \tag{2.33}$$
$$\phi(\xi) = \phi_1(1.0-\xi) + \phi_2\xi + q_6\xi(1.0-\xi) \tag{2.34}$$
$$\theta(\xi) = \theta_1(1.0-\xi) + \theta_2\xi + q_7\xi(1.0-\xi) \tag{2.35}$$
$$\psi(\xi) = \psi_1(1.0-\xi) + \psi_2\xi + q_8\xi(1.0-\xi) \tag{2.36}$$

For each element, the stiffness tensors corresponding to each node, $\boldsymbol{C}_1$ and $\boldsymbol{C}_2$, may be different, and thus at any given point along the element, the stiffness tensor is expressed as shown below.

$$\boldsymbol{C}(\xi) = (1-\xi)\boldsymbol{C}_1 + \xi\boldsymbol{C}_2 \tag{2.37}$$

Lastly, the strains and curvatures are expressed in terms of the degrees of freedom as follows.

$$\begin{bmatrix} \underline{\varepsilon}^{\mathrm{T}} & \underline{\kappa}^{\mathrm{T}} \end{bmatrix} = \begin{bmatrix} \frac{1}{l_0}\frac{\partial u}{\partial \xi} & \frac{1}{l_0}\frac{\partial x}{\partial \xi} - \psi & \frac{1}{l_0}\frac{\partial w}{\partial \xi} + \theta & \frac{1}{l_0}\frac{\partial \phi}{\partial \xi} & \frac{1}{l_0}\frac{\partial \theta}{\partial \xi} & \frac{1}{l_0}\frac{\partial \psi}{\partial \xi} \end{bmatrix} \tag{2.38}$$

The strains and curvatures may be expressed as a matrix containing shape functions, multiplied by a vector of displacements in each degree of freedom, as shown below.

$$\begin{bmatrix} \underline{\varepsilon} \\ \underline{\kappa} \end{bmatrix} = \boldsymbol{N}\left[\begin{array}{cccccccccccc|cc} u_1 & v_1 & w_1 & \phi_1 & \theta_1 & \psi_1 & u_2 & v_2 & w_2 & \phi_2 & \theta_2 & \psi_2 & q_1 & q_2 \cdots\cdots q_8 \end{array}\right]^{\mathrm{T}} = \boldsymbol{N}\underline{p}_{\mathrm{e}} \tag{2.39}$$

With the expressions defined previously, Equation (2.29) may be re-written as follows.

$$\mathcal{U} = \underline{p}_{\mathrm{e}}^{\mathrm{T}}\left[\frac{l_0}{2}\int_0^1 \boldsymbol{N}^{\mathrm{T}}\left[(1-\xi)\boldsymbol{C_1} + \xi\boldsymbol{C_2}\right]\boldsymbol{N}\,d\xi\right]\underline{p}_{\mathrm{e}} \tag{2.40}$$

This expression has been used to obtain the local structural stiffness matrix, which is defined as the second derivative with respect to the degrees of freedom, as shown below.

$$\left[\boldsymbol{K}^{\mathbf{L}}_{\mathbf{20x20}}\right]_{ij} = \frac{\partial^2 \mathcal{U}}{\partial p_{\mathrm{e}_i} \partial p_{\mathrm{e}_j}} \implies \boldsymbol{K}^{\mathbf{L}}_{\mathbf{20x20}} = \frac{l_0}{2}\int_0^1 \boldsymbol{N}^{\mathrm{T}}\left[(1-\xi)\boldsymbol{C}_1 + \xi\boldsymbol{C}_2\right]\boldsymbol{N}\,d\xi \tag{2.41}$$

The resulting stiffness matrix in this case is 20-by-20, while only the twelve degrees of freedom located at the two end nodes of each element are required for applying loads and computing deformations. The resulting equilibrium expression in this case is provided below. Note that the displacements vector, $\underline{p}_{\mathrm{e}}$, has been partitioned into two groups. The first 12 entries contain displacements at the end nodes, and the remaining 8 entries contain components of displacements within the interior of the element. Thus, the force vector will always have at least eight trailing zeros, since it is not possible for loads to be applied through degrees of freedom that act within the interior of each element.

$$\begin{bmatrix} \boldsymbol{K}_{\mathbf{1,1}} & \boldsymbol{K}_{\mathbf{1,2}} \\ \boldsymbol{K}_{\mathbf{2,1}} & \boldsymbol{K}_{\mathbf{2,2}} \end{bmatrix} \cdot \begin{bmatrix} \underline{p}_{\mathrm{e},1} \\ \underline{p}_{\mathrm{e},2} \end{bmatrix} = \begin{bmatrix} \underline{F}_l \\ \underline{0} \end{bmatrix} \tag{2.42}$$

The trailing 8 degrees of freedom must be eliminated, and this has been done using the method of static condensation from [60] to yield the condensed stiffness matrix, as shown below.

$$\boldsymbol{K}^{\mathbf{L}}_{\mathbf{12x12}} = \boldsymbol{K}_{\mathbf{1,1}} - \boldsymbol{K}_{\mathbf{1,2}}\boldsymbol{K}_{\mathbf{2,2}}{}^{-1}\boldsymbol{K}_{\mathbf{2,1}} \tag{2.43}$$

$$\boldsymbol{K}^{\mathbf{L}}_{\mathbf{12x12}} \cdot \underline{p}_{\mathrm{e},1} = \underline{F}_l \tag{2.44}$$

2.2.5. PROPELLER BLADE REFERENCE FRAMES

Coordinate transformations are required to ensure that blade loads and deformations are all expressed within the same global coordinate system. For a propeller blade with zero sweep and zero lean, the global $\hat{e}^b_2$-axis points along the span of the blade, and the $\hat{e}^b_1$-axis points in the chordwise direction of the blade at 70% of its total span. Because both fixed- and variable-pitch propellers may be analysed during this project, the physical definition of the blade relative to the global coordinate system must also be modified due to changes in pitch setting. During this project, the axis of rotation is always considered to be coincident with the $\hat{e}^b_3$-axis. Thus, the entire blade is rotated about its structural axis with changes in pitch setting. This representation is convenient when comparing the deformations of different blade geometries, since the thrust axis will always remain constant. For each element of the blade structure, the $\hat{e}^0_1$-axis is aligned with the structural axis, the $\hat{e}^0_2$-axis is always aligned with the local chord line, and the $\hat{e}^0_3$-axis is positive in the downward direction. The two reference frames are shown in Figure 2.13.

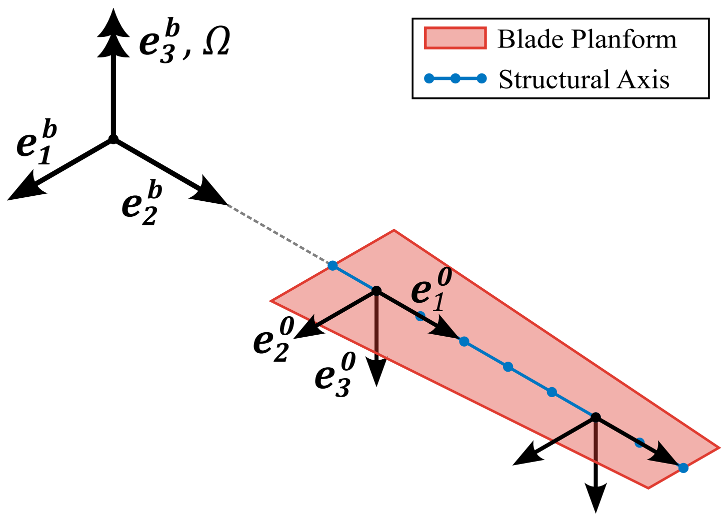

Figure 2.13: A diagram of the global and local reference frames used in the finite element model.

Because the axis of rotation is always aligned with the $\hat{z}_0$-axis irrespective of the blade pitch setting, the angular velocity vector of the propeller blade will always take the following form. The angular velocity vector may also be represented as a skew-symmetric matrix, as shown in Equation (2.45). This form is useful for computing the centrifugal force vector and stiffness matrix, as described in Section 2.2.6.

$$\underset{\sim}{\Omega} = \begin{bmatrix} 0 \\ 0 \\ \Omega \end{bmatrix}, \qquad \mathbf{\Omega} = \begin{bmatrix} 0 & -\Omega & 0 \\ \Omega & 0 & 0 \\ 0 & 0 & 0 \end{bmatrix} \tag{2.45}$$

COROTATIONAL FRAMEWORK

While not pictured in Figure 2.13, the corotational framework that was applied to account for geometrical nonlinearities decomposes large beam displacements and rotations into rigid displacements and small elastic deformations. The linear elastic part is still solved in the element frame, and geometric nonlinearity is introduced through rigid deformations of each element reference frame. In this way, large displacements are evaluated iteratively as local coordinate systems rotate with each local beam element. At every iteration, a new local coordinate system is defined for each element using the corresponding angular deformations at each node. A complete discussion concerning the corotational formulation that was used within this work is provided by De Breuker [48]. The advantage of this approach is that it allows the linearized structural solution to remain valid even for nonlinear cases involving large displacements through a decomposition of large displacements into several smaller displacements that are defined within coordinate systems that corotate with the deforming structure. Maintaining the same convention that was used in Figure 2.13, the corotational framework is visually explained using Figure 2.14. Note that the flow velocity and rotor speed are always expressed in the body-fixed frame, which is denoted by $\mathcal{T}^{\mathbf{b}}$. The undeformed local frames attached to each node are denoted by $\mathcal{T}^{\mathbf{0}}$, and the rigid element frames are denoted by $\mathcal{T}^{\mathbf{r}}_k$ for the k^{th} element. Elastic frames for each node are denoted by $\mathcal{T}^{\mathbf{l}}_j$ for the j^{th} node.

The body-fixed frame is transformed into the initial orientation frame using the rotation matrix, $\mathcal{R}_{\mathbf{0}}$, which is defined in $\mathcal{T}^{\mathbf{b}}$. Maintaining the previously discussed conventions, this matrix is defined as follows.

$$\mathcal{R}_{\mathbf{0}} = \begin{bmatrix} 0 & 1 & 0 \\ 1 & 0 & 0 \\ 0 & 0 & -1 \end{bmatrix} \cdot \begin{bmatrix} 1 & 0 & 0 \\ 0 & \cos(\theta) & -\sin(\theta) \\ 0 & \sin(\theta) & \cos(\theta) \end{bmatrix} = \begin{bmatrix} 0 & \cos(\theta) & -\sin(\theta) \\ 1 & 0 & 0 \\ 0 & -\sin(\theta) & -\cos(\theta) \end{bmatrix} \tag{2.46}$$

The global frame is used to describe the loads and blade axis geometry, whereas the initial orientation frame, the rigid element frame, and the elastic frame are used to express local quantities such as deformations. Because the nonlinear static structural analysis computes deformations iteratively, local element quantities must be converted into global quantities, and vice versa. On the other hand, the linear static structural analysis does not require an iterative solution procedure, and thus the load vector as well as the mass and stiffness matrices do not need to be updated during the analysis. Thus, the linear analysis requires that transformations between local and global coordinates are only applied before and after deformations have been computed, and not during the analysis. The rigid element frame is always defined as being aligned with the deformed geometry, and for an undeformed blade axis, it is identical to the initial orientation frame. Thus, this frame is defined based on the "rigid rotation" of each element. After computing the rigid element frame, the beam node orientations are evaluated in terms of their rigid element orientations. This allows for the local deformations of each node to be evaluated, as required for calculating strains. The nonlinear structural analysis requires that the global stiffness matrix is updated iteratively using the local coordinate frames. The rigid element frame is also used to evaluate local deformations, which are required to evaluate beam strains.

There are two ways to transform the initial orientation frame to the elastic frame. First, the body-fixed frame can be transformed into the rigid element frame (for the k^{th} element) using $\mathcal{R}_{\mathbf{r},k}$, and then the rigid element frame can be transformed to the elastic frame of the j^{th} node using $\mathcal{R}^{\mathbf{l}}_j$. The second approach is to transform the initial orientation frame directly to the elastic frame using the rotation matrix that is defined by $\mathcal{R}^{\mathbf{g}}_j$. Thus, $\mathcal{R}^{\mathbf{g}}_j$ and $\mathcal{R}_{\mathbf{r},k}$ are respectively defined in $\mathcal{T}^{\mathbf{0}}$ and $\mathcal{T}^{\mathbf{b}}$, and $\mathcal{R}^{\mathbf{l}}_j$ is defined in $\mathcal{T}^{\mathbf{r}}_k$.

Further details on the corotational framework that was applied in this work have been provided by De Breuker [48], Werter [30], and Hegberg [26], and thus have been left out of this report for brevity.

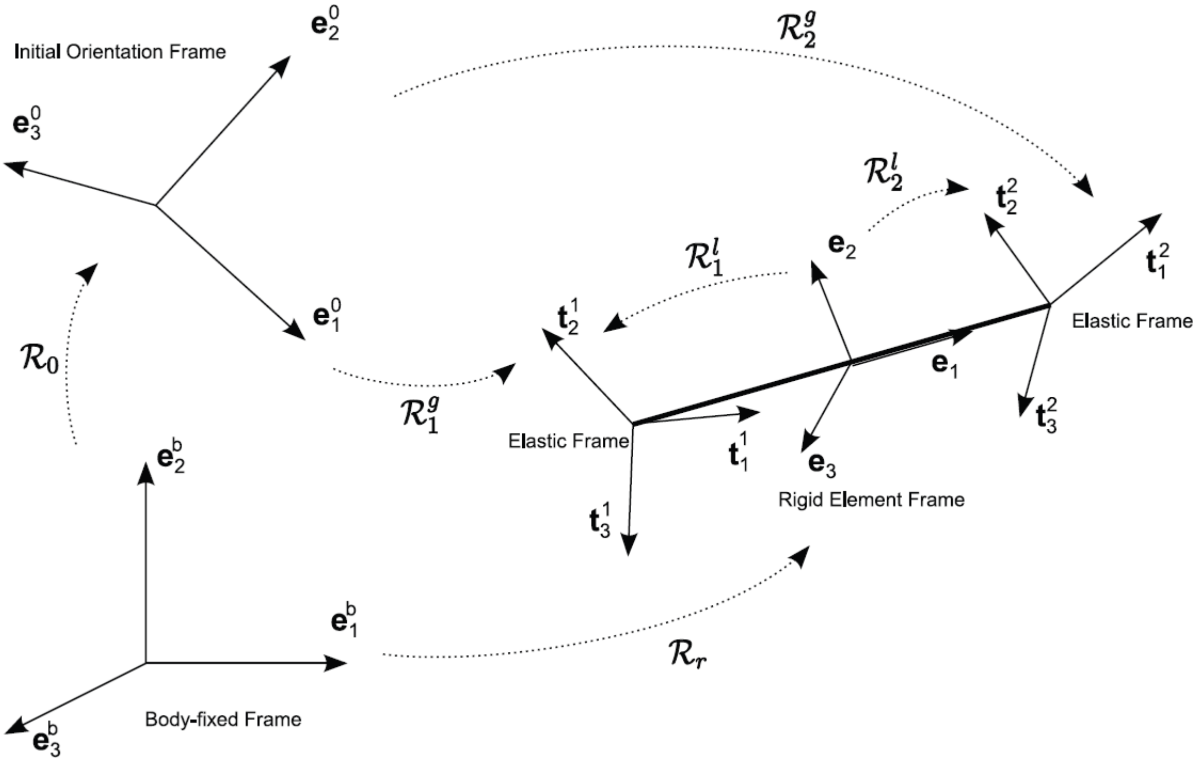

Figure 2.14: A notional diagram indicating the relative positions and transformations between global and local frames within the corotational framework [48].

2.2.6. INCLUDING THE EFFECTS OF CENTRIFUGAL FORCES

Because the propeller blade is always assumed to be rotating at a constant angular velocity, each node of the blade structure will encounter a centrifugal force that acts outwards in the radial direction from its axis of rotation. The result of this force is that it introduces a stiffening effect, which makes the blade structure resistant to transverse loads. As the blade structure deforms due to transverse loading, the centrifugal force will continue to act in the radial direction. Thus, the centrifugal force component that acts orthogonally to the structural axis of the beam will continue to grow. This effect is shown in Figure 2.15, and is known as the spin-softening effect. This is only included with a nonlinear finite element model.

A nonlinear finite element model must be used because the way that the undeformed geometry reacts to centrifugal loads is different from how the deformed geometry will react to loads. This is clear from the diagrams shown in Figure 2.15, as the centrifugal force direction does not change in either diagram, although there is only an axial centrifugal force component and no transverse component present in Figure 2.15a. Conversely, a transverse centrifugal force component is clearly present in Figure 2.15b. Thus, the structural response must be iteratively computed until convergence. It is therefore not sufficient to use a linear finite element model for this project, as structural deformations of the propeller blade would be significantly overestimated in the absence of the centrifugal stiffening effect.

(a) Undeformed structure (only axial loading).

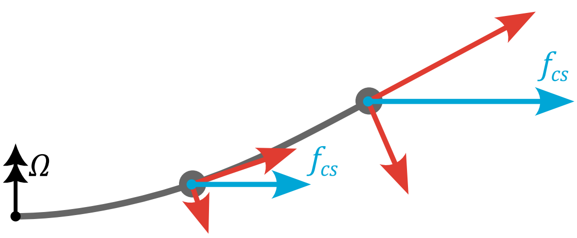

(b) Deformed structure (axial and transverse loading).

Figure 2.15: A diagram indicating how the centrifugal stiffening effect resists bending deformations.

To calculate the contribution due to centrifugal forces, it is first important to calculate the global mass matrix. This is done by calculating either the lumped or consistent mass matrix of each element within their respective local coordinate systems. The lumped mass matrix is evaluated by simply splitting the total mass of each element evenly to its nodes. This results in a diagonal matrix which has the following form for a single element with 6 translational and 6 rotational degrees of freedom.

$$\boldsymbol{M}^{\mathbf{L,\,lumped}}_{\mathbf{12x12}} = \frac{\rho_{\mathrm{s}} A l_0}{2} \left[\begin{array}{cc} \begin{array}{cc} \boldsymbol{I}_{\mathbf{3x3}} & \mathbf{0}_{\mathbf{3x3}} \\ \mathbf{0}_{\mathbf{3x3}} & \mathbf{0}_{\mathbf{3x3}} \end{array} & \mathbf{0}_{\mathbf{6x6}} \\ \mathbf{0}_{\mathbf{6x6}} & \begin{array}{cc} \boldsymbol{I}_{\mathbf{3x3}} & \mathbf{0}_{\mathbf{3x3}} \\ \mathbf{0}_{\mathbf{3x3}} & \mathbf{0}_{\mathbf{3x3}} \end{array} \end{array}\right] \tag{2.47}$$

In this way, the lumped mass matrix here has zero rotational inertia, which is sufficient for this project because the rotational degrees of freedom do not contribute to the centrifugal forces experienced by each element and the mass matrix is not required for any other calculation within this project.

The consistent mass matrix gets its name from being evaluated using the same displacement model that is being used to evaluate the local stiffness matrix. In this way, it is obtained for one-dimensional elements by starting from the expression for total kinetic energy, as shown within Equation (2.48), where the mass per unit length is constant for each element and therefore may be taken out of the integral.

$$\mathcal{V} = \frac{l_0}{2}\int_0^1 \bar{m}\, \dot{\underline{p}}_{\mathrm{e}}^{\mathrm{T}} \boldsymbol{N}^{\mathrm{T}} \boldsymbol{N}\, \dot{\underline{p}}_{\mathrm{e}}\, d\xi = \dot{\underline{p}}_{\mathrm{e}}^{\mathrm{T}} \left[\frac{l_0\,\bar{m}}{2}\int_0^1 \boldsymbol{N}^{\mathrm{T}}\boldsymbol{N}\, d\xi\right] \dot{\underline{p}}_{\mathrm{e}} \qquad \bar{m} = \rho_{\mathrm{s}} A \tag{2.48}$$

Knowing that the consistent mass matrix is defined as the second derivative of the kinetic energy with respect to the velocity, the consistent mass matrix is defined using Equation (2.49). The number of degrees of freedom for each element is 20, meaning that the calculated mass matrix is 20-by-20. Thus, the static condensation method of Guyan [60] must be applied to reduce the mass matrix to correspond to only the 12 degrees of freedom defined at the end nodes of the element, shown in Equation (2.50).

$$\left[\boldsymbol{M}^{\mathbf{L,\,consistent}}_{\mathbf{20x20}}\right]_{ij} = \frac{\partial^2 \mathcal{V}}{\partial \dot{p}_{\mathrm{e}_i} \partial \dot{p}_{\mathrm{e}_j}} \implies \boldsymbol{M}^{\mathbf{L,\,consistent}}_{\mathbf{20x20}} = \frac{l_0\,\bar{m}}{2}\int_0^1 \boldsymbol{N}^{\mathrm{T}}\boldsymbol{N}\, d\xi = \left[\begin{array}{c:c} \boldsymbol{M}_{\mathbf{1,1}} & \boldsymbol{M}_{\mathbf{1,2}} \\ \hdashline \boldsymbol{M}_{\mathbf{2,1}} & \boldsymbol{M}_{\mathbf{2,2}} \end{array}\right] \tag{2.49}$$

$$\implies \boldsymbol{M}^{\mathbf{L,\,consistent}}_{\mathbf{12x12}} = \boldsymbol{M}_{\mathbf{1,1}} - \boldsymbol{M}_{\mathbf{1,2}}\boldsymbol{K}^{-1}_{\mathbf{2,2}}\boldsymbol{K}_{\mathbf{2,1}} - \left(\boldsymbol{K}^{-1}_{\mathbf{2,2}}\boldsymbol{K}_{\mathbf{2,1}}\right)^{\mathrm{T}} \left(\boldsymbol{M}_{\mathbf{2,1}} - \boldsymbol{M}_{\mathbf{2,2}}\boldsymbol{K}^{-1}_{\mathbf{2,2}}\boldsymbol{K}_{\mathbf{2,1}}\right) \tag{2.50}$$

During this project, both the lumped and consistent mass matrices were calculated. The consistent mass matrix is used in cases that are not limited by computational cost, where greater precision is required, for example when only a structural analysis must be performed. The lumped mass matrix is used instead for cases that are limited by computational cost, where the decreased computational cost resulting from its use compensates for any losses in precision, such as during optimization.

After calculating the global mass matrix, $\boldsymbol{M}$, the centrifugal force is evaluated using the following expression, where $\boldsymbol{\Omega}$ is the skew-symmetric version of $\underline{\Omega}$.

$$\underline{f}_{\mathrm{c}}(\underline{p}) = -\boldsymbol{M}\cdot\boldsymbol{\Omega}\cdot\boldsymbol{\Omega}\cdot(\underline{r}+\underline{p}) \tag{2.51}$$

From this expression, it is easy to see that the derivative of the centrifugal force by the structural deformations is given by the following expression. The mass matrix is always a positive definite matrix, and the term $\boldsymbol{\Omega}\cdot\boldsymbol{\Omega}$ is always a negative semidefinite matrix (all eigenvalues of $\boldsymbol{\Omega}\cdot\boldsymbol{\Omega}$ are zero only if the rotor speed is zero). Thus, the matrix given by $\boldsymbol{M}\cdot\boldsymbol{\Omega}\cdot\boldsymbol{\Omega}$ is negative semidefinite. With the additional minus sign, $\boldsymbol{K}_{\mathbf{c}}$ is always positive semidefinite. This term therefore decreases the effect of the structural stiffness matrix, thus working against the centrifugal stiffening effect. For this reason, it is usually referred to as the spin-softening matrix.

$$\frac{\partial \underline{f}_{\mathrm{c}}}{\partial \underline{p}}(\underline{p}) = -\boldsymbol{M}\cdot\boldsymbol{\Omega}\cdot\boldsymbol{\Omega}\cdot\underline{p} = \boldsymbol{K}_{\mathbf{c}}\cdot\underline{p} \tag{2.52}$$

Neglecting any other external forces, the equations that govern the deformations of the propeller blade structure are defined as follows, if the structure is subjected to an initial deformation, $\underline{p}_0$.

$$\boldsymbol{K}_{\mathbf{s}}\cdot(\underline{p}_0+\underline{p}) = \underline{f}_{\mathrm{c}}(\underline{p}_0+\underline{p}) = \underline{f}_{\mathrm{c}}(\underline{0}) + \boldsymbol{K}_{\mathbf{c}}\cdot(\underline{p}_0+\underline{p}) \tag{2.53}$$

$$\boldsymbol{K}_{\mathbf{s}}\cdot(\underline{p}_0+\underline{p}) - \boldsymbol{K}_{\mathbf{c}}\cdot(\underline{p}_0+\underline{p}) = \underline{f}_{\mathrm{c}}(\underline{0}) \tag{2.54}$$

The spin-softening effect is normally small and more than compensated for by the aforementioned centrifugal stiffening effect that is depicted in Figure 2.15. For this reason, the spin-softening matrix, $\boldsymbol{K_c}$, has not been included during linear analyses of the blade structure (where the spin-stiffening effect may not be observed), although it has been included within all nonlinear analyses.

2.3. AEROELASTIC MODELLING

During the aeroelastic analysis, aerodynamic loads are evaluated using blade element momentum theory at the quarter-chord location of each blade element. These loads are passed to the structural model, which projects the loads evaluated at each blade element onto the structural grid. The aeroelastic analysis couples the aerodynamic and structural models using calculated derivatives of each load vector in terms of the structural degrees of freedom. In this way, a closely coupled solution strategy was established, which minimizes the residual function defined as the difference between internal and external forces, as shown in Equation (2.55). The resultant external force vector is obtained by a summing together the aerodynamic, centrifugal, and additional eccentric forces. The eccentric force vector is included to maintain generality.

$$\underset{\sim}{R}\left(\underset{\sim}{p}\right) = \underbrace{\left[\underset{\sim}{f}_{\mathrm{s}}\left(\underset{\sim}{p}\right)\right]}_{\text{internal}} - \underbrace{\left[\underset{\sim}{f}_{\mathrm{a}}\left(\underset{\sim}{p}\right) + \underset{\sim}{f}_{\mathrm{c}}\left(\underset{\sim}{p}\right) + \underset{\sim}{f}_{\mathrm{e}}\left(\underset{\sim}{p}\right)\right]}_{\text{external}} \tag{2.55}$$

The external and internal forces encountered by the structure are purely dependent on structural deformations, as operating conditions and initial geometric parameters are otherwise fixed. Thus, the residual function also depends solely on structural deformations. When this residual function is equal to zero, the internal structural forces resulting from the blade's deformations are exactly equal to the forces acting on the blade, and thus the aeroelastic system reaches equilibrium. This residual function is minimized iteratively using Newton's method, which relies on a linearization of $\underset{\sim}{R}$ at the i^{th} iteration around $\underset{\sim}{p}_i$, as shown in Equation (2.56). Deformations at each iteration are found using Equation (2.57).

$$\underset{\sim}{R}\left(\underset{\sim}{p}_{i+1}\right) \approx \underset{\sim}{R}\left(\underset{\sim}{p}_i\right) + \left[\frac{\partial \underset{\sim}{R}}{\partial \underset{\sim}{p}}\left(\underset{\sim}{p}_i\right)\right] \cdot \left(\underset{\sim}{p}_{i+1} - \underset{\sim}{p}_i\right) := \underset{\sim}{0} \tag{2.56}$$

$$\implies \underset{\sim}{p}_{i+1} = \underset{\sim}{p}_i - \left[\frac{\partial \underset{\sim}{R}}{\partial \underset{\sim}{p}}\left(\underset{\sim}{p}_i\right)\right]^{-1} \underset{\sim}{R}\left(\underset{\sim}{p}_i\right) \tag{2.57}$$

Expanding Equation (2.56) results in the following expression, where the derivative of each force defines a corresponding stiffness matrix. The difference between the structural stiffness matrix and the stiffness matrices due to aerodynamic, centrifugal, and eccentric forces will be referred to as the Jacobian matrix, since it corresponds to the complete derivative matrix of the residual function, $\underset{\sim}{R}$.

$$-\underset{\sim}{R}\left(\underset{\sim}{p}_i\right) = \left(\underset{\sim}{f}_{\mathrm{a}}\left(\underset{\sim}{p}_i\right) + \underset{\sim}{f}_{\mathrm{c}}\left(\underset{\sim}{p}_i\right) + \underset{\sim}{f}_{\mathrm{e}}\left(\underset{\sim}{p}_i\right)\right) - \underset{\sim}{f}_{\mathrm{s}}\left(\underset{\sim}{p}_i\right) = \left[\frac{\partial \underset{\sim}{f}_{\mathrm{s}}}{\partial \underset{\sim}{p}} - \frac{\partial \underset{\sim}{f}_{\mathrm{a}}}{\partial \underset{\sim}{p}} - \frac{\partial \underset{\sim}{f}_{\mathrm{c}}}{\partial \underset{\sim}{p}} - \frac{\partial \underset{\sim}{f}_{\mathrm{e}}}{\partial \underset{\sim}{p}}\right]\Bigg|_{\underset{\sim}{p}_i} \left(\underset{\sim}{p}_{i+1} - \underset{\sim}{p}_i\right) \tag{2.58}$$

$$\left(\underset{\sim}{f}_{\mathrm{a}}\left(\underset{\sim}{p}_i\right) + \underset{\sim}{f}_{\mathrm{c}}\left(\underset{\sim}{p}_i\right) + \underset{\sim}{f}_{\mathrm{e}}\left(\underset{\sim}{p}_i\right)\right) - \underset{\sim}{f}_{\mathrm{s}}\left(\underset{\sim}{p}_i\right) = \left[\boldsymbol{K_s} - \boldsymbol{K_a} - \boldsymbol{K_c} - \boldsymbol{K_e}\right]\left(\underset{\sim}{p}_{i+1} - \underset{\sim}{p}_i\right) \tag{2.59}$$

$$\implies \left(\underset{\sim}{f}_{\mathrm{a}}\left(\underset{\sim}{p}_i\right) + \underset{\sim}{f}_{\mathrm{c}}\left(\underset{\sim}{p}_i\right) + \underset{\sim}{f}_{\mathrm{e}}\left(\underset{\sim}{p}_i\right)\right) - \underset{\sim}{f}_{\mathrm{s}}\left(\underset{\sim}{p}_i\right) = \boldsymbol{J} \cdot \left(\underset{\sim}{p}_{i+1} - \underset{\sim}{p}_i\right) \tag{2.60}$$

2.3.1. DERIVATIVE CALCULATION FOR AEROELASTIC ANALYSIS

To reduce the computational cost involved with iteratively solving the aeroelastic system of equations, it is essential to ensure that sensitivities shown in Equation (2.58) are correct. Moreover, these sensitivities were computed analytically wherever possible by directly differentiating the necessary equations with respect to the structural degrees of freedom. This approach circumvents the evaluation of finite differences during the analysis procedure, thus reducing the number of function evaluations required during the aeroelastic analysis to further decrease computational cost. The method that was applied to compute the spin-softening matrix, $\boldsymbol{K_c}$, has been outlined in Section 2.2.6, and the derivation of the structural stiffness matrix, $\boldsymbol{K_s}$, has been provided in Section 2.2.3. The remaining two sensitivities to compute are the derivative matrices for the external and aerodynamic forces.

EXTERNAL FORCES

If an applied external force or moment is located at one of the structural nodes, then it is relatively straightforward to include it within the analysis. However, in most cases, applied loads are eccentric, and thus must be appropriately handled by the finite-element solver, such that equivalent loads are applied at the structural degrees of freedom instead. The calculation of external forces and their sensitivities is based on the work of De Breuker [48] and Werter [30], who applied the formulation developed by Battini and Pacoste [61] to allow for both constant and follower external forces and moments. For completeness, a discussion on the formulation used to define external loads and their derivatives has been provided within this section, although further details may be found within references [30, 48, 61]. This derivation has been repeated in this work because it is essential for the calculation of sensitivities for the aerodynamic forces, as they always act at points that are eccentric to the structural nodes.

For any structural element, external forces can be applied at any location, at a distance of $\underline{v}_0$ from the line that joins the two end nodes of the element. Considering nodes k and $k+1$ of the structure, which have position vectors given by $\underline{x}_k$ and $\underline{x}_{k+1}$, an input external force and moment can be applied at a location of $\underline{x}_\mathrm{a} + \underline{v}_0$, where $\underline{x}_\mathrm{a}$ is a point on the element that joins $\underline{x}_k$ and $\underline{x}_{k+1}$.

The normalized distance between $\underline{x}_\mathrm{a}$ and $\underline{x}_k$ is given by ξ, which is defined as follows.

$$\xi = \frac{||\underline{x}_\mathrm{a} - \underline{x}_k||}{||\underline{x}_{k+1} - \underline{x}_k||} \implies 1 - \xi = \frac{||\underline{x}_{k+1} - \underline{x}_\mathrm{a}||}{||\underline{x}_{k+1} - \underline{x}_k||}$$

Diagrams of this scenario are provided in Figure 2.16 for clarity.

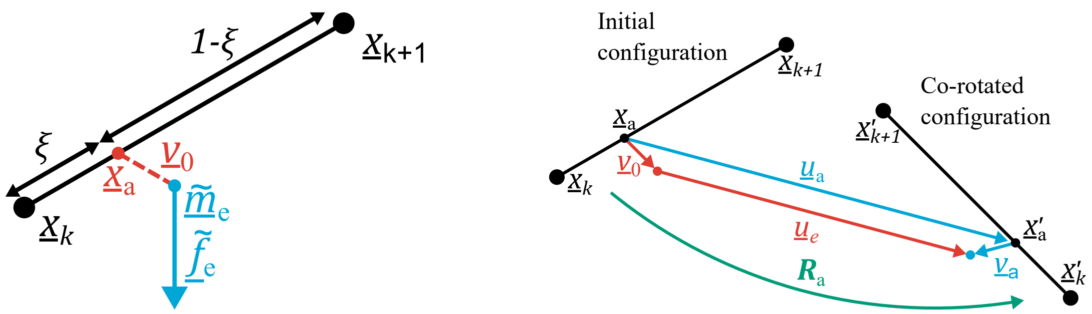

(a) A diagram of the external force applied to the undeformed structure.

(b) A diagram of the displacement of external forces.

Figure 2.16: Schematic diagrams of the external forces and moments (adapted from [30]).

The location of the applied force in the initial configuration is given by the following expression, where $\underline{v}_0$ is defined as a rigid link that is orthogonal to the beam element, as depicted in Figure 2.16a.

$$\underline{x}_\mathrm{e} = \underline{x}_\mathrm{a} + \underline{v}_0 \tag{2.61}$$

Figure 2.16b indicates that the rigid link may be converted into its corotated orientation as follows.

$$\underline{v}_\mathrm{a} = \boldsymbol{\mathcal{R}}_\mathbf{a} \cdot \underline{v}_0 \tag{2.62}$$

Using Figure 2.16, the displacements of the location of the applied load can be related to the deformation of the nearest point on the beam element, $\underline{x}_\mathrm{a}$, as shown below.

$$\underline{u}_\mathrm{a} + \underline{v}_\mathrm{a} = \underline{v}_0 + \underline{u}_\mathrm{e} \tag{2.63}$$

$$\implies \underline{u}_\mathrm{e} = \underline{u}_\mathrm{a} + \left[\boldsymbol{\mathcal{R}}_\mathbf{a} - \boldsymbol{I}\right] \underline{v}_0 \tag{2.64}$$

To transfer the applied load acting at $\underline{x}_\mathrm{e}$ onto the two nodes of the beam element, it must be ensured that the virtual work of the equivalent loads acting at the two nodes must be equal to the virtual work of the eccentric load. This is expressed using the following expression, where the total rotational pseudo-vector of the eccentric point is given by $\underline{\theta}_\mathrm{e}$, the total rotational pseudo-vectors of the two end nodes are given by $\underline{\theta}_k$ and $\underline{\theta}_{k+1}$, and displacement vectors of the two nodes are denoted by $\underline{u}_k$ and $\underline{u}_{k+1}$.

$$\delta \underline{p}_\mathrm{e}^\mathrm{T} \begin{bmatrix} \underline{\tilde{f}}_\mathrm{e} \\ \underline{\tilde{m}}_\mathrm{e} \end{bmatrix} = \begin{bmatrix} \delta \underline{p}_k^\mathrm{T} & \delta \underline{p}_{k+1}^\mathrm{T} \end{bmatrix} \begin{bmatrix} \underline{f}_k \\ \underline{m}_k \\ \underline{f}_{k+1} \\ \underline{m}_{k+1} \end{bmatrix} \qquad \underline{p} = \begin{bmatrix} \underline{u} \\ \underline{\theta} \end{bmatrix} \tag{2.65}$$

Using the relations derived above and the assumption of equivalent virtual work, Werter [30] derived a relationship between deformations of the eccentric node and global deformations of the two end nodes of the beam element in variational form, where $\underline{\vartheta}_{\mathrm{a}}$ is the spatial angular variation at the eccentric node.

$$\delta \underline{u}_{\mathrm{e}} = \delta \underline{u}_{\mathrm{a}} + \delta \boldsymbol{\mathcal{R}}_{\mathbf{a}} \underline{v}_0 \tag{2.66}$$

$$\delta \boldsymbol{\mathcal{R}}_{\mathbf{a}} = \delta \boldsymbol{\vartheta}_{\mathbf{a}} \boldsymbol{\mathcal{R}}_{\mathbf{a}} \tag{2.67}$$

$$\implies \delta \underline{u}_{\mathrm{e}} = \delta \underline{u}_{\mathrm{a}} + \delta \boldsymbol{\vartheta}_{\mathbf{a}} \boldsymbol{\mathcal{R}}_{\mathbf{a}} \underline{v}_0 = \delta \underline{u}_{\mathrm{a}} + \delta \boldsymbol{\vartheta}_{\mathbf{a}} \underline{v}_{\mathrm{a}} = \delta \underline{u}_{\mathrm{a}} - \boldsymbol{v}_{\mathbf{a}} \delta \underline{\vartheta}_{\mathrm{a}} \tag{2.68}$$

$$\implies \delta \underline{p}_{\mathrm{e}} = \begin{bmatrix} \delta \underline{u}_{\mathrm{e}} \\ \delta \underline{\theta}_{\mathrm{e}} \end{bmatrix} = \begin{bmatrix} (1-\xi)\boldsymbol{I}_{\mathbf{3x3}} & -(1-\xi)\boldsymbol{v}_{\mathbf{a}} & \xi \boldsymbol{I}_{\mathbf{3x3}} & -\xi \boldsymbol{v}_{\mathbf{a}} \\ \mathbf{0}_{\mathbf{3x3}} & (1-\xi)\boldsymbol{I}_{\mathbf{3x3}} & \mathbf{0}_{\mathbf{3x3}} & \xi \boldsymbol{I}_{\mathbf{3x3}} \end{bmatrix} \begin{bmatrix} \delta \underline{u}_k \\ \delta \underline{\vartheta}_k \\ \delta \underline{u}_{k+1} \\ \delta \underline{\vartheta}_{k+1} \end{bmatrix} = \boldsymbol{B}_{\mathbf{e}} \cdot \begin{bmatrix} \delta \underline{p}^{\mathrm{g}}_k \\ \delta \underline{p}^{\mathrm{g}}_{k+1} \end{bmatrix} \tag{2.69}$$

To transform the spatial angular variation into the variation of the total rotational pseudo-vector, the relation that was derived by Ibrahimbegovic [62] has been applied as follows.

$$\boldsymbol{\mathcal{T}}_{\boldsymbol{\theta}} = \frac{\sin(||\underline{\theta}||)}{||\underline{\theta}||} \boldsymbol{I} + \left(1 - \frac{\sin(||\underline{\theta}||)}{||\underline{\theta}||}\right) \underline{u} \otimes \underline{u} + \frac{1}{2}\left(\frac{\sin(||\underline{\theta}||/2)}{||\underline{\theta}||/2}\right)^2 \boldsymbol{\theta} \tag{2.70}$$

$$\begin{bmatrix} \delta \underline{u}_k \\ \delta \underline{\theta}_k \\ \delta \underline{u}_{k+1} \\ \delta \underline{\theta}_{k+1} \end{bmatrix} = \begin{bmatrix} \begin{matrix} \mathbf{0}_{\mathbf{3x3}} & \mathbf{0}_{\mathbf{3x3}} \\ \mathbf{0}_{\mathbf{3x3}} & \boldsymbol{\mathcal{T}}^{-1}_{\boldsymbol{\theta_k}} \end{matrix} & \mathbf{0}_{\mathbf{6x6}} \\ \mathbf{0}_{\mathbf{6x6}} & \begin{matrix} \mathbf{0}_{\mathbf{3x3}} & \mathbf{0}_{\mathbf{3x3}} \\ \mathbf{0}_{\mathbf{3x3}} & \boldsymbol{\mathcal{T}}^{-1}_{\boldsymbol{\theta_{k+1}}} \end{matrix} \end{bmatrix} \cdot \begin{bmatrix} \delta \underline{u}_k \\ \delta \underline{\vartheta}_k \\ \delta \underline{u}_{k+1} \\ \delta \underline{\vartheta}_{k+1} \end{bmatrix} = \boldsymbol{H} \begin{bmatrix} \delta \underline{p}_k \\ \delta \underline{p}_{k+1} \end{bmatrix} \tag{2.71}$$

The full conversion between displacements at the eccentric node and displacements at the degrees of freedom of the element is given by the following relation, which is used as shown to compute loads.

$$\delta \underline{p}_{\mathrm{e}} = \boldsymbol{B}_{\mathbf{e}} \cdot \boldsymbol{H} \cdot \begin{bmatrix} \delta \underline{p}_k \\ \delta \underline{p}_{k+1} \end{bmatrix} \implies \delta \underline{p}^{\mathrm{T}}_{\mathrm{e}} = \begin{bmatrix} \delta \underline{p}^{\mathrm{T}}_k & \delta \underline{p}^{\mathrm{T}}_{k+1} \end{bmatrix} (\boldsymbol{B}_{\mathbf{e}} \cdot \boldsymbol{H})^{\mathrm{T}} \tag{2.72}$$

$$\implies (\boldsymbol{B}_{\mathbf{e}} \cdot \boldsymbol{H})^{\mathrm{T}} \begin{bmatrix} \tilde{\underline{f}}_{\mathrm{e}} \\ \tilde{\underline{m}}_{\mathrm{e}} \end{bmatrix} = \boldsymbol{H}^{\mathrm{T}} \cdot \boldsymbol{B}^{\mathrm{T}}_{\mathbf{e}} \cdot \begin{bmatrix} \tilde{\underline{f}}_{\mathrm{e}} \\ \tilde{\underline{m}}_{\mathrm{e}} \end{bmatrix} = \begin{bmatrix} \underline{f}_k \\ \underline{m}_k \\ \underline{f}_{k+1} \\ \underline{m}_{k+1} \end{bmatrix} \tag{2.73}$$

This method of mapping forces from eccentric nodes to the nodes of the structural mesh has been applied also to convert aerodynamic loads from the aerodynamic grid points to the structural nodes. Centrifugal forces are already calculated at the nodes of the structure and thus are not converted.

The derivative of the external forces is calculated by taking the variation of the external force vector.

$$\begin{bmatrix} \delta \underline{f}_k \\ \delta \underline{m}_k \\ \delta \underline{f}_{k+1} \\ \delta \underline{m}_{k+1} \end{bmatrix} = \underbrace{\left(\delta \boldsymbol{H}^{\mathrm{T}}\right) \cdot \boldsymbol{B}^{\mathrm{T}}_{\mathbf{e}} \cdot \begin{bmatrix} \tilde{\underline{f}}_{\mathrm{e}} \\ \tilde{\underline{m}}_{\mathrm{e}} \end{bmatrix}}_{\text{geometric moment stiffness}} + \underbrace{\boldsymbol{H}^{\mathrm{T}} \cdot \left(\delta \boldsymbol{B}^{\mathrm{T}}_{\mathbf{e}}\right) \cdot \begin{bmatrix} \tilde{\underline{f}}_{\mathrm{e}} \\ \tilde{\underline{m}}_{\mathrm{e}} \end{bmatrix}}_{\text{geometric rotation stiffness}} \underbrace{+ \boldsymbol{H}^{\mathrm{T}} \cdot \boldsymbol{B}^{\mathrm{T}}_{\mathbf{e}} \cdot \begin{bmatrix} \delta \tilde{\underline{f}}_{\mathrm{e}} \\ \delta \tilde{\underline{m}}_{\mathrm{e}} \end{bmatrix}}_{\text{material stiffness}} = \boldsymbol{K}_{\mathbf{e}} \begin{bmatrix} \delta \underline{p}_k \\ \delta \underline{p}_{k+1} \end{bmatrix} \tag{2.74}$$

$$\implies [\boldsymbol{K}_{\mathbf{h}} + \boldsymbol{K}_{\mathbf{g}} + \boldsymbol{K}_{\mathbf{m}}] \begin{bmatrix} \delta \underline{p}_k \\ \delta \underline{p}_{k+1} \end{bmatrix} = \boldsymbol{K}_{\mathbf{e}} \begin{bmatrix} \delta \underline{p}_k \\ \delta \underline{p}_{k+1} \end{bmatrix} \tag{2.75}$$

The complete derivation of the derivative matrix of the external forces has been provided by Werter [30], and thus the full derivation of the external force derivative matrix will not be repeated here for brevity. Nevertheless, the material stiffness has been briefly revisited within this section, as it has been treated differently during the calculation of the aerodynamic stiffness matrix. The geometric moment stiffness and the geometric rotation stiffness are not dependent on the nature of the applied forces, and thus their form remains unchanged from what has been presented in [30].

To calculate the material stiffness, the variation of the applied force must be calculated, as all remaining quantities are already known. This has been defined as the derivative of the eccentric forces with respect to the degrees of freedom, multiplied by the variation of the degrees of freedom.

$$\begin{bmatrix} \delta \underline{\tilde{f}}_{\mathrm{e}} \\ \delta \underline{\tilde{m}}_{\mathrm{e}} \end{bmatrix} = \left(\frac{d}{d\underline{p}_{\mathrm{e}}} \begin{bmatrix} \underline{\tilde{f}}_{\mathrm{e}} \\ \underline{\tilde{m}}_{\mathrm{e}} \end{bmatrix} \right) \cdot \delta \underline{p}_{\mathrm{e}} \tag{2.76}$$

Substituting Equation (2.72) into the above expression yields the following expression for the variation of the eccentric loads. This expression can then be used to determine the material stiffness matrix.

$$\begin{bmatrix} \delta \underline{\tilde{f}}_{\mathrm{e}} \\ \delta \underline{\tilde{m}}_{\mathrm{e}} \end{bmatrix} = \left(\frac{d}{d\underline{p}_{\mathrm{e}}} \begin{bmatrix} \underline{\tilde{f}}_{\mathrm{e}} \\ \underline{\tilde{m}}_{\mathrm{e}} \end{bmatrix} \right) \cdot \boldsymbol{B}_{\mathbf{e}} \cdot \boldsymbol{H} \cdot \begin{bmatrix} \delta \underline{p}_{k} \\ \delta \underline{p}_{k+1} \end{bmatrix} \Longrightarrow \boldsymbol{K}_{\mathbf{m}} = \boldsymbol{H}^{\mathrm{T}} \cdot \boldsymbol{B}_{\mathbf{e}}{}^{\mathrm{T}} \cdot \left(\frac{d}{d\underline{p}_{\mathrm{e}}} \begin{bmatrix} \underline{\tilde{f}}_{\mathrm{e}} \\ \underline{\tilde{m}}_{\mathrm{e}} \end{bmatrix} \right) \cdot \boldsymbol{B}_{\mathbf{e}} \cdot \boldsymbol{H} \tag{2.77}$$

This derivation has only been used to evaluate the material stiffness matrix for aerodynamic forces, while the original derivation that was provided by Werter [30] has been used for the evaluation of the material stiffness matrix for all other externally applied forces.

To calculate the derivative matrix for aerodynamic forces, it has been assumed that they depend solely on the blade twist angle, β, thus yielding the following expression. Note that the subscript "e" has been replaced by "a" to indicate that the loads being discussed are due to aerodynamic effects.

$$\left(\frac{d}{d\underline{p}_{\mathrm{a}}} \begin{bmatrix} \underline{\tilde{f}}_{\mathrm{a}} \\ \underline{\tilde{m}}_{\mathrm{a}} \end{bmatrix} \right) = \begin{bmatrix} \underline{0} & \underline{0} & \underline{0} & \underline{0} & \frac{d}{d\beta} \underline{\tilde{f}}_{\mathrm{a}} & \underline{0} \\ \underline{0} & \underline{0} & \underline{0} & \underline{0} & \frac{d}{d\beta} \underline{\tilde{m}}_{\mathrm{a}} & \underline{0} \end{bmatrix} \tag{2.78}$$

The following section contains details on how these derivatives have been determined. Appendix D also contains an extension of this derivation to include sensitivities in terms of radial deformations.

AERODYNAMIC LOADS

Sensitivities for the aerodynamic forces are evaluated on the aerodynamic grid using blade element momentum theory because all aerodynamic quantities are already known at these locations. This makes it possible to analytically evaluate derivatives of the aerodynamic forces and moments. The sensitivities are then mapped onto the finite element grid using the approach that was outlined in the previous section so that they may be applied within Equation (2.58). The process of evaluating derivatives of aerodynamic loads at the aerodynamic grid locations has accordingly been discussed in this section.

At a point on the aerodynamic grid, the aerodynamic forces and moments are given by the following expression, which is solved for using blade element momentum theory, outlined within Section 2.1.

$$\begin{bmatrix} \underline{\tilde{f}}_{\mathrm{a}} \\ \underline{\tilde{m}}_{\mathrm{a}} \end{bmatrix} = q_{\infty} \Delta S(r) \begin{bmatrix} C_x(\alpha, \varphi, Re, Ma) & 0 & C_z(\alpha, \varphi, Re, Ma) & 0 & C_m(\alpha, Re, Ma)c & 0 \end{bmatrix}^T \left(\frac{V}{V_{\infty}} \right)^2 \tag{2.79}$$

The force coefficients, C_x and C_z, are directly evaluated using Equation (2.15). Thus, they depend entirely on the lift and drag coefficients and the flow angle, φ, of the blade section.

To calculate the derivatives in terms of structural degrees of freedom, the following two assumptions have been applied. First, it has been assumed that only pitch deformations contribute to changes in aerodynamic loads. Thus, only derivatives with respect to blade twist, β, have been computed. It is recognized that loads are also dependent on the radial position of the blade element, although these derivatives are relatively small and therefore can be omitted without losses in precision during the aeroelastic analysis. For this reason, the derivation of sensitivities with respect to radial deformations has not been included in this section, although a complete derivation for this may be found in Appendix C. Because the axial and tangential induction factors, a and a', depend on the twist of any given blade section, the inflow angle, φ, also depends on the blade twist. This implies that it is not possible to simply assume that derivatives of aerodynamic quantities with respect to angle of attack are equivalent to derivatives of aerodynamic quantities with respect to blade twist.

$$\begin{aligned} \frac{d}{d\beta} \begin{bmatrix} \underline{\tilde{f}}_{\mathrm{a}} \\ \underline{\tilde{m}}_{\mathrm{a}} \end{bmatrix} = q_{\infty} \Delta S \Bigg(& \begin{bmatrix} C_{x_\alpha} & 0 & C_{z_\alpha} & 0 & C_{m_\alpha} c & 0 \end{bmatrix}^T \left(\frac{d\alpha}{d\beta} \right) \left(\frac{V}{V_{\infty}} \right)^2 + \\ & \begin{bmatrix} C_x & 0 & C_z & 0 & C_m c & 0 \end{bmatrix}^T \left(\frac{2V}{V_{\infty}^2} \right) \left(\frac{dV}{d\beta} \right) \Bigg) \end{aligned} \tag{2.80}$$

The only unknown contained within the second term of Equation (2.80) is $dV/d\beta$, which is computed using the following expression, shown in Equation (2.81). The only unknown quantities in Equation (2.81) are the derivatives of the induction factors with respect to the pitch setting, $da/d\beta$ and $da'/d\beta$.

$$V = \sqrt{(V_\infty(1+a))^2 + (\omega r(1-a'))^2} \implies \frac{dV}{d\beta} = \frac{V_\infty^2(1+a)\frac{da}{d\beta} - (\omega r)^2(1-a')\frac{da'}{d\beta}}{V} \tag{2.81}$$

The first term of Equation (2.80) requires slightly more work to evaluate. First, the normal and tangential force coefficients, C_z and C_x, are differentiated with respect to α using Equation (2.82).

$$\begin{bmatrix} C_{z_\alpha} \\ C_{x_\alpha} \end{bmatrix} = \begin{bmatrix} \cos(\varphi) & -\sin(\varphi) \\ \sin(\varphi) & \cos(\varphi) \end{bmatrix} \begin{bmatrix} C_{l_\alpha}(\alpha, Re, Ma) \\ C_{d_\alpha}(\alpha, Re, Ma) \end{bmatrix} \tag{2.82}$$

Derivatives of the lift, drag, and moment coefficients with respect to the angle of attack can be easily obtained numerically using polar data, since all aerodynamic quantities are already obtained using the BEM equations. Thus, the only term that is missing is the derivative of the angle of attack with respect to the twist, $d\alpha/d\beta$. Using Figure 2.6 and differentiating the expression for the angle of attack that is shown in Equation (2.16), an expression for this derivative may be obtained as follows.

$$\frac{d\alpha}{d\beta} = \frac{d\beta}{d\beta} - \frac{d\varphi}{d\beta} = 1 - \frac{d\varphi}{d\beta} \tag{2.83}$$

$$\frac{d\varphi}{d\beta} = \frac{d}{d\beta}\left(\arctan\left(\frac{V_\infty(1+a)}{\omega r(1-a')}\right)\right) = \frac{V_\infty \omega r\left(\frac{da}{d\beta}(1-a') + \frac{da'}{d\beta}(1+a)\right)}{(\omega r(1-a'))^2 + (V_\infty(1+a))^2} \tag{2.84}$$

$$\implies \frac{d\alpha}{d\beta} = 1 - \frac{V_\infty}{V}\frac{\omega r}{V}\left(\frac{da}{d\beta}(1-a') + \frac{da'}{d\beta}(1+a)\right) \tag{2.85}$$

Derivatives of the angle of attack with respect to the blade twist have also been calculated using blade element theory and momentum theory to obtain two other expressions for derivatives of the angle of attack with respect to the blade twist. With momentum theory, thrust and torque coefficient expressions are provided in terms of the axial and tangential induction factors, whereas blade element theory relates the thrust and torque coefficients to the angle of attack and inflow angle.

$$\frac{dC_t}{d\beta} = \frac{\partial C_t}{\partial a}\frac{\partial a}{\partial \beta} + \frac{\partial C_t}{\partial a'}\frac{\partial a'}{\partial \beta} = \frac{dC_t}{d\alpha}\frac{d\alpha}{d\beta} \tag{2.86}$$

$$\frac{dC_q}{d\beta} = \frac{\partial C_q}{\partial a}\frac{\partial a}{\partial \beta} + \frac{\partial C_q}{\partial a'}\frac{\partial a'}{\partial \beta} = \frac{dC_q}{d\alpha}\frac{d\alpha}{d\beta} \tag{2.87}$$

With momentum theory, the thrust and torque coefficient derivatives with respect to the blade twist are given by Equation (2.88) and Equation (2.89). These expressions maintain all the same assumptions as outlined in Section 2.1.1, in addition to the simplifications discussed in this section.

$$\frac{dC_t^{\mathrm{M}}}{d\beta} = \begin{cases} 4\left((1+2a)F + a(1+a)\frac{\partial F}{\partial a}\right)\frac{da}{d\beta} & a \geq -0.326 \\ \left(1.39F + (1.39(1+a) - 1.816)\frac{\partial F}{\partial a}\right)\frac{da}{d\beta} & a < -0.326 \end{cases} \tag{2.88}$$

$$\frac{dC_q^{\mathrm{M}}}{d\beta} = 4(1+a)\frac{\omega r}{V_\infty}\left(F + a'\frac{\partial F}{\partial a'}\right)\frac{da'}{d\beta} + 4a'\frac{\omega r}{V_\infty}\left(F + (1+a)\frac{\partial F}{\partial a}\right)\frac{da}{d\beta} \tag{2.89}$$

Differentiating the root and tip loss factors, F_{root} and F_{tip}, with respect to the incoming flow angle, φ, yields the following two expressions, which are directly found using Equation (2.7).

$$\frac{dF_{\mathrm{root}}}{d\varphi} = -\frac{N_{\mathrm{b}}}{\pi}\left(\frac{r - r_{\mathrm{root}}}{r|\sin(\varphi)|}\right)\frac{\cos(\varphi)}{\sin(\varphi)}\left(\frac{\exp\left[-\frac{N_{\mathrm{b}}}{2}\left(\frac{r-r_{\mathrm{root}}}{r|\sin(\varphi)|}\right)\right]}{\sqrt{1-\exp\left[-N_{\mathrm{b}}\left(\frac{r-r_{\mathrm{root}}}{r|\sin(\varphi)|}\right)\right]}}\right) \tag{2.90}$$

$$\frac{dF_{\mathrm{tip}}}{d\varphi} = -\frac{N_{\mathrm{b}}}{\pi}\left(\frac{r_{\mathrm{tip}} - r}{r|\sin(\varphi)|}\right)\frac{\cos(\varphi)}{\sin(\varphi)}\left(\frac{\exp\left[-\frac{N_{\mathrm{b}}}{2}\left(\frac{r_{\mathrm{tip}}-r}{r|\sin(\varphi)|}\right)\right]}{\sqrt{1-\exp\left[-N_{\mathrm{b}}\left(\frac{r_{\mathrm{tip}}-r}{r|\sin(\varphi)|}\right)\right]}}\right) \tag{2.91}$$

The derivatives of the Prandtl tip-loss factor, F, with respect to the axial and tangential induction factors are given by Equation (2.92) and Equation (2.93), which are obtained by applying the chain rule.

$$\frac{\partial F}{\partial a} = \left[\frac{dF_{\text{root}}}{d\varphi}F_{\text{tip}} + F_{\text{root}}\frac{dF_{\text{tip}}}{d\varphi}\right]\overbrace{\left[\frac{V_\infty}{V}\frac{\omega r}{V}(1-a')\right]}^{\partial\varphi/\partial a} \tag{2.92}$$

$$\frac{\partial F}{\partial a'} = \left[\frac{dF_{\text{root}}}{d\varphi}F_{\text{tip}} + F_{\text{root}}\frac{dF_{\text{tip}}}{d\varphi}\right]\underbrace{\left[\frac{V_\infty}{V}\frac{\omega r}{V}(1+a)\right]}_{\partial\varphi/\partial a'} \tag{2.93}$$

With these expressions, all terms within Equation (2.88) and Equation (2.89) are known except for $da/d\beta$ and $da'/d\beta$. Derivatives of the thrust and torque coefficients with respect to the blade twist may also be evaluated using blade element theory to isolate for the derivatives of the axial and tangential induction factors, as shown below. This yields three expressions for $da/d\beta$.

$$\frac{dC_t^{\text{BE}}}{d\beta} = C_{z_\alpha}\,\sigma(r)\left(\frac{V}{V_\infty}\right)^2\frac{d\alpha}{d\beta} \implies \left(\frac{d\alpha}{d\beta}\right)_t = \begin{cases} \dfrac{4\left((1+2a)F+a(1+a)\frac{\partial F}{\partial a}\right)\frac{da}{d\beta}}{C_{z_\alpha}\,\sigma(r)}\left(\frac{V_\infty}{V}\right)^2 & a \geq -0.326 \\ \dfrac{\left(1.39F+(1.39(1+a)-1.816)\frac{\partial F}{\partial a}\right)\frac{da}{d\beta}}{C_{z_\alpha}\,\sigma(r)}\left(\frac{V_\infty}{V}\right)^2 & a < -0.326 \end{cases} \tag{2.94}$$

$$\frac{dC_q^{\text{BE}}}{d\beta} = C_{x_\alpha}\,\sigma(r)\left(\frac{V}{V_\infty}\right)^2\frac{d\alpha}{d\beta} \implies \left(\frac{d\alpha}{d\beta}\right)_q = \frac{4\omega r V_\infty\left[(1+a)\left(F+a'\frac{\partial F}{\partial a'}\right)\frac{da'}{d\beta} + a'\left(F+(1+a)\frac{\partial F}{\partial a}\right)\frac{da}{d\beta}\right]}{C_{x_\alpha}\,\sigma(r)\,V^2} \tag{2.95}$$

With three expressions and three unknowns, the derivatives $da/d\beta$ and $da'/d\beta$, may be iteratively solved for using Newton's method by constructing a residual vector, as shown below, and evaluating the system of equations shown in Equation (2.97) (presented at the i^{th} iteration) until convergence.

$$\underset{\sim}{R} = \left[\left(\frac{d\alpha}{d\beta}\right)_t - \frac{d\alpha}{d\beta} \quad \left(\frac{d\alpha}{d\beta}\right)_q - \frac{d\alpha}{d\beta}\right]^T := \underset{\sim}{0} \tag{2.96}$$

$$\begin{bmatrix} \frac{da}{d\beta} \\ \frac{da'}{d\beta} \end{bmatrix}_{i+1} = \begin{bmatrix} \frac{da}{d\beta} \\ \frac{da'}{d\beta} \end{bmatrix}_{i} - \begin{bmatrix} \frac{\partial R_1}{\partial(da/d\beta)} & \frac{\partial R_1}{\partial(da'/d\beta)} \\ \frac{\partial R_2}{\partial(da/d\beta)} & \frac{\partial R_2}{\partial(da'/d\beta)} \end{bmatrix}_i^{-1} \cdot \underset{\sim}{R} \tag{2.97}$$

After solving for both $da/d\beta$ and $da'/d\beta$, $d\alpha/d\beta$ can be evaluated by substituting these terms into either Equation (2.85), Equation (2.94), or Equation (2.95). All three of these equations will, of course, yield the same result. With this, all terms required to evaluate Equation (2.80) are known.

As already mentioned, the advantage of the approach proposed in this section is that it requires significantly less computational time in comparison to if the derivatives were to be evaluated using finite differences. To verify that the derivative calculation routine performs as anticipated, comparisons were made between the derivatives evaluated using equations shown in this section to derivatives evaluated using a central differencing scheme, which proceeds according to Equation (2.98) and has a truncation error of $\mathcal{O}\left(\Delta\beta^2\right)$, where h is the aerodynamic quantity being differentiated.

$$\frac{dh}{d\beta}(\beta) \approx \frac{h(\beta+\Delta\beta) - h(\beta-\Delta\beta)}{2\Delta\beta} \tag{2.98}$$

To demonstrate differences observed between the sensitivities evaluated analytically and numerically, the TUD-XPROP propeller (with geometry information provided in Appendix A) has been analysed at a pitch setting of 20° over a range of advance ratios between 0.6 and 1.5. The step size used for the numerical calculation was given by $\Delta\beta = 10^{-6}$, while the step size for the lift curve slopes calculated during the analytical calculation are given by $\Delta\alpha = 10^{-6}$. Values for the step sizes were determined heuristically, as smaller step sizes were found to yield negligible improvements in precision. The results of this investigation are shown in Figure 2.17. The absolute difference plots shown in Figure 2.17 were calculated by taking the absolute value of the difference between the derivative obtained analytically and the derivative obtained numerically. The sensitivities shown correspond to the force and moment coefficients, the induction factors, and the flow angles. The derivatives have been computed analytically respectively using Equation (2.79), Equation (2.97), and Equation (2.85).

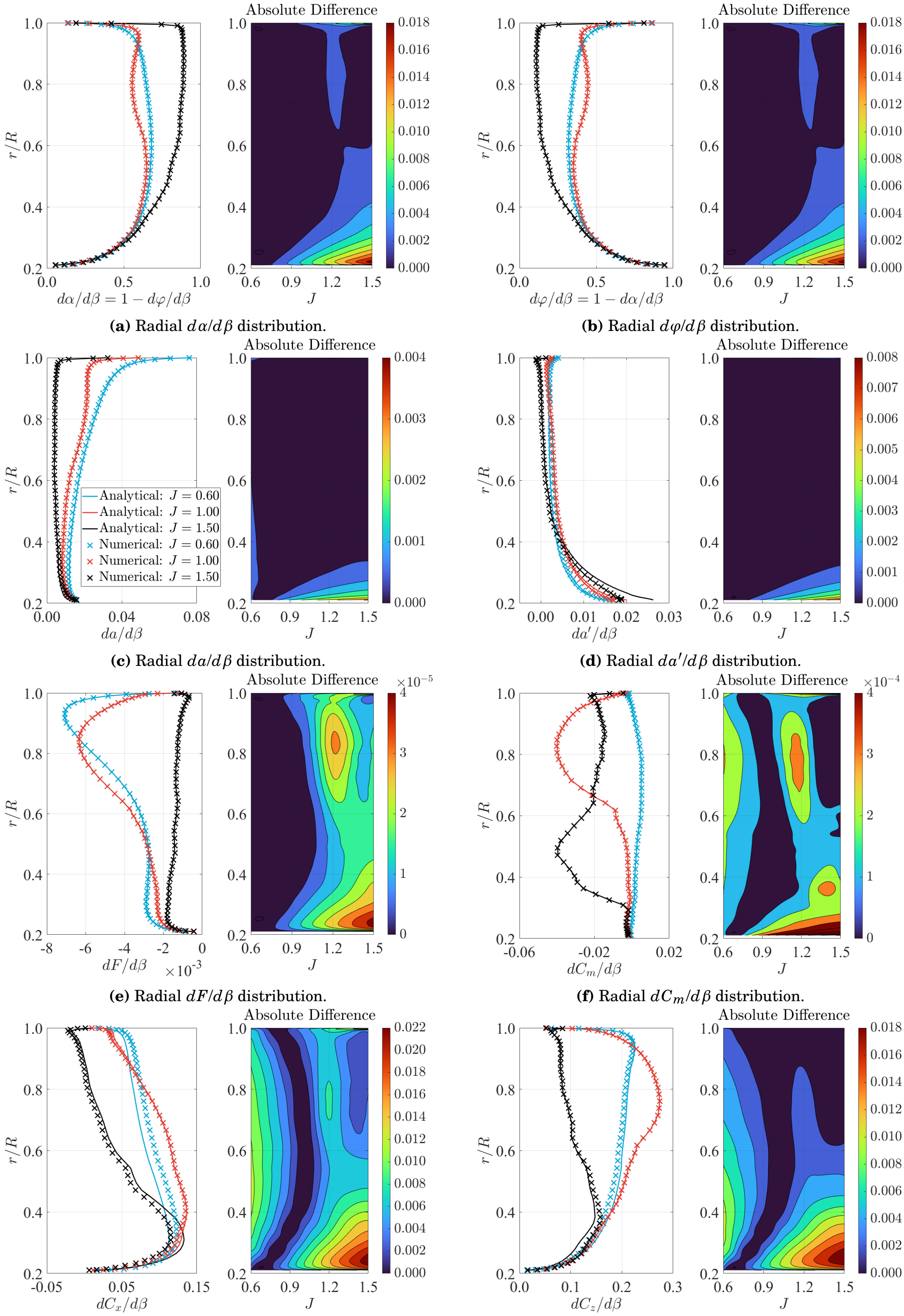

(a) Radial $d\alpha/d\beta$ distribution.

(b) Radial $d\varphi/d\beta$ distribution.

(c) Radial $da/d\beta$ distribution.

(d) Radial $da'/d\beta$ distribution.

(e) Radial $dF/d\beta$ distribution.

(f) Radial $dC_m/d\beta$ distribution.

(g) Radial $dC_x/d\beta$ distribution.

(h) Radial $dC_z/d\beta$ distribution.

Figure 2.17: Comparisons between derivatives computed numerically and analytically for the TUD-XPROP (see Appendix A for geometry details) at a blade collective pitch setting of 20°.

The results indicate that the unknown quantities, $d\alpha/d\beta$, $d\varphi/d\beta$, $da/d\beta$, $da'/d\beta$, $dF/d\beta$, and $dC_m/d\beta$ are nearly identical between the two methods. Errors were generally observed near the root section at relatively high advance ratios, possibly due to modelling difficulties in this region, as viscous effects have an important influence on the flow. This causes the slope of the lift and drag coefficients to be more difficult to predict, thus leading to a larger error. In particular, significant uncertainties are observed in results for the derivatives of the normal and tangential force coefficients, respectively $dC_z/d\beta$ and $dC_x/d\beta$. This, of course, also affects results obtained for derivatives of the dimensional forces. The derivative of the pitching moment coefficient is predicted with more precision than derivatives of the thrust and torque coefficients because it is not evaluated using an iterative method. Nevertheless, the results obtained indicate that the general trends are predicted correctly using the analytical approach, which verifies this method.

2.3.2. AEROELASTIC ANALYSIS PROCEDURE

The static aeroelastic analysis procedure that was applied during this research can be used to perform either a linear or a nonlinear analysis. The linear analysis is performed by solving Equation (2.60) for one iteration only, whereas the nonlinear analysis is performed by solving Equation (2.60) for several iterations until the residual function decays to zero. Thus, the nonlinear analysis is an extension of the linear analysis, which guarantees that energy is conserved at all degrees of freedom, while the linear method does not ensure the conservation of energy. The linear approach has been described for completeness, although the nonlinear method was exclusively applied during this project unless specified otherwise.

LINEAR ANALYSIS

A UML activity diagram depicting the linear analysis procedure has been provided within Figure 2.18.

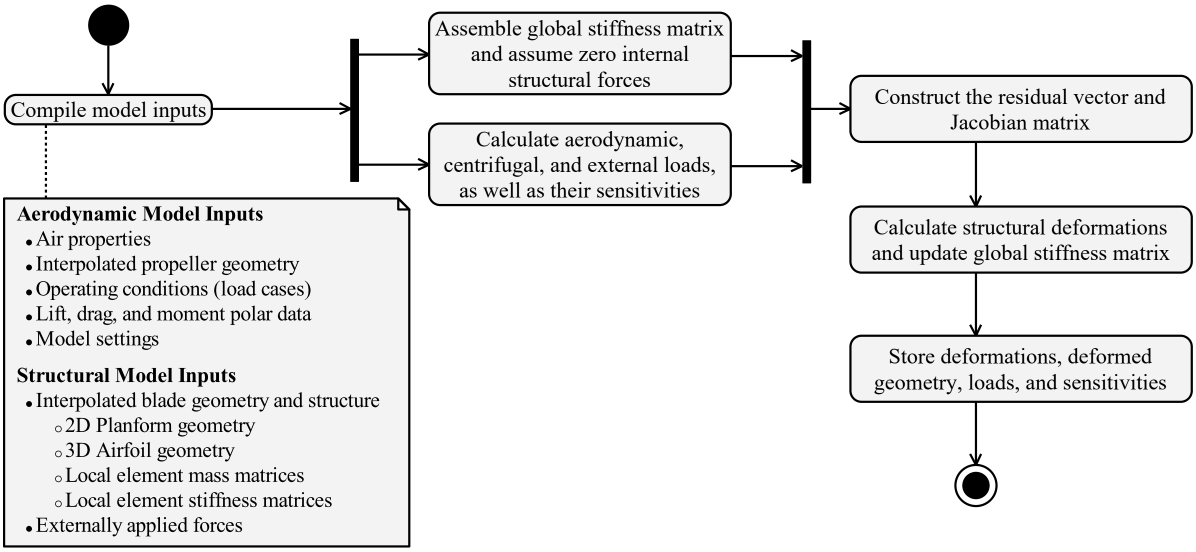

Figure 2.18: A schematic diagram indicating the linear aeroelastic analysis procedure.

Because the linear analysis only performs one iteration, structural deformations are evaluated using the following expression. Thus, all loads and their sensitivities are evaluated exactly once.

$$\left(\underline{f}_{\mathrm{a}}\left(\underline{p}\right)+\underline{f}_{\mathrm{c}}\left(\underline{p}\right)+\underline{f}_{\mathrm{e}}\left(\underline{p}\right)\right)-\underline{f}_{\mathrm{s}}\left(\underline{p}\right)=\underline{R}=\boldsymbol{J}\cdot\underline{p}\implies\underline{p}=\boldsymbol{J}^{-1}\underline{R} \tag{2.99}$$

Because structural deformations are initially assumed to be zero, it must initially be assumed that the internal structural forces are equal to zero. Thus, the real form of the equation solved during the linear analysis is given by the following expression, as shown in Equation (2.100).

$$\boldsymbol{J}^{-1}\left[\underline{f}_{\mathrm{a}}\left(\underline{p}\right)+\underline{f}_{\mathrm{c}}\left(\underline{p}\right)+\underline{f}_{\mathrm{e}}\left(\underline{p}\right)\right]=\underline{p} \tag{2.100}$$

The linear method is suitable for systems that only encounter small deformations, where geometric nonlinearities are not significant, as the sensitivities embedded within the Jacobian matrix are applied through a linearization of the full nonlinear system about the initial geometry. Moreover, this method is incapable of accurately accounting for the nonlinear centrifugal stiffening effect because only the initial geometry is considered during the evaluation of loads and sensitivities. Lastly, because the aerodynamic loads and sensitivities are evaluated only once, for the initial geometry, the aerodynamic loads will be inaccurate with large changes in twist distribution because the aerodynamic model used during this project is nonlinear. Thus, the linear aeroelastic method is insufficient for this project.

NONLINEAR ANALYSIS

The nonlinear analysis proceeds similarly to the linear analysis, although now Equation (2.60) is solved iteratively. To stabilize the iterations, a scale factor (λ_s) is applied as shown in Equation (2.101) and gradually increased from zero to one. The nonlinear analysis thus proceeds as follows. First, the scale factor is initialized between zero and one, and then the residual function is minimized for the aeroelastic system with scaled loads. After convergence is reached, the scale factor is increased and the residual function is minimized again. This process is repeated until convergence with a scale factor that is equal to one, thus being equivalent to Equation (2.58). Values for the scale factor and its step size were determined heuristically, and fast convergence was observed with an initial λ_s value of 0.5 and a step size of 0.25.

$$\left(\underline{f}_a\left(\underline{p}_i\right)+\underline{f}_c\left(\underline{p}_i\right)+\underline{f}_e\left(\underline{p}_i\right)\right)\lambda_s-\underline{f}_s\left(\underline{p}_i\right)=\left[\frac{\partial \underline{f}_s}{\partial \underline{p}}-\left(\frac{\partial \underline{f}_a}{\partial \underline{p}}+\frac{\partial \underline{f}_c}{\partial \underline{p}}+\frac{\partial \underline{f}_e}{\partial \underline{p}}\right)\lambda_s\right]\Bigg|_{\underline{p}_i}\left(\underline{p}_{i+1}-\underline{p}_i\right) \tag{2.101}$$

A UML activity diagram depicting the nonlinear analysis procedure is shown within Figure 2.19.

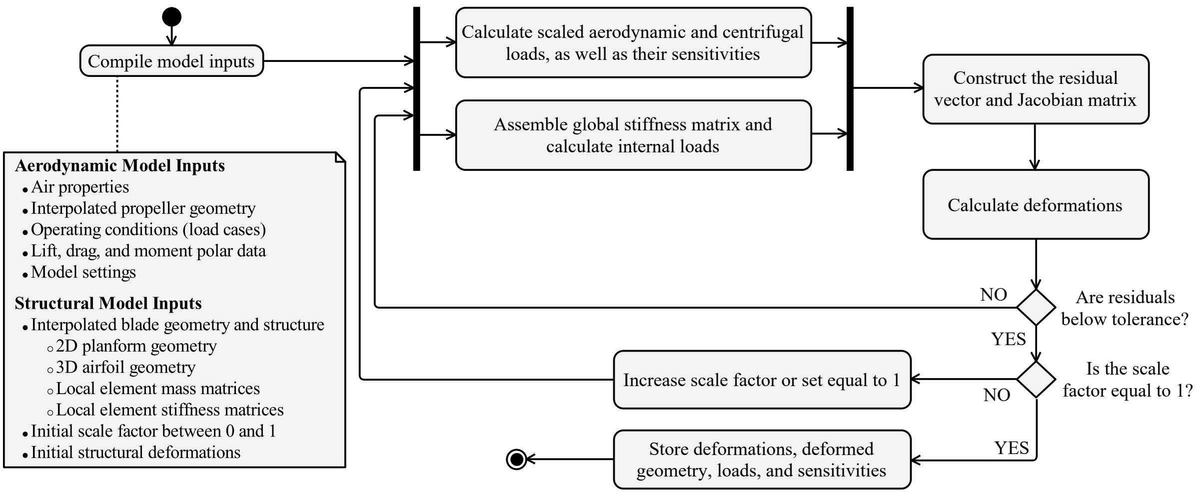

Figure 2.19: A schematic diagram indicating the nonlinear aeroelastic analysis procedure.

It is clear from Figure 2.19 and Equation (2.101) that the nonlinear analysis evaluates the linearized aeroelastic system at each iteration. The converged solution corresponds exactly to the nonlinear aeroelastic system, satisfying Equation (2.55) because the linearized expression is updated to correspond to the deformed geometry at each iteration. The residual vector usually does not equal zero when using the linear analysis. The proposed nonlinear analysis method generally reaches full convergence relatively quickly, in fewer than ten iterations. It is additionally usually possible to initialize the scale factor with a value of 1 to decrease the number of iterations that are required in a single analysis.

2.4. MODEL OVERVIEW

After presenting the formulation used for the aeroelastic analysis within the preceding three sections, a summary of the workflow and limitations of the analysis procedure are discussed in this section.

2.4.1. FULL ANALYSIS WORKFLOW

A UML activity diagram of the analysis procedure that was developed is provided within Figure 2.20, starting from the definition of model inputs and ending at the post-processing of results.

In the first step, the blade geometry and structural design is read by the program. The geometry input is defined as spanwise distributions of airfoils, chord lengths, twist angles, leading edge locations, reference axis locations, and composite skin configurations. For each spanwise laminate of the structural design, eight lamination parameters and a constant thickness are defined. With the provided lamination parameters and thicknesses, the program calculates the structural properties of each laminate along the span of the blade. The analysis program then interpolates the geometric and structural information to spanwise locations defining the nodes of the structural mesh. Lastly, airfoil polar plots are generated, and aerodynamic coefficients are interpolated along the span of the blade before the analysis begins. After processing all the inputs and storing information on the operating conditions to be studied, the interpolated laminate properties and cross-sectional geometry are processed by the cross-sectional modeller to represent the structure as an equivalent Timoshenko beam element mesh. The static aeroelastic analysis is then performed using the beam element model. After the aeroelastic analysis is completed, post-processing of results is possible. For example, the cross-sectional modeller may be used again to recover strains over the 3D geometry or propeller performance trends can be evaluated.

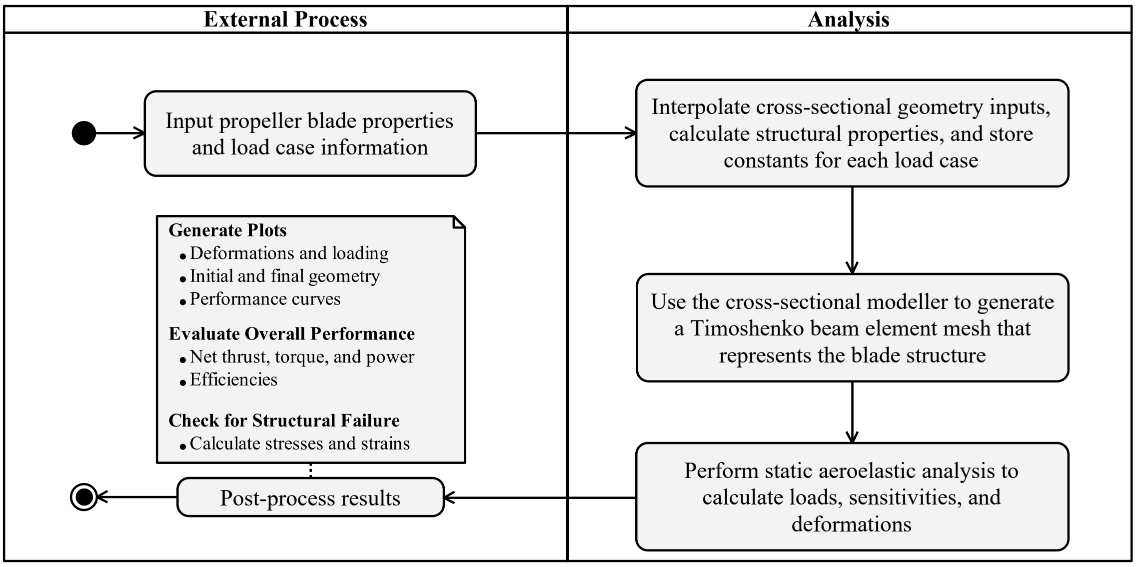

Figure 2.20: A UML activity diagram indicating the full analysis workflow.

2.4.2. MODEL LIMITATIONS

The most important feature of the model that has been developed is that it is computationally efficient, which thus makes it especially suitable for the preliminary design of propellers. By prioritizing computational efficiency, some limiting assumptions have been introduced that may adversely affect the accuracy or precision of the model. The main limitations on the models that were applied are provided below.

- As discussed in Appendix B.1, blade element momentum theory cannot intrinsically represent three-dimensional phenomena and thus must rely on approximate engineering correction models to account for some of their effects. One way to address this would be to implement a higher fidelity aerodynamic model (such as with a lifting-line or vortex-lattice method), like the approach of Hegberg [26].
- By using the Prandtl-Glauert correction, results are only considered valid up to a Mach number of approximately 0.75. The selected aerodynamic model is also incapable of modelling drag-divergence, which has significant effects on aerodynamic loads at high Mach numbers.
- It has been assumed that the cross-sectional geometry of the blade does not change during its deformation. This implies that the cross-sectional modeller is only required at the beginning and end of the analysis, and airfoil polar plots remain unchanged during the analysis.
- Because laminate properties have been represented with lamination parameters, a post-processing step is required to retrieve an applicable ply stacking sequence for a given parametrization. This procedure usually results in a decrease in performance, and has not been considered in this work.
- Buckling has been neglected during this project, although a suitable method for this work was developed and applied by Dillinger [63]. The decision to neglect buckling was justified, as compressive strains were nearly negligible in all results that were presented.

3

Aeroelastic Tailoring Approach

Details on the optimization framework that was developed for this project, including a description of the optimization problem that was formulated for this work, have been provided in this chapter. The developed optimization framework has been used to demonstrate the potential to apply aeroelastic tailoring towards the improvement of propeller performance. Section 3.1 first covers the formulation of the optimization problems, which were considered during the design studies, including descriptions of the objective function, design variables, and constraints. Section 3.2 then contains an overview of the design study that was performed during this research, including descriptions of the propeller blade geometry and materials being considered, operating conditions used, optimization goals and cases under consideration as well as a brief discussion on the methods applied to perform the optimization.

3.1. Formulating the Optimization Problem

A multi-objective optimization problem has been formulated to ensure that the final propeller design always maintains reasonable performance characteristics during all phases of flight, corresponding to both propulsive and regenerative operation. A broad range of operating conditions has been considered during the structural blade optimization procedure through the use of a climb-cruise-descent mission profile to quantify propeller performance. This mission has also been used to define realistic operating conditions for the propeller, whilst appropriately accounting for their relative importance toward the overall design. To maintain a low computational cost during the evaluation of the objective and constraint functions, propeller performance in each mission segment was quantified by a single operating condition. More specifically, the climb, cruise, and descent segments were each defined by a single operating point. Nevertheless, the code that was developed is capable of defining the mission either by four segments (first climb, second climb, cruise, and descent), or by three segments (climb, cruise, and descent). Despite the greater accuracy of the mission with four segments, the three-segment mission was accordingly used throughout this project to maintain a low computational cost. Notional diagrams depicting the mission profiles considered during this work have been provided below in Figure 3.1. In each mission segment, operating conditions and thrust requirements were defined at the median altitude. Further details on the selection of operating conditions for the propeller are provided in Section 3.2.1.

During the optimization, equality constraints on the thrust requirements were set, and the mission profile under consideration corresponds to a realistic aircraft configuration, to guarantee that realistic values were set. By establishing equality constraints on the thrust output of the propeller, the advance ratio and pitch setting values in each mission segment can be treated as design variables during the optimization. In this way, the optimizer is free to select operating conditions that minimize the power consumption or maximize power regeneration while maintaining the thrust requirements.

The size of the propeller under consideration during this project was scaled up to match the size of the reference aircraft that it would otherwise be installed on. This decision was made because including blade flexibility prevents the results obtained on a scaled model from being scaled up to realistic flight conditions because the deformations between the scaled and full models will be of a different magnitude unless (the laminate stiffness properties are also adjusted), which will impact the overall performance.

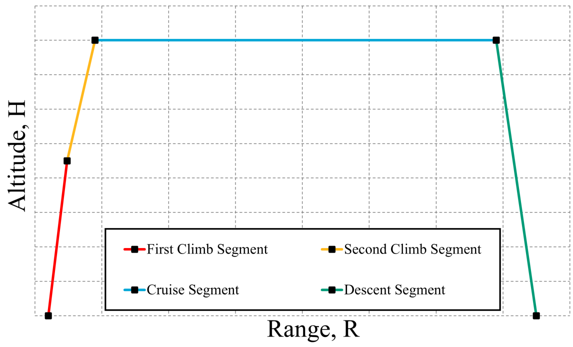

(a) Four-segment mission profile (not used during this project).

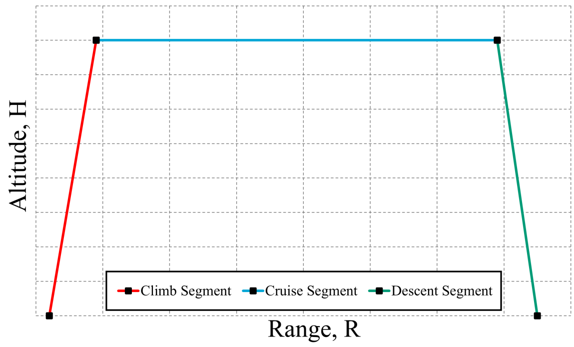

(b) Three-segment mission profile.

Figure 3.1: Notional diagrams of the two mission profiles that may be evaluated using the optimization framework that was developed and applied during this project.

3.1.1. OBJECTIVE FUNCTION

The generic multi-objective optimization problem shown below in Equation (3.1) has been used to formulate the optimization problem considered during this project. It is more convenient to reformulate this problem as a single objective optimization problem. There are several approaches that are suitable for evaluating multi-objective optimization problems, although the so-called *weighted sum* method that is outlined by Martins and Ning [64] has been applied because it offers an intuitive method of quantifying overall propeller performance that appropriately accounts for all mission segments.

$$\begin{aligned} &\text{Minimize} && f_k(\underline{\Phi}) && k \in \{1,\ldots,N_{\text{obj}}\} \\ &\text{subject to} && g_j(\underline{\Phi}) \le 0 && j \in \{1,\ldots,N_{\text{con},\,1}\} \\ & && h_l(\underline{\Phi}) = 0 && l \in \{1,\ldots,N_{\text{con},\,2}\} \\ &\text{with bounds} && \Phi_n^{\text{L}} \le \Phi_n \le \Phi_n^{\text{U}} && n \in \{1,\ldots,N_{\text{var}}\} \end{aligned} \tag{3.1}$$

The primary goal of the aeroelastic tailoring methodology is to obtain a structural blade design that maximizes efficiency within each mission segment. By maintaining a constant thrust requirement in each mission segment, minimizing the power consumption will cause the optimizer to attempt to maximize the efficiency. This approach is well-suited for this problem because it guarantees that all feasible solutions to the optimization problem will satisfy the mission requirements. Thus, the optimizer should attempt to minimize the power consumption in each mission segment, subject to applicable inequality constraints as well as equality constraints on the required thrust in each mission segment. To reformulate this multi-objective optimization problem as a single-objective optimization problem, the objective function was defined as the total mission energy consumption, which is computed using Equation (3.2). The energy consumption in each mission segment is accordingly evaluated by multiplying the power consumption in each segment by the time spent. The energy consumption in each mission segment can then be summed together to yield the total energy consumption. Thus, corresponding to the *weighted sum* method, the multiple objectives are given by the power consumption values in each mission segment, and their corresponding weight factors are given by the time spent in each mission segment.

$$E = \sum_{k=1}^{N_{\text{obj}}} P_k \cdot t_k \tag{3.2}$$

With this definition, the multi-objective optimization problem has been reformulated as a single objective optimization problem, as shown in Equation (3.3).

$$\begin{aligned} &\text{Minimize} && E = \sum_{k=1}^{N_{\text{obj}}} P_k \cdot t_k && k \in \{1,\ldots,N_{\text{obj}}\} \\ &\text{subject to} && g_j(\underline{\Phi}) \le 0 && j \in \{1,\ldots,N_{\text{con},\,1}\} \\ & && h_l(\underline{\Phi}) = 0 && l \in \{1,\ldots,N_{\text{con},\,2}\} \\ &\text{with bounds} && \Phi_n^{\text{L}} \le \Phi_n \le \Phi_n^{\text{U}} && n \in \{1,\ldots,N_{\text{var}}\} \end{aligned} \tag{3.3}$$

Some potential challenges with the chosen formulation have been identified. First, only a single mission profile was analysed during this project, corresponding to a fixed aircraft configuration. By decoupling the mission strategy from the design of an aircraft configuration, the power consumption of the propeller has no effect on the thrust requirement and the time spent in each mission segment. Thus, the time spent and the thrust required in each mission segment have been held constant during each optimization case. This may be inaccurate, as these values can vary as the required power changes in realistic scenarios. To mitigate this drawback, the propeller optimization framework would need to include modifications to the overall aircraft design, which would then lead to changes in thrust requirements and time spent in each mission segment. This approach was not taken during this work because the propeller blade design is the primary focus, and decoupling the propeller design from the design of an aircraft configuration prevents the results from being dependent on external and potentially unrelated factors that could otherwise bias the results. Moreover, it is expected that the relative difference in time spent between mission segments would not change by a significant amount as the energy consumption varies, and because this mission analysis is only being used to provide weighting factors between objectives during the optimization.

The second main drawback of this approach is that the optimal propeller blade design corresponds only to the fixed mission under consideration during this project, while it may be interesting to consider other mission types such as traffic pattern circuits, which were considered by Erzen *et al.* [2], or loiter-dash mission profiles, which were investigated by Dorfling and Rokhsaz [65]. This limits the applicability of outputs from the optimization to only be suitable for the mission strategy under consideration. A more generic result may be obtained through the use of additional mission strategies to quantify overall propeller performance. During this project, the selection of a climb-cruise-descent mission profile was deemed sufficient because it features both the propulsive and regenerative operating conditions in a realistic setting. It would have been interesting to also consider traffic pattern circuits during this project, although the selected mission profile is more commonly flown with the aircraft being considered. While the climb and descent segments were never adjusted, this problem was partially addressed by performing multiple optimization studies at differing cruise distances, to show how results depend on cruise distance.

Finally, the climb and descent segments would be most realistically represented using several operating conditions at varying altitude levels. As already mentioned, the climb and descent segments were only represented using one operating condition each at the median altitude. Because the cruise altitude is relatively low during this project, losses in precision through the selection of only a single operating point have a minimal effect on the results. Furthermore, general design trends were still obtained through the use of just a single operating condition in climb and descent, although the energy consumption values yielded by the optimizer will not be as precise as they otherwise would be with a greater number of mission segments. Decreases in computational cost resulting from the definition of less operating conditions were prioritized over any potential improvement in accuracy or precision.

3.1.2. DESIGN VARIABLES

The structural design variables used for the optimization are the lamination parameters and the laminate thicknesses. The blade was parametrized with only one laminate on each of its upper and lower surfaces over its full span due to limitations on computational cost. The upper and lower skins of each blade section were parametrized with eight lamination parameters and one thickness variable, while the spar webs of each blade section were approximated as quasi-isotropic and thus have zero-valued lamination parameters over the full span of the blade. As discussed previously, eight lamination parameters were used instead of twelve, since only symmetric laminates have been considered during this project. The decision to ensure that the spar webs are quasi-isotropic was made to reduce computational cost significantly, as the spar webs were found to provide a negligible influence on the deformations due to their small size. Thus, the total blade structure was parametrized with four laminates, one for each surface. Thus, four laminate thicknesses were defined in addition to eight lamination parameters each for the upper and lower surfaces. This yields 20 structural design variables in total to completely represent the blade structure.

The optimization framework that was developed and applied during this project is also capable of representing each laminate of the blade structure using reduced sets of structural design variables, as indicated in Table 3.1. In particular, five different sets of structural design variables may be considered. The largest and second-largest sets of design variables respectively correspond to blades constructed out of either symmetric or symmetric-balanced laminates. Symmetric-balanced laminates feature six lamination parameters, and can exhibit coupling between out-of-plane bending and twisting curvatures. Symmetric laminates are defined by all eight lamination parameters, and can include coupling between out-of-plane bending and twisting curvatures, as well as between in-plane normal and shear strains. The third-smallest set of design variables corresponds to a blade that is constructed from orthotropic laminates. In this case, each laminate features only four lamination parameters and one thickness, with zero coupling between in-plane normal and shear strains, as well as between out-of-plane bending and twisting curvatures. The fourth set of design variables corresponds to a blade that has isotropic laminates, in this case, only the thickness of each laminate can be modified. For isotropic laminates, deformations in each degree of freedom are only coupled through geometric characteristics, and a straight blade will not exhibit any coupling between degrees of freedom. Finally, the fifth and smallest set of design variables corresponds to a rigid propeller blade, which features zero structural design variables, and thus only operating conditions can be optimized. The rigid blade optimization was only used to provide baseline performance metrics.

Despite the numerous available sets of structural design variables that may be considered by the optimizer when defining the laminates of the blade structure, only the largest set of structural design variables was used during aeroelastic tailoring. This is because it was found during sensitivity studies that the performance characteristics of propeller blades constructed out of symmetric-balanced laminates are relatively insensitive to structural changes. The rigid propeller was also considered initially to identify the baseline minimum power consumption in each mission segment considered during the optimization study. Using the minimum energy consumption of the rigid propeller guarantees that all further decreases in energy consumption yielded by the flexible propeller result from aeroelastic tailoring, and not the selection of otherwise more suitable operating conditions. This prevents the results from being biased.

Table 3.1: Sets of structural design variables that can be included in the optimization procedure.

Number	Laminate Type	Design Variables Included Per Laminate
1	Symmetric only	All lamination parameters and thickness: $\xi_1^A, \xi_2^A, \xi_3^A, \xi_4^A, \xi_1^D, \xi_2^D, \xi_3^D, \xi_4^D$; $t > 0$
2	Symmetric & balanced	Six lamination parameters and thickness: $\xi_2^A = \xi_4^A = 0$; $t > 0$
3	Orthotropic	Four lamination parameters and thickness: $\xi_2^A = \xi_4^A = \xi_2^D = \xi_4^D = 0$; $t > 0$
4	Isotropic	Only laminate thickness: $\xi_1^A = \xi_2^A = \xi_3^A = \xi_4^A = \xi_1^D = \xi_2^D = \xi_3^D = \xi_4^D = 0$; $t > 0$
5	Rigid	No structural design variables included; thickness is constant

The remaining design variables include advance ratios and pitch settings for each mission segment. Using advance ratio values as design variables is equivalent to using rotor speeds as design variables because the freestream velocity in each mission segment does not change throughout the optimization procedure. These design variables have been selected to allow the optimizer to always find an operating condition that enables the thrust requirements to be met. During the optimization, both constant-pitch and variable-pitch propellers were evaluated, and thus either a single pitch setting is defined and used for all three mission segments or a unique pitch setting is used in each mission segment. The advance ratio is always different between each mission segment being considered by the optimizer.

3.1.3. CONSTRAINTS

INEQUALITY CONSTRAINTS

Several inequality constraints have been applied to ensure that the propeller blade structure is feasible. First, inequality constraints defining known feasible regions for lamination parameters have been included to ensure that it is possible to extract a feasible ply stacking sequence from the resulting set of lamination parameters. Details on these feasible regions have been provided in Appendix B. Constraints corresponding to the maximum allowable normal and shear strains of the material were applied to ensure that strains evaluated within the structure are always below these limits. The maximum allowable shear strains are evaluated from the material properties of the composite material being used. Because the stacking sequence of the composite materials is not known during the optimization procedure, it is not possible to use the classical composite strength failure criteria. Instead, the method of IJsselmuiden *et al.* [66] is used, which is expressed in the lamination parameter design space and is based on the Tsai-Wu failure criterion. This method guarantees that structural failure does not occur for any set of ply orientations. During this project, the implementation of this theory from Khani *et al.* [67] has been used, which defines the failure envelope using the material stiffness invariants that were presented in Section 2.2.1. Lastly, the power consumption of the propeller was constrained by the maximum shaft power of the reference aircraft under consideration, and blade tip displacements were constrained to prevent excessive deformations. Table 3.2 contains a summary of the inequality constraints that were applied.

Table 3.2: A list of inequality constraints used during the optimization procedure.

Category	Constraint Name
Structural	• Maximum normal strain (tensile), $\varepsilon^{\mathrm{T}}_{\mathrm{max}}$ • Minimum normal strain (compressive), $\varepsilon^{\mathrm{C}}_{\mathrm{min}}$ • Maximum shear strain, τ_{max} • Maximum tip displacement, p_{max}
Feasibility	• Feasible regions for lamination parameters (see Equation (B.11))
Performance	• Maximum shaft power, P_{max}

EQUALITY CONSTRAINTS
The only equality constraints considered during the optimization are for the thrust that is produced by the propeller. By maintaining a constant thrust during the optimization, it is ensured that any decreases in power consumption that the optimizer obtains will not come at the cost of a decrease in thrust. In doing this, it is ensured that the optimized propeller can still be used to meet the requirements of the mission. By minimizing the power consumption for a constant thrust, the goal of the optimizer is to effectively increase the efficiency of the propeller (propulsive efficiency during positive thrust conditions and turbine efficiency during energy-harvesting conditions).

3.1.4. NORMALIZATION
To ensure that the optimizer can correctly assess the sensitivities of the design variables, it is essential that the design vector, objective function, and constraints are normalized so that all variable values and function outputs are within approximately the same orders of magnitude.

DESIGN VARIABLES
All design variables of the optimization have been normalized to take values between -1 and 1. For this normalization, the mean value between the bounds of each design variable is computed first as follows.

$$\underline{\Phi}_0 = \frac{1}{2}\left(\underline{\Phi}^{\mathrm{L}} + \underline{\Phi}^{\mathrm{U}}\right)$$

As shown in Equation (3.4), the normalization of the design vector is computed by subtracting the midpoint between the upper and lower bounds of the design vector from the original design vector and then multiplying this value by a so-called normalization matrix $\boldsymbol{N}$. The normalization matrix in this case is defined as shown in Equation (3.5).This normalization guarantees that all design variables are between -1 and 1, with the midpoint between the upper and lower bounds occurring at a normalized value of 0.

$$\hat{\underline{\Phi}} = \boldsymbol{N}\left(\underline{\Phi} - \underline{\Phi}_0\right) \tag{3.4}$$

$$\boldsymbol{N} = \mathrm{diag}\left\{\left(\frac{1}{2}\left(\underline{\Phi}^{\mathrm{U}} - \underline{\Phi}^{\mathrm{L}}\right)\right)^{-1}\right\} \tag{3.5}$$

CONSTRAINT FUNCTIONS
Each constraint function is normalized by their limit values, as shown below.

Maximum Normal Strain (Tensile): $$\frac{\varepsilon^{\mathrm{T}} - \varepsilon^{\mathrm{T}}_{\mathrm{max}}}{\varepsilon^{\mathrm{T}}_{\mathrm{max}}} \leq 0 \tag{3.6}$$

Minimum Normal Strain (Compressive): $$\frac{\varepsilon^{\mathrm{C}} - \varepsilon^{\mathrm{C}}_{\mathrm{min}}}{\varepsilon^{\mathrm{C}}_{\mathrm{min}}} \leq 0 \tag{3.7}$$

Maximum Shear Strain: $$\frac{\tau - \tau_{\mathrm{max}}}{\tau_{\mathrm{max}}} \leq 0 \tag{3.8}$$

Maximum Tip Displacement: $$\frac{p - p_{\mathrm{max}}}{p_{\mathrm{max}}} \leq 0 \tag{3.9}$$

Maximum Shaft Power: $$\frac{P - P_{\mathrm{max}}}{P_{\mathrm{max}}} \leq 0 \tag{3.10}$$

Thrust Equality Constraints: $$\frac{T - T_{\mathrm{required}}}{T_{\mathrm{required}}} = 0 \tag{3.11}$$

OBJECTIVE FUNCTIONS

The objective function is the total mission energy, which is normalized by the value corresponding to the rigid propeller, as shown in Equation (3.12). This normalization was selected because the rigid propeller performance is considered as the baseline during this work.

$$f = \frac{E}{|E_{\text{rigid}}|} \tag{3.12}$$

3.2. DESIGN STUDY OVERVIEW

A design study was performed to identify the effect of aeroelastic tailoring on performance. During the design study, parameter studies were first performed to identify how performance varies with changes in laminates. After completing the sensitivity studies, the propeller blade was optimized using the framework that was described in Section 3.1. Results from this investigation were used to answer the research questions. To summarize the design study that was completed during this project, this section contains information on the reference aircraft configuration and mission, propeller blades and materials, optimization cases, and the optimization routine that was applied.

3.2.1. PROPELLER OPERATING CONDITIONS

During the propeller optimization study, only one high-speed mission was defined using the *Pipistrel Panthera*. This aircraft falls within the *light* category and was selected because it operates at relatively high speeds and because hybrid- and full-electric versions of this aircraft are currently in development by the manufacturer [68]. Physical dimensions and performance characteristics presented in this section have been assumed to correspond to its full-electric variant. A mission profile defined by relatively higher speeds was selected so that the loads encountered by the propeller would be relatively high. This enables the maximum effect of aeroelastic tailoring to be relatively large. Additionally, it is anticipated that this aircraft would primarily be used to perform climb-cruise-descent missions, which makes it suitable for the chosen mission profile. To define the thrust requirements and operating conditions of the aircraft in each mission segment, the methods applied in the M.Sc. theses of van Neerven [33] and Scholtens [34] have been applied. Geometry and performance details for the aircraft under consideration are provided in Table 3.3. Lastly, Figure 3.2 contains images of the Pipistrel Panthera for reference.

Table 3.3: A list of performance characteristics for the Pipistrel Panthera, used to motivate the definition of a mission profile for the optimization study (considered primarily as a guideline).

Metric (at MTOM)	**Value** [68]
Stall speed (flaps extended)	62 KEAS
Stall speed (flaps retracted)	68 KEAS
Manoeuvring speed	143 KEAS
Cruise speed	140 KEAS (55% power)
Never exceed speed	220 KEAS
Climb rate at best climb speed	5.8 m/s
Best climb speed	100 KEAS*
Range (with maximum payload)	1000 nm (1852 km)
Cruise condition for range calculation	155 KTAS, FL 120
Best glide ratio speed	85 KEAS*
Maximum power	200 kW (150 kW continuous)
Maximum takeoff weight, W	13300 N
Wing aspect ratio, AR	10.53
Wing taper ratio, λ	0.4*
Wing sweep, Λ	0.0°
Wing span, b	10.9 m
Wing area, S_W	11.2 m^2
Fuselage width, d_F	1.5 m

* Quantities marked with an asterisk have been estimated using values obtained for similar reference aircraft from [69].

(a) Dimetric view.

(b) Side view.

Figure 3.2: Images of the Pipistrel Panthera, the reference aircraft selected for this project [68].

OBTAINING DRAG AND GLIDE RATIO POLAR PLOTS

The first step to evaluating the mission performance of the Pipistrel Panthera is to obtain the drag and glide ratio polars. For this, the potentially oversimplified relationship shown in Equation (3.13) has been used from [69]. With this representation for the drag coefficient, the lift coefficient corresponding to the minimum drag coefficient has been approximated as exactly zero, this is potentially inaccurate, as the minimum drag coefficient may occur for a slightly non-zero lift coefficient. The approximation of the drag polar using this approach requires the evaluation of the Oswald factor. The Oswald factor has been calculated using the statistical method from Niţă and Scholz [70], which is provided in Equation (3.14), Equation (3.15), and Equation (3.16). Because compressibility effects have been considered to be negligible, $k_{e,M}$ has been set to 1. Lastly, k_{e,D_0} has been set to 0.804 for general aviation aircraft [70].

$$C_D = C_{D_{\min}} + \frac{1}{\pi AR\, e} C_L^2 = C_{D_{\min}} + k C_L^2 \tag{3.13}$$

$$f(\lambda) = 0.0524\lambda^4 - 0.15\lambda^3 + 0.1659\lambda^2 - 0.0706\lambda + 0.0119 \tag{3.14}$$

$$k_{e,\mathrm{F}} = 1 - 2\left(\frac{d_\mathrm{F}}{b}\right)^2 \tag{3.15}$$

$$e = \frac{k_{e,\mathrm{F}}\, k_{e,D_0}\, k_{e,M}}{1 + f(\lambda) AR} \tag{3.16}$$

To estimate the minimum drag coefficients for the Pipistrel Panthera, the best glide ratio speed was substituted into Equation (3.17). This approximation may yield a very low precision, although it is sufficient for this analysis, as it is only important that the propeller operating conditions defined for each mission are realistic. The derivation for this expression has been left out of this report for brevity, although it may be found in [69], starting from Equation (3.13). The best glide ratio may subsequently be evaluated using Equation (3.18). This expression was used to verify that the minimum drag coefficient is reasonably predicted, using the maximum glide ratio that is computed from Equation (3.13).

$$L = W\cos(\gamma_\mathrm{d}) \implies V = \sqrt{\frac{2\cos(\gamma_\mathrm{d})}{\rho C_L}\frac{W}{S_\mathrm{W}}} \approx \sqrt{\frac{2}{\rho\, C_L}\frac{W}{S_\mathrm{W}}} = \sqrt{\frac{2}{\rho}\frac{W}{S_\mathrm{W}}}\sqrt{\frac{k}{C_{D_{\min}}}} \tag{3.17}$$

$$\left(\frac{C_L}{C_D}\right)_{\max} = \frac{1}{\sqrt{4 C_{D_{\min}} k}} \tag{3.18}$$

Both van Neerven [33] and Scholtens [34] analysed the *Pipistrel Alpha Electro* in their work, which has almost identical performance and geometry characteristics to the *Velis Electro* [71]. For this reason, polar plots of the Velis Electro were also evaluated and compared to the results obtained by Scholtens [34] to verify that the drag and glide ratio polars are being reasonably computed using the method proposed in this section. Table 3.4 contains the calculated quantities that are required to construct the two-term parabolic drag polar for both the Pipistrel Panthera and the Pipistrel Velis Electro. Using these quantities, the drag and glide ratio polar plots for each aircraft have been shown in Figure 3.3.

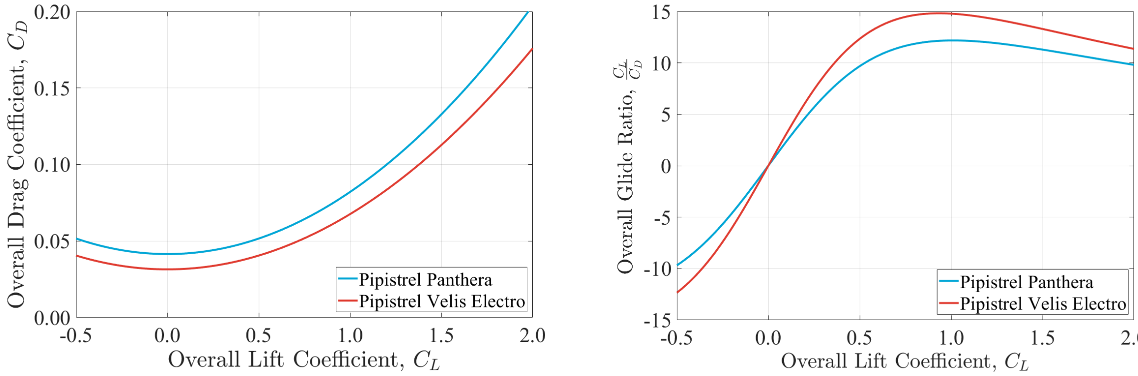

(a) Drag polar plots. **(b)** Glide ratio polar plots.

Figure 3.3: Estimated drag and glide ratio polar plots for the Pipistrel Panthera and Velis Electro.

The maximum glide ratio for the Velis Electro is reported by the manufacturers in [71] as having a value of 15, whereas the value obtained using the method discussed in this section is 14.85. This level of agreement is considered sufficient for this study. Values for the maximum glide ratio of the Panthera are not reported by the manufacturers. For the Pipistrel Alpha Electro, Scholtens [34] obtained a value of 0.031 for the minimum drag coefficient and a value of 0.66 for the Oswald factor. The method applied by Scholtens [34] is slightly different, although the polar plots are similar enough in appearance to verify that the approach used in this work is sufficient for defining the operating conditions of the mission.

Table 3.4: Calculated quantities that were used to construct the polar plots shown in Figure 3.3.

Performance Metric	Panthera	Velis Electro (Verification Only)
k	0.041	0.036
$C_{D_{\text{min}}}$	0.041	0.031
e	0.745	0.732

With reference performance and geometry data for the Pipistrel Panthera shown in Table 3.3, corresponding to the polar data for the overall aircraft that is shown in Figure 3.3, it is now possible to calculate the thrust requirements in each mission segment. A separate analysis was completed for each segment.

CLIMB ANALYSIS

A free-body diagram of the climbing aircraft is shown in Figure 3.4. From this diagram, the full equations of motion are given as follows. These equations assume zero steady rotation around the global y-axis.

$$L - W\cos\left(\gamma_{\text{cl}}\right) + T\sin\left(\varepsilon\right) = \frac{W}{g}\frac{d}{dt}\left(V\sin\left(\gamma_{\text{cl}}\right)\right) \tag{3.19}$$

$$-D - W\sin\left(\gamma_{\text{cl}}\right) + T\cos\left(\varepsilon\right) = \frac{W}{g}\frac{d}{dt}\left(V\cos\left(\gamma_{\text{cl}}\right)\right) \tag{3.20}$$

Several simplifications have been made during this analysis to adapt the above equations to represent a steady climbing flight. First, the time derivative of the flight velocity is assumed to be zero. Additionally, the angle of attack and angle of incidence of the propeller are assumed to be negligible. With these assumptions, the lift and drag of the aircraft in climbing flight are reformulated as shown in Equation (3.21) and Equation (3.22). These expressions have been used to obtain the required thrust during the climb.

$$L = W\cos\left(\gamma_{\text{cl}}\right) \tag{3.21}$$

$$T = W\sin\left(\gamma_{\text{cl}}\right) + D \tag{3.22}$$

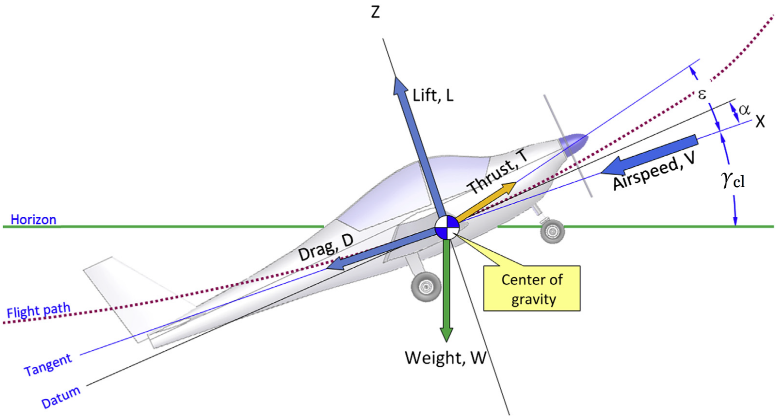

Figure 3.4: A free-body-diagram of an aircraft in a climb manoeuvre [69].

CRUISE ANALYSIS

A free-body-diagram of the aircraft in cruise is shown in Figure 3.5. From this diagram, the equations of motion are provided in Equation (3.23) and Equation (3.24).

$$L = W \tag{3.23}$$

$$D = T \tag{3.24}$$

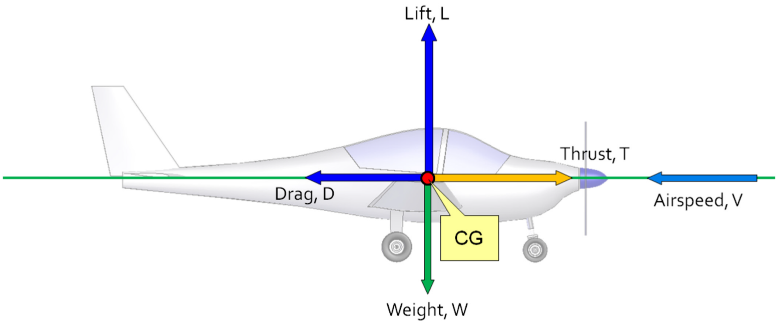

Figure 3.5: A free-body-diagram of an aircraft in cruise conditions [69].

DESCENT ANALYSIS

The equations of motion for the aircraft in descending flight, corresponding to Figure 3.6, are very similar to the aircraft in climbing flight. Like before, the generalized equations have been provided below.

$$L - W\cos(\gamma_{\text{des}}) + T\sin(\varepsilon) = \frac{W}{g}\frac{d}{dt}\left(V\sin(\gamma_{\text{des}})\right) \tag{3.25}$$

$$-D + W\sin(\gamma_{\text{des}}) + T\cos(\varepsilon) = \frac{W}{g}\frac{d}{dt}\left(V\cos(\gamma_{\text{des}})\right) \tag{3.26}$$

The same simplifications as applied for the climbing aircraft have again been applied to result in the following two expressions. The descent rate at zero negative thrust was calculated as 3.64 m/s for the Pipistrel Panthera, with a corresponding descent angle of 4.87°. The choice of a descent rate for regeneration is largely arbitrary, although for safety and practical reasons, the maximum descent rate was prevented from exceeding 5 m/s. A similar bound was applied by van Neerven [33]. An investigation on the optimal descent rate for regeneration was considered outside the scope of this project, although this should be considered in a future study. For this project, the descent rate was held constant.

$$L = W\cos(\gamma_{\text{des}}) \tag{3.27}$$

$$D = W\sin(\gamma_{\text{des}}) + T \tag{3.28}$$

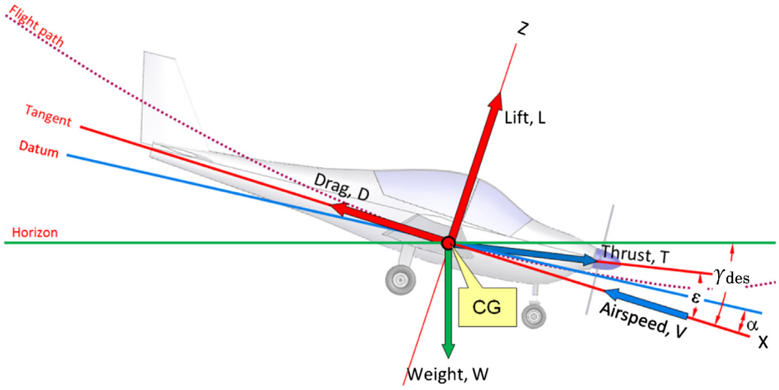

Figure 3.6: A free-body-diagram of an aircraft during a descent [69].

TOP-LEVEL OPERATING CONDITIONS

As already mentioned, the three-segment mission was considered during the optimization study despite the more precise representation that would be offered by the four-segment mission, which is also possible to evaluate with the code that was developed. This decision was made because it is still possible to address the main focus of this research with the less precise mission, although a more precise mission would be useful to investigate in a future project. The averaged operating conditions considered in this project are provided in Table 3.5 for the Pipistrel Panthera. The climb is assumed to be taking place at a constant equivalent airspeed. The descent rate for regeneration is taken to be slightly greater than the descent rate at the best glide ratio speed. The computed thrust requirements in each mission segment have been provided in Table 3.5 as well, including their corresponding thrust coefficient, T_C, values.

Table 3.5: Quantities defining the climb-cruise-descent mission used during the optimization study.

Operating Condition	Value
Climb altitude	1000 m
Climb speed	55 m/s (107 KTAS)
Climb rate	5.5 m/s
Climb distance	20 km
Time spent in climbing flight	6 min
Climb thrust requirement	2585 N ($T_C = 0.230$)
Cruise altitude	2000 m
Cruise speed	80 m/s (156 KTAS)
Cruise distances	{0, 50, 100, 150, 200, 400} km
Time spent in cruise conditions	{0, 10, 21, 31, 42, 83} min
Cruise thrust requirement	1780 N ($T_C = 0.083$)
Descent altitude	1000 m
Descent speed	45 m/s (88 KTAS)
Descent rate	4.8 m/s
Descent distance	22 km
Time spent in descending flight	7 min
Descent thrust requirement	-380 N ($T_C = -0.051$)

3.2.2. PROPELLER BLADES AND MATERIALS CONSIDERED

The propeller blade used during this study is the three-bladed version of the TUD-XPROP, which is the propeller that was used to verify that the aeroelastic analysis was implemented correctly in Section 4.3. The main difference is that the propeller has a scale factor of 4.5 instead of 5 in this case to ensure that the diameter of the propeller matches the blade diameter of the referenced aircraft. A diagram of this propeller is shown in Figure 3.7. Additionally, the number of elements used in both the structural and aerodynamic models have been selected accordingly to maintain a low computational cost whilst ensuring an acceptable level of precision. Table 3.6 contains details on the spacial discretization schemes used.

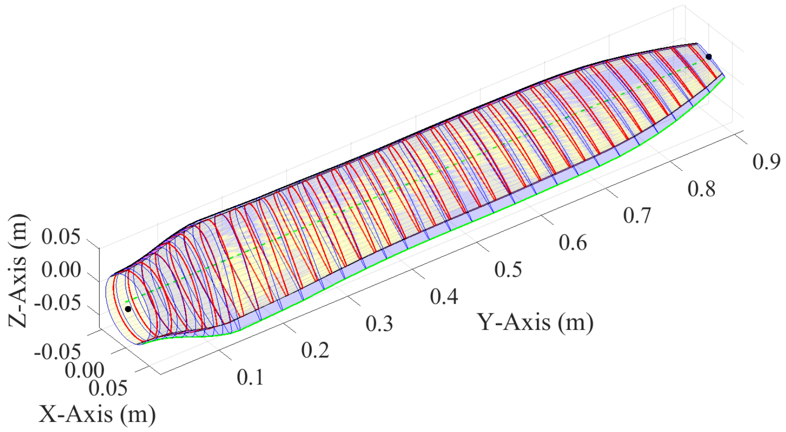

Figure 3.7: A diagram of the propeller blade geometry used during the optimization study.

The composite material chosen for all laminates of the propeller blade considered during the optimization is *AS4/APC2*, all of its material properties are provided in Table B.3. This material was selected because it has relatively low values for E_{11} and E_{22} in comparison to the other carbon fibres, whilst maintaining a significant enough difference in stiffness between the two in-plane axes, thus enabling a substantial amount of coupling between deformations in each degree of freedom.

Table 3.6: Parameters defining the discretization schemes applied during the optimization study.

Quantity	**Value**
Maximum number of spanwise laminates	5
Number of chordwise laminates at each spanwise laminate location	1
Minimum number of structural beam elements	35
Minimum number of cross-sectional shell elements	100
Number of blade elements for the aerodynamic analysis	75
Angle of attack values used for polar plots (blade element theory)	{-25°, -24°, ..., 25°}
Range of Reynolds numbers used for the polar plots (blade element theory)	$\{1.0, 3.0, \ldots, 99.0\} \times 10^5$

3.2.3. OVERVIEW OF OPTIMIZATION CASES

The main purpose of the optimization study is to address the top-level research objectives, as provided in Chapter 1. To address these objectives, the following goals have been defined for the optimization study.

(1) Design Space Exploration: Sensitivity studies with structural variables (i.e. ply orientations and laminate thicknesses)

(2) Evaluate difference between laminate types and their potential to improve performance

(3) Identify the optimal design for each isolated mission segment and for the full mission

(4) Identify the effect of the cruise length on the result obtained from the optimization

(5) Evaluate the effect of aeroelastic tailoring on variable- and constant-pitch propellers

Sensitivity analyses and optimization studies have been constructed to satisfy the listed objectives. The sensitivity studies were performed for the propeller operating at conditions that represent the propulsive and regenerative case before completing the blade optimization. This was done to identify general design trends and to explore the overall design space. For the sensitivity studies, effects of variations in ply orientations on maximum deformations and overall performance have been investigated to identify trends with ply orientations. Additionally, blades with different laminate types have been analysed and compared in both propulsive and operating conditions to identify in particular how the blade's deformations and performance differ when using either symmetric-unbalanced or symmetric-balanced laminates.

After developing an intuition for the propeller design problem, the optimization studies were completed and the results were analysed to address the remaining objectives. First, each mission segment was considered individually as the objective function in addition to the full mission with a varying cruise distance to determine the optimal laminate configurations for maximum performance in climb, cruise, and descent in comparison to the full mission. This investigation was used to quantify the effect of the cruise length on the optimal blade structure, in addition to the extent that performance may be enhanced as the cruise length increases. These optimization studies have been performed for both variable-pitch and constant-pitch propellers. The rigid propeller performance at its best pitch setting has been used as a baseline for comparisons with the flexible propeller performance during all investigations to prevent the results from being biased. This difference in performance between flexible and rigid propeller blades has been used to identify the extent that performance may be enhanced through aeroelastic tailoring. Table 3.7 contains a list of all the cases that were considered during the optimization.

Table 3.7: An overview of the 15 optimization cases considered during this project.

#	Laminate Type	Objective Type	Cruise Lengths (km)	Propeller Type
1	1, 5	Climb Only	N/A	N/A
2	1, 5	Cruise Only	N/A	N/A
3	1, 5	Descent Only	N/A	N/A
4	1, 5	Full Mission	0, 50, 100, 150, 200, 400	CPVR, VPVR

3.2.4. APPLIED OPTIMIZATION METHOD

The propeller optimization was completed using fmincon, a gradient-based optimization function that is built into MATLAB. Sensitivities are computed using a numerical forward-differencing scheme, and the *sequential quadratic programming* (SQP) algorithm was found to be the most suitable for all optimization cases under consideration. Figure 3.8 contains a UML activity diagram of the optimization procedure.

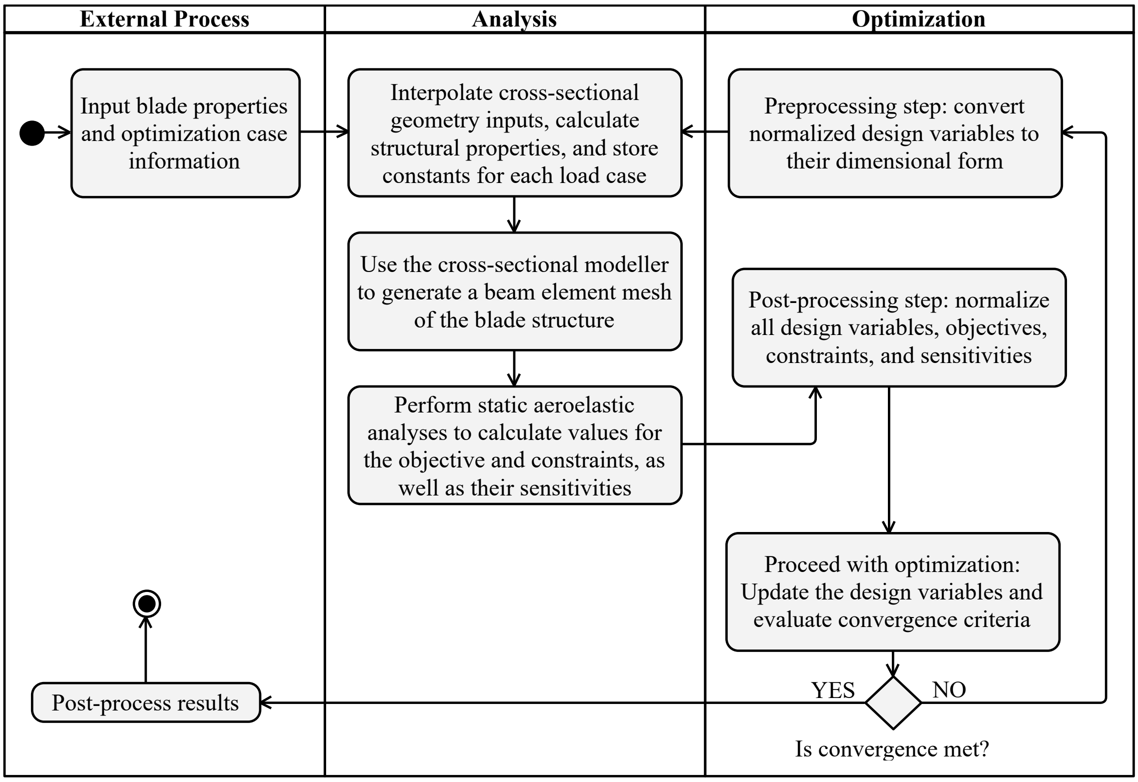

Figure 3.8: A UML activity diagram of the aeroelastic optimization procedure.

4

Verification and Validation

Verification and validation of the aeroelastic analysis framework was completed in three steps during this project. First, the aerodynamic analysis routine was verified against results from an existing BEM code and validated against experimental data in Section 4.1. The structural model was then verified through comparisons with the commercial finite element code, ABAQUS, in Section 4.2. Validation of the structural model was determined to not be necessary for this project, as near-perfect agreement was obtained between results from the present method in comparison to ABAQUS, and most of the structural analysis routine was left unchanged from the work of De Breuker [48] and Werter [30]. Finally, verification of the tightly coupled aeroelastic analysis routine was completed and documented in Section 4.3 through comparisons with a loosely coupled method. Validation of the aeroelastic analysis was not performed because it was not possible to obtain experimental data to compare with.

4.1. Propeller Aerodynamic Model

The BEM code that was used during this project was previously validated by Goyal *et al.* [10] through comparisons to experimental data obtained with the TUD-XPROP propeller (shown in Appendix A). The authors considered only a pitch setting of 15° during their comparisons, although the model's sensitivity to changes in pitch are important for this project. Thus, further comparisons have been made at pitch settings between 10° and 30° using the experimental results of Nederlof *et al.* [13]. To ensure that the aerodynamic model will be suitable for optimization, computational cost was significantly reduced by decreasing the amount of data that is used for evaluating the lift and drag coefficients corresponding to each blade element. Goyal *et al.* evaluated the lift and drag coefficient for angles of attack between −25° and 25° with increments of 0.1°, whereas polar plots were generated using angles of attack between −24° and 24° with increments of 3° during this work. Comparisons were made with the results obtained by Goyal *et al.* [10] to demonstrate that this adjustment does not noticeably affect the model's precision.

4.1.1. Input Data

The TUD-XPROP-3 propeller was studied for all results that have been presented. Geometric information has been provided for this propeller in Appendix A. This includes details on the outer diameter, twist and chord distributions, and airfoil shapes at varying spanwise locations. Additionally, all results have been collected for a fixed freestream velocity of $V_\infty = 30$ m/s. All BEM calculations were performed using 50 elements with widths defined by a cosine spacing law from the blade root to tip, and details on the experimental setup that was used to collect the data that was used for comparison is provided by Nederlof *et al.* in [13]. Finally, Table 4.1 contains details on the ranges of operating conditions being considered.

Table 4.1: Advance ratio sweeps for different pitch settings at $V_\infty = 30$ m / s.

$\beta_{0.7} = 10°$	$\beta_{0.7} = 15°$	$\beta_{0.7} = 20°$	$\beta_{0.7} = 25°$	$\beta_{0.7} = 30°$
$0.50 \le J \le 1.50$	$0.55 \le J \le 1.50$	$0.65 \le J \le 1.90$	$0.80 \le J \le 2.00$	$0.90 \le J \le 2.10$

Because experimental lift and drag coefficient curves do not exist for the airfoils of the TUD-XPROP propeller, all results have been collected through numerical calculations. It is recommended by the researchers who created RFOIL to fix the location that the transition from laminar to turbulent flow occurs at [11]. However, the location of transition has not been fixed during this work, and instead the well-established e^N method was used to predict the location of transition to match the approach of Goyal *et al.*. A critical amplification factor of $N = 4.5$ was used during this project, which was also used by Goyal *et al.*. This method may lead to a decrease in accuracy because RFOIL is incapable of accounting for the effect of rotation on transition. Nevertheless, an investigation involving the effect of the transition location on propeller performance is considered outside the scope of the present work. Sample lift and drag polar plots are shown in Figure 4.1. Lift and drag has been computed within these plots at three radial locations to represent the blade root, middle, and tip. Results have also been shown for low, medium, and high Reynolds numbers to indicate the effect of variations in Reynolds number on lift and drag coefficients.

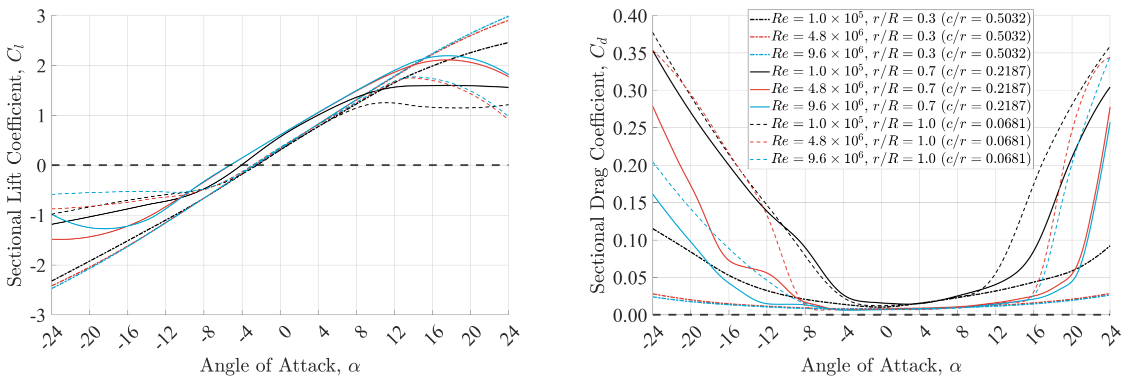

(a) C_l vs. α. **(b)** C_d vs. α.

Figure 4.1: Plots of the lift and drag coefficient for varying Reynolds numbers and radial locations.

As expected, the maximum lift coefficient tends to increase and the drag coefficient tends to decrease with increasing Reynolds number. Additionally, despite the differing airfoils at each radial position, the stall-delay effect is clearly present, as the angle of attack where separation occurs tends to decrease with increasing radial position. The underlying physical mechanism is caused by the outward displacement of fluid particles, which leads to a thinner boundary layer at the root section. This effect is more noticeable at positive angles of attack, as the positively cambered airfoils of the propeller are not designed to operate at negative angles of attack. Moreover, because increasing the Reynolds number decreases viscous effects, the effect of blade rotation should become less pronounced with increasing Reynolds number. This is indeed indicated by a less noticeable delay in separation with decreasing radial position for the high Reynolds number results in comparison to the low Reynolds number results. The decrease in drag coefficient with decreasing radial position also appears less apparent at high Reynolds numbers.

4.1.2. RESULTS

Figure 4.2 contains plots of the calculated power and thrust coefficient of the propeller at varying pitch angles, in comparison to the experimental results collected by Nederlof *et al.* [13] and the calculated results (using BEM with rotational effects included) from Goyal *et al.* [10].

At all pitch settings that were considered, the calculated power and thrust coefficients appear to exhibit the same general trends as the experimental data at operating conditions corresponding to positive and low negative power coefficients. Although, with more negative thrust settings, BEM tends to overpredict the amount of power that is recovered by the propeller. This is most likely caused by an incorrect prediction in the lift and drag coefficients at large negative angles of attack. These discrepancies grow as the amount of flow separation increases because RFOIL cannot be used to predict results in regions of completely separated flow, and generally can only provide an acceptable result for attached and slightly separated flows [11]. In regions of separated flow, the assumption of zero aerodynamic interaction between neighbouring blade elements also becomes invalid [1]. The prediction of performance may be improved by providing more accurate lift and drag polar input data at large negative angles of attack. This is not possible for the propeller model under consideration, as experimental data for the airfoils does not exist.

Although it is not possible to accurately predict performance at very high thrust settings, an acceptable range of advance ratios has been considered for each pitch setting to limit the amount of blade loading, and excellent agreement with the calculated results from Goyal *et al.* [10] has been demonstrated, which indicates that the BEM analysis is performing as expected. Lastly, it is undesirable to operate in the presence of large amounts of negative thrust, and thus the required limitations on advance ratios will not noticeably hinder this project, and realistic bounds have accordingly been set during the optimization.

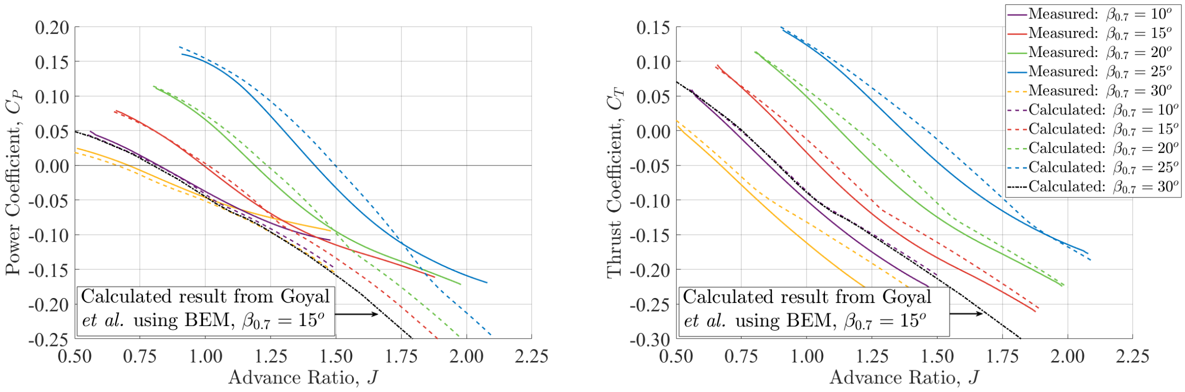

(a) C_P vs. J.

(b) C_T vs. J.

Figure 4.2: Plots of the power and thrust coefficient for varying blade pitch settings in comparison to experimental results from [13] and calculated results from [10] (using the same BEM methodology).

Efficiency curves have been plotted in Figure 4.3 for varying pitch settings in comparison to the experimental results of Nederlof *et al.*. Because the energy harvesting efficiency is simply a normalization of the power generated by the propeller, the same conclusions drawn from the comparison of the power coefficients may be drawn from the comparison of the energy harvesting efficiencies.

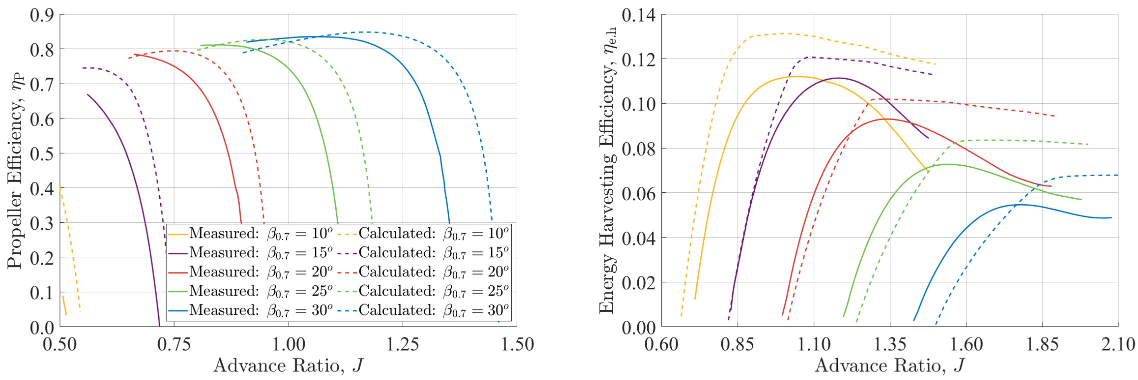

(a) η_P vs. J.

(b) η_{eh} vs. J.

Figure 4.3: Calculated efficiency curves in comparison to experimental results from [13].

The trends in propeller efficiency appear consistent between the calculated and experimental results. However, there is an offset in advance ratio between the two sets of results, which appears to increase with increasing pitch setting. This offset also appears to be present in the thrust and power coefficient results. The reason for this has been hypothesized by Goyal *et al.* as being due to differences in the location of transition. In this case, the real-life model may encounter an earlier transition, which would decrease the lift coefficient and increase the drag, ultimately resulting in a decreased efficiency and thrust. The power coefficient can either decrease or increase, depending on the relative contributions from lift and drag components towards the torque. This effect cannot be mitigated unless a more accurate method of calculating lift and drag polar plots is applied, such as if experimental polar plots were obtained.

To motivate the selection of upper-limits on the advance ratio at each pitch setting, Figure 4.4 contains plots of the percent error between the experimental results and the calculated results for the thrust and power coefficients. From these results, it was considered reasonable to maintain a maximum error of approximately 20%, as errors in the power coefficient appear to grow quite fast beyond this point. Errors in the thrust coefficient appear to always remain within an acceptable range, despite relatively large amounts of negative thrust being produced at the maximum advance ratio that the BEM model is considered to be valid for at each pitch setting. Table 4.2 contains the maximum advance ratios that will be considered at each pitch setting. The chosen upper limits on advance ratio also enable the peak energy harvesting efficiency to be included at all pitch settings, as shown in Figure 4.3.

Table 4.2: Maximum advance ratios for different pitch settings at $V_\infty = 30$ m / s.

$\beta_{0.7} = 10°$	$\beta_{0.7} = 15°$	$\beta_{0.7} = 20°$	$\beta_{0.7} = 25°$	$\beta_{0.7} = 30°$
$J \leq 1.2$	$J \leq 1.4$	$J \leq 1.6$	$J \leq 1.7$	$J \leq 1.9$

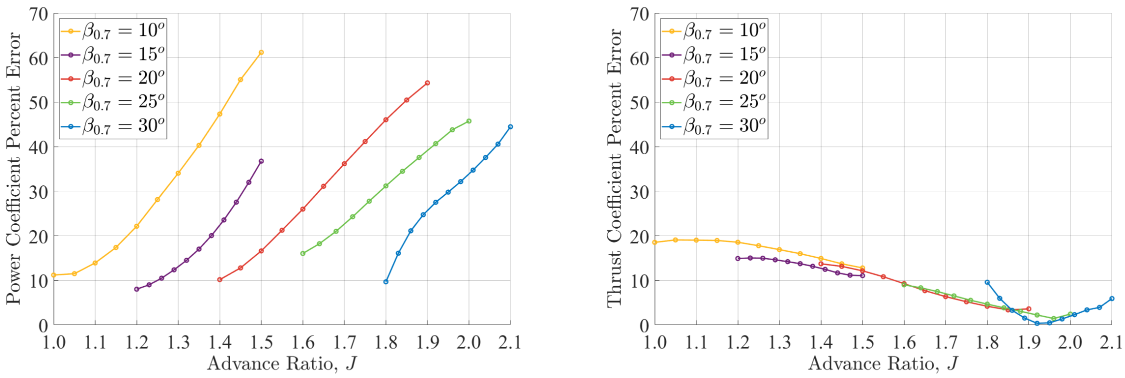

(a) Power: $100 \times \left|\left(C_P^{\text{exp.}} - C_P^{\text{calc.}}\right)/C_P^{\text{exp.}}\right|$

(b) Thrust: $100 \times \left|\left(C_T^{\text{exp.}} - C_T^{\text{calc.}}\right)/C_T^{\text{exp.}}\right|$

Figure 4.4: Percent error between calculated and experimental power and thrust coefficient results (corresponding to the results shown in Figure 4.2) at varying pitch settings.

Finally, load distributions obtained by Goyal *et al.* have been reproduced using the present calculation approach in Figure 4.5. In addition to the results shown in Figure 4.2, the results shown in Figure 4.5 indicate that the load distributions obtained with the present calculation method are in close agreement with the BEM results obtained by Goyal *et al.*. The result from RANS indicates that BEM tends to overpredict loads in the presence of separated flow. Furthermore, the characteristic of the blade load distribution is only poorly predicted at an advance ratio of 1.60, which is very high anyway.

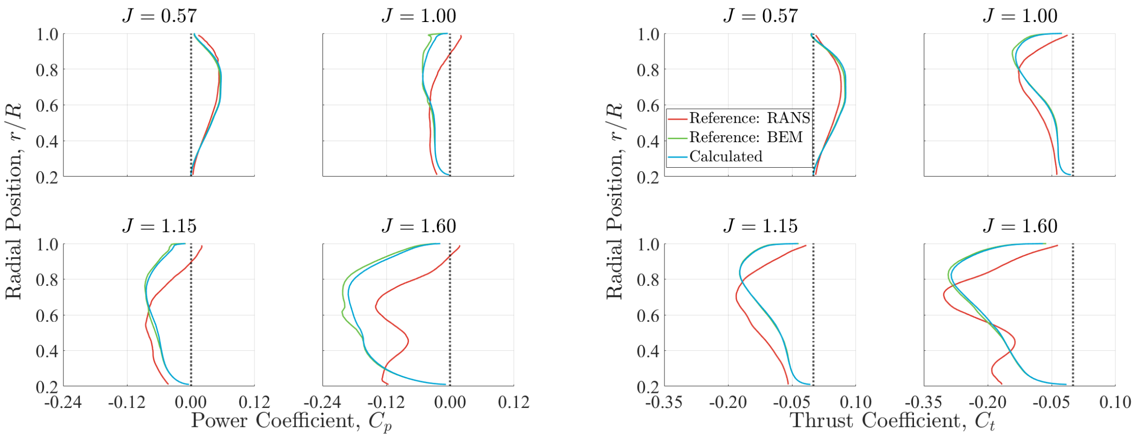

(a) Power coefficient distributions.

(b) Thrust coefficient distributions.

Figure 4.5: Thrust and power coefficient distributions computed using the current method and compared with BEM and RANS results obtained by Goyal *et al.* [10] ($\beta_{0.7} = 15°$).

4.2. STRUCTURAL MODEL

The linear and nonlinear structural analysis programs were verified by considering three simple cantilever beam models. All details on the three models are shown in Table 4.3 and Table 4.4.

First, a cantilever box beam with a point force acting at the tip along the global z_0-axis and subjected to centrifugal forces (due to rotation about the z_0-axis) was analysed. This case was considered to ascertain that the centrifugal force calculation was implemented correctly, and that the nonlinear analysis is capable of capturing the spin-stiffening effect. Because it is possible to define a structure with or without spars, the box-beam geometry was selected to ensure that the spars are being defined correctly. The second case that was analysed is identical to the first, except a constant distributed transverse load is applied through the full length of the beam along the z_0-axis instead of the point force at the tip of the beam. This load case represents the actual loading that will be encountered by the propeller blade, as the aerodynamic force will generate a distributed force and pitching moment. Through this case, it was shown that the structural model appropriately represents loads that will be typically encountered by the structure. The third case features the same load case as the first case, except the box beam is subjected to a pitch setting that varies between 0° and 60°. This model was analysed to verify that the structural analysis continues to perform correctly for geometries of varying pitch setting. In cases 1 and 2, the applied forces act along the $\hat{z}_0$-axis, while in case 3, the applied force rotates with the beam as it changes in pitch setting. Moreover, applied forces do not follow pitch deformations in all cases. Cases 1 and 2 were analysed at rotational speeds ranging from 0 through 100 RPS, with increments of 10 RPS. Case 3 was analysed only at 100 RPS, at pitch settings ranging from 0° through 60°, with increments of 10°.

Table 4.3: Geometry information for each case that was analysed to verify the structural model.

Case	Material	Profile	Height (mm)	Width (mm)	Thickness (mm)	Length (mm)
1	Aluminium	Rectangular	60	110	10	1200
2	Aluminium	Rectangular	60	110	10	1200
3	Aluminium	Rectangular	60	110	10	1200

Table 4.4: Loading information for each case that was analysed to verify the structural model.

Case	Rotation Rate (RPS)	Tip Force (N)	Distributed Load (N/m)	Pitch Setting (^{o})
1	0, 10, . . . , 100	3000	–	0
2	0, 10, . . . , 100	–	5000	0
3	100	3000	–	0, 10, . . . , 60

The height and width dimensions provided in Table 4.3 denote the outermost dimensions. Images indicating each beam model's geometry and loading (generated using PROTEUS) are shown in Figure 4.6. The structural mesh has 200 elements of equal length in both ABAQUS and PROTEUS, as this grid size was found to provide a sufficient level of precision in all three cases.

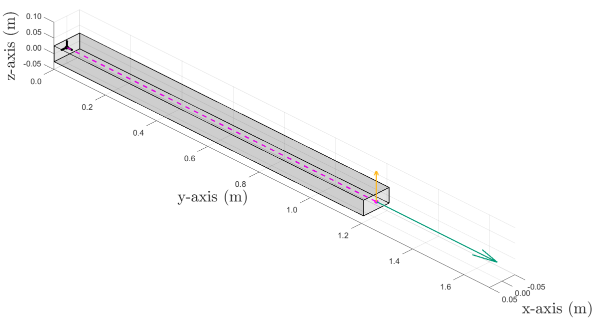

(a) Cases 1 and 3 (0° pitch)

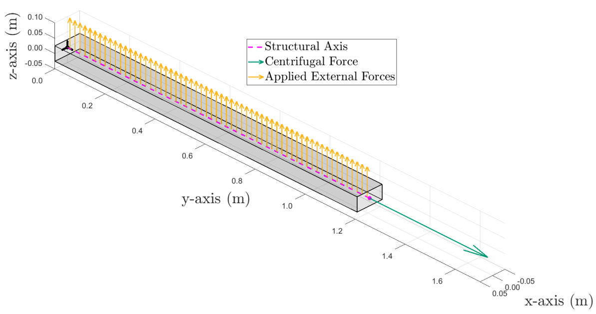

(b) Case 2

Figure 4.6: Beam models that were analysed to provide verification for the structural analysis.

4.2.1. RESULTS

Reaction forces at the beam root, the tip deformations, and the full beam deformations are compared in this section. Components that have not been plotted in this section are small and thus provide a negligible contribution. Figure 4.7 contains plots of the reaction forces acting through the three principal axes of the global coordinate system for an increasing rotational velocity in cases 1 and 2, and for a changing axis of rotation in case 3. In all results shown, the percent error is below 1%, which verifies the proposed method.

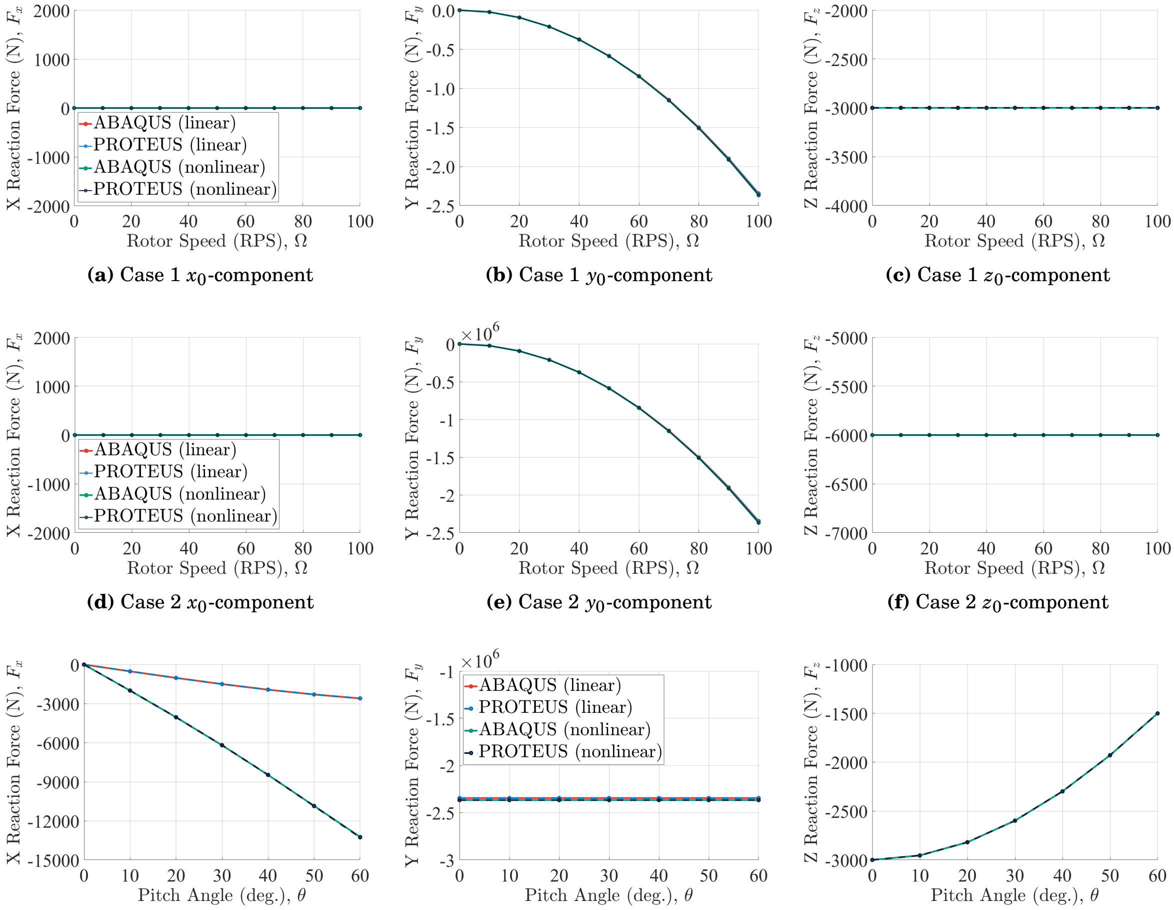

(a) Case 1 x_0-component **(b)** Case 1 y_0-component **(c)** Case 1 z_0-component

(d) Case 2 x_0-component **(e)** Case 2 y_0-component **(f)** Case 2 z_0-component

(g) Case 3 x_0-component **(h)** Case 3 y_0-component **(i)** Case 3 z_0-component

Figure 4.7: Reaction forces obtained for case 3 for a range of pitch settings.

Figure 4.8 contains plots of the root bending moment about the x_0-axis for cases 1 and 2, and Figure 4.9 contains plots of the root bending moment about the x_0- and z_0-axes for case 3.

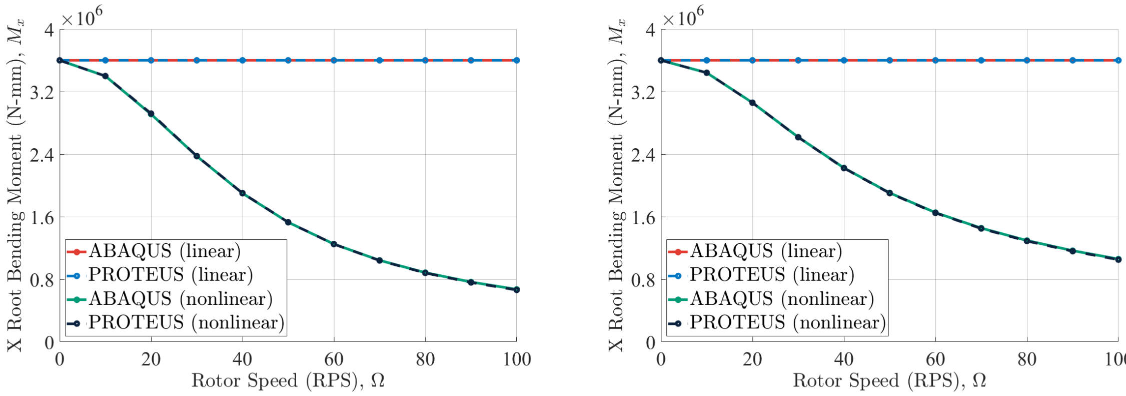

(a) Case 1 **(b)** Case 2

Figure 4.8: Root bending moment plots about the global x_0-axis for cases 1 and 2.

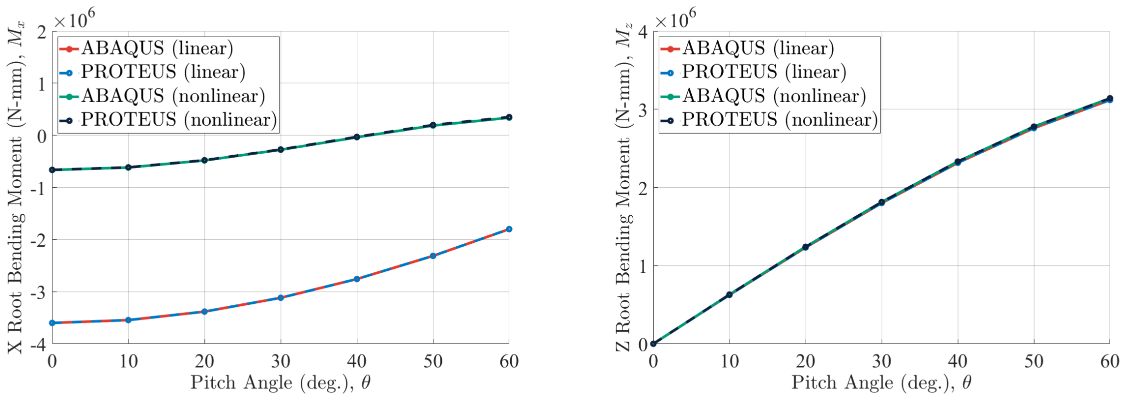

(a) Moment about the global x_0-axis

(b) Moment about the global z_0-axis

Figure 4.9: Root bending moment plots for case 3.

As expected, the reaction forces in the global $\hat{x}_0$ and $\hat{z}_0$ axes remained constant for case 1 and case 2, since they are orthogonal to the axis of rotation. The reaction force in the y_0-axis naturally increases in magnitude as the rotation rate increases. Because the centrifugal force is proportional to the squared rotation speed, the reaction force in the y_0-axis grows quadratically. For case 3, the reaction forces in the $\hat{z}_0$-axis decreases and the reaction force in the $\hat{x}_0$-axis increases as the pitch setting increases because the applied force vector becomes more aligned with the global $\hat{x}_0$-axis with increasing pitch setting. The x reaction force also grows in magnitude due to the centrifugal forces that act with increasing magnitude along the $\hat{x}_0$-axis, as the x-distance between the deformed beam axis and the axis of rotation increases. This effect becomes more significant with increasing pitch setting, as deformations in the $\hat{x}_0$ axis increase with increasing pitch setting. The linear analysis is incapable of accounting for this effect, since loads are only computed for the undeformed beam geometry, whereas the nonlinear procedure involves iteratively recalculating loads and deformations. Thus, the large difference in magnitude observed between linear and nonlinear reaction forces in the $\hat{x}_0$-axis is entirely due to centrifugal forces. Because the centrifugal force acts along the $\hat{z}_0$-axis, there is no difference between the linear and nonlinear z reaction forces, as the centrifugal force will not act in this direction. The difference in x root bending moment between the linear and nonlinear analysis is directly caused by the centrifugal stiffening effect. The resultant centrifugal force acts radially relative to the $\hat{z}_0$ axis, and thus does not contribute to the moment about the $\hat{z}_0$-axis.

Plots of the deformations over the full length of each beam are shown in Figure 4.10 and Figure 4.11. Figure 4.12 through Figure 4.14 subsequently contain plots of the tip displacement of each beam model in global coordinates. It is shown that the nonlinear analysis is capable of capturing the spin-stiffening effect, as deformations are significantly reduced in comparison to the linear case. The physical interpretation of the deformations identically follows the reasoning that was provided for the calculated reaction forces.

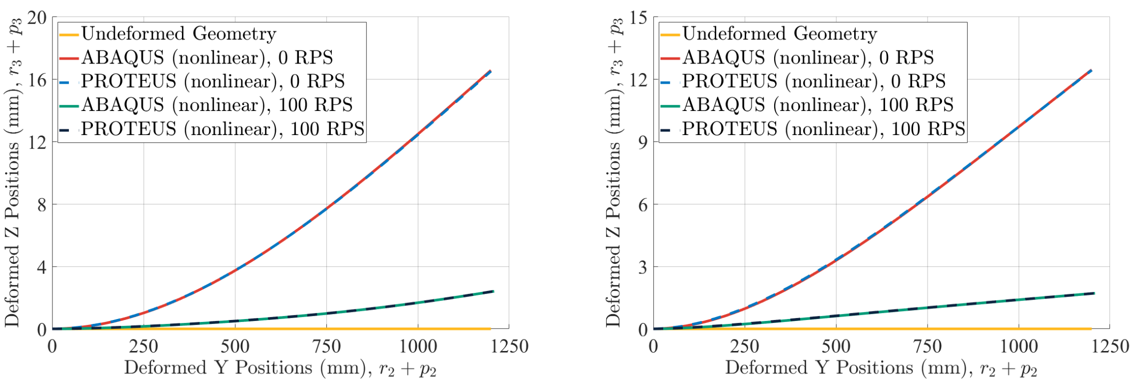

(a) Case 1

(b) Case 2

Figure 4.10: Full beam deformations for cases 1 and 2 at two different rotation speeds (not to scale).

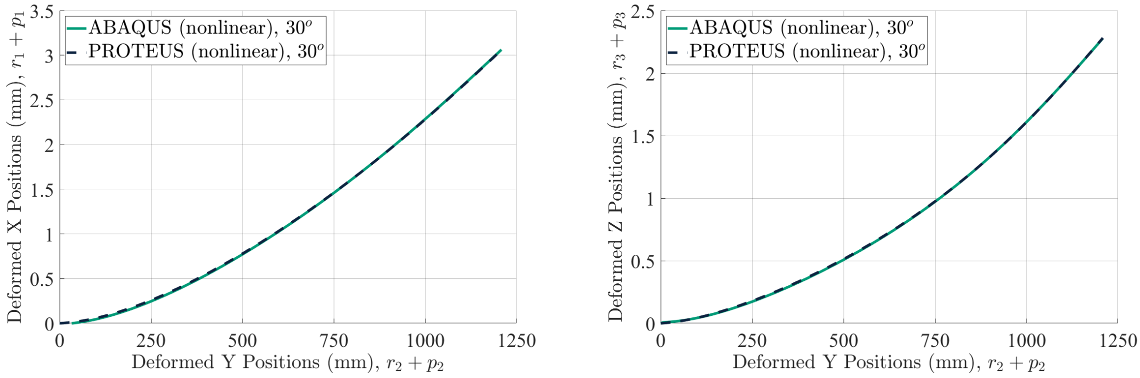

(a) y_0-component **(b)** z_0-component

Figure 4.11: Full beam deformations for case 3 at a pitch angle of 30° (not to scale).

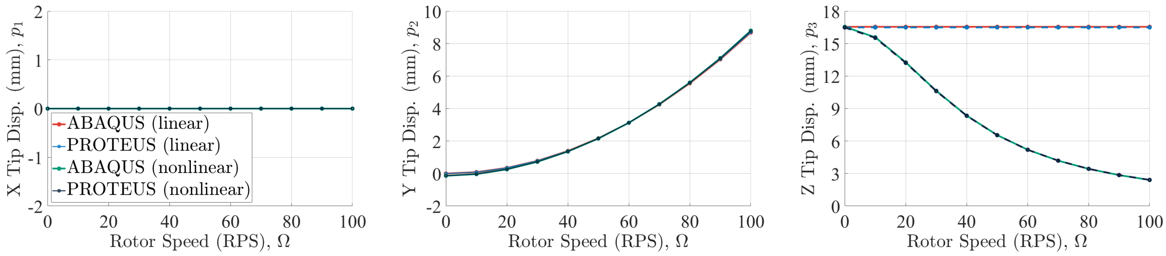

(a) x_0-component **(b)** y_0-component **(c)** z_0-component

Figure 4.12: Calculated tip displacement values for case 1 over a range of rotation rates.

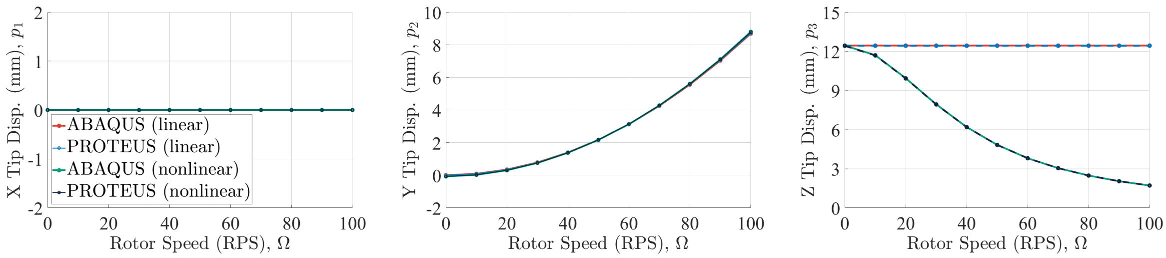

(a) x_0-component **(b)** y_0-component **(c)** z_0-component

Figure 4.13: Calculated tip displacement values for case 2 over a range of rotation rates.

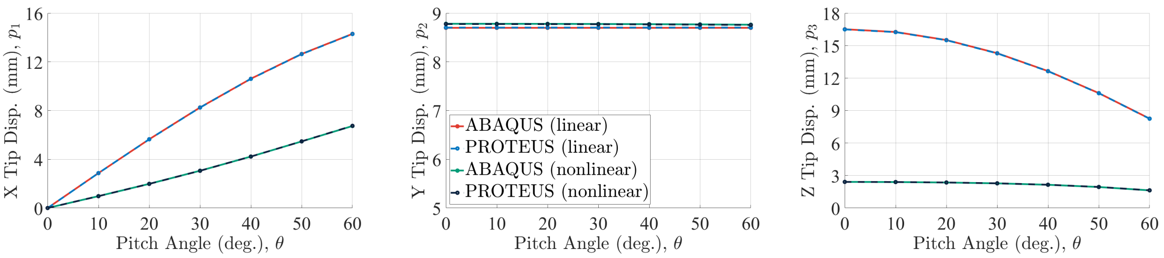

(a) x_0-component **(b)** y_0-component **(c)** z_0-component

Figure 4.14: Calculated tip displacement values for case 3 over a range of pitch settings.

4.3. AEROELASTIC ANALYSIS PROCEDURE

Due to a shortage of available experimental results to compare with during the validation of the aeroelastic analysis, verification was performed through comparisons to a loosely coupled method that proceeds by iteratively running the structural and aerodynamic analyses separately until the difference between deformations computed during two subsequent iterations is sufficiently small. This approach to providing validation for the aeroelastic analysis was considered sufficient because both the aerodynamic and structural models have already been validated, and thus the final remaining step is to demonstrate that the iterative scheme discussed in Section 2.3 is performing as intended. The loosely coupled method is very similar to the methods applied by Khan [4] and Sodja *et al.* [3], which do not require derivatives of aerodynamic forces with respect to structural degrees of freedom, and it proceeds as follows.

(1) Provide model inputs and initial conditions.

(2) Calculate aerodynamic and centrifugal loads.

(3) Apply loads to nodes of the structural mesh.

(4) Compute deformations using the finite element method.

(5) Modify the geometry input to the aerodynamic model (twist distribution and blade axis).

(6) If differences in deformations between subsequent iterations are above the defined tolerance, recompute aerodynamic loads. Otherwise, evaluate performance and end calculations.

The three-bladed version of the TUD-XPROP propeller was analysed, as shown in Figure 4.15. Details on the structure and loading considered are provided in Table 4.5 and Table 4.6. Details on the lamination parameter values considered in this case have also been provided in Table 4.7, corresponding to the layup stacking sequence indicated in Equation (4.1). All ply angles are defined relative to the spanwise axis of the blade, positive towards the trailing edge for the upper and lower surfaces, and positive downwards for the spar webs.

$$\mathcal{S} = \left\{ 0^\circ \quad 15^\circ \quad 30^\circ \quad 30^\circ \quad 45^\circ \quad 45^\circ \quad 60^\circ \quad 60^\circ \quad 75^\circ \quad 90^\circ \right\}_s \tag{4.1}$$

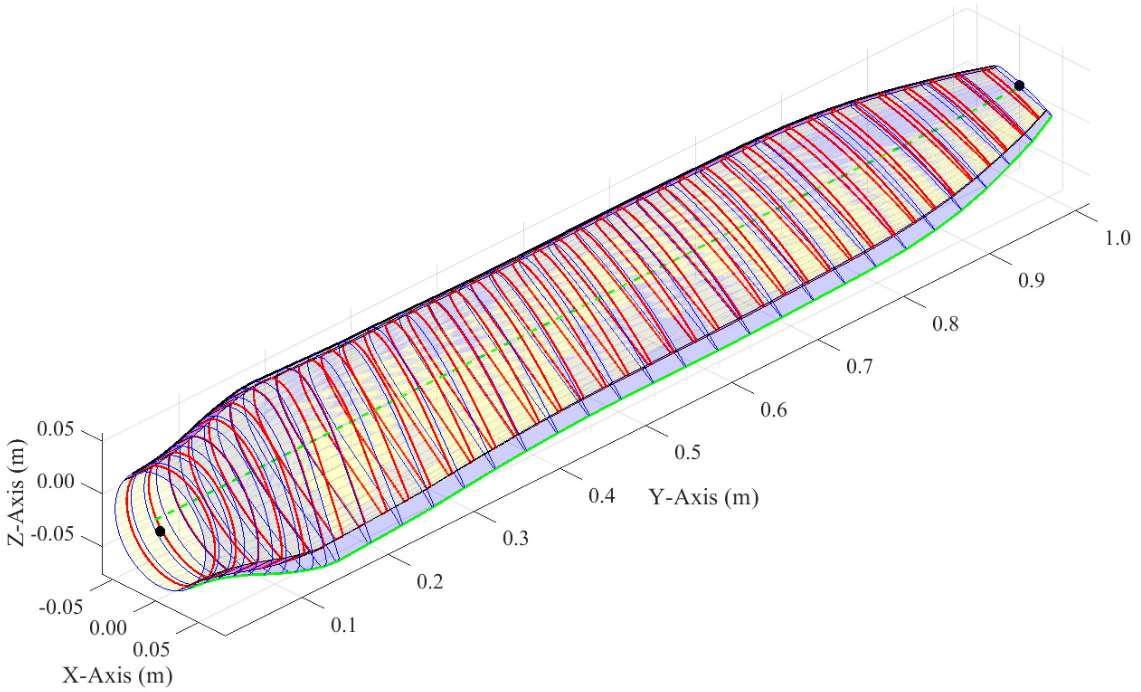

Figure 4.15: A visual depiction of the geometry that was used during verification of the aeroelastic analysis. Spar webs are shown in magenta, node locations of the structural mesh are shown in red, structural surface skins are shown in yellow, and the exterior geometry is shown in blue. The coordinates denoted by (X, Y, Z) correspond to the $\left(e_1^{\mathrm{b}}, e_2^{\mathrm{b}}, e_3^{\mathrm{b}}\right)$ coordinates from the corotational framework.

The front and rear spar webs were placed as near as possible to the leading and trailing edges within each blade section to prevent numerical difficulties, since the airfoils of the TUD-XPROP do not have a closed trailing edge. Moreover, each surface of the structure was defined using one constant thickness laminate, meaning that four laminates were used to describe the blade. Lastly, 35 linearly spaced beam elements were used for the structural analysis, 75 cosine-spaced elements were used for the BEM analysis, and each 3D structural cross-section was represented with 100 shell elements.

Table 4.5: Structural information for the cases analysed to verify the aeroelastic model.

Case	Material	Geometry	Front Spar (%c)[a]	Rear Spar (%c)[a]	Laminate Thickness (mm)
1	AS4 / APC2	TUD-XPROP	0.02	0.90	0.75
2	AS4 / APC2	TUD-XPROP	0.02	0.90	0.75

[a] Front and rear spars have been added because the cross-sectional modeller could not represent the stiffness properties of the leading and trailing edge sections. This change should not have any noticeable influence on general design trends.

Table 4.6: Loading information for each case that was analysed to verify the structural model.

Case	Rotor Speed (RPS)	Advance Ratio	Altitude (m)	Pitch Setting (^{o})
1	40	0.75	0	25
2	20	2.00	0	25

Table 4.7: Lamination parameter values considered during verification of the aeroelastic analysis.

Surface	ξ_1^A	ξ_2^A	ξ_3^A	ξ_4^A	ξ_1^D	ξ_2^D	ξ_3^D	ξ_4^D
Upper	0.000	-0.646	-0.100	0.000	-0.572	-0.569	0.056	0.390
Lower	0.000	0.646	-0.100	0.000	-0.572	0.569	0.056	-0.390
Spars	0.000	0.000	0.000	0.000	0.000	0.000	0.000	0.000

Figure 4.16 contains diagrams of the loading encountered by the blade in both the regenerative and propulsive operating conditions. Loads have been scaled for visibility, and mapped in three-dimensions onto the three-dimensional deformed blade geometry. The same scale factors have been used for the loads in both images, and thus it is possible to visually compare the magnitudes and directions of the loads between the two cases, although the numerical values do not have any physical meaning. The shapes of the force distributions and directions of the forces have additionally been represented accurately.

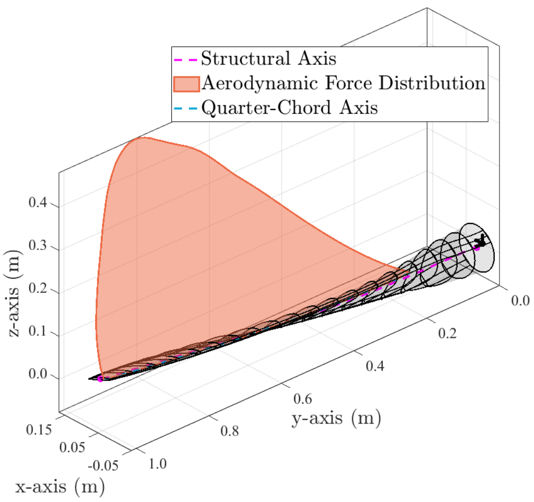

(a) Case 1 (propulsive operation)

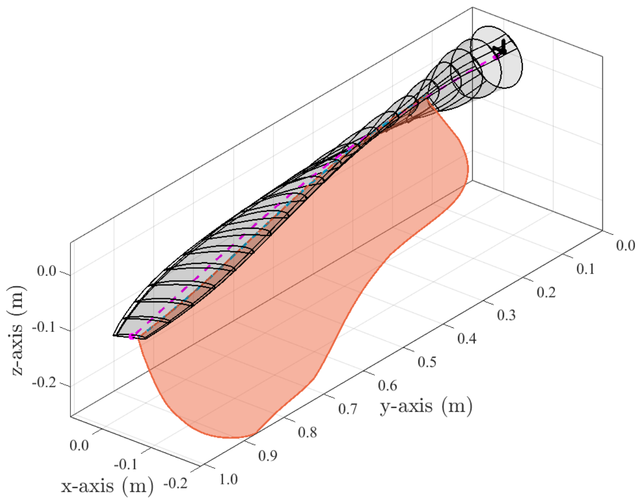

(b) Case 2 (regenerative operation)

Figure 4.16: Blade models that were analysed to provide verification for the aeroelastic analysis. The coordinates denoted by (x, y, z) correspond to $\left(e_1^b, e_2^b, e_3^b\right)$ coordinates from the corotational framework.

Deformations and performance characteristics were compared between the two methods. Figure 4.17 contains plots of the translational and rotational deformations obtained for each case in the coordinate system shown in Figure 4.15, whereas Table 4.8 contains a summary of the overall propeller performance evaluated for each case, including the percent difference between the results from each method. Excellent agreement was obtained between the two analysis methods, with a maximum difference that is below 0.01% for all quantities of interest. This level of agreement is expected, as the main advantage of the tightly coupled method is that it is faster and more robust in comparison to the loosely coupled method.

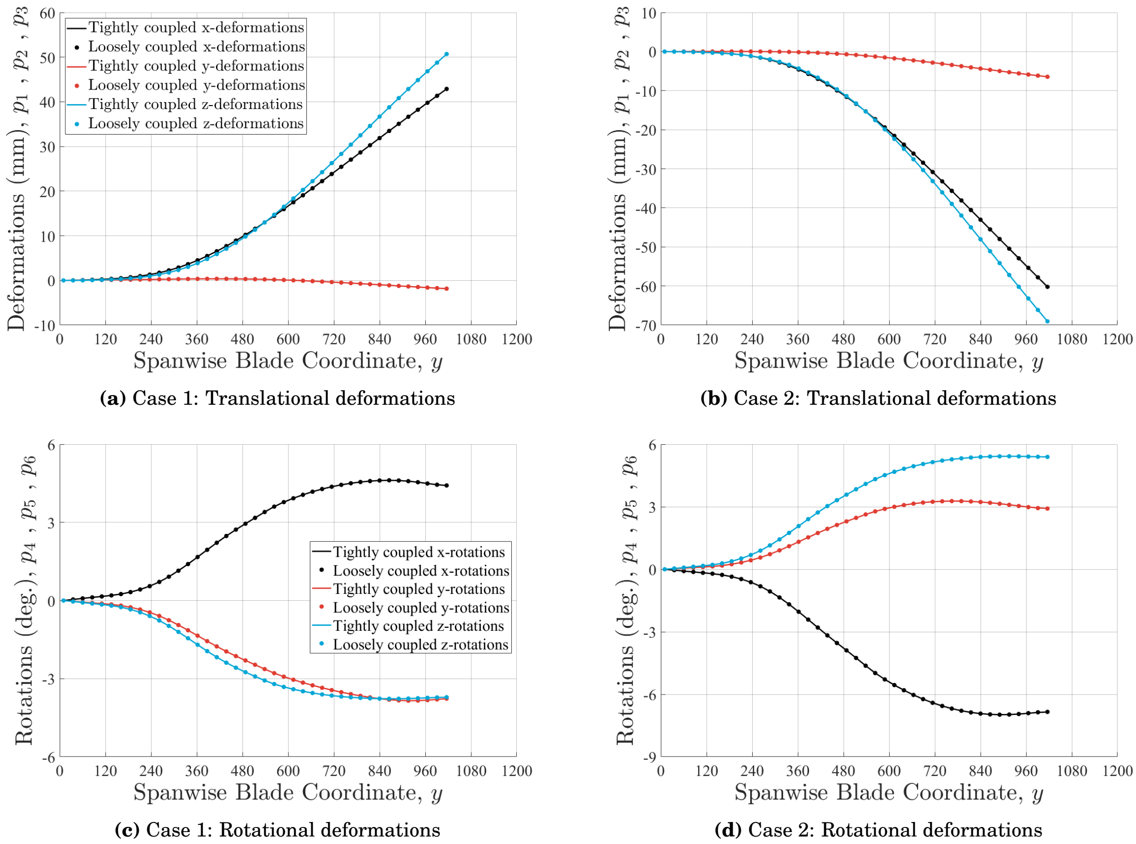

(a) Case 1: Translational deformations

(b) Case 2: Translational deformations

(c) Case 1: Rotational deformations

(d) Case 2: Rotational deformations

Figure 4.17: Translational and rotational deformations obtained for the two cases under consideration.

Table 4.8: Performance results obtained for cases 1 and 2, indicating close agreement.

Case	Method	C_T	C_Q	C_P	T_C	P_C	η_P	η_T	η_{eh}
1	Tightly Coupled	0.098	0.014	0.090	0.175	0.213	0.820	N/A	N/A
	Loosely Coupled	0.098	0.014	0.090	0.175	0.213	0.820	N/A	N/A
	(Percent Difference)	(0.001%)	(0.001%)	(0.001%)	(0.001%)	(0.001%)	(0.001%)		
2	Tightly Coupled	-0.218	-0.056	-0.354	-0.054	-0.044	N / A	0.809	0.111
	Loosely Coupled	-0.218	-0.056	-0.354	-0.054	-0.044	N / A	0.809	0.111
	(Percent Difference)	(0.010%)	(0.010%)	(0.010%)	(0.010%)	(0.010%)		(0.010%)	(0.010%)

Three-dimensional plots of the blade deformations in each case have been shown in Figure 4.18 to indicate how deformations in each degree of freedom are represented on the three-dimensional structure. The comparison shown in Figure 4.17 are considered sufficient for comparison, and thus the plots shown in Figure 4.18 were generated using results from the tightly coupled analysis. Finally, plots of the performance trends for the propeller configuration under consideration have been shown in Figure 4.19, corresponding to constant rotor speeds of 40 and 20 RPS respectively in positive and negative thrust conditions. These results have also been generated using the tightly coupled analysis, as the results shown in Table 4.8 have been considered sufficient for comparisons.

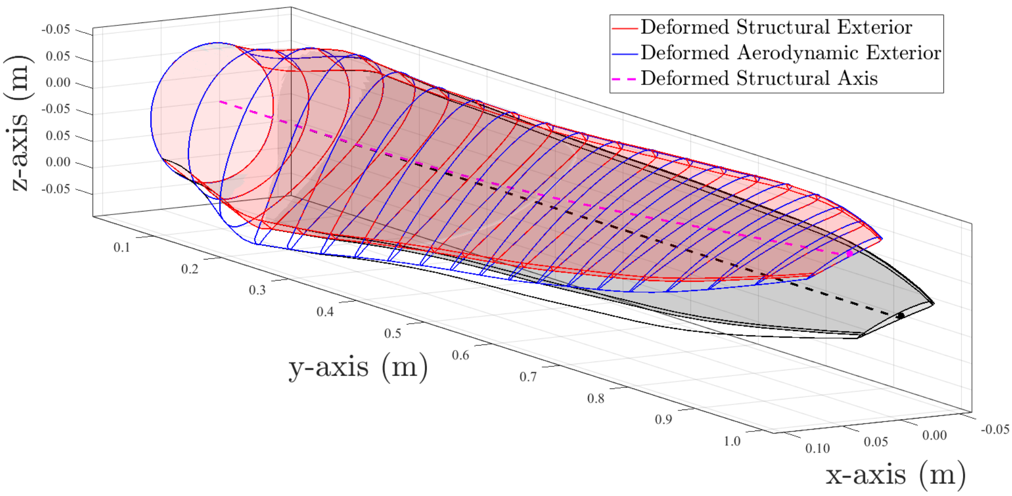

(a) Case 1 (propulsive operation)

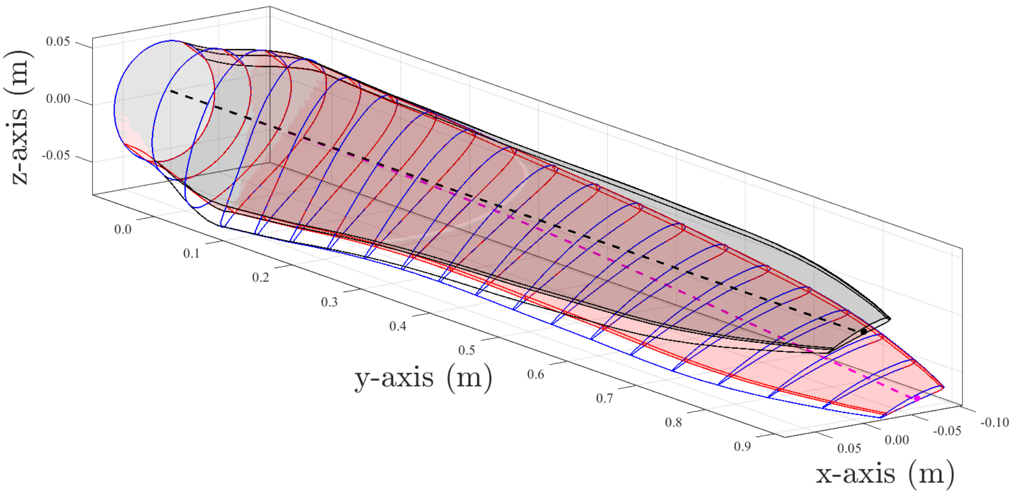

(b) Case 2 (regenerative operation)

Figure 4.18: Three-dimensional plots of the deformations encountered by the propeller blade during verification of the aeroelastic analysis, generated using the tightly coupled method. The coordinates denoted by (x, y, z) correspond to the $\left(e_1^{\mathrm{b}}, e_2^{\mathrm{b}}, e_3^{\mathrm{b}}\right)$ coordinates from the corotational framework.

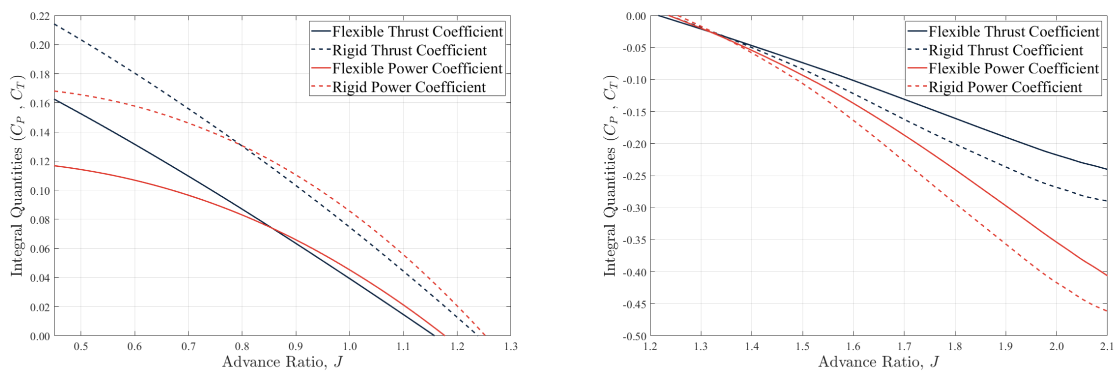

(a) Case 1 (propulsive operation), $\Omega = 40$ RPS **(b)** Case 2 (regenerative operation), $\Omega = 20$ RPS

Figure 4.19: Performance curves for the flexible and rigid propellers used during verification of the aeroelastic analysis, generated using the tightly coupled method.

5

Aeroelastic Tailoring Results

Results from the aeroelastic optimization and sensitivity studies have been presented in this chapter to address the research objectives concerning this project. Section 5.1 contains results from the sensitivity studies that performed through variations in ply orientation and laminate thickness. Section 5.2 subsequently contains all results from the optimization studies.

5.1. Sensitivity Studies

Before beginning the optimization, sensitivity studies were completed to develop an intuition for the propeller design problem. The propeller blade discussed in Section 3.2.2 has been used during the collection of results from the sensitivity studies to maintain commonality, as the same blade design has been considered during the optimization as well as during the verification and validation studies documented in Chapter 4. Ply orientations have been varied to identify their influence on performance (Section 5.1.2) and deformations (Section 5.1.3). A summary of the main conclusions from the sensitivity studies in terms of ply orientation is provided in Section 5.1.4. Lastly, the laminate thickness has been varied for two constant stacking sequences in Section 5.1.5 to motivate the selection of bounds during the optimization. Supplementary results to sensitivity studies are also shown in Appendix D.

5.1.1. Laminate Inputs

The TUD-XPROP-3 propeller blade, with a structure that is defined by one laminate each on its upper and lower surfaces, was analysed over a range of ply stacking sequences. The stacking sequence for the upper surface and lower surface laminates is defined by Equation (5.1), with trends being evaluated at varying angles given by Θ_1 and Θ_2. Results obtained from the sensitivity studies were divided into two groups. In the first group, symmetric-balanced and symmetric-unbalanced laminates were exclusively studied through variations in the ply orientations that respectively maintain the relations given by $\Theta_1 = -\Theta_2 = \Theta$ and $\Theta_1 = \Theta_2 = \Theta$. This sensitivity study was performed to directly identify differences between performance trends corresponding to symmetric-balanced and symmetric-unbalanced laminates. After completing the first sensitivity study, a second investigation was performed by continuously varying both Θ_1 and Θ_2 to yield performance and deformation results corresponding to any combination of the two angles. This investigation was completed to provide a more complete picture of the observed trends.

$$\mathcal{S} = \left\{ 90^\circ \quad 0^\circ \vdots \Theta_1 \quad \Theta_2 \quad \Theta_1 \quad \Theta_2 \quad \Theta_1 \quad \Theta_2 \vdots 0^\circ \quad 90^\circ \right\}_s \qquad \Theta_1 \, , \Theta_2 \in \left\{ -90^\circ \, , -75^\circ \, , \ldots , 90^\circ \right\} \tag{5.1}$$

Table 5.1: Structural and geometric inputs for the sensitivity studies in terms of ply orientation.

Material	Geometry	Spars (%c)	Laminate Thickness (mm)	Rotor Speed (RPS)	Pitch Setting
AS4 / APC2	TUD-XPROP-3	0.02, 0.90	1.5	23	25°

Note that all results presented in this section correspond to a pitch setting of 25°, although additional results have been shown in Appendix D for a pitch setting of 15° and a rotor speed of 30 RPS to indicate that the general trends remain unchanged.

For the sensitivity study that was performed through variations in a single variable, Equation (5.2) defines the ply stacking sequence for the symmetric-unbalanced laminates, and Equation (5.3) defines the ply stacking sequence for the symmetric-balanced laminates. For all ply stacking sequences defined in this section, ply angles are defined relative to the spanwise axis and positive towards the trailing edge.

$$\text{Symmetric-Unbalanced:} \qquad \mathcal{S} = \left\{ 90^\circ \quad 0^\circ \;\vdots\; \Theta \quad \Theta \quad \Theta \quad \Theta \quad \Theta \quad \Theta \;\vdots\; 0^\circ \quad 90^\circ \right\}_s \tag{5.2}$$

$$\text{Symmetric-Balanced:} \qquad \mathcal{S} = \left\{ 90^\circ \quad 0^\circ \;\vdots\; \Theta \quad -\Theta \quad \Theta \quad -\Theta \quad \Theta \quad -\Theta \;\vdots\; 0^\circ \quad 90^\circ \right\}_s \tag{5.3}$$

5.1.2. PERFORMANCE RESULTS

For the sensitivity studies evaluated through variations in a single variable, propeller performance was evaluated through comparisons in thrust, power, and efficiency. For symmetric-unbalanced laminates, changing the ply orientation directly changes the major principal stiffness axis, as it will always align with the angle $\Theta = \Theta_1 = \Theta_2$. Conversely, for symmetric-balanced laminates, the major principal stiffness axis will either have an angle of 0° or 90°, depending on which angle $\Theta = \Theta_1 = -\Theta_2$ is closest to. Variations in two ply orientations were subsequently performed to identify trends in the thrust and power coefficients at an operating point characterizing either propulsive or regenerative mode.

VARIATIONS IN A SINGLE VARIABLE: BALANCED VS. UNBALANCED LAMINATES

Plots of the thrust and power coefficient are shown in Figure 5.1 for both symmetric-unbalanced and symmetric-balanced laminates. The coefficients C_T and C_P were used since the rotor speed was held constant when varying the advance ratio, and thus the normalization is constant over the full range of operating points. This means that the trends in C_T and C_P are equivalent to trends in thrust and power. Nevertheless, the coefficients T_C and P_C were found to exhibit the same trends corresponding to ply orientation variations for both laminate types, their plots have been omitted for brevity.

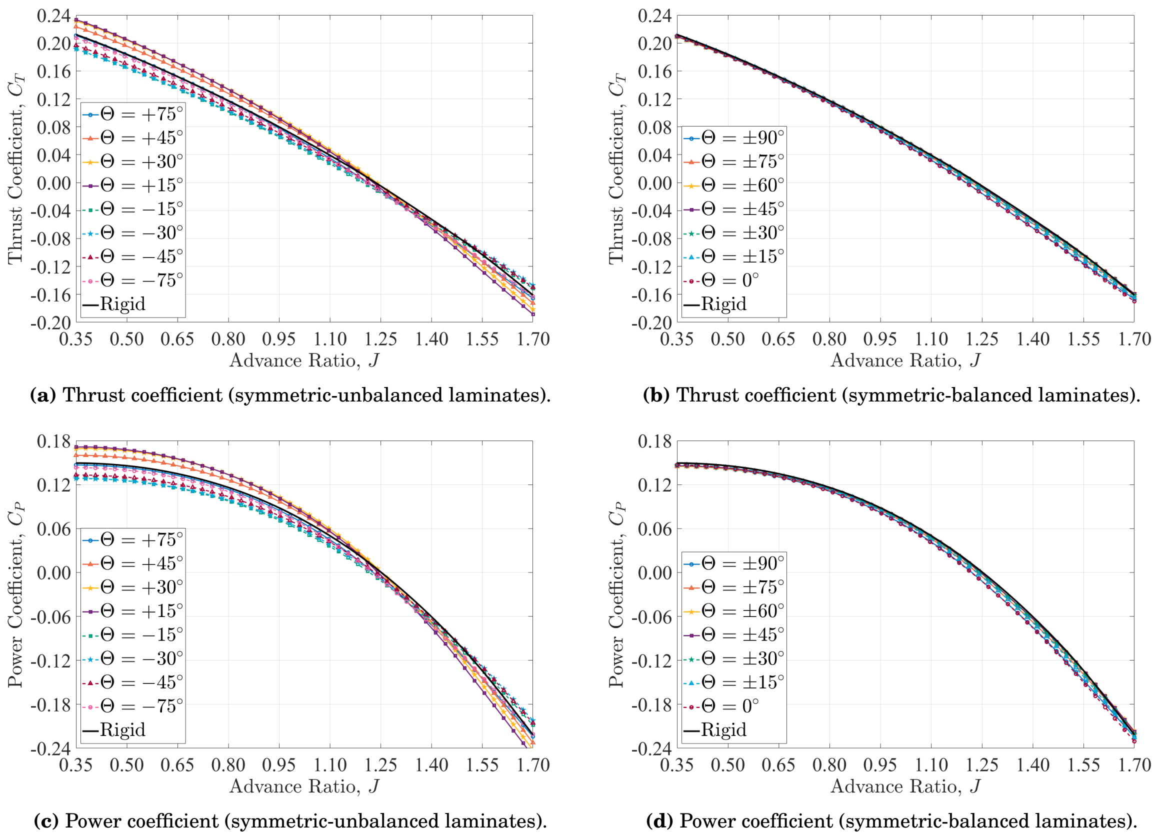

(a) Thrust coefficient (symmetric-unbalanced laminates).

(b) Thrust coefficient (symmetric-balanced laminates).

(c) Power coefficient (symmetric-unbalanced laminates).

(d) Power coefficient (symmetric-balanced laminates).

Figure 5.1: Thrust and power coefficient plots obtained from sensitivity studies.

For symmetric-unbalanced laminates, Figure 5.1a and Figure 5.1c indicate that ply orientations yielding a decrease in thrust coefficient will also cause the power coefficient to decrease. This was found to occur for negative ply orientations, which generally induce an aerodynamic wash-out effect as the blade deforms. For symmetric-unbalanced laminates with positive ply orientations, an aerodynamic wash-in effect is observed as the blade deforms. The wash-out effect resulting from negative ply orientations causes the upward bending and shear deformations to result in leading-edge-down pitch rotations that reduce the loading. At positive ply orientations, the wash-in effect causes upwards bending and shear deformations to yield leading-edge-up pitch deformations that increase the amount of loading. Figure 5.1b and Figure 5.1d indicate that variations in performance for symmetric-balanced laminates are significantly smaller in comparison to performance variations for symmetric-unbalanced laminates. This difference is caused by the absence of extension-shear coupling and the negligible bend-twist coupling, which may be discerned from Figure D.9b, as ξ_2^{A} and ξ_4^{A} are zero, and ξ_2^{D} and ξ_4^{D} are small for all ply orientations.

For symmetric-unbalanced laminates, the largest decrease in thrust and power appears to be present at ply orientations between $-30°$ and $-15°$. Conversely, the largest increase in thrust and power appears to be present at ply orientations between 15° and 30°. This is consistent with the observation that changes in performance are closely linked to the presence of bend-twist and extension-shear coupling, as it is indicated in Figure D.9 that coupling terms (given by ξ_2^{A} and ξ_4^{A} for extension-shear coupling, and ξ_2^{D} and ξ_4^{D} for bend-twist coupling) are largest in magnitude between these angles. Trends for symmetric-balanced laminates are difficult to discern in comparison to the trends observed for symmetric-unbalanced laminates. This is because variations in performance are less sensitive to variations in ply orientation in this case. It appears that the performance trends approximately overlap for ply orientations of 90° and 0°, ±75° and ±15°, as well as ±60° and ±30°. The laminates corresponding to each pair are the same, except offset from each other by 90°. Thus, they have the same amount of torsional and shear stiffness. This is made clear in Figure D.9b by following the curves corresponding to ξ_3^{A} and ξ_3^{D}, which exhibit the same characteristic and appear to reach a minimum at ±45°, suggesting that this is the point of maximum torsional stiffness. This observation was made by recognizing through Equation (2.27) that ξ_3^{A} and ξ_3^{D} are the only terms that respectively contribute to the shear and torsional stiffness, with increasing values for ξ_3^{A} and ξ_3^{D} yielding a decrease in stiffness. Because the aerodynamic loads exert a leading-edge-down pitching moment on the blade that increases with advance ratio (as indicated in Figure 5.8b), the loading is always decreased relative to the rigid propeller and this difference in loading grows with increasing advance ratio.

The most important conclusion to draw from the results presented in Figure 5.1 is that the difference in performance is largely dependent on pitch deformations of the propeller, and thus aeroelastic tailoring may only be used to enhance performance through the inclusion of extension-shear or bend-twist coupling. In this way, symmetric-balanced laminates provide a minimal change in performance because they provide a negligible amount of bend-twist and extension-shear coupling. Symmetric-unbalanced laminates have the potential to provide a substantial amount of bend-twist and extension-shear coupling, and thus may yield a significant change in thrust and power that can either enhance or degrade performance, depending on the type of coupling that is present. The application of symmetric-unbalanced laminates towards the improvement of performance has accordingly been explored further through the optimization studies.

To clarify the trends in performance that have been shown up to this point, the power consumption (C_P) has been plotted against the thrust (C_T) for both laminate types under consideration in Figure 5.2.

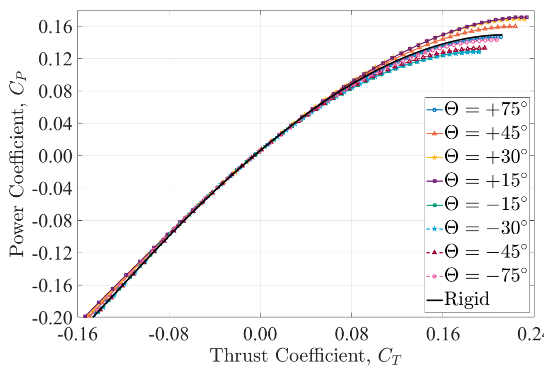

(a) C_P vs. C_T (symmetric-unbalanced laminates).

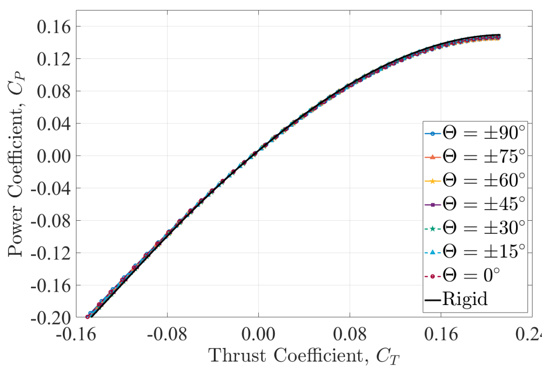

(b) C_P vs. C_T (symmetric-balanced laminates).

Figure 5.2: Plots of power (C_P) as a function of thrust (C_T), obtained from sensitivity studies.

The trends observed in Figure 5.2a confirm the previous finding of negative ply orientations providing favourable performance in comparison to positive ply orientations, with the least amount of power being consumed at a constant thrust in propulsive conditions and either more or equal energy being harvested in regenerative conditions for ply orientations between approximately −30° and −15°. Differences between the flexible and rigid propeller performance are difficult to discern from Figure 5.2b, which is consistent with the observations that were previously made corresponding to Figure 5.1.

Efficiency plots are shown in Figure 5.3 for both balanced and unbalanced laminates. The propeller efficiency appears to either be increased or decreased depending on the ply orientations, although the turbine efficiency appears to always decrease through the consideration of blade flexibility.

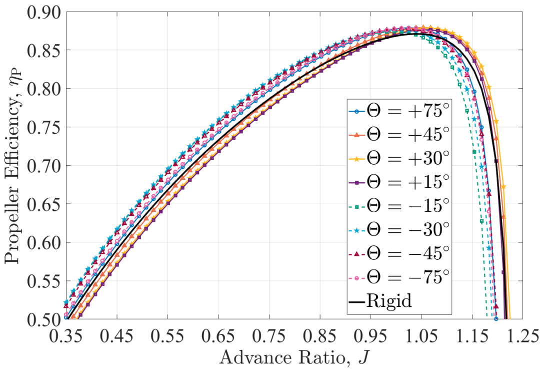

(a) Propeller efficiency (symmetric-unbalanced laminates).

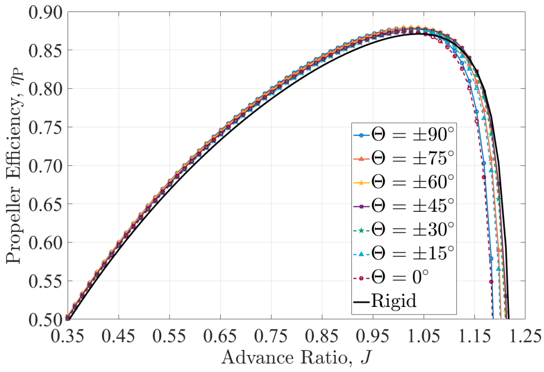

(b) Propeller efficiency (symmetric-balanced laminates).

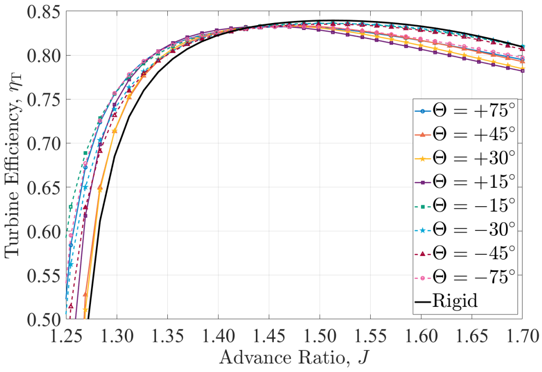

(c) Turbine efficiency (symmetric-unbalanced laminates).

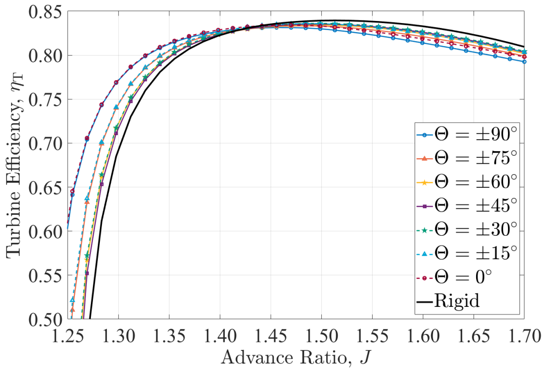

(d) Turbine efficiency (symmetric-balanced laminates).

Figure 5.3: Propeller and turbine efficiency plots obtained from sensitivity studies.

The trends in efficiency vs. advance ratio are less clear than the trends in thrust and power. This is because the blade loading is different at each ply orientation, for a constant advance ratio. Thus, it is difficult to make a direct comparison in the efficiency yielded by each ply orientation when plotted against advance ratio. For symmetric-unbalanced laminates, Figure 5.3a indicates that negative ply orientations result in a larger efficiency in comparison to positive ply orientations, with a similar peak value that always appears to exceed the peak efficiency yielded by the rigid propeller. For symmetric-balanced laminates, the efficiency curves shown in Figure 5.3b are less spread apart due to the lack of extension-shear and bend-twist coupling. For symmetric-unbalanced laminates, Figure 5.3c indicates that the turbine efficiency is always lower or close to equivalent for the flexible propeller in comparison to the rigid propeller, although the ply orientations between approximately −30° and −15° appear to exhibit the greatest turbine efficiency, whilst also yielding favourable performance in propulsive conditions. For symmetric-balanced laminates, Figure 5.3d indicates that the flexible propeller always underperforms in comparison to the rigid propeller, with the best turbine efficiency unsurprisingly being demonstrated for ply orientations of ±45°, which exhibits performance trends that are closest to that of the rigid propeller.

VARIATIONS IN TWO VARIABLES

To provide a more holistic representation of the general trends shown through the sensitivity studies as a function of a single variable, sensitivity studies have also been performed by varying Θ_1 and Θ_2 in Equation (5.1) continuously. Figure 5.4 contains plots of the thrust and power coefficient at a single constant advance ratio value that represents either propulsive or regenerative operating conditions. The power coefficient has also been plotted at a single constant thrust coefficient value in either propulsive or regenerative conditions in Figure 5.5. As expected, all plots are periodic across their four outer edges, and they are also symmetric across the diagonal line connecting the bottom-left and top-right corners due to the assumption of smeared material properties through the thickness of each laminate.

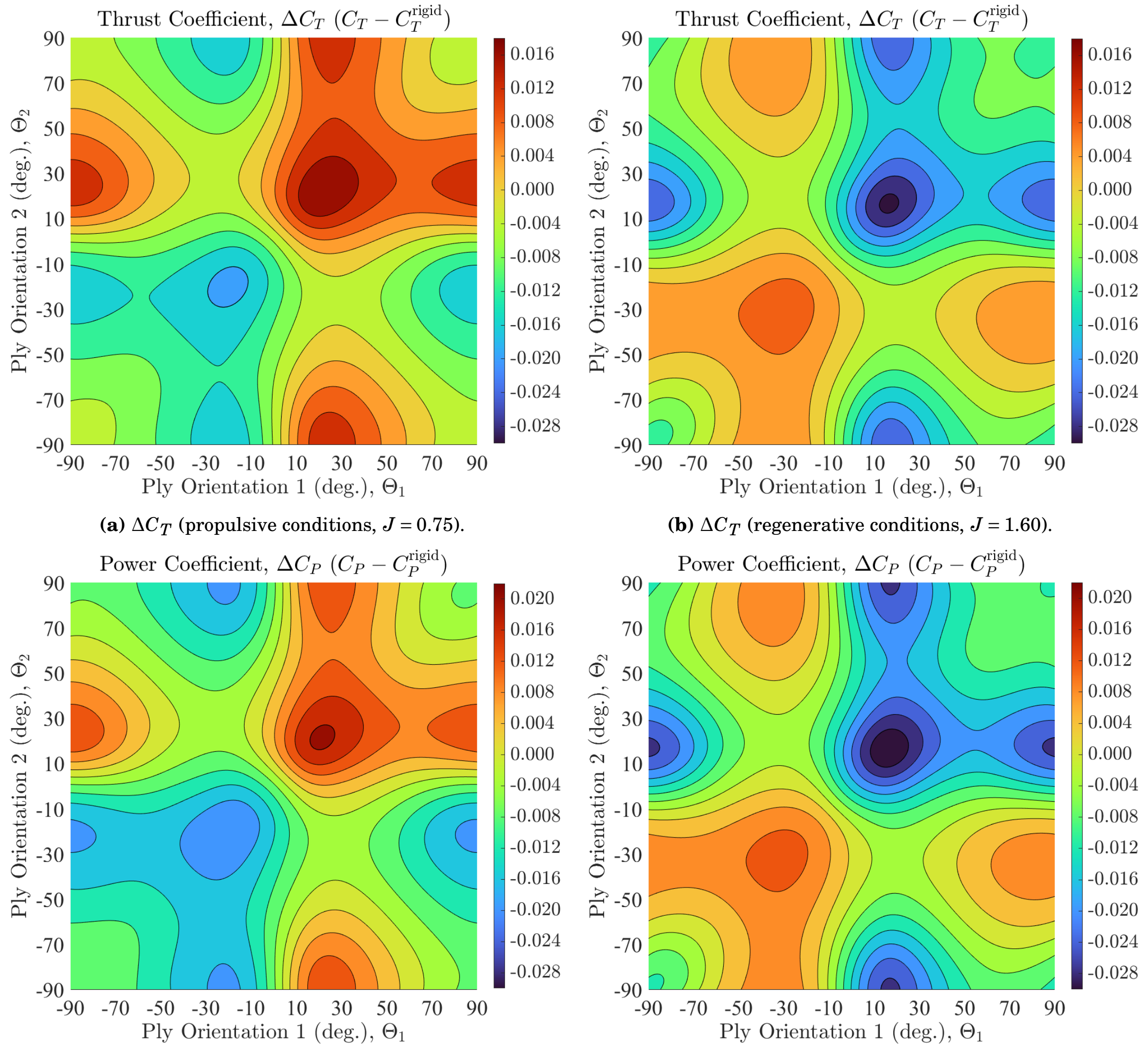

(a) ΔC_T (propulsive conditions, $J = 0.75$).

(b) ΔC_T (regenerative conditions, $J = 1.60$).

(c) ΔC_P (propulsive conditions, $J = 0.75$).

(d) ΔC_P (regenerative conditions, $J = 1.60$).

Figure 5.4: Plots of ΔC_T or ΔC_P obtained from sensitivity studies for the TUD-XPROP-3 made from laminates defined by Equation (5.1) through variations of Θ_1 and Θ_2 at a constant advance ratio.

The trends shown in Figure 5.4 appear consistent with the trends that were observed in Figure 5.1. In particular, when the thrust coefficient of the flexible blade is below that of the rigid blade, the power coefficient of the flexible blade is also below that of the rigid blade, and vice versa. The local maximum and minimum values of thrust and power also indeed appear to be present at 15° and −15°, respectively. Lastly, the variations in both thrust and power with ply orientation appear to exhibit the same general trends, with all local maxima and minima appearing at the same locations. The general trends appear to match the trends in pitch displacement that are shown in Figure 5.14a for propulsive conditions and in Figure 5.14b for regenerative conditions. In particular, local minima and maxima in pitch deformations respectively correspond to local minima and maxima in both thrust and power. This result is consistent with the observation that the performance trends are driven primarily by the presence of extension-shear and bend-twist coupling, as pitch deformations are primarily driven by the presence of extension-shear or bend-twist coupling since the aerodynamic and centrifugal forces acting on each blade produce a minimal amount of torsional loading when no coupling is present.

The trends discussed in the previous paragraph may be further explained using velocity diagrams shown in Figure 1.1. In general, if the twist changes to increase the angle of attack, then the magnitude of both the lift and drag will increase. In propulsive mode, this always results in an increase in torque, although it is possible for the thrust to decrease if the decrease in thrust caused by the drag rise is greater than the increase in thrust caused by the increase in lift. Nevertheless, the change in drag is usually significantly smaller than the change in lift (especially in the linear regime), as shown in Figure 4.1, and thus the thrust usually decreases due to an increase in angle of attack. In regenerative conditions, a more negative angle of attack generally causes the thrust to increase in magnitude, although the torque can either increase or decrease depending on the relative change in lift and drag. The blades of the propeller are designed exclusively for propulsive operation, and thus the cambered airfoils of the propeller may more readily yield a change in drag that exceeds the change in lift (especially in the presence of flow separation). For the operating conditions considered in this study, power still decreased as the thrust decreased.

Lastly, Figure 5.5 clearly indicates that ply orientations corresponding to favourable performance in propulsive conditions also correspond to favourable performance in regenerative conditions. In propulsive conditions, Figure 5.5 confirms the trends that were observed in both Figure 5.1 and Figure 5.2, where symmetric-unbalanced laminates with negative ply orientations were shown to decrease power consumption, and particularly that at a constant thrust, the power consumption can be reduced. The trends for symmetric-balanced laminates are also confirmed, where it is shown that the difference in power consumption for a constant thrust is minimal. It is also clear from Figure 5.5 that ply orientations that increase power consumption during propulsive mode also tend to reduce the amount of energy that may be recovered during regenerative conditions; this trend was also observed in Figure 5.2. In particular, the point of maximum power consumption (and minimum energy-harvesting) appears to be at approximately $\Theta_1 = \Theta_2 = +15°$. The point of minimum power consumption (and maximum energy-harvesting) conversely emerges at approximately $\Theta_1 = \Theta_2 = -15°$. The trends accordingly match trends in pitch deformations, shown in Figure 5.14a (positive thrust) and Figure 5.14b (negative thrust), as pitch deformations that yield an aerodynamic wash-out effect result in a decrease in power consumption, and vice versa.

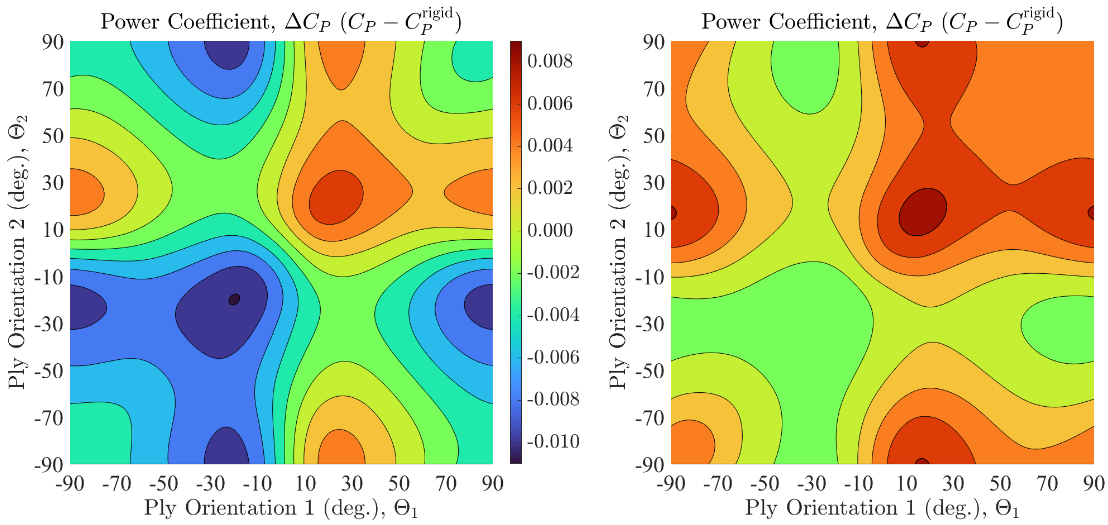

(a) Propulsive conditions ($C_T = 0.12$).

(b) Regenerative conditions ($C_T = -0.12$).

Figure 5.5: Plots of ΔC_P obtained from sensitivity studies for the TUD-XPROP-3 made from laminates defined by Equation (5.1) through variations of Θ_1 and Θ_2 at a constant thrust coefficient.

The most important conclusions to draw from the results presented for 2D variations, is that changes in performance are closely linked to the blade's pitch deformations. Additionally, that the presence of an aerodynamic wash-out effect leads to decreases in power consumption during propulsive conditions and increases in power recovered during regenerative conditions. The opposite is also true, as the presence of an aerodynamic wash-in effect tends to degrade performance. The largest improvement was notably observed for symmetric-unbalanced laminates, with both ply angles having values of approximately $-15°$. The worst performance was seen also for symmetric-unbalanced laminates, with both plies having angles of approximately $+15°$. Additionally, it was unsurprisingly observed that ply orientations yielding a decrease in thrust coefficient were also found to yield a decrease in power coefficient. Finally, all results from 2D variations confirm the trends observed from the 1D variations shown previously.

5.1.3. DEFORMATION RESULTS

The blade's deformations have been plotted as a percentage of its radius, and angular deformations have been expressed in degrees. As discussed in Section 3.2.2, the TUD-XPROP-3 has been scaled by a factor of 4.5, and thus has an outer radius of 0.9144 m. This scale factor has also been used for the optimization, and was selected to ensure that the size of the propeller matches the selected reference aircraft.

VARIATIONS IN A SINGLE VARIABLE: NOT INCLUDING AERODYNAMIC LOADS

Plots of the tip displacements for the case where the blade is subjected to zero aerodynamic loads (with only the centrifugal force being applied) are presented in Figure 5.6. Rotational deformations of the blade tip under zero aerodynamic loads are additionally shown in Figure 5.7.

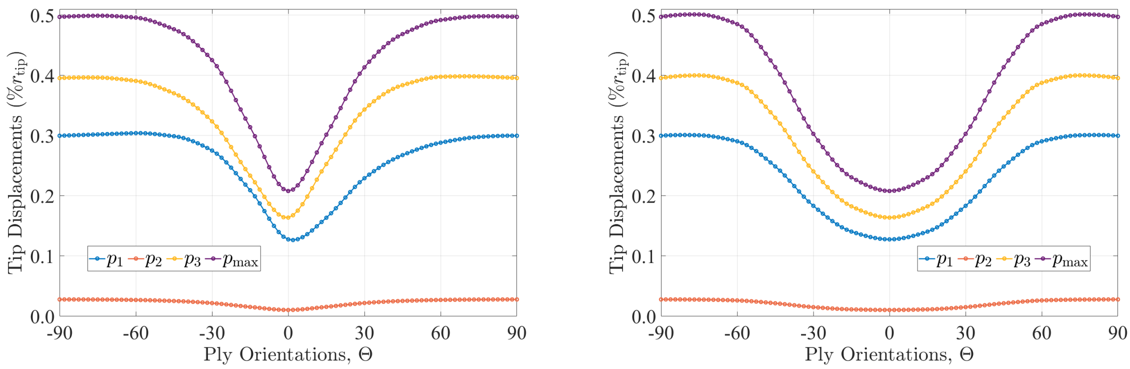

(a) Symmetric-unbalanced laminates ($\Theta_1 = \Theta_2$). **(b)** Symmetric-balanced laminates ($\Theta_1 = -\Theta_2$).

Figure 5.6: Plots of the blade tip displacements obtained from sensitivity studies of the TUD-XPROP-3 when subjected to zero aerodynamic loads ($\Omega = 23$ RPS), $p_{max} = \sqrt{p_1^2 + p_2^2 + p_3^2}$.

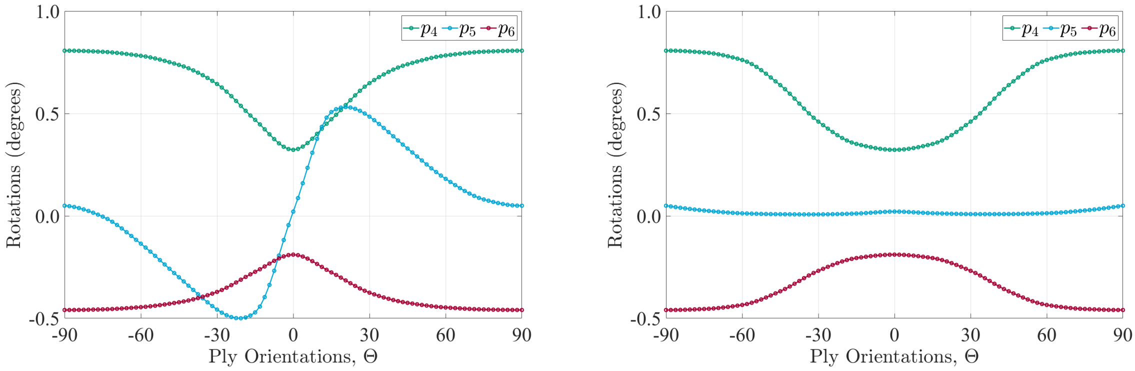

(a) Symmetric-unbalanced laminates ($\Theta_1 = \Theta_2$). **(b)** Symmetric-balanced laminates ($\Theta_1 = -\Theta_2$).

Figure 5.7: Plots of the blade tip rotations obtained from sensitivity studies of the TUD-XPROP-3 when subjected to zero aerodynamic loads ($\Omega = 23$ RPS), $p_{max} = \sqrt{p_1^2 + p_2^2 + p_3^2}$.

In the case where zero aerodynamic loads are present, the only force experienced by the blade acts along its axis, since only the centrifugal loads are present. Large axial and bending deformations are present at 90°, since the fibres are aligned with the chord line in this case, and thus the lowest amount of structural stiffness acts along the axial direction to resist the applied load. Conversely, when the ply orientations are all set to 0°, the fibres are directly aligned with the blade axis, and thus the greatest amount of stiffness acts in the axial direction, which directly opposes the applied load. Thus, the axial and bending deformations are minimal when $\Theta = 0°$. The general trends in displacements and rotations are different between the two laminate types under consideration, due to the presence of extension-shear and bend-twist coupling. Finally, the axial deformations, p_2, are minimal in all cases under consideration, as the blade is highly resistant to deformations along this axis due to its construction.

For symmetric-balanced laminates, the amount of bend-twist coupling is small at all ply orientations considered (with zero bend-twist coupling being present at $\Theta \in \{0°, 90°\}$), and there is always zero extension-shear coupling. As a result of this minimal amount of coupling, it is unsurprising that the rotations about the y-axis are small. The small amount of bend-twist coupling that is present prevents rotations about the y-axis from being exactly zero, as bending deformations always appear to be present. The amount of twist deformations present for symmetric-balanced laminates is still nevertheless small enough to be disregarded. Bending deformations, p_1 and p_3, appear to always be within the same order of magnitude for the two types of laminates under consideration, although it appears that the symmetric-balanced laminates appear to yield less bending deformations over a broader range of ply orientations centred around zero degrees in comparison to the symmetric-unbalanced laminates. For symmetric-balanced laminates, bending deformations are smaller due to their lack of extension-shear coupling, which leaves only the geometry to influence most of the shear deformations.

Plots of the rotations are more interesting in comparison to plots of the translations, as there is a clear discrepancy in the rotations obtained about the y-axis between the two considered laminate types. The symmetric-unbalanced laminates show a clear trend in twist deformations due to the strong presence of bend-twist and extension-shear coupling. In particular, the extension-shear coupling causes the blade to experience more shear deformations when subjected to an axial load. This increase in shear deformations causes the blade to encounter more bending deformations, which then result in twist deformations due to the presence of bend-twist coupling. The ply orientations corresponding to a maximum twist deformation are approximately the angles corresponding to the most substantial amount of performance variations found in Section 5.1.2 (with approximately $\Theta \in \{-20°, +20°\}$), and these angles appear to also yield maximum extension-shear and bend-twist coupling according to Figure D.9. Upward bending and shear deformations naturally yield leading-edge-down pitch deformations for negative ply angles, and vice versa for positive ply angles. Finally, with significantly less extension-shear and bend-twist coupling, the symmetric-balanced laminates conversely encounter a negligible amount of twist deformations.

VARIATIONS IN A SINGLE VARIABLE: BALANCED VS. UNBALANCED LAMINATES

The first set of deformation results presented with aerodynamic loads included concerns the plots of twist deformations around the y-axis, shown in Figure 5.8 as a function of both the advance ratio and thrust coefficient. These results are most interesting because they precisely indicate the presence and type of bend-twist coupling, as the aerodynamic loads that the blade is subjected to provide a relatively small pitching moment contribution when no coupling is present. These results may also be used to show the pitch deformation tendencies of the blade in the absence of any coupling.

For symmetric-unbalanced laminates, the significant differences in pitch deformations are primarily caused by the presence of extension-shear and bend-twist coupling. This is indicated by the significant differences observed between symmetric-balanced and symmetric-unbalanced laminates. The negative slope of pitch angle deformations with increasing advance ratio for symmetric-unbalanced laminates with positive ply orientations shown in Figure 5.8a and Figure 5.8a indicate a positive bend-twist coupling, where upward bending deformations (positive x- and z-displacements, as well as positive x- and negative z-rotations) of the blade will yield leading-edge-up pitch rotations (positive rotations about the y-axis). This is consistent with the results shown in Figure 5.1a and Figure 5.2a, which indicated positive ply orientations to yield more thrust and power at a constant advance ratio in comparison to negative ply orientations of the same absolute angle value. For laminates with negative ply orientations, the opposite type of coupling exists, as indicated by the positive slope with respect to advance ratio, and upward bending of the blade results in a node-down pitch deformation. For laminates with ply orientations of equivalent values and opposite signs, the positive ply orientations have a slope with a slightly greater magnitude in comparison to the negative ply orientations because the pitching moment due to aerodynamic forces tends to increase in the leading-edge-up direction with increasing thrust. Thus, using positive ply orientations yields a similar structural response to the forward-swept blade that was studied by Sodja *et al.* [3], whereas negative ply orientations yield a similar structural response to the backward-swept blade that was investigated by Sodja *et al.* [3]. Lastly, the most significant amount of coupling was found at ply orientations near 15° and 30°. This is unsurprising, as the largest variations in performance were identified near these angles in Figure 5.1a, Figure 5.2a, Figure 5.4, and Figure 5.5 from Section 5.1.2.

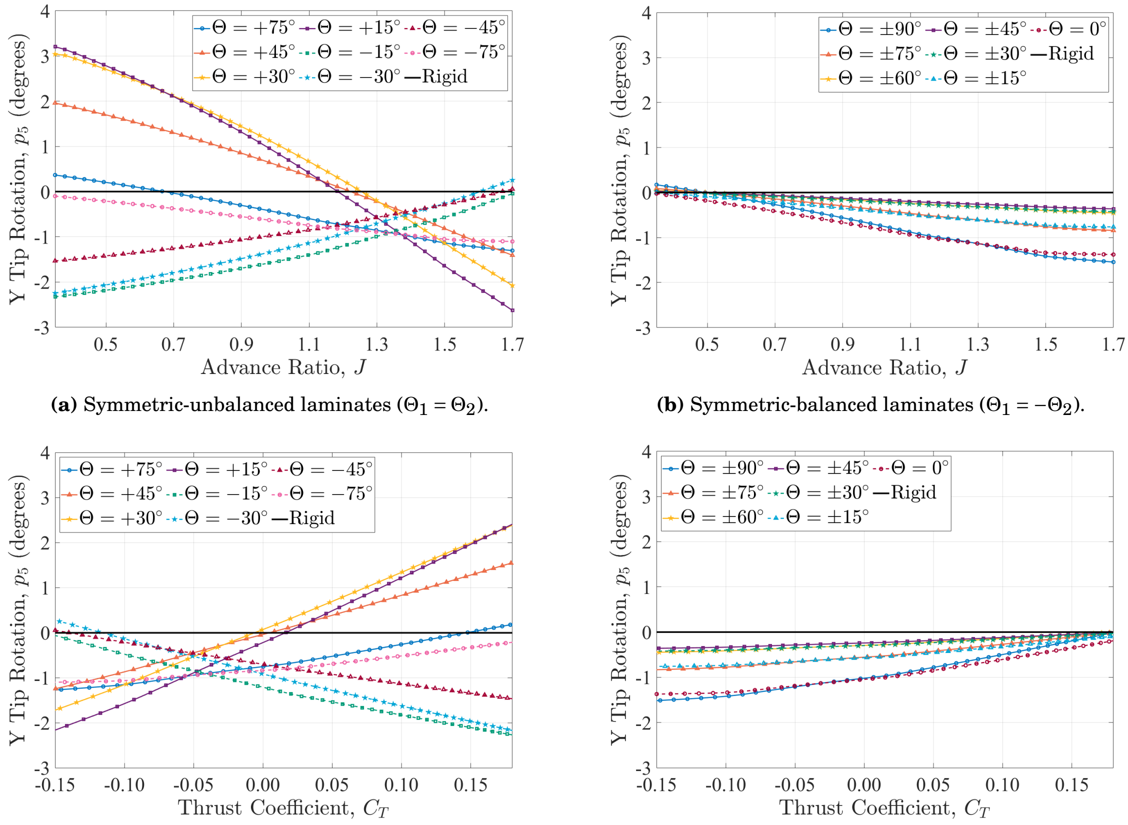

(a) Symmetric-unbalanced laminates ($\Theta_1 = \Theta_2$).

(b) Symmetric-balanced laminates ($\Theta_1 = -\Theta_2$).

(c) Symmetric-unbalanced laminates ($\Theta_1 = \Theta_2$).

(d) Symmetric-balanced laminates ($\Theta_1 = -\Theta_2$).

Figure 5.8: Blade tip torsional deformation plots obtained from sensitivity studies.

For symmetric-balanced laminates, Figure 5.8b and Figure 5.8d indicate that the propeller blade structure encounters an aerodynamic wash-in effect with increasing thrust. This is expected since the blade does not have any sweep and lean, and the aerodynamic forces generate a pitching moment that increases in the leading-edge-up direction as the thrust increases because the structural axis is aft of the quarter-chord line. As shown in Figure D.9, the point of maximum torsional stiffness corresponds to ply orientations of ±45°. As the laminates become more closely aligned, the torsional stiffness decreases, and thus the magnitude of torsional deformations increases as ply orientations approach 0° and 90°. As already mentioned, the torsional stiffness is equivalent for laminates with ply orientations of 0° and ±90°, ±15° and ±75°, and ±30° and ±60°, although the smaller angles in each pair have more stiffness in bending and thus have a slightly decreased slope in comparison to their counterparts.

The remaining figures contain plots of bending deformations and tip displacements that were obtained with aerodynamic loads included. Figure 5.9 and Figure 5.10 respectively contain plots of the blade tip shear displacements and bending rotations with either symmetric-balanced or symmetric-unbalanced laminates. Lastly, the net tip displacements are shown in Figure 5.11.

The bending and shear deformation plots follow analogous trends because bending deformations are driven by shear deformations and vice versa. The discussion concerning bending and shear deformations has thus been combined. With minimal extension-shear and bend-twist coupling for symmetric-balanced laminates, magnitudes of deformations shown in Figure 5.9b, Figure 5.9d, Figure 5.10b, and Figure 5.10d appear to be primarily affected by the changing stiffness contributions as the ply orientations change, and aligning laminates with the blade axis will increase the structure's ability to resist axial and transverse loads. Accordingly, laminates with $\Theta = 90°$ appear to yield the largest deformations because the majority of the plies are aligned with the chord line of the blade and thus the stiffness in response to axial and transverse loads will be the lowest. This is indicated as well in Figure D.8, which shows plots of the stiffness rosettes, as the majority of the stiffness points in the $\hat{e}_2^0$-axis for laminates with most plies that have an orientation of $\Theta = 90°$. The magnitude of deformations also clearly decreases as the laminates become more closely aligned with the structural axis of the blade (i.e. as $\Theta \to 0°$). This may also be explained by the stiffness rosettes shown in Figure D.8, as the direction of maximum stiffness becomes more closely aligned with the blade axis as ply orientations approach 0°.

The changing stiffness with ply orientation appears to play a dominant role in the shear and bending deformation results obtained for symmetric-unbalanced laminates, as Figure 5.9a, Figure 5.9c, Figure 5.10a, and Figure 5.10c indicate that the magnitude of deformations increases with ply orientation. Moreover, Figure D.9 indicates that plane-stiffness terms for laminates with angles of either $(+\Theta, +\Theta)$ or $(+\Theta, -\Theta)$ are equivalent, and thus differences in the deformations of symmetric-balanced and symmetric-unbalanced laminates are driven by the extension-shear and bend-twist coupling. In particular, the presence of bend-twist and extension-shear coupling causes positive ply orientations to experience a higher loading than negative ply orientations of the same angle value. As a consequence, positive ply orientations yield larger deformations at fixed operating conditions in comparison to their negative counterparts.

The main conclusions from the bending and shear deformations plots shown in Figure 5.9 and Figure 5.10 are that the stiffness increases as the ply orientations become more closely aligned with the blade axis, and because the loading is negligibly affected by the ply orientation for symmetric-balanced laminates, the change in deformations is equivalent for laminates with orientations of either $(+\Theta, -\Theta)$ or $(-\Theta, +\Theta)$. This trend still exists for symmetric-unbalanced laminates, as the plane stiffness increases equivalently as $\Theta \to 0^\circ_+$ or $\Theta \to 0^\circ_-$. The presence of bend-twist coupling affects the amount of loading that the blade experiences, and thus unbalanced laminates with positive ply orientations will encounter larger deformations than laminates with negative ply orientations of the same angle.

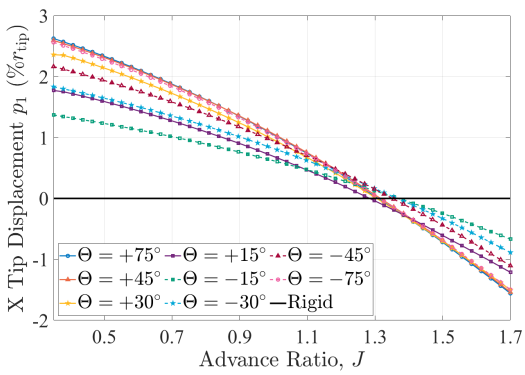

(a) Displacements along the x-axis (symmetric-unbalanced).

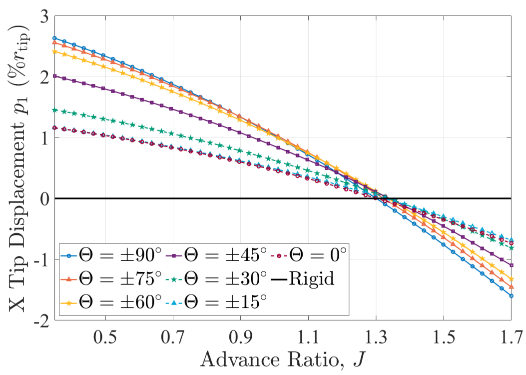

(b) Displacements along the x-axis (symmetric-balanced).

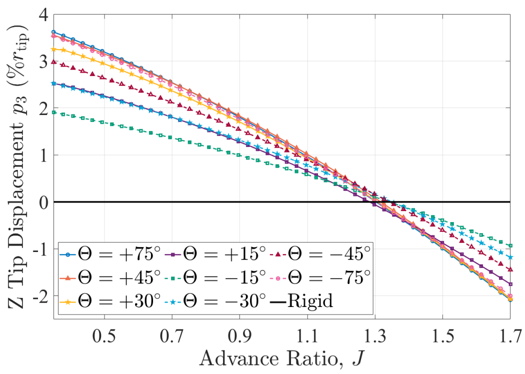

(c) Displacements along the z-axis (symmetric-unbalanced).

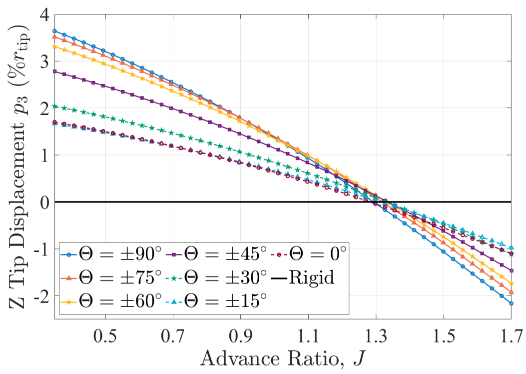

(d) Displacements along the z-axis (symmetric-balanced).

Figure 5.9: Blade tip shear deformation plots obtained from sensitivity studies.

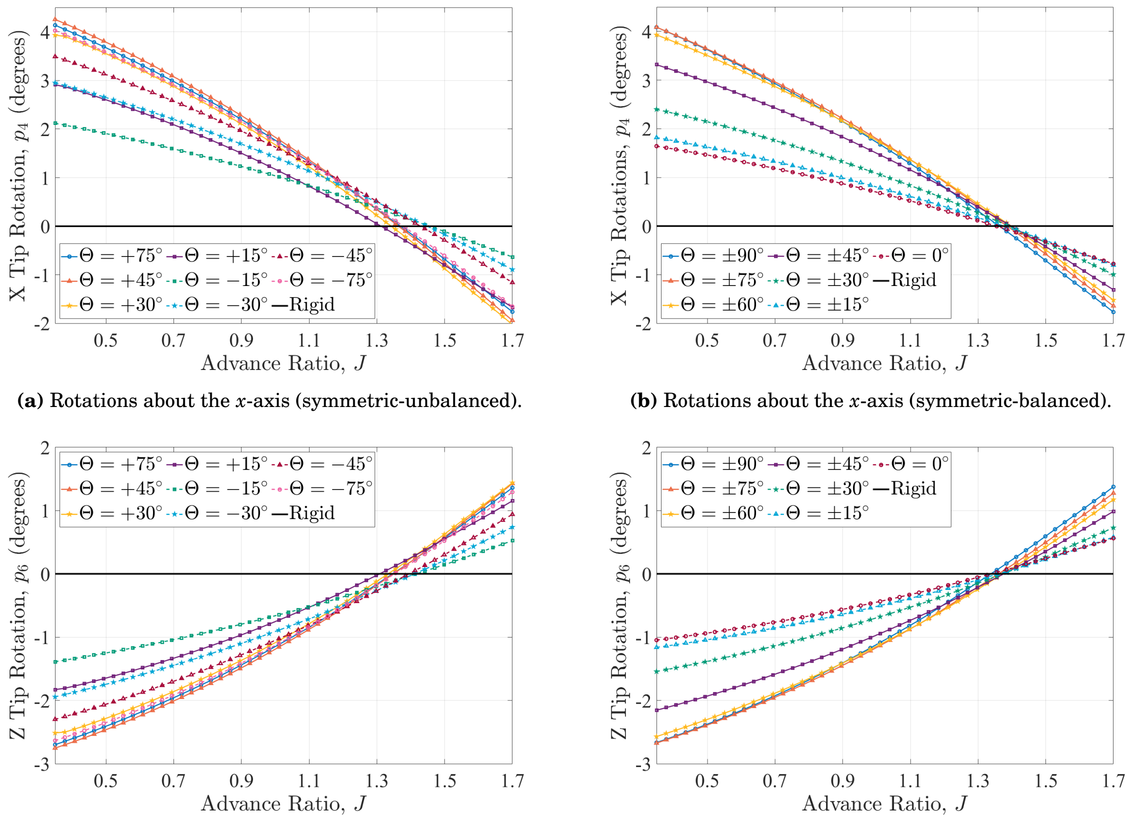

(a) Rotations about the x-axis (symmetric-unbalanced).

(b) Rotations about the x-axis (symmetric-balanced).

(c) Rotations about the z-axis (symmetric-unbalanced).

(d) Rotations about the z-axis (symmetric-balanced).

Figure 5.10: Blade tip bending deformation plots obtained from sensitivity studies.

Trends in net displacements shown in Figure 5.11a and Figure 5.11b are consistent with the trends shown in Figure 5.9 respectively for both symmetric-unbalanced and symmetric-balanced laminates. This is because displacements along the x- and z-axes always have a considerably larger magnitude in comparison to displacements along the y-axis. Tip displacements along the y-axis have not been plotted for this reason. To reduce the effect of the differences in loading between results at different ply orientations, the net tip displacement been shown as a function of the thrust coefficient in Figure 5.11c for symmetric-unbalanced laminates and in Figure 5.11d for symmetric-balanced laminates.

When plotting the tip displacement as a function of the advance ratio, it is clear that the magnitude decreases as plies become more closely aligned with the blade axis. This is especially clear for the symmetric-balanced laminates, which have minimal extension-shear and bend-twist coupling, although the trend in maximum displacement is still apparent for symmetric-unbalanced laminates despite being less clear due to the presence of bend-twist coupling. These trends have also been observed in Figure 5.9 and Figure 5.10, and their physical explanation is the same as provided in the discussion on these results.

In the plots of tip displacement vs. thrust, the more consistent loading makes it somewhat easier to observe the trend in magnitude with changing ply orientation. This is especially true for symmetric-balanced laminates, where it has been shown in Figure 5.2b that the power coefficient is quite similar between each ply orientation for a constant thrust coefficient (especially in propulsive conditions), indicating a similar amount of loading at each constant thrust coefficient. For symmetric-unbalanced laminates, Figure 5.2a indicated a much larger difference in power coefficient for a constant thrust coefficient (especially in propulsive conditions), suggesting more considerable differences in the amount of loading encountered for symmetric-unbalanced laminates of differing ply orientations. Lastly, the displacement magnitude appears to vary linearly with thrust coefficient for both laminate types considered.

The deformations of positive ply orientations being notably more sensitive to changes in performance in comparison to negative ply orientations of the same angle value causes the point of minimum tip displacement to be different for different ply orientations. In particular, the advance ratio and thrust coefficient of minimal tip displacements are both approximately coincident for all symmetric-balanced laminates considered, whereas the symmetric-unbalanced laminates with positive ply orientations reach minimal deformations at lower advance ratios and higher thrust coefficient values in comparison to the negative ply orientations. This is because positive ply orientations have an aerodynamic wash-in effect, whereas negative ply orientations have a negative wash-out effect. Indeed, the local minima are spread symmetrically, with the lowest advance ratio (and highest thrust) occurring for the ply orientation of $+15°$, and the highest advance ratio (and lowest thrust) occurring for the ply orientation of $-15°$. The difference in sensitivity is strongest between ply orientations of $-15°$ and $+15°$, and it is least apparent between ply orientations of $-75°$ and $+75°$. This is consistent with the fact that the most amount of bend-twist coupling was found for symmetric-unbalanced laminates with lower ply orientations near $15°$, and the least amount of coupling being present at higher ply orientations towards $90°$. Differences in slope for tip displacement plots of symmetric-balanced laminates are purely affected by the changing stiffness properties, as the points of minimum tip displacement (when plotted against both thrust and advance ratio) are approximately coincident for all ply orientations considered.

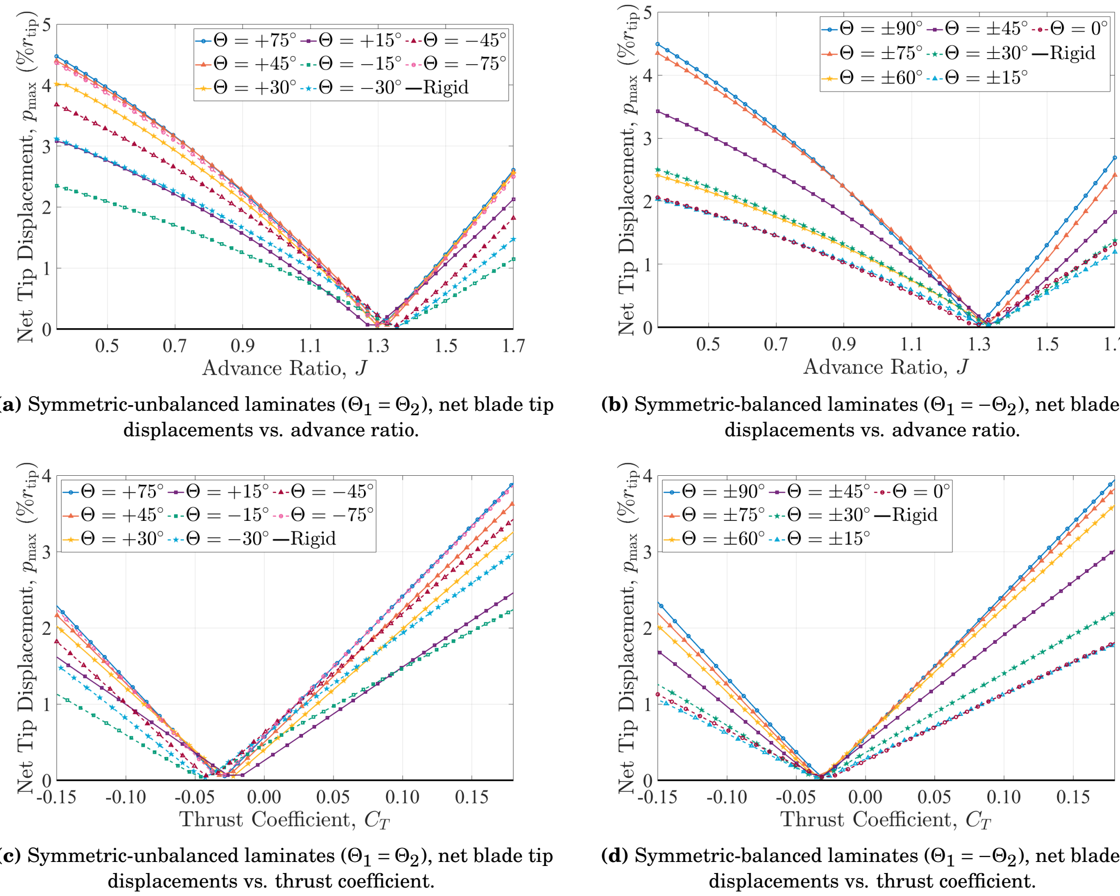

(a) Symmetric-unbalanced laminates ($\Theta_1 = \Theta_2$), net blade tip displacements vs. advance ratio.

(b) Symmetric-balanced laminates ($\Theta_1 = -\Theta_2$), net blade tip displacements vs. advance ratio.

(c) Symmetric-unbalanced laminates ($\Theta_1 = \Theta_2$), net blade tip displacements vs. thrust coefficient.

(d) Symmetric-balanced laminates ($\Theta_1 = -\Theta_2$), net blade tip displacements vs. thrust coefficient.

Figure 5.11: Blade tip displacement plots obtained from sensitivity studies, $p_{\max} = \sqrt{p_1^2 + p_2^2 + p_3^2}$.

VARIATIONS IN TWO VARIABLES: NOT INCLUDING AERODYNAMIC LOADS

To further elucidate the trends that were observed concerning the deformations for different laminate types and ply orientations, continuous variations of two ply orientations, Θ_1 and Θ_2 corresponding to Equation (5.1), were performed analogous to the approach that was taken for investigating variations in performance from Section 5.1.2. Like the variations in a single variable that were shown in the previous two sections, plots of deformations under zero aerodynamic loads are first presented in Figure 5.12.

Figure 5.12a confirms the plot shown in Figure 5.6, as the tip displacement appears to decrease as ply orientations become more closely aligned with the blade axis, with minimal tip displacements corresponding to the laminate with most plies having an angle of $0°$. The plot of torsional deformations shown in Figure 5.12b indicates trends of ply orientations corresponding to maximum extension-shear and bend-twist coupling, which match the general trends shown in Figure 5.4 and Figure 5.14. As seen in other results, the ply orientations of maximum coupling are approximately −20° and +20°. This also confirms the trend shown in Figure 5.7, which showed significant torsional deformations for symmetric-unbalanced laminates and minimal torsional deformations for symmetric-balanced laminates, indicating a strong dependency on the presence of extension-shear and bend-twist coupling.

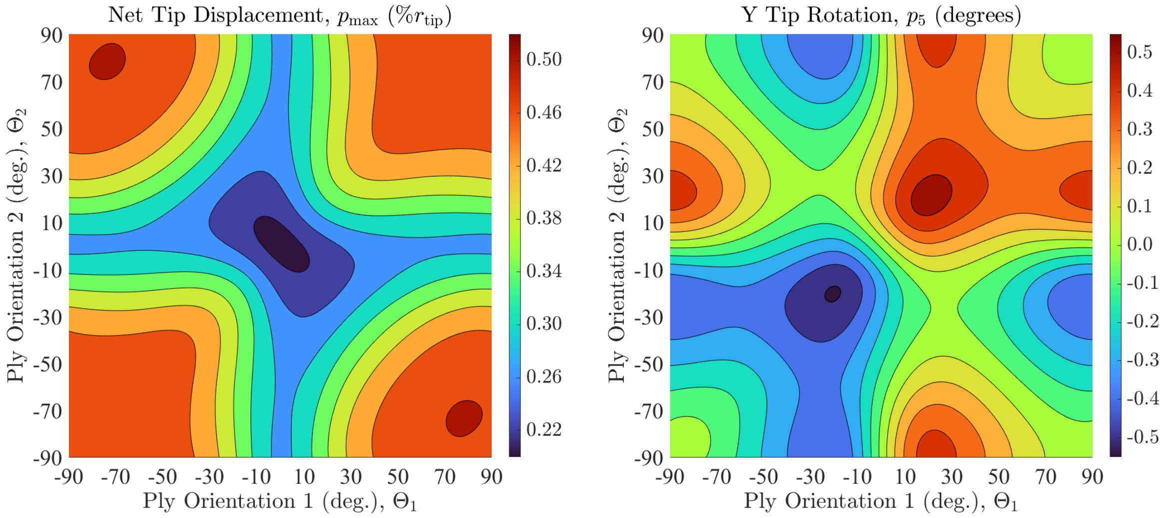

(a) Net blade tip displacement.

(b) Blade tip torsional deformation.

Figure 5.12: Net displacements and torsional deformations of the blade tip under zero aerodynamic loads.

VARIATIONS IN TWO VARIABLES: INCLUDING AERODYNAMIC LOADS

Deformations results presented with aerodynamic loads present are provided in this section. Tip displacements are shown in Figure 5.13 and torsional deformations are shown in Figure 5.14. At one operating condition each for the propulsive case and the regenerative case.

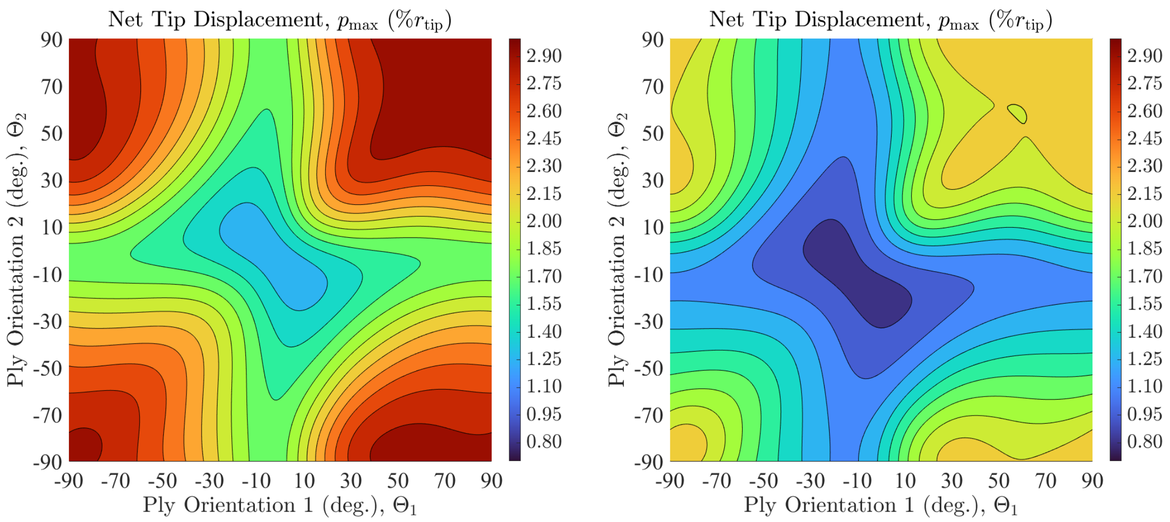

(a) Propulsive conditions ($J = 0.75$).

(b) Regenerative conditions ($J = 1.60$).

Figure 5.13: Net blade tip displacement plots obtained from 2D sensitivity studies.

The trend in pitch deformations that are shown in Figure 5.14 appear to match the trends in thrust and power coefficient variations that are shown in Figure 5.4, unlike the trend in tip displacements that shown in Figure 5.13. In particular, the tip displacement of the blade reaches a maximum for plies of 90°, which have the least amount of stiffness under the loads encountered by the blade. The tip displacement accordingly decreases as plies become aligned with the blade axis. Moreover, the presence of bend-twist and extension-shear coupling appears to provide a small influence on the tip displacement, as the majority of displacements are caused directly by the transverse and centrifugal forces that the blade encounters. Thus, like the case with zero aerodynamic loads, tip displacements are driven by the stiffness of the laminate, whereas pitch deformations are governed almost entirely by the presence of bend-twist or extension-shear coupling. This suggests that coupling may be used to enhance the blade's performance without significantly altering its maximum tip displacements. This is also why the trends shown in Figure 5.13 and Figure 5.14 respectively match the trends shown in Figure 5.12a and Figure 5.12b.

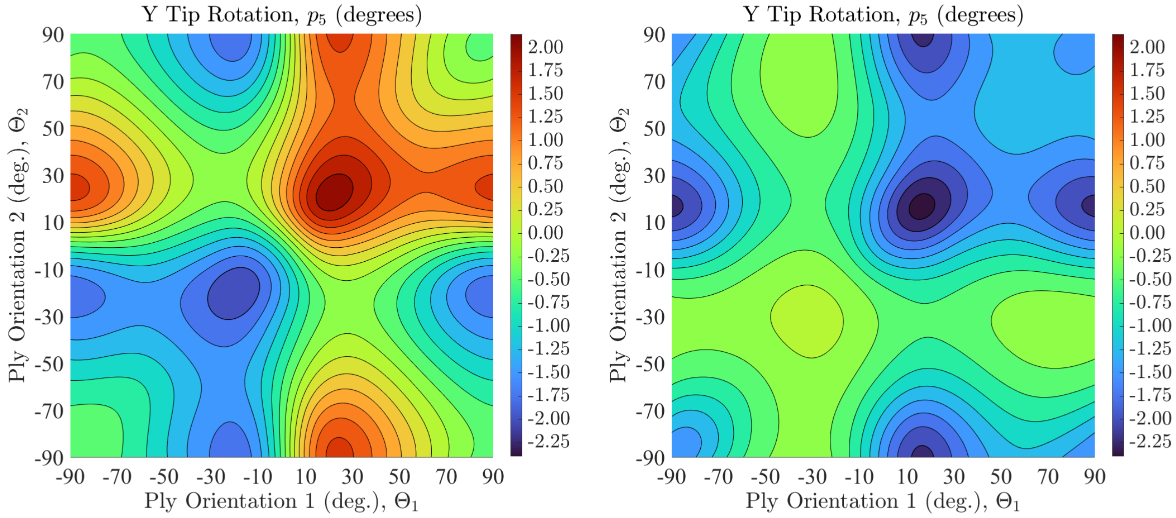

(a) Propulsive conditions ($J = 0.75$).

(b) Regenerative conditions ($J = 1.60$).

Figure 5.14: Blade tip torsional deformation plots obtained from 2D sensitivity studies.

5.1.4. SUMMARY OF RESULTS FROM PLY ORIENTATION VARIATIONS

Conclusions that were drawn from the variations in ply orientation are summarized below.

- Flexible blades constructed out of symmetric-unbalanced laminates were shown to yield substantial variations in thrust and power when compared to the rigid (baseline) blade due to the strong presence of bend-twist and extension-shear coupling, whereas all flexible blades constructed out of symmetric-balanced laminates yielded small variations in performance when compared to the rigid propeller due to their lack of extension-shear coupling and their negligible amounts of bend-twist coupling. As a result of the strong dependence on bend-twist and extension-shear coupling, trends in pitch deformations matched the trends in thrust and power variations. This is expected because pitch angle deformations drive changes in angle of attack at fixed operating conditions.

- Symmetric-unbalanced laminates with negative ply orientations yield an aerodynamic wash-out effect with increasing thrust. Hence, upward displacements (positive along x- and z-axes) yield a leading-edge-down pitch rotation and downward displacements yield a leading-edge-up pitch rotation. Symmetric-unbalanced laminates with positive ply orientations were instead found to yield an aerodynamic wash-in effect. This suggests that using positive ply orientations results in a similar structural response to the forward-swept blade that was studied by Sodja *et al.* [3], whereas negative ply orientations yield a similar structural response to the backward-swept blade that was investigated by Sodja *et al.* [3].
  - As expected, laminates yielding a decrease in thrust at fixed operating conditions will yield a decrease in power, whereas laminates yielding an increase in thrust will yield an increase in power.
  - The presence of an aerodynamic wash-out effect accordingly results in a decrease in power consumption during propulsive mode and an increase in power recovered during regenerative mode.

- For a constant thrust, symmetric-unbalanced laminates with negative ply orientations were found to reduce the amount of power consumption through a decrease in the amount of loading, whereas symmetric-unbalanced laminates with positive ply orientations were found to increase the amount of power consumption through an increase in loading. A negligible change in power consumption was naturally observed for symmetric-balanced laminates.

- Larger variations in power consumption were observed during propulsive mode in comparison to the variations in power recovery observed during regenerative mode for an equivalent amount of thrust. Because the amount of negative thrust that the propeller will generate during regenerative conditions will always be significantly below the amount of positive thrust that the propeller produces during propulsive mode, variations in performance obtained during propulsive mode will always be significantly greater than the variations in performance observed during regenerative conditions.
- The largest performance improvements were observed for symmetric-unbalanced laminates with ply orientations between $-30°$ and $-15°$ because they feature large amounts of bend-twist coupling and relatively small amounts of stiffness under shear and torsional loads. Despite also having large amounts of bend-twist and extension-shear coupling, ply orientations of $\pm 45°$ have the most stiffness under shear and torsional loads and thus yield smaller pitch deformations in comparison to plies with smaller angle values. The largest performance decreases were observed for symmetric-unbalanced laminates with ply orientations between $15°$ and $30°$ according to same physical reasoning.
- While pitch deformations are almost entirely driven by the presence of extension-shear and bend-twist coupling as well as the amount of stiffness that the laminate has in shear and torsion, bending and shear deformations are almost entirely driven by the amount of stiffness that the blade has along its structural axis. The presence of extension-shear and bend-twist coupling has a smaller effect on bending and shear deformations in comparison. This is because the loads encountered by the blade are mostly axial and transverse, with only a small pitching moment being generated by the aerodynamics.
- Because the stiffness of the blade under bending and transverse loading increases as ply orientations become more closely aligned with the blade axis, bending and shear deformations always decrease as the majority of ply orientations approach $0°$ at fixed operating conditions. Bending and shear deformations will accordingly reach a maximum as the majority of ply orientations approach $90°$.
  - For blades with symmetric-balanced laminates at fixed operating conditions, the magnitudes of shear and bending deformations are almost entirely influenced by how the blade's overall stiffness changes with ply orientation because the amount of loading is approximately independent of ply orientation in this case due to the negligible amount of extension-shear and bend-twist coupling.
  - For blades with symmetric-unbalanced laminates, the magnitudes of shear and bending deformations are equivalently influenced by how the blade's overall stiffness is affected by changes in ply orientation, although there is notably more extension-shear and bend-twist coupling, which has a substantial effect on the amount of loading encountered at fixed operating conditions. Thus, blades with symmetric-unbalanced laminates that have mostly positive ply orientations will yield larger deformations than those with negative ply orientations, due to differences in loading caused by twist deformations.

5.1.5. LAMINATE THICKNESS VARIATIONS

Before beginning the optimization, bounds on the laminate thicknesses must be established to ensure that the optimization problem is defined appropriately. To determine bounds for the laminate thicknesses, a sensitivity study was performed by varying the laminate thickness and evaluating the structural deformations and change in performance. The upper bound was selected at a point of diminishing returns, and the lower bound was selected at the lowest value that the solver converged for, to prevent numerical problems during the optimization procedure. The ply stacking sequence used in this case is defined by Equation (5.2), and $\Theta \in \{-30°, +30°\}$, since these ply orientations were found to yield the largest amount of twist deformations and accordingly also the largest change in performance according to the analysis provided in Section 5.1.2. For variations in laminate thickness, Figure 5.15 contains plots of the change in thrust and power, whereas Figure 5.16 contains plots of the tip displacement and twist deformations.

Figure 5.15 indicates that variations in performance become negligible for laminate thicknesses beyond 20 millimetres, although differences in performance between the flexible and rigid propeller are already small for laminate thicknesses around 10 millimetres. Nevertheless, because the blade structure is being defined with only one laminate each on its upper and lower surfaces, the maximum laminate thickness is limited by the thinnest point of the blade structure. Thus, the upper bound of the laminate thickness was instead set to a value of 1.75 millimetres during the optimization. The minimum laminate thickness was set to a value of 0.50 millimetres, as the solver never encountered convergence problems for thicknesses greater than this value. A laminate thickness of 0.50 millimetres will also consist of approximately ten plies, which already restricts the feasibility of a given set of lamination parameters. Nevertheless, the selected upper and lower bounds for thicknesses still provide a sufficient level of design freedom. This study lastly shows that aeroelastic effects will always be non-negligible during the optimization.

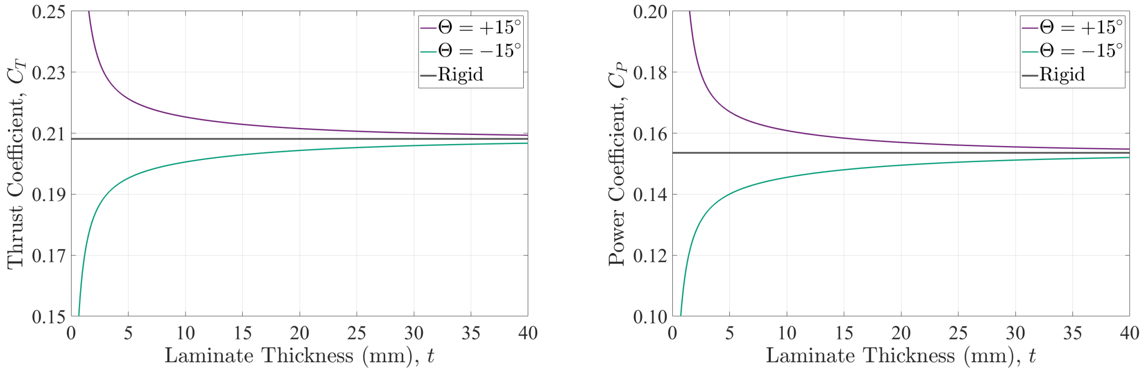

(a) Thrust Coefficient. **(b)** Power Coefficient.

Figure 5.15: Plots of thrust and power coefficients as a function of laminate thickness for ply orientations with approximately maximum bend-twist coupling.

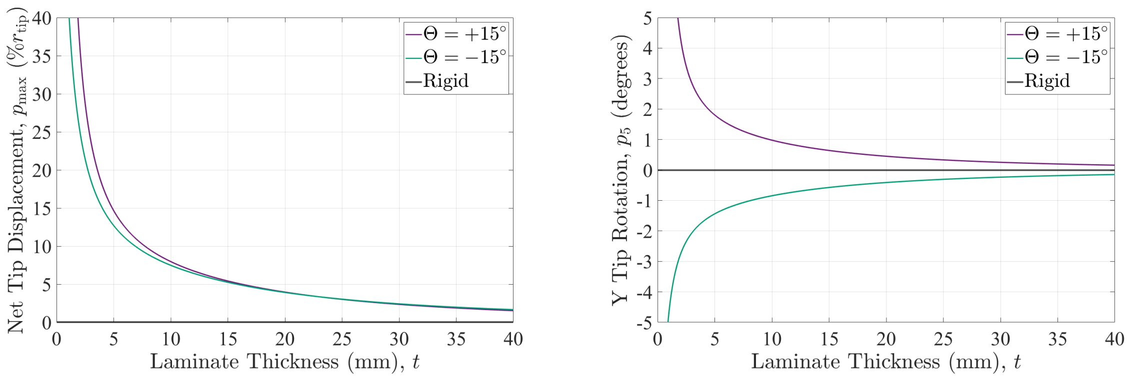

(a) Net tip displacements. **(b)** Torsional Deformations.

Figure 5.16: Plots of torsional deformations and tip displacements as a function of laminate thickness for ply orientations with approximately maximum bend-twist coupling.

5.2. Optimization Results

The ideal operating conditions and best performance metrics of the rigid propeller were first calculated to determine the baseline energy consumption values to consider during the flexible propeller optimization. Results for the best pitch settings, maximum efficiency, minimum energy consumption, and peak efficiency are shown in Section 5.2.1. Results obtained from the flexible propeller optimization study, including performance trends, ideal operating conditions, and stiffness rosettes, are shown in Section 5.2.2.

5.2.1. Rigid (Baseline) Propeller Results

The baseline propeller performance used during the optimization has been defined as the performance of the rigid propeller at its best pitch setting for each case that is under consideration. For variable pitch propellers, this best pitch setting was found through an evaluation of the efficiency as a function of the pitch setting in each mission segment (for a constant T_C). The pitch settings yielding maximum efficiency in each segment were selected for all optimization studies involving the variable-pitch propeller. For the constant-pitch propeller, the total energy consumption over the entire mission was evaluated at each pitch setting, for a variable cruise length. For each optimization study involving constant-pitch propellers, the pitch setting that was found to minimize the overall energy consumption was selected.

Figure 5.17a contains plots of the efficiency as a function of the pitch setting in climb, cruise, and descent. The annotations correspond to the pitch settings that yielded peak efficiency. These pitch settings were used to define the baseline performance of the variable-pitch propeller for all cases of the optimization, as well as the baseline performance of the constant-pitch propeller during optimization studies involving only a single mission segment. For the constant-pitch propeller, Figure 5.17b contains plots of the best pitch setting as a function of the cruise distance. Horizontal lines indicating the best pitch settings in climb, cruise, and descent have been shown for reference. As expected, the best pitch setting of the constant-pitch propeller approaches the best pitch setting for only the cruise segment as the cruise distance increases. Because the climb and descent are of approximately equal length, when the cruise distance is zero, the best pitch setting is approximately in between the best climb and descent pitch settings.

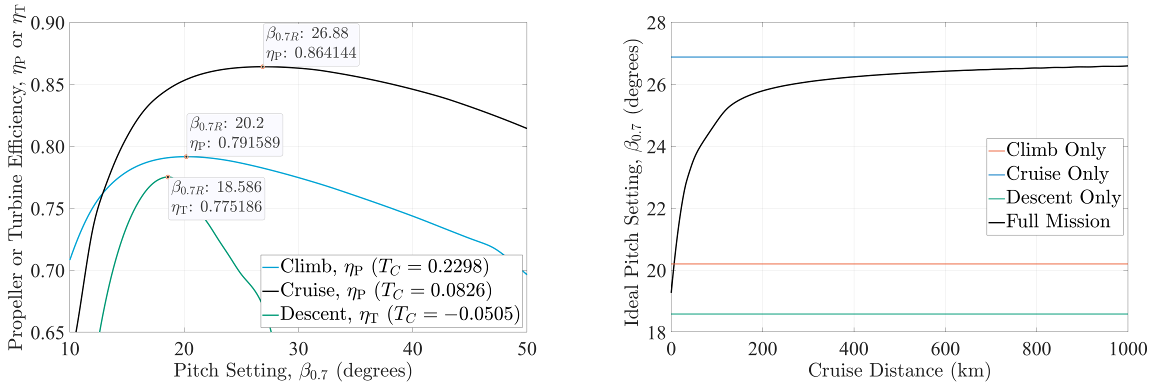

(a) Plots of the efficiency vs. pitch setting for climb, cruise, and descent segments, used to inform the selection of ideal rigid blade pitch settings for the variable-pitch propeller optimization.

(b) Plots of the best pitch setting vs. cruise distance for the constant-pitch propeller, used to select ideal rigid blade pitch settings for the constant-pitch propeller optimization.

Figure 5.17: Plots indicating the best pitch settings for both the variable- and constant-pitch propellers corresponding to individual mission segments as well as the full mission with a varying cruise distance.

Figure 5.18 contains plots comparing the total mission energy for a varying cruise distance. Values for the energy consumption of the constant- and variable-pitch propellers are always within 1% of each other because the ideal pitch settings between the three operating conditions under consideration are very close to each other, and the efficiency in climb and cruise change by a small amount within the range of pitch settings corresponding to the constant-pitch propeller as the cruise distance increases. This is indicated in Figure 5.17. The difference between the minimum energy consumption of the constant- and variable-pitch propellers accordingly decreases as the cruise distance increases because the climb and descent segments constitute a decreasing proportion of the total energy consumption with increasing cruise distance.

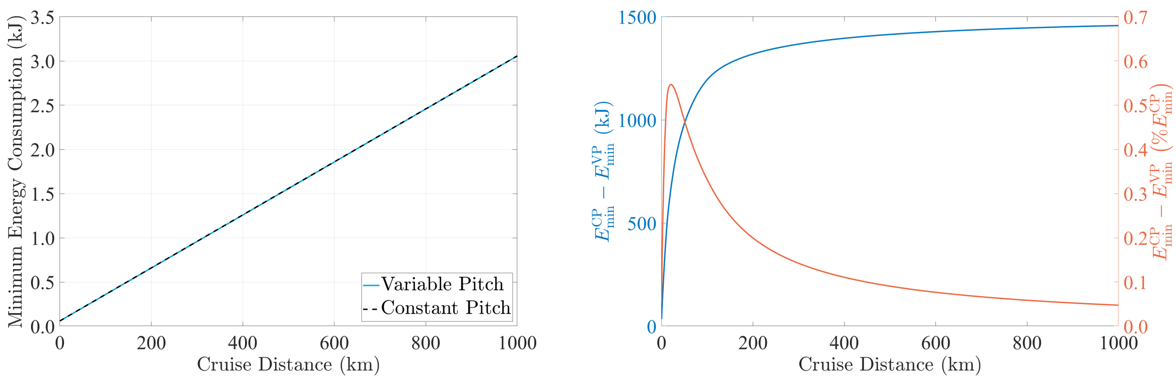

(a) Minimum energy consumption vs. cruise distance for the variable- and constant-pitch propellers.

(b) The difference in minimum energy consumption between variable- and constant-pitch propellers vs. cruise distance.

Figure 5.18: Plots used to compare the minimum total energy consumption for the variable- and constant-pitch propellers for varying cruise distances.

5.2.2. FLEXIBLE PROPELLER RESULTS

This section contains results obtained from the flexible propeller optimization studies. First, the most important performance trends, including plots for the efficiency and energy consumption in each mission segment, have been plotted and compared with results for the ideal rigid propeller. The optimized propeller operating conditions (pitch setting and advance ratio values) of each mission segment were subsequently shown in comparison to the ideal rigid propeller operating conditions. These results indicate the ideal on-design performance, improvements, and operating conditions. Stiffness rosettes were additionally shown for the optimized laminate configuration corresponding to each case to indicate the optimal structural design in each case. After presenting results from the optimization studies, performance maps were produced using the optimized flexible propeller blades and compared to results obtained with the ideal rigid propeller. These results indicate how the optimized flexible propellers would perform at off-design conditions. Finally, convergence history plots are shown in Appendix E for all considered cases.

PERFORMANCE TRENDS

Plots of the optimal efficiency for the rigid and flexible propellers are shown in Figure 5.19. Following this, the objective function and inequality constraint values for each propeller configuration have been shown respectively in Figure 5.20 and Figure 5.21 for comparison.

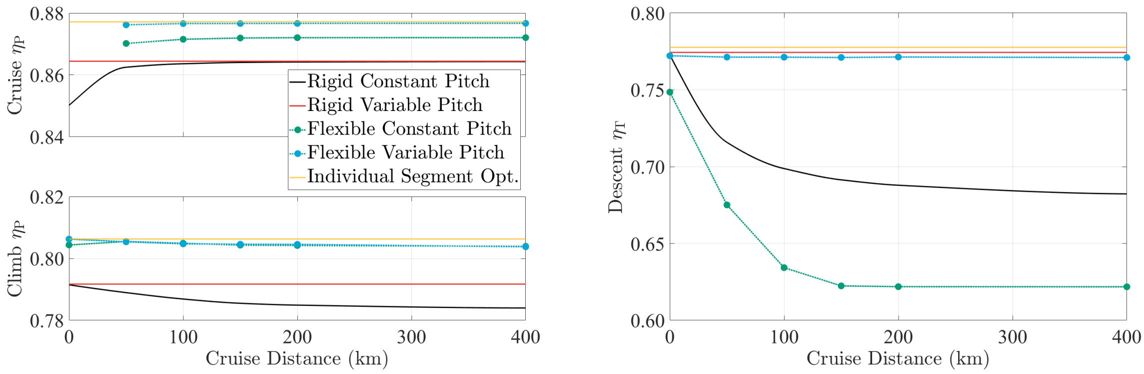

(a) Propeller efficiency (climb and cruise)

(b) Turbine efficiency (descent)

Figure 5.19: Efficiencies corresponding to each optimal propeller configuration in each mission segment.

As expected, optimizing for each segment individually results in the greatest efficiency. It is interesting to observe that the full-mission optimization with a variable-pitch propeller yields efficiency values that are very close to the individual segment optimization results, independently of the cruise distance being considered. This is particularly unsurprising in climb and cruise, where the ideal structural design was shown to be similar in Figure 5.23 and Figure 5.24, and the full-mission optimization yielded similar structural designs to the ideal climb and cruise structure. However, in descent, it was shown that the ideal structural design differs considerably from the ideal structural design for the climb and cruise segments. Nevertheless, the turbine efficiency of the ideal flexible variable-pitch propeller is very close to that of the rigid variable-pitch propeller. This result is consistent with findings from Section 5.1, where it was shown that the change in energy-harvesting performance is considerably less than the change in propulsive performance, and negative ply orientations yielded similar power consumption values in comparison to the rigid blade for a constant thrust setting. This result also makes physical sense, as the blade loading encountered in descent is considerably smaller than the blade loading encountered in propulsive conditions due to the relatively low rotor speeds and freestream velocities that characterize regenerative conditions. Thus, deformations observed in the descent will be considerably smaller than deformations observed in the climb or cruise segments, accordingly leading to a decreased effect of aeroelastic tailoring.

It is clear from Figure 5.19 that the climb performance of the constant-pitch propeller is always very similar to the climb performance of the variable-pitch propeller, although the cruise performance can never be improved. This is because the optimizer must always maintain the thrust requirement in descent, due to the presence of an equality constraint on the thrust coefficient in each mission segment. Thus, the pitch setting of the constant-pitch propeller cannot be increased beyond a value of approximately 29° while still maintaining the desired amount of negative thrust in descent. This is further confirmed through the turbine efficiency results, as the turbine efficiency values of the constant-pitch propeller reach excessively low values, before levelling off beyond a cruise distance of 150 km. If the negative thrust requirement in descent were either reduced in magnitude or removed completely, then the efficiency of the constant-pitch propeller in cruise would approach the efficiency of the variable-pitch propeller as the cruise distance increased, and the climb efficiency of the constant-pitch propeller would decrease as the cruise distance increased. Despite the optimal flexible constant-pitch propeller being forced to remain at a suboptimal pitch setting during the majority of the optimization cases, it maintains a better overall performance than both the rigid constant-pitch and variable-pitch propellers, as indicated by Figure 5.20.

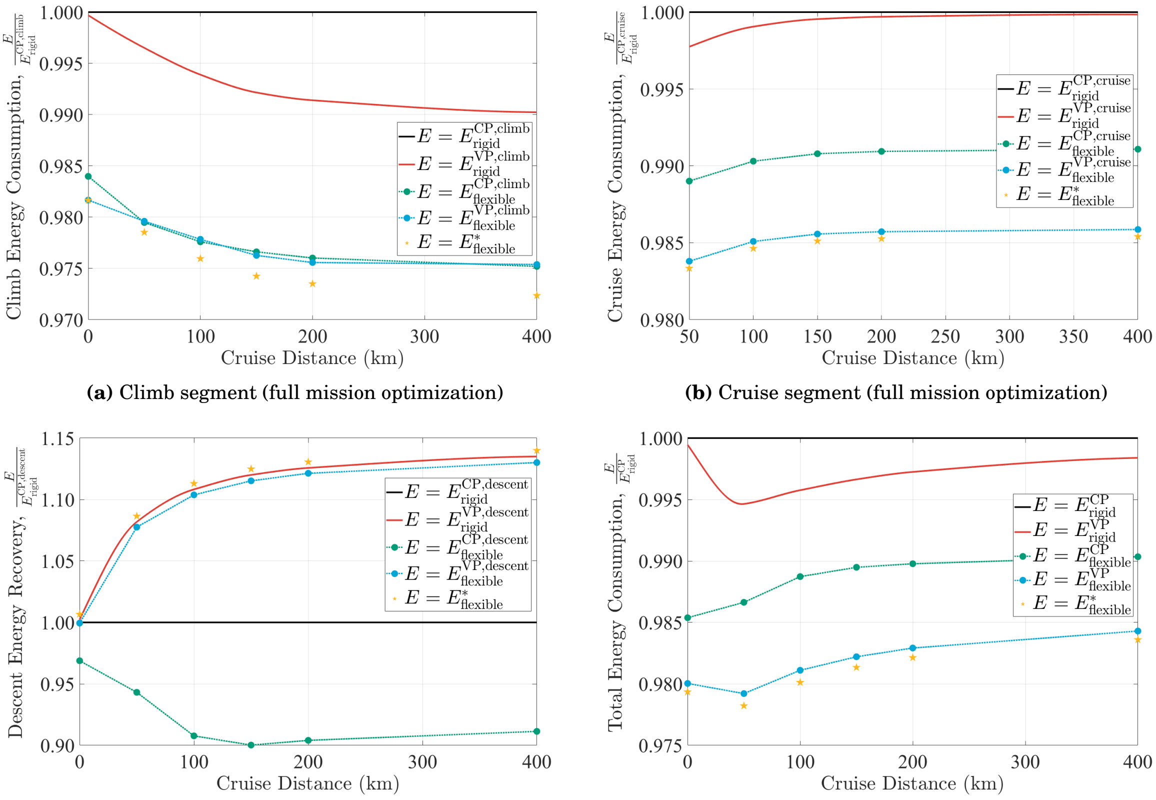

(a) Climb segment (full mission optimization)

(b) Cruise segment (full mission optimization)

(c) Descent segment (full mission optimization)

(d) Total mission (objective function)

Figure 5.20: Mission energy consumption or recovery compared between different optimal propellers.

In Figure 5.20, E^* represents a theoretical maximum improvement that may be achieved through aeroelastic tailoring of propellers. This was computed using the energy consumption of the optimal flexible climb-only propeller in climb, the optimal flexible cruise-only propeller in cruise, and the optimal flexible descent-only propeller in descent. With one structural design alone, it is likely not possible to obtain the decrease in energy consumption (or increase in energy recovered). Therefore, it is useful to observe values for E^* as theoretical upper-limits on the extent that performance may be enhanced through the application of aeroelastic tailoring. It is interesting to observe that the energy consumption or recovery values of the optimal flexible variable-pitch propeller are generally quite close to this upper limit already.

Results for the energy consumption in each individual mission segment follow directly from the efficiency results shown in Figure 5.19. For the total energy consumption, shown in Figure 5.20d, the results appear very promising. It appears that the flexible constant- and variable-pitch propellers always perform better than the rigid constant- and variable-pitch propellers. Due to the somewhat high thrust requirement in descent, the flexible constant-pitch energy consumption never converges towards the flexible variable-pitch energy consumption, and instead appears to maintain an almost constant offset beyond cruise distances of 100 km. It is expected that if the constraint on thrust required during descent were relaxed, then the energy consumption of the flexible constant-pitch propeller would converge toward the energy consumption of the flexible variable-pitch propeller beyond a cruise distance of 50 km. It is likely possible to observe even further enhancements in performance with more design regions or a different flight pattern being considered during the optimization. Nevertheless, when compared with the rigid variable-pitch propeller across all optimization cases that were considered, the energy consumption decrease by 1.5 – 2.0% for flexible variable-pitch propellers and by 0.7 – 1.4% for flexible constant-pitch propellers is already quite substantial. In comparison to the rigid constant-pitch propeller, the decrease in energy consumption is even greater, at approximately 1.5 – 2.0% for flexible variable-pitch propellers and 1.0 – 1.5% for flexible constant-pitch propellers. Moreover, the similar values yielded between the flexible variable-pitch and theoretical maximum performance improvement suggests that it may not be possible to yield significant further decreases in total energy consumption unless more design regions are included.

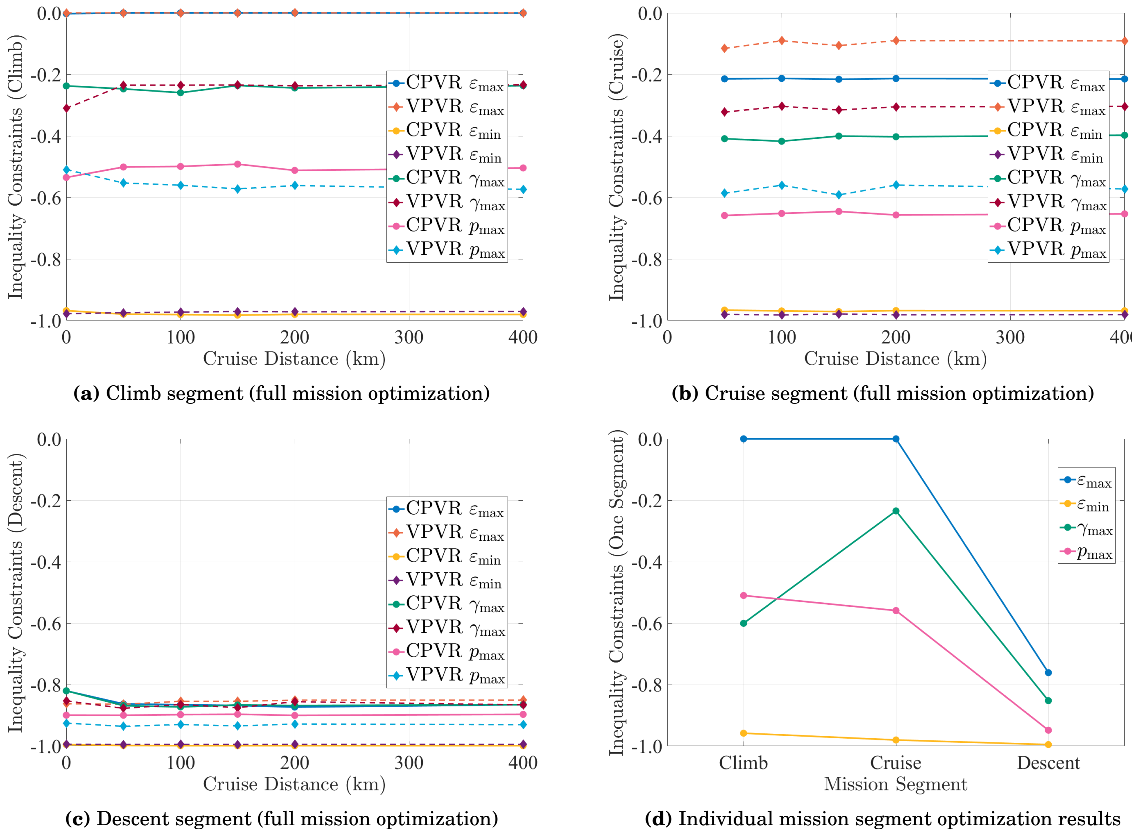

(a) Climb segment (full mission optimization)

(b) Cruise segment (full mission optimization)

(c) Descent segment (full mission optimization)

(d) Individual mission segment optimization results

Figure 5.21: Inequality constraint values obtained during the flexible propeller optimization studies.

Plots of the inequality constraints for the full mission optimization (Figure 5.21a, Figure 5.21b, and Figure 5.21c) are consistent with expectations, as the relative amount of loading that the blade experiences is different in each mission segment. In particular, the loading is greatest in climb due to the thrust requirement being the highest, and thus the strains experienced by the blade are also largest in climb, the loading is slightly reduced during the cruise segment, although it is still quite high, due to the relatively high cruise speed that was chosen for the optimization studies. However, the blade loading is relatively small in descent, and thus the strains and deformations are also small. This is expected, as the descent is characterized by low rotor speeds and a low flight velocity. It is also expected that the optimizer would converge on a blade design that features at least one inequality constraint being active. This suggests that the blade is deforming as much as possible before encountering a structural failure. The critical strain in this case is the maximum tensile strain, which is consistent with expectations, as the blade is primarily loaded under tension through its centrifugal force, which acts along the blade axis, and its transverse aerodynamic force which also places at least one of the surfaces under tension. In this case, the high centrifugal forces negate the compressive load from the aerodynamic forces, resulting in a maximum compressive strain that is close to zero. This confirms the initial assumptions made during this project, and it suggests that the structure has a negligible risk of buckling under the loads being applied.

Operating Conditions

Plots of the propeller advance ratio and pitch setting corresponding to each optimization case are provided in Figure 5.22 for climb, cruise, and descent. Plots of the operating conditions present an important limitation on the applicability of the application of aeroelastic tailoring towards enhancing propeller performance. In particular, the operating conditions associated with optimal propeller performance are considerably different in comparison to the rigid propeller, and generally very difficult to predict, as they depend on blade size, structure, loading, freestream velocity, and rotor speed. The results shown are consistent with initial expectations, motivated by the sensitivity study results from Section 5.1, which suggest that the presence of aerodynamic wash-out yields favourable performance.

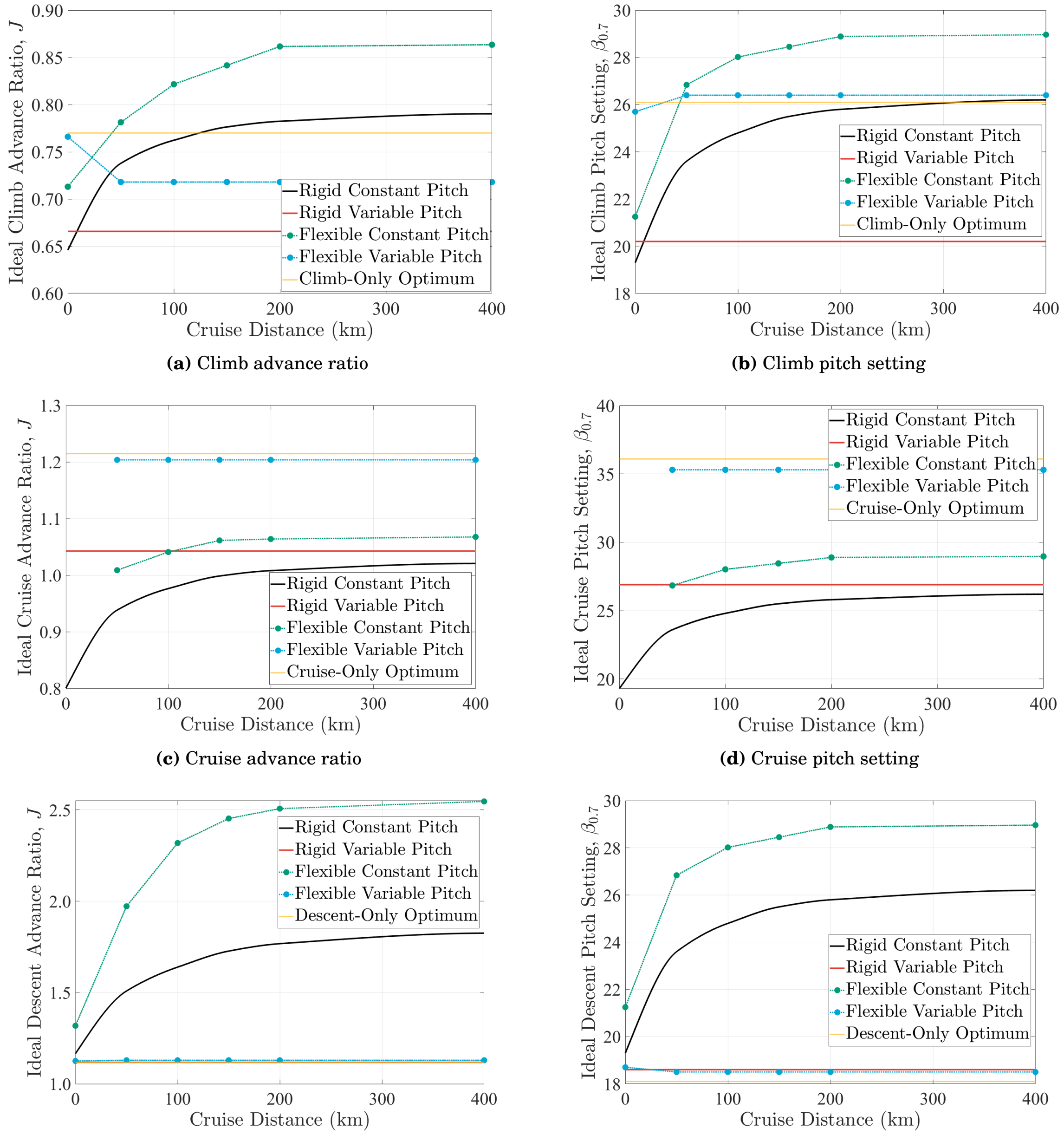

(a) Climb advance ratio

(b) Climb pitch setting

(c) Cruise advance ratio

(d) Cruise pitch setting

(e) Descent advance ratio

(f) Descent pitch setting

Figure 5.22: Operating conditions for rigid and flexible optimal propeller configurations.

The ideal pitch setting of the flexible propeller tends to increase in comparison to that of the rigid propeller in propulsive mode because the optimizer is exploiting the effect of aerodynamic wash-out to enhance performance through the alleviation of loads encountered by the propeller. In descent, an aerodynamic wash-in effect is instead present and exploited by the optimizer, which leads to a lower optimal pitch setting for the flexible decent-only propeller in comparison to the rigid variable-pitch propeller. For descent-only optimization only, the optimizer increases the loading encountered by the blade at a constant thrust, thus yielding a larger amount of recovered power. Lastly, the optimizer always prioritizes the climb and cruise segments over the descent segment when optimizing for the full mission, and thus the optimal pitch setting of the flexible constant-pitch propeller is always greater than that of the rigid constant-pitch propeller, as downward deformations will yield leading-edge-down pitch deformations due to the presence of an aerodynamic wash-out effect. This occurs because the effect of aeroelastic tailoring is small in the descent compared to the climb and cruise, particularly due to the decreased loading in descent. The minimal effect of aeroelastic tailoring in descent is also indicated by the small difference in descent operating conditions for the rigid variable-pitch propeller in comparison to the optimal flexible variable-pitch and descent-only propellers. Advance ratio trends follow from the pitch setting trends. As the pitch setting increases, the advance ratio must increase to maintain the same thrust.

OPTIMAL BLADE STIFFNESS DISTRIBUTIONS

Stiffness rosettes obtained for the blade upper surface are shown in Figure 5.23, whereas the stiffness rosettes obtained for the blade lower surface are shown in Figure 5.24. For each design study, the optimizer adjusted the thicknesses of the upper and lower surface laminates until the strains reached an acceptable level. Plots of the laminate thicknesses have been omitted from this section for brevity, although they may be inferred from the plots shown in Appendix E. Stiffness orientations are defined relative to the spanwise axis of the blade, positive toward the trailing edge on both the upper and lower surface laminates. Thus, a principal stiffness axis with an angle of 90° will point directly towards the leading edge and a principal stiffness axis with an angle of 0° will point directly towards the blade tip.

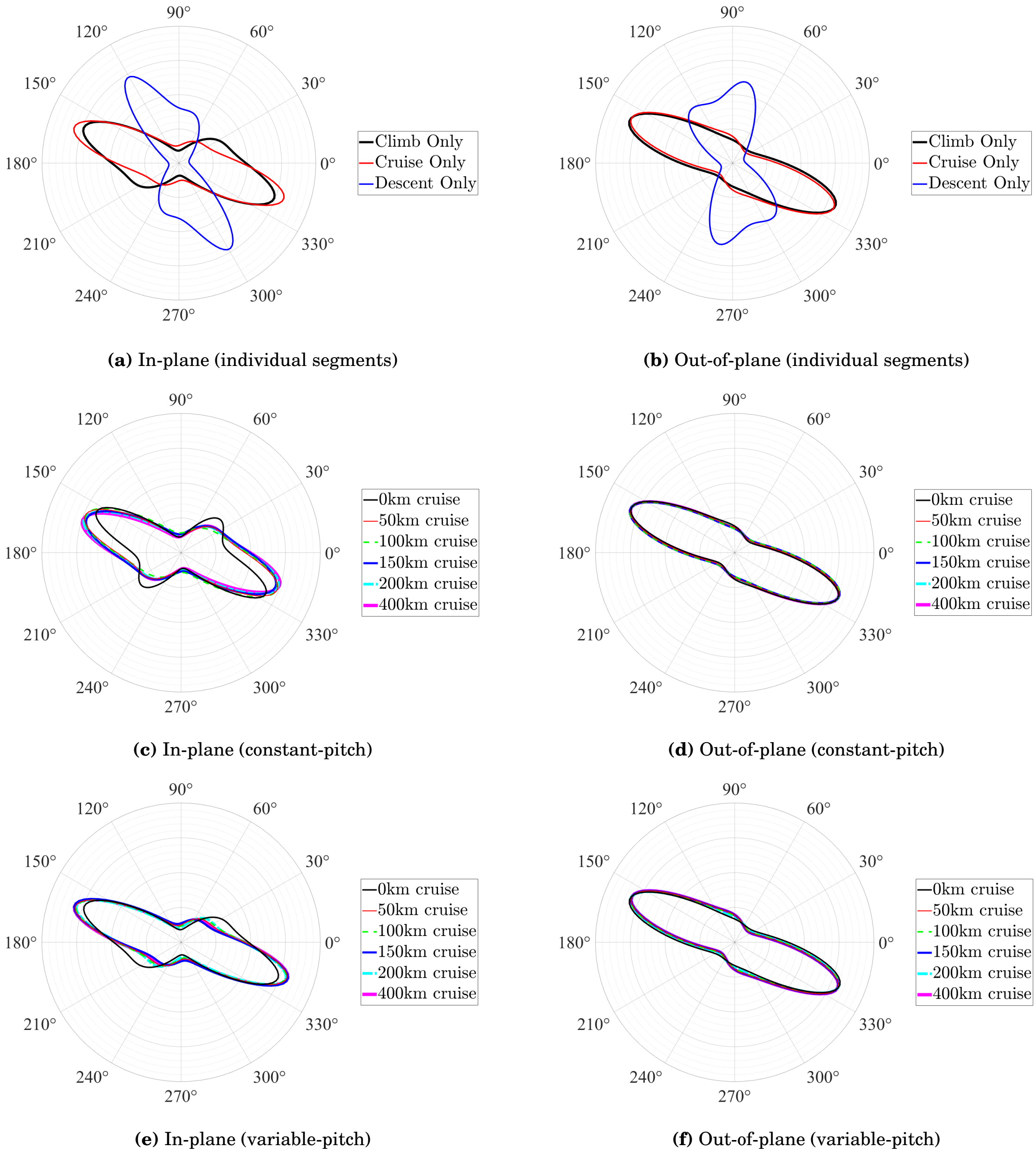

(a) In-plane (individual segments)

(b) Out-of-plane (individual segments)

(c) In-plane (constant-pitch)

(d) Out-of-plane (constant-pitch)

(e) In-plane (variable-pitch)

(f) Out-of-plane (variable-pitch)

Figure 5.23: Upper surface stiffness rosettes obtained from optimization studies.

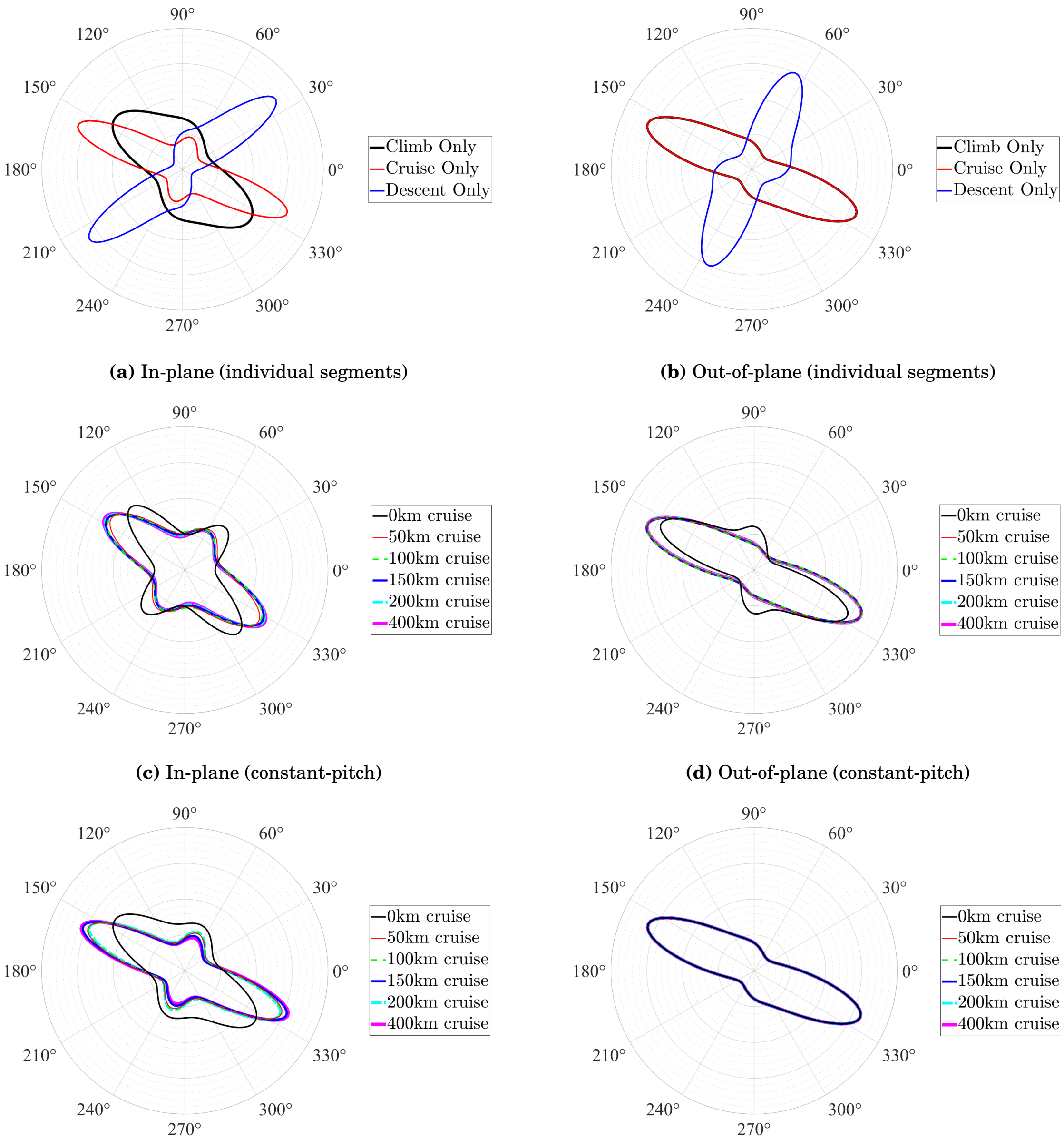

(a) In-plane (individual segments)
(b) Out-of-plane (individual segments)
(c) In-plane (constant-pitch)
(d) Out-of-plane (constant-pitch)
(e) In-plane (variable-pitch)
(f) Out-of-plane (variable-pitch)

Figure 5.24: Lower surface stiffness rosettes obtained from optimization studies.

Starting with the individual mission optimization studies, the stiffness rosettes associated with the climb- and cruise-only optimization studies appear to have a similar shape on both the upper and lower surfaces. This is expected based on findings obtained from the sensitivity studies, as it was found that ply orientations between $-30°$ and $-15°$ yielded the lowest power consumption at a constant thrust setting at all advance ratios corresponding to propulsive mode. This is especially true for the upper surface laminate, whereas the stiffness rosette of the lower surface laminate associated with the climb-only optimization is more balanced in comparison to the cruise-only rosette. This is because the loading is higher during climb in comparison to cruise, and thus the blade structure must have more balanced stiffness properties in the climb segment to prevent the maximum normal strain from exceeding the maximum allowable strain. In Figure 5.21d, it is shown that the maximum shear strain constraint is active in both the climb and cruise missions, which suggests that the optimizer is attempting to maximize the blade's deformations to yield the largest possible difference in performance. For the climb- and cruise-only cases, blade tip displacements accordingly yield an aerodynamic wash-out effect.

As initially hypothesized, the optimal stiffness rosette configuration for the descent-only case appears considerably different from the ideal climb- and cruise-only results. In all optimization cases besides the descent-only case, the optimizer maintained all laminate thicknesses on or near the lower bound of 0.5 millimetres, whereas in the descent, the upper surface has a laminate thickness that is exactly on the upper bound of 1.75 millimetres. On the lower surface, the laminate thickness was found to be 0.9 millimetres. In descent, it appears that the optimizer tends to prioritize the extension-shear coupling rather than the bend-twist coupling. This is clear due to the outer surface rosettes shown in Figure 5.23b and Figure 5.24b being near 90°. The presence of extension-shear coupling yields a slight aerodynamic wash-in effect during descent, as the blade elongation results in twist deformations due to the laminate shear deformations because the shared edges of the upper and lower surfaces must remain connected to ensure that the leading and trailing edges of the upper and lower surfaces remain connected.

For both constant-pitch and variable-pitch propellers, the upper and lower laminates obtained by the optimizer yield the same stiffness rosette plots at all non-zero cruise distances under consideration. Additionally, similar stiffness rosettes appear to be obtained for both the constant- and variable-pitch cases, which appears to be a combination between the ideal stiffness distributions found during the climb- and cruise-only optimization cases. Moreover, the stiffness distribution results for optimization studies involving the non-zero cruise distance appear consistent with the sensitivity studies that were shown in Section 5.1, as it was found that ply orientations between $-30°$ and $-15°$ yielded the lowest power consumption at a constant thrust setting. When the cruise distance was set to zero kilometres, the upper and lower surface stiffness rosettes appear slightly different from the remaining stiffness rosettes, as the optimizer appears to be compensating slightly for the descent segment. Otherwise, the descent appears to be almost wholly neglected by the optimizer, which is expected as the recovered energy in descent is small, and the loads encountered during descent are also considerably decreased in comparison to the loading in cruise and climb, which provides a substantial limitation on the amount that regenerative performance may be affected. This appears to be beneficial, as the ideal laminate configuration in climb or cruise is significantly different from the ideal laminate configuration in descent. In all cases featuring the full mission, the optimizer therefore exploits both bend-twist and extension-shear coupling to yield an aerodynamic wash-out effect that reduces power consumption for a constant thrust.

OVERALL PERFORMANCE MAPS

After completing the optimization studies, performance maps of the optimal flexible blades were computed and compared with the rigid blade. Only two representative variable-pitch and two constant-pitch propeller blades were considered: one of each type that was designed for a mission with a non-zero cruise distance, and one of each type that was designed for a mission that does not include the cruise. This choice was made because most of the blade structural designs were found to be approximately the same during optimization studies involving the full mission. All three of the blades obtained from optimization studies involving only a single mission segment were also included. Thus, seven blades in total were analysed. For each blade under consideration, upper surface lamination parameters are provided in Table 5.2 and lower surface lamination parameters are provided in Table 5.3. Operating conditions considered during the analysis are additionally provided in Table 5.4. The three pitch settings of 15°, 25°, and 35° were studied because the ideal flexible cruise pitch setting is approximately 35°, and the ideal descent pitch setting is approximately 18°. This ensures that performance is evaluated over the full range of relevant operating points.

Table 5.2: Blade structures that were analysed during the collection of performance maps, indicating the mission type, cruise distance, and upper surface lamination parameter values.

ID	Type	Cruise Length (km)	ξ_1^A	ξ_2^A	ξ_3^A	ξ_4^A	ξ_1^D	ξ_2^D	ξ_3^D	ξ_4^D
Blade 1	CPVR	0	0.4337	-0.2036	-0.4127	-0.4955	0.4351	-0.5763	0.0313	-0.6299
Blade 2	CPVR	150	0.5593	-0.2676	-0.0467	-0.5166	0.4712	-0.5517	0.0316	-0.6301
Blade 3	VPVR	0	0.6300	-0.2580	-0.0907	-0.4687	0.4964	-0.5374	0.0315	-0.6306
Blade 4	VPVR	150	0.6015	-0.3365	0.0521	-0.6776	0.4371	-0.5750	0.0319	-0.6306
Blade 5	climb	N/A	0.6314	-0.2619	-0.0843	-0.4595	0.4885	-0.5418	0.0315	-0.6306
Blade 6	cruise	N/A	0.6019	-0.3573	0.0842	-0.6741	0.4228	-0.5850	0.0319	-0.6306
Blade 7	descent	N/A	-0.5338	-0.4254	-0.3875	0.2451	-0.5563	-0.2043	-0.0333	-0.2740

Table 5.3: Blade structures that were analysed during the collection of performance maps, indicating the mission type, cruise distance, and lower surface lamination parameter values.

ID	Type	Cruise Length (km)	ξ_1^A	ξ_2^A	ξ_3^A	ξ_4^A	ξ_1^D	ξ_2^D	ξ_3^D	ξ_4^D
Blade 1	CPVR	0	-0.0758	0.1766	-0.6619	-0.1129	0.2000	0.5202	0.0313	0.6283
Blade 2	CPVR	150	0.1209	0.3353	-0.4075	0.4417	0.4620	0.5591	0.0320	0.6303
Blade 3	VPVR	0	0.0007	0.3374	-0.2819	0.3507	0.4227	0.5848	0.0316	0.6306
Blade 4	VPVR	150	0.3263	0.4139	-0.0223	0.7934	0.4228	0.5850	0.0319	0.6306
Blade 5	climb	N/A	-0.0310	0.4015	-0.1794	0.2638	0.4223	0.5853	0.0316	0.6311
Blade 6	cruise	N/A	0.3974	0.4777	0.0471	0.8612	0.4228	0.5850	0.0319	0.6305
Blade 7	descent	N/A	0.0453	-0.7663	-0.4815	-0.4667	-0.2996	-0.5416	0.0599	0.5758

During the collection of performance data, either the rotor speed or the freestream velocity was held constant. This enables a complete set of results to be obtained. With variations at a constant rotor speed (defined by *case 1*), C_T vs. J, C_P vs. J, and C_P vs. C_T plots were generated. With variations in freestream velocity (defined by *case 2*), T_C vs. J, P_C vs. J, P_C vs. T_C, η_P vs. J, η_T vs. J, η_P vs. T_C, and η_T vs. T_C plots were generated. This decision was made to ensure that the absolute loading is comparable between each blade configuration at each constant thrust or advance ratio point being used for comparison, which ensures that the effect of aeroelastic tailoring is compared without the presence of biases due to operating conditions. Moreover, when plotting efficiency against the thrust output, η_P vs. T_C plots must be generated, as this prevents the efficiency curve from being dependent on advance ratio (as given by $\eta_\mathrm{P} = \eta_\mathrm{T}^{-1} = JC_T/C_P = T_C/P_C$). Lastly, when varying the advance ratio at a constant rotor speed, it is possible to maintain realistic operating conditions in climb and cruise, although the loading encountered in descent will be overestimated (because the freestream velocity must be increased to increase the advance ratio). Conversely, when varying the advance ratio at a constant freestream velocity, realistic operating conditions in descent and climb can be maintained by setting a realistic freestream velocity, although the loading encountered in cruise will be underestimated due to the freestream velocity being set too low. Evaluating performance trends through both types of variations therefore enables the relative changes in performance between all mission segments to be appropriately assessed.

Table 5.4: Operating conditions considered during the collection of performance maps.

Case	Constant $\beta_{0.7}$	Constant Ω (RPS)	Constant V_∞ (m/s)	Variable J
1	25°	25	N/A	0.8 – 1.8
	35°	20	N/A	1.0 – 2.2
2	15°	N/A	30	0.5 – 1.3
	25°	N/A	40	1.1 – 1.9
	35°	N/A	50	1.7 – 2.5

As shown in Table 5.4, only the two pitch settings of 25° and 35° were considered for performance maps obtained with a constant rotor speed. This is because the operating conditions for descent are unrealistic in this case, and thus only the pitch settings that are close to ideal in climb and cruise conditions have been shown. Corresponding to *case 1*, Figure 5.25 contain C_T vs. J and C_P vs. J plots. Lastly, Figure 5.26 contains C_P vs. C_T plots for both pitch settings. Similar trends were observed at both pitch settings. All blades that were optimized for the full mission behave similarly at all operating conditions that were investigated during this study, as they all exhibit an aerodynamic wash-out effect that tends to alleviate the loading that is encountered. This wash-out effect has already been shown to reduce the power consumption for a given thrust setting. All flexible blades appear to exhibit almost no difference in the amount of power that is recovered in regenerative conditions, despite the unusually high amount of loading that the blade is experiencing during this investigation. This is consistent with the performance trends observed during the sensitivity studies documented in Section 5.1. For example, Figure 5.2a indicates a greater difference in performance during propulsive mode in comparison to regenerative mode.

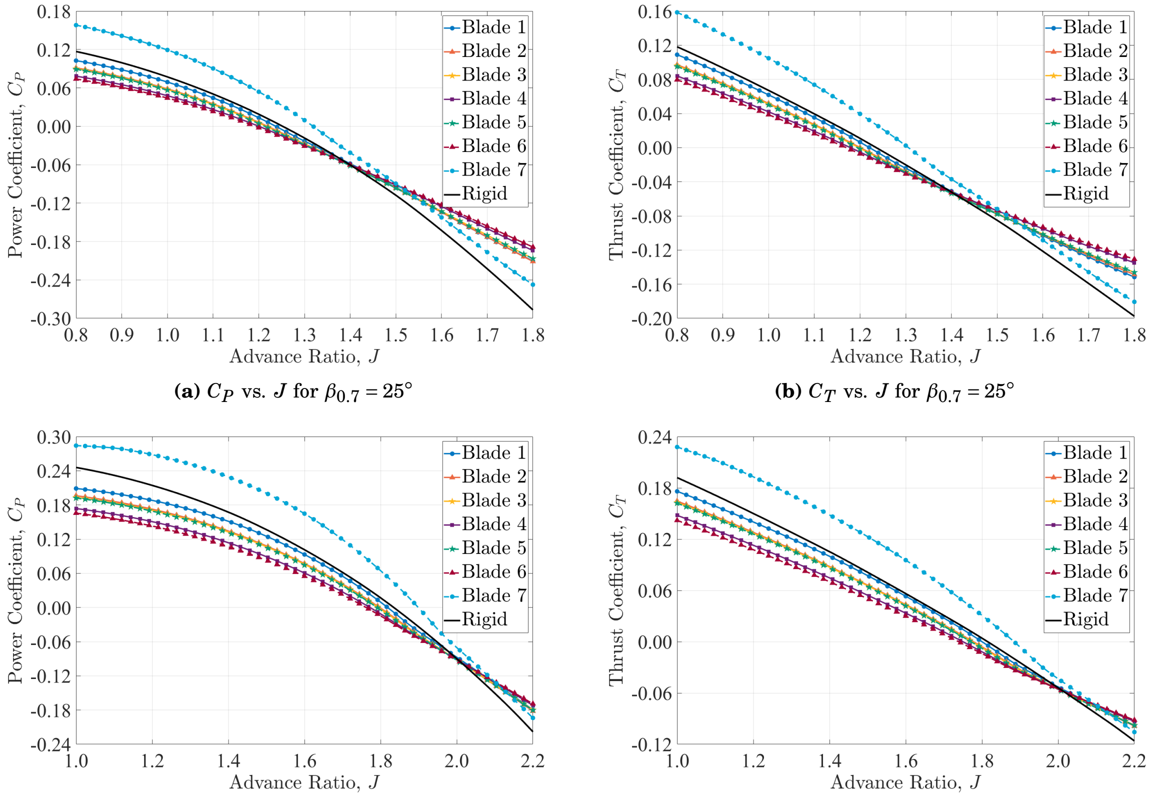

(a) C_P vs. J for $\beta_{0.7} = 25°$ **(b)** C_T vs. J for $\beta_{0.7} = 25°$

(c) C_P vs. J for $\beta_{0.7} = 35°$ **(d)** C_T vs. J for $\beta_{0.7} = 35°$

Figure 5.25: Power and thrust coefficients, C_P and C_T, plotted against advance ratio, J, for *case 1*.

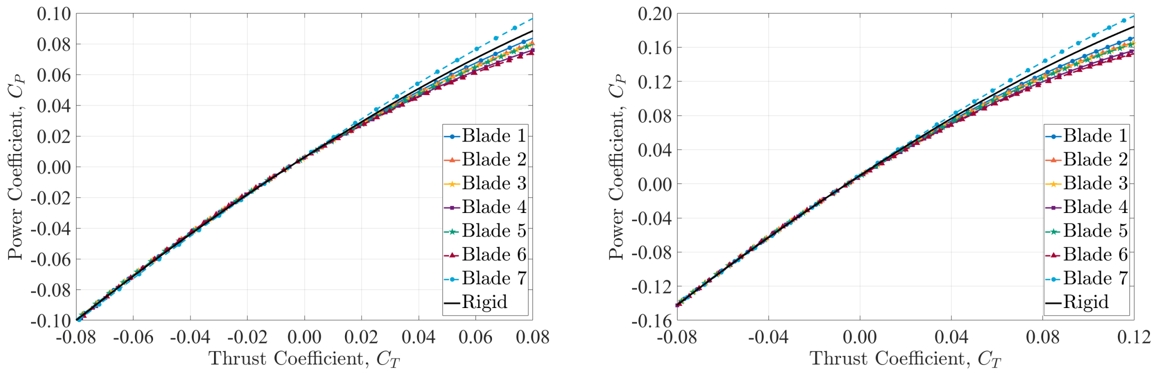

(a) $\beta_{0.7} = 25°$ **(b)** $\beta_{0.7} = 35°$

Figure 5.26: Power coefficient, C_P, plotted against the thrust coefficient, C_T, for *case 1*.

In addition to the noticeable differences in behaviour between the ideal propeller for descent only in comparison to the others, there is also a clear difference in the amount of bend-twist coupling that each blade type has. As expected, *blade 6* has the largest amount of aerodynamic wash-out, as its deformations are limited by strains encountered during the cruise segment, while the deformations of *blade 1* through *blade 5* are limited by strains encountered during climb, and the loads encountered in climb are greater than the loads encountered in cruise. *Blade 2*, *blade 3*, and *blade 5* perform similarly, whereas *blade 4* performs similarly to the cruise-optimized blade and noticeably better than the rest in propulsive mode.

It is clear that the optimizer heavily prioritized performance in propulsive mode for the blades that were optimized for the full mission with a non-zero cruise length, as aeroelastic tailoring appears to have a pronounced effect in propulsive conditions and a minimal effect in regenerative conditions. There is also a significant amount of energy being consumed in propulsive mode and only a minimal amount of energy being recovered during descent, which further contributes to this. It is also indicated by the performance of *blade 1*, that the optimizer partially accounts for the performance in descent when the constant-pitch propeller is used for a climb-descent mission, as this blade exhibits the most amount of compromise between minimizing power consumption in propulsive mode and maximizing power recovered during descent. With variable-pitch capabilities, it is no longer necessary to compromise between propulsive and regenerative performance, as *blade 3* and *blade 4* have a much stronger wash-out effect than *blade 1*, thus yielding better performance in propulsive mode, with *blade 2* and *blade 3* performing similarly.

For *case 2*, plots of the thrust and power coefficients, T_C and P_C have been shown as a function of the advance ratio in Figure 5.27. The trends appear consistent with trends that were observed in Figure 5.25.

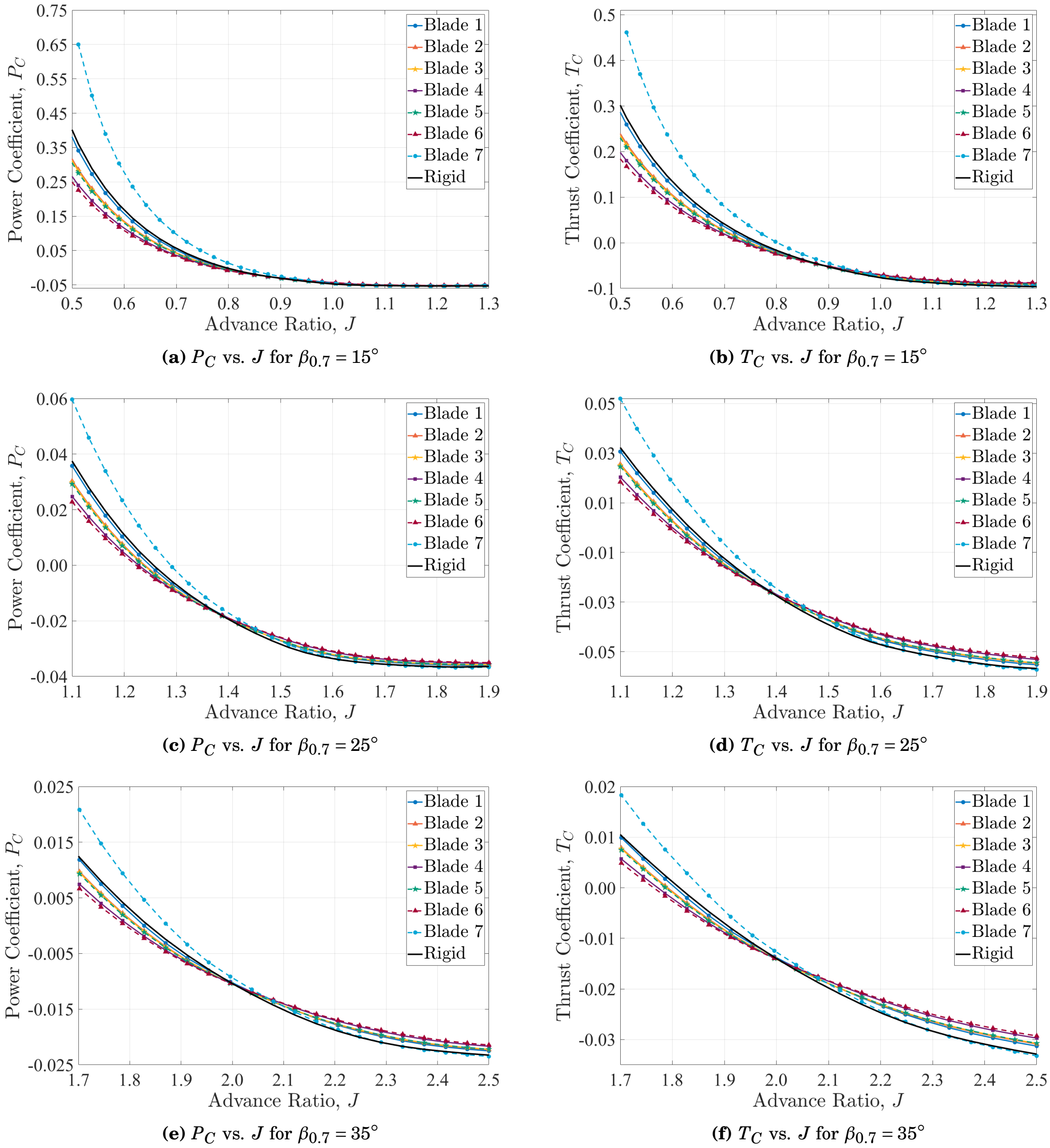

(a) P_C vs. J for $\beta_{0.7} = 15°$

(b) T_C vs. J for $\beta_{0.7} = 15°$

(c) P_C vs. J for $\beta_{0.7} = 25°$

(d) T_C vs. J for $\beta_{0.7} = 25°$

(e) P_C vs. J for $\beta_{0.7} = 35°$

(f) T_C vs. J for $\beta_{0.7} = 35°$

Figure 5.27: Power and thrust coefficients, P_C and T_C, plotted against advance ratio, J, for *case 2*.

For *case 2*, plots of the propeller and turbine efficiency as a function of the advance ratio are shown in Figure 5.28, and plots of the propeller efficiency as a function of the thrust coefficient are shown in Figure 5.29. Similar trends were observed in Figure 5.29 in comparison to Figure 5.26, where aeroelastic tailoring causes significant variations in power consumption in propulsive mode and only minor variations in power recovery during regenerative mode. As expected, the blades that feature an aerodynamic wash-out effect with increasing load tend to yield better performance in propulsive conditions with increasing pitch setting. Due to the presence of the aerodynamic wash-in effect, the blade that was optimized only for descent (*blade 7*) underperforms considerably during propulsive mode. During the descent, this blade appears to exhibit the best performance within a very narrow range of advance ratio values at all pitch settings, while also exhibiting the worst performance outside this region. Moreover, the difference in turbine efficiency between the descent-optimized blade and the others is almost not noticeable at the point where it reaches its best performance. Thus, it is unsurprising that the optimizer would tend to almost completely neglect the descent when performing the full mission optimization.

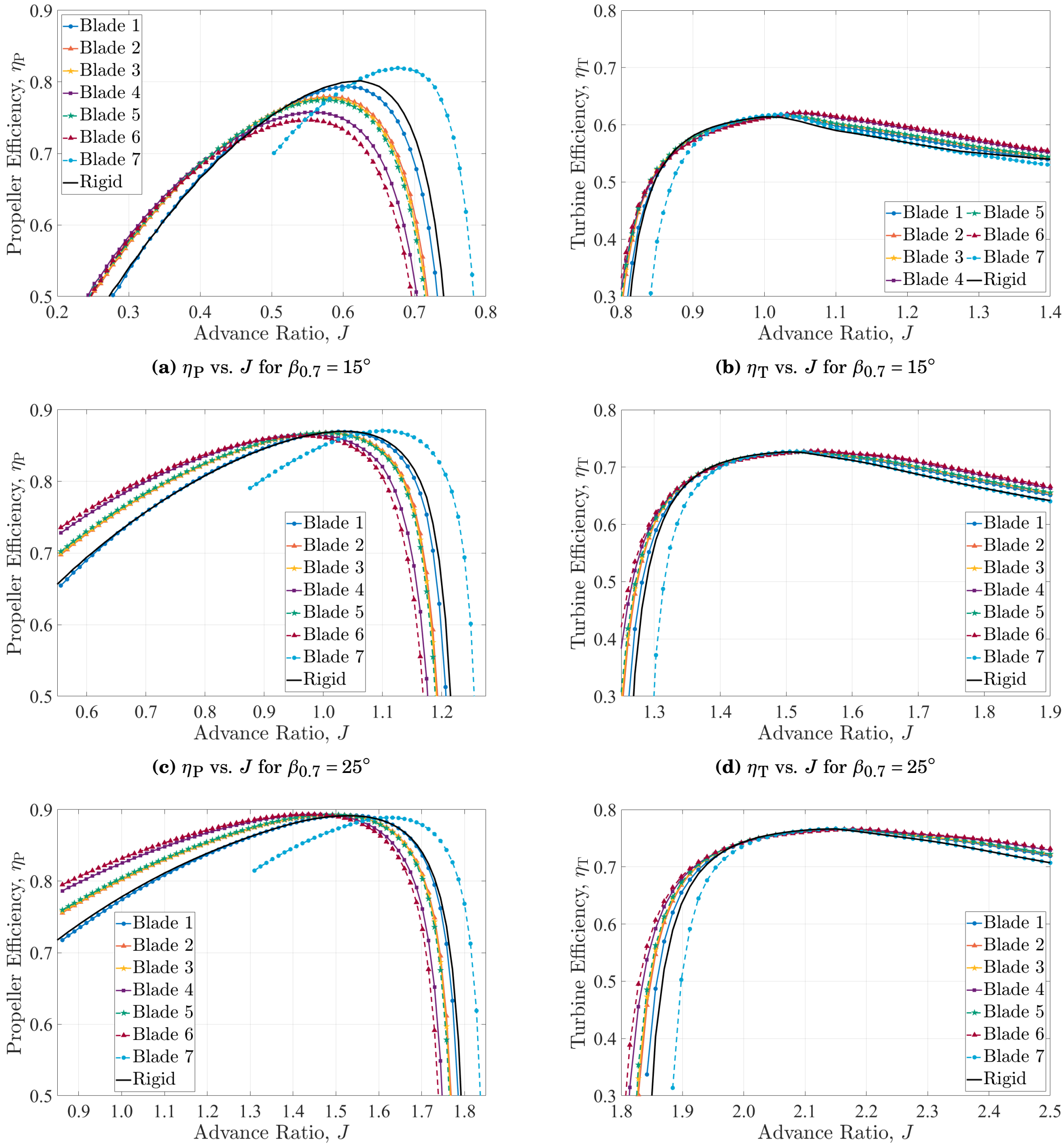

(a) η_P vs. J for $\beta_{0.7} = 15°$

(b) η_T vs. J for $\beta_{0.7} = 15°$

(c) η_P vs. J for $\beta_{0.7} = 25°$

(d) η_T vs. J for $\beta_{0.7} = 25°$

(e) η_P vs. J for $\beta_{0.7} = 35°$

(f) η_T vs. J for $\beta_{0.7} = 35°$

Figure 5.28: Efficiencies, η_P and η_T, plotted against advance ratio, J, for *case 2*.

After observing results from efficiency curves, it appears that *blade 4* is closest to a local optimum in comparison to the remaining blades, when considering propeller performance over the entire range of advance ratios. On the other hand, *blade 7* appears furthest from a local optimum when considering the full mission, despite reaching the greatest efficiency at very low thrust outputs. This is because it underperforms considerably at moderate-to-high thrust coefficients, especially with increasing pitch-setting. Because its efficiency is lowest by a significant margin at the thrust coefficients characterizing the climb and cruise segments, *blade 7* should not be considered as a suitable candidate. While *blade 6* shows the best performance, its maximum normal strain in climb is greater than the maximum allowable strain of the composite material, and thus it cannot be considered. *Blade 1* was optimized for the constant pitch propeller performing only a climb-descent mission and thus features the most amount of compromise between propulsive and regenerative conditions. The effect of tailoring is least noticeable in this case, and thus the remaining blades obtained from optimization studies of either the full mission or the propulsive mode appear to perform better. The remaining three blades appear to perform similarly, which suggests that the ideal blade design obtained from the full mission optimization is similar to the ideal blade design obtained from the climb-only optimization.

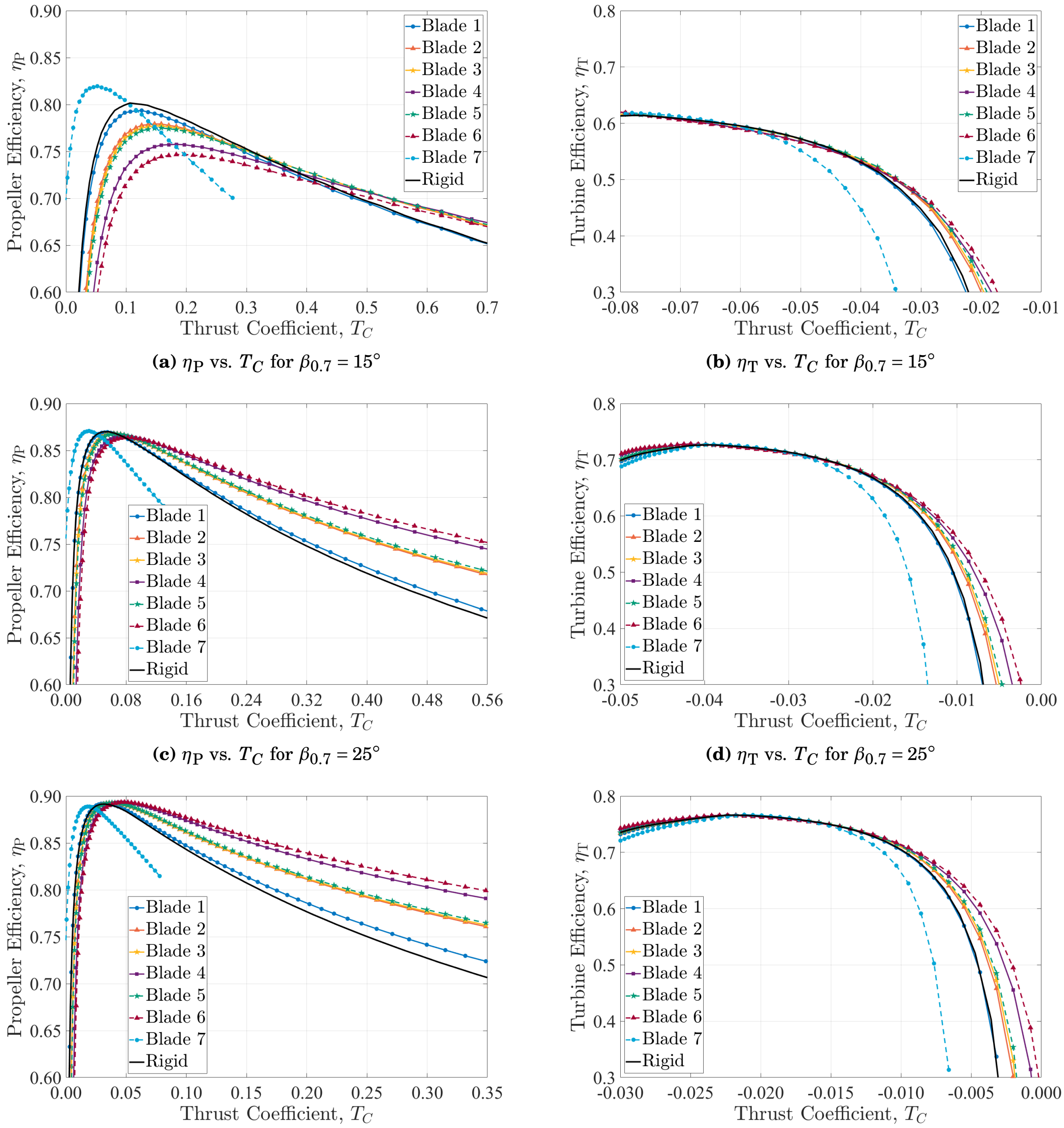

(a) η_P vs. T_C for $\beta_{0.7} = 15°$

(b) η_T vs. T_C for $\beta_{0.7} = 15°$

(c) η_P vs. T_C for $\beta_{0.7} = 25°$

(d) η_T vs. T_C for $\beta_{0.7} = 25°$

(e) η_P vs. T_C for $\beta_{0.7} = 35°$

(f) η_T vs. T_C for $\beta_{0.7} = 35°$

Figure 5.29: Efficiencies, η_P and η_T, plotted against thrust coefficient, T_C, for *case 2*.

In maintaining the maximum strain requirements in climb and cruise, it is possible that *blade 1* through *blade 6* all yield similar efficiencies in climb and cruise, as the optimizer will maintain the maximum loading before exceeding the maximum allowable strain through modifications in pitch setting and advance ratio. Thus, there is likely only a small difference in the minimum mission energy consumption that is yielded by either *blade 2*, *blade 3*, *blade 4*, or *blade 5*.

5.2.3. SUMMARY OF RESULTS

Conclusions that were drawn from the mission-weighted optimization studies are summarized below.

- Variable-pitch propeller blades obtained from full mission optimization studies were found to yield similar efficiencies in each mission segment in comparison to the blades obtained from individual mission segment optimization studies, independently of the cruise distance.
- The optimal flexible constant-pitch propeller yielded a lower energy consumption than both the rigid constant- and variable-pitch propellers, despite remaining at suboptimal pitch settings over long cruise distances due to the thrust requirement in descent.
  - In comparison to the rigid variable-pitch propellers, energy consumption decreased by 1.5-2.0% for flexible variable-pitch propellers and by 0.7-1.4% for flexible constant-pitch propellers. In comparison to the rigid constant-pitch propellers, energy consumption decreased by 1.5-2.0% for flexible variable-pitch propellers and by 1.0-1.5% for flexible constant-pitch propellers.
- In every case except for the descent-only optimization, the maximum tensile strain constraint was active, and the compressive strains were negligible. This suggests that the optimizer maximized the effect of aeroelastic tailoring without exceeding critical strains. The negligible compressive strains verify the prior decision to not consider buckling as a potential failure mode.
- The optimal operating conditions of the flexible blades are always considerably different from the rigid blades for all considered cases. This limits the applicability of aeroelastic tailoring, as the ideal operating conditions will be difficult to predict during in-flight conditions due to their dependence on blade size, structure, loading, freestream velocity, and rotor speed.
- The optimal blade structure obtained exclusively for propulsive conditions yields an aerodynamic wash-out effect that tends to reduce the loading encountered at a constant thrust, thus resulting in a decreased power requirement. This is consistent with the results obtained in Section 5.1 and by Sodja *et al.* [3], where the backward-swept blade always yielded the best performance in propulsive mode.
- The optimal blade obtained from the descent-only optimization featured an aerodynamic wash-in effect, which severely degrades performance in propulsive mode. This is consistent with the results from Sodja *et al.* [3], where the forward-swept blade always yielded the worst performance in propulsive mode.
- In all full-mission optimization cases, the optimizer heavily prioritized the minimizing energy consumption in propulsive mode over maximizing energy recovered in descent. For missions involving a non-zero cruise distance, the optimizer entirely ignored the descent segment.
  - This behaviour occurred for two reasons. First, a large amount of energy is consumed during climb and cruise in comparison to the small amount of energy that may be recovered during descent. Second, the loading encountered in descent is significantly smaller than the loading encountered during propulsive mode, which causes the effect of aeroelastic tailoring to be heightened considerably during propulsive mode in comparison to during regenerative mode.
- All propeller blades obtained from the full mission optimization studies in addition to the climb- and cruise-only optimization studies yielded similar performance trends, featuring the presence of an aerodynamic wash-out effect. The performance encountered during the descent by all of these blade designs was only marginally degraded at on-design conditions despite being improved at off-design conditions, as indicated by their trends in efficiency as a function of the thrust coefficient. The aerodynamic wash-out effect always yielded favourable off-design performance trends, characterized by a broad range of advance ratio values corresponding to high values for η_P or η_T.
  - The optimal descent-only blade design, which featured an aerodynamic wash-in effect, only performed favourably at on-design conditions, with significantly degraded off-design performance that is characterized by a narrow region of advance ratio values corresponding to high values for η_P or η_T.

6
CONCLUSIONS

6.1. CONCLUSIONS

During this thesis, the application of aeroelastic tailoring towards the enhancement of dual role propeller performance was investigated. The scope of this project included the development, verification, validation, and application of a nonlinear static aeroelastic analysis and optimization code. Blade element momentum theory was applied to assess the aerodynamics, and *PROTEUS* was used for the structure, with modifications to account for the centrifugal force experienced by the propeller blade. A tightly coupled aeroelastic analysis routine was implemented to ensure a high level of computational efficiency and numerical stability. The structural, aerodynamic, and aeroelastic analysis routines were verified through comparisons with pre-existing numerical procedures. Near-perfect agreement was obtained from all verification studies, indicating that the three models were implemented correctly. Additionally, the aerodynamic model was validated through comparisons with experimental data, yielding reasonable agreement in general trends, thus providing confidence in the applicability of the selected modelling approach.

Using the developed analysis tools, the TUD-XPROP-3 propeller, scaled to realistic flight conditions, was evaluated with varying configurations of symmetric-unbalanced and symmetric-balanced laminates. The purpose of this investigation was to determine how the performance and deformations of the blade differ with changes in structure. Through this investigation, it was found that the flexible blades constructed out of symmetric-unbalanced laminates yield a significant variation in thrust and power through the presence of bend-twist and extension-shear coupling, which results in an increasing change in twist distribution with increasing deflection or elongation. Only small variations in performance were observed from symmetric-balanced laminates, as the minimal bend-twist coupling and zero extension-shear coupling resulted in negligible twist deformations, caused only by the aerodynamic moment. Thus, changes in performance are almost entirely dependent on the presence of bend-twist and extension-shear coupling, which is consistent with initial expectations, as variations in performance that are computed using blade element momentum theory are almost completely driven by changes to the blade twist distribution.

During the sensitivity studies, it was found that the symmetric-unbalanced laminates with negative ply orientations (using a reference system where positive angles point toward the trailing edge and downward) yield a favourable aerodynamic wash-out effect, where upward deflections of the blade axis (positive in the global x- and z-axis) yield leading-edge-down pitch deformations and vice versa. Accordingly, laminates with positive ply orientations were found to yield an unfavourable aerodynamic wash-in effect, with positive displacements of the blade axis yielding a leading-edge-up pitch rotation and vice versa. While maintaining a constant thrust requirement, it was found that blades exhibiting an aerodynamic wash-out effect will yield a decrease in power consumption during propulsive conditions and a potential increase in power recovery during regenerative conditions. Moreover, for an equivalent thrust magnitude, larger variations in power consumption were observed during propulsive mode in comparison to regenerative mode. Because the amount of negative thrust generated by the propeller in descent is significantly lower than the positive thrust required during climb or cruise, it is expected that the effect of aeroelastic tailoring will always be more pronounced in propulsive conditions in comparison to descent. With the presence of an aerodynamic wash-out effect at negative ply angles, the largest improvement in performance was found for ply orientations between $-30°$ and $-15°$, whereas performance was worsened the most for ply orientations between $15°$ and $30°$. This is a result of the large amount of bend-twist and extension-shear coupling that is present at these angles, in addition to the smaller shear and torsional stiffness in comparison to larger ply angles near $45°$. Finally, as expected, the bending and shear deformations of the blade under a constant loading are primarily driven by the amount of stiffness that the blade has along its structural axis, with the presence of bend-twist and extension-shear coupling having a relatively small influence on blade axis deformations, this is because the aerodynamic and centrifugal loads act primarily in the axial and transverse directions, and thus any changes in deformations through structural coupling will be less visible in comparison to deformations that are directly caused by loads acting on the blade.

After completing the sensitivity studies, optimization studies were performed using the same scaled version of the TUD-XPROP-3 blade that was used during the sensitivity studies. The optimization problem was formulated by integrating the propeller onto an existing aircraft configuration, the Pipistrel Panthera, which was analysed over a constant climb-cruise-descent mission profile. During the optimization, the thrust requirements in climb, cruise, and descent were set *a priori* according to performance requirements of the chosen aircraft configuration. Additionally, the cruise length was varied over a range of $0-400$ kilometres. In all optimization cases, the propeller was considered to feature just one laminate on each of its upper and lower surfaces, as well as one laminate for each of its spar webs. The objective of the optimization was to reduce the overall energy consumption over the full mission and over each segment individually. Ideal performance of the rigid propeller either with constant- or variable-pitch capabilities was then compared with the ideal performance of the optimal flexible propeller with either constant- or variable-pitch capabilities. Constraints on the maximum allowable shear and normal (tensile and compressive) strains, tip displacements, and shaft power were applied during the optimization to guarantee a converged blade design that is feasible both structurally and for the aircraft configuration of interest.

During the optimization, it was found that the ideal blade design during climb or cruise features symmetric-unbalanced laminates that have negative ply orientations, which is consistent with the sensitivity studies that were previously performed. The ideal blade design during only the descent was found to be notably different from that of the climb or cruise segments, and it featured primarily extension-shear coupling with minimal bend-twist coupling to yield an aerodynamic wash-in effect that appears to only maximize performance at the one operating point considered during descent. For the full mission optimization, the optimizer almost completely neglected the descent when finding the optimal structural design, as the optimal stiffness rosettes obtained from the full mission optimization featured the same characteristic shape in comparison to the climb- or cruise-only cases. The results obtained from all optimization cases involving at least one mission segment in propulsive mode suggest that the optimizer is exploiting the aerodynamic wash-out effect that was found to provide a more favourable performance during the sensitivity studies. Consistency between results from optimization studies in comparison to the sensitivity studies provides confidence in the optimal stiffness distribution results that were obtained.

The best performance of the optimal flexible blades was found to be considerably greater than the best performance of the rigid blade. In particular, the flexible variable-pitch propeller was found to have an increase of 1.4% in cruise efficiency in comparison to the rigid variable-pitch propeller, and the flexible constant-pitch propeller was found to yield approximately an increase of 0.9% in cruise efficiency at all cruise distances under consideration. This is because the constant-pitch propeller was required to maintain the thrust requirement in descent, and thus was forced to operate at a suboptimal pitch setting in cruise even at very long cruise lengths, even despite the regenerative performance otherwise yielding a negligible change in energy consumption. In the absence of the descent, the cruise efficiency of the flexible constant-pitch propeller would converge toward the same cruise efficiency as the flexible variable-pitch propeller. During climb, both the flexible constant-pitch and variable-pitch propellers yielded an increase in efficiency from the rigid variable-pitch propeller by approximately 1.5%. At long cruise distances, the improvement in climb efficiency approached 2.5% for both flexible propellers in comparison to the rigid constant-pitch propeller. The efficiency in climb of the flexible constant-pitch propeller did not decrease with increasing cruise distance due to the thrust requirement in descent, as the blade was restricted from operating at higher pitch settings that would otherwise be more favourable for cruise and less favourable for climb. In descent, the flexible constant-pitch propeller performed considerably worse than both rigid propellers, with a turbine efficiency that is approximately 10% below the second-lowest turbine efficiency corresponding to the rigid constant-pitch propeller. The flexible variable-pitch propeller maintained a very similar turbine efficiency to the rigid variable-pitch propeller, despite the structural design being primarily conducive to the climb and cruise mission segments. This is because the loading in descent is significantly reduced from the loading in climb or cruise, and thus the effect of aeroelastic tailoring is significantly reduced in descent when compared with climb or cruise.

Despite the significantly degraded regenerative performance of the flexible constant-pitch propeller, the energy consumption of the flexible constant-pitch propeller was consistently found to be below that of both the rigid constant- and variable-pitch propellers, which potentially suggests that enhancing performance through the application of aeroelastic tailoring has greater energy-saving benefits in comparison to the application of energy-harvesting during descent. A decrease in energy consumption by 0.7 – 1.4% was found for the flexible constant-pitch propeller in comparison to the rigid variable-pitch propeller, and a decrease by 1.0 – 1.5% was found in comparison to the rigid constant-pitch propeller. For the variable-pitch propeller, a decrease in energy consumption of 1.5 – 2.0% was found in comparison to both the rigid constant-pitch and rigid variable-pitch propellers. Lastly, the flexible variable-pitch propeller yielded very similar performance in comparison to the optimal blade designs obtained through optimization studies with only a single mission segment. Indeed, the flexible variable-pitch propeller yielded a 0.1% greater energy consumption in comparison to the theoretical maximum decrease in energy consumption that may be obtained through the application of aeroelastic tailoring. The theoretical maximum decrease in energy consumption was computed using the optimal climb-only, cruise-only, and descent-only energy consumption values. This suggests that the optimal variable-pitch propeller is generally very close to the maximum potential enhancement in performance that may be obtained through aeroelastic tailoring.

During the optimization, the blade was primarily loaded in tension, with maximum tensile normal strains being considerably larger in magnitude than the maximum compressive normal strains. Additionally, the maximum tensile normal strain was an active constraint for all cases featuring the propeller operating in propulsive conditions, although the loading in descent was never large enough for the optimizer to find a structural design that yielded large strains. The maximum compressive normal strain was always found to be close to zero, which confirms the decision to neglect buckling as a failure mode.

Finally, the ideal pitch setting and advance ratio values of the flexible propeller are considerably different from those of the rigid propeller, especially in propulsive conditions where deformations are particularly high. This is expected due to the optimal flexible blade featuring the aerodynamic wash-out effect, which alleviates the loads encountered by the blade, thus requiring it to operate at a higher pitch setting and lower rotor speed. This presents an important limitation on the results that were presented, as it is generally difficult to predict the ideal operating conditions of the propeller with flexible blades. This is because the deformations, and consequently the performance, vary depending on the blade size, structure, loading, dynamic pressure, and rotor speed. Nevertheless, the performance enhancement yielded through aeroelastic tailoring was considerable, suggesting that this may be interesting to investigate further.

Elaborating on the above discussion regarding higher-level conclusions, answers to the research questions outlined in Section 1.3.1 are explicitly provided below.

(1) To what extent can further enhancements in dual-role propeller performance be obtained solely through the application of aeroelastic tailoring? This question was answered using results obtained from the optimization studies. During this project, a reference aircraft was analysed over a mission involving relatively high speeds, which suggests that the loads encountered by the propeller are relatively large. This heightens the effect of aeroelastic tailoring. Additionally, the propeller under consideration features straight blades, with no sweep or lean, and aerodynamic design was not considered during the optimization. This directly enables the extent of performance enhancements obtained solely through aeroelastic tailoring to be assessed. Performance enhancements in this case are characterized by the amount that energy consumption is decreased over the mission, as well as the amount that propeller or turbine efficiency may be increased at each mission segment.

During the climb segment, it was possible to obtain a maximum increase in propeller efficiency by approximately 1.4% in comparison to the ideal rigid variable-pitch propeller when considering the full mission with either the constant- or variable-pitch propeller. Both flexible propellers optimized for the full mission with a long cruise distance saw an increase in propeller efficiency of 2.5% from the efficiency of the rigid constant-pitch propeller. Neither of these values are more than 0.3% below the maximum propeller efficiency obtained by the flexible propeller that is optimized for climb only.

During the cruise segment, the flexible variable-pitch propeller yielded a noticeably greater efficiency in comparison to the flexible constant-pitch propeller at all cruise distances. This is because the constant-pitch propeller always needed to maintain a compromise in pitch setting that allowed the thrust requirement in descent to be met. The flexible propeller yielded a 1.4% greater propeller efficiency in cruise in comparison to the rigid variable-pitch propeller for optimization cases involving either only the cruise segment or the full mission with the variable-pitch propeller. For optimization cases involving the full mission with the constant-pitch propeller, a propeller efficiency was obtained that is approximately 0.9% greater than that of the rigid variable-pitch propeller. This shows that aeroelastic tailoring may still be used to yield performance improvements for the constant-pitch propeller over the rigid variable-pitch propeller, even when a suboptimal pitch setting must be used.

During descent, all optimized flexible propeller blades underperformed in comparison to the rigid variable-pitch propeller, although the difference in turbine efficiency that was yielded by the flexible variable-pitch propeller was negligibly smaller than that of the rigid propeller. The flexible descent-optimized propeller yielded an ideal turbine efficiency that is 0.4% greater than that of the ideal rigid propeller, which is very insignificant due to the already small amount of energy being recovered during descent. This demonstrates that aeroelastic tailoring is only effective during propulsive mode, while its effects during regenerative mode will not be noticed.

(a) **Which structural characteristics (i.e. material properties, ply orientations, and laminate thicknesses) have an important influence on dual-role propeller performance, and how are performance quantities and deformations affected by variations in these structural characteristics?** For aeroelastic tailoring, it is essential to use unidirectional fibre composites to exploit the effects of coupling. In particular, bend-twist and extension-shear coupling mechanisms were exploited during this work and thus each laminate must be symmetric-unbalanced or symmetric-balanced. Orthotropic laminates do not exhibit any coupling between strains or curvatures, and thus may not yield any substantial variations in performance. Moreover, it was even shown that symmetric-unbalanced laminates may be used to yield noticeable effects on performance through aeroelastic effects, whereas considerably smaller variations in performance were obtained with symmetric-balanced laminates. Carbon fibres with a relatively low maximum stiffness were considered most suitable for aeroelastic tailoring and thus were used exclusively during this project. Unidirectional glass fibres do not have enough difference between their two elastic moduli to yield a significant enough amount of coupling.

    The laminate thickness influences the magnitude of deformations, and thus decreasing the laminate thickness will yield increases in strains, deformations, and performance variations.

    The most important parameters affecting dual-role propeller performance are the ply orientations. It was shown during sensitivity studies that symmetric-unbalanced laminates yielded substantial variations in performance, whereas symmetric-balanced laminates did not. This is due to the presence of extension-shear and bend-twist coupling. In general, the presence of an aerodynamic wash-out effect tends to augment the range of advance ratio values where the propeller operates with high efficiency, whereas the presence of an aerodynamic wash-in effect tends to narrow the range of advance ratio values where the propeller operates with high efficiency. Symmetric-unbalanced laminates with negative ply orientations (defined relative to the spanwise axis of the blade and positive towards the trailing edge) yielded an aerodynamic wash-out effect, whereas positive ply orientations yielded an aerodynamic wash-in effect. Thus, negative and positive ply orientations respectively yield similar performance characteristics to the backward- and forward-swept blades that were studied by Sodja *et al.* [3].

    Pitch deformations are almost entirely driven by the presence of bend-twist and extension-shear coupling, in addition to the amount of stiffness the laminate has in torsion and shear. Blade pitch deformations also drive the variations in performance. The largest performance improvements were observed for ply orientations between $-30°$ and $-15°$, as they feature large amounts of bend-twist and extension-shear coupling in addition to relatively small amounts of shear and torsional stiffness. The largest decrease in performance was observed for ply orientations between $+15°$ and $+30°$ through the same physical reasoning. Despite also having large amounts of bend-twist and extension-shear coupling, ply orientations of $\pm45°$ have a large amount of shear and torsional stiffness, which negates the effect of bend-twist and extension-shear coupling, resulting in a weaker effect of aeroelastic tailoring in comparison to the aforementioned smaller angles. Similar trends in terms of ply orientations were also observed by Khan [4, 24].

(b) How do structural modifications in favour of improving performance during propulsive operation affect performance during regenerative operation? Propeller blades optimized for propulsive mode yielded either equivalent or worse performance during regenerative mode, although the presence of an aerodynamic wash-out effect appears to always yield favourable effects on performance at both on- and off-design conditions by broadening of the range of advance ratio values corresponding to high-efficiency operation. Nevertheless, maximizing performance during climb and cruise through aeroelastic tailoring still yielded a decrease in performance during descent. Because the loading encountered in descent is significantly smaller than the loading encountered in climb and cruise, the effect of aeroelastic tailoring is significantly greater in propulsive mode compared to regenerative mode. Moreover, because the amount of energy that is recovered during descent is orders of magnitude below the amount of energy that is required for the climb and cruise, aeroelastic tailoring has a small effect on energy recovered in descent.

Results from the full-mission optimization studies suggest that the optimizer neglected the descent completely, yielding a structural design featuring the presence of an aerodynamic wash-out effect. Considerable improvements in propeller efficiency were obtained for the optimal flexible variable-pitch propeller at both climb and cruise conditions, independently of the cruise distance, at the expense of a negligible decrease in turbine efficiency. The optimal flexible constant-pitch propeller also exhibited noticeable improvements in propeller efficiency during climb and cruise, at the expense of a substantial decrease in turbine efficiency during descent in comparison to its rigid counterparts. Nevertheless, the optimal flexible constant-pitch propeller still yielded a considerable decrease in total energy consumption in comparison to both the rigid constant- and variable-pitch propellers. This demonstrates that performance decreases in descent have a lesser effect on the total energy consumption in comparison to the effect of performance enhancements that are otherwise obtained in propulsive mode. Lastly, the optimal blade design obtained from the descent-only optimization study featured an aerodynamic wash-in effect that yielded greater turbine efficiency at on-design conditions only, with significantly degraded performance at both propulsive and regenerative conditions outside the single operating point characterizing the descent segment under consideration. Thus, the blade design obtained from the descent-only optimization study was deemed unsuitable for use over the full mission.

(2) How does the application of aeroelastic tailoring impact overall energy consumption over a generic climb-cruise-descent mission profile for constant-pitch or variable-pitch dual-role propellers? The optimal flexible constant-pitch propeller yielded a lower energy consumption than both the rigid constant- and variable-pitch propellers, and the flexible variable-pitch propeller naturally yielded an even lower total energy consumption than the flexible constant-pitch propeller. More specifically, the ideal flexible constant- and variable-pitch propellers respectively yielded decreases in total energy consumption in comparison to the rigid variable-pitch propeller by $0.7-1.4\%$ and $1.5-2.0\%$. In comparison to the rigid constant-pitch propeller, the ideal flexible constant- and variable-pitch propellers respectively yielded decreases in total energy consumption by $1.0-1.5\%$ and $1.5-2.0\%$. This shows that propeller performance may be noticeably improved through the application of aeroelastic tailoring. The theoretical total energy consumption obtained by summing together the energy consumption of the ideal climb-, cruise-, and descent-only propellers in their respective mission segments was consistently found to be approximately 0.1% below the total energy consumption of the flexible variable-pitch propeller. This suggests that the energy consumption of the optimal flexible variable-pitch propeller is near the theoretical minimum total energy consumption that may be obtained with aeroelastic tailoring. This also confirms that the effect of aeroelastic tailoring on performance in descent may be neglected in favour of improving performance during propulsive mode.

The results obtained correspond to the flexible propellers optimized for a fixed mission profile and with only one design region for each of its surfaces. Thus, it may be possible to yield even further decreases in energy consumption either through the use of a different mission profile or through the inclusion of a greater number of design regions. The aircraft configuration was also selected *a priori* and held constant throughout the optimization studies, and thus it may even be possible to yield further decreases in energy consumption through the use of a different aircraft configuration. Finally, the propeller blade axis geometry and aerodynamic design was held constant throughout all optimization studies, whereas the inclusion of additional design variables for the blade geometry may increase the extent of performance enhancements obtained with aeroelastic tailoring.

(a) How does the blade structure that is optimized for each individual mission segment differ from the blade structure that is optimized for a mission with a variable cruise distance? The climb- and cruise-optimized blade structures have a similar characteristic, with the principal in-plane and out-of-plane stiffness axes pointing towards the leading edge at similar angles between $-30°$ and $-20°$. Thus, both blades exhibit an aerodynamic wash-out effect that tends to alleviate the loading encountered in propulsive conditions, thereby reducing the power required for a given thrust output. The cruise-optimized blade features more bend-twist and extension-shear coupling, whereas the climb-optimized blade features more balanced stiffness properties. This is because the loading in climb is higher than the loading in cruise, and thus a stiffer structure is required for the climb to prevent the maximum strain constraint from being active. The descent-optimized blade structure appears considerably different from the other two blades. The lower surface principal in-plane stiffness points towards the trailing edge instead of the leading edge, and the lower surface principal out-of-plane stiffness axis also points toward the trailing edge with a relatively large angle of approximately $60°$. On the upper surface, the principal out-of-plane stiffness axis points toward $90°$ and the principal in-plane stiffness axis points toward $-60°$. As a result, the descent-optimized blade exhibits an aerodynamic wash-in effect instead of the wash-out effect that was observed from all other optimal blade structures.

Trends observed from full mission optimization studies for constant- and variable-pitch propellers appear to match, and thus the discussion for both cases has been combined. For a cruise distance of zero kilometres, the resulting blade structures from the full mission optimization appeared to match the ideal climb-only blade structure. For a non-zero cruise distance, the ideal blade structure appeared to yield a compromise between the ideal climb- and cruise-only blade structures, with the variable-pitch propeller appearing more similar to the cruise-only blade structure. In all full mission optimization cases, the descent was ignored, resulting in structural designs that do not bear any resemblance to the ideal descent-only blade. It is interesting to observe that the ideal blade structure obtained from all optimization cases involving a non-zero cruise distance are the same, whereas a different blade structure was obtained from full mission optimization studies that did not include the cruise distance. Furthermore, it is unsurprising that the descent segment was ignored by the optimizer in all full mission optimization cases, as the descent-only blade yields significant decreases in performance during propulsive mode.

(b) How do energy consumption results from optimization studies involving each individual mission segment compare with results from optimization studies involving the full mission? As expected, the blades optimized for each mission segment individually yield a lower energy consumption (or greater amount of recovered energy) in their respective mission segments in comparison to both the constant and variable-pitch propellers optimized for the full mission at all cruise distances. In climb, the flexible constant- and variable-pitch propellers yield a similar energy consumption at all cruise distances. If the thrust requirement in descent were not included, then the climb energy consumption of the constant-pitch propeller would increase in comparison to that of the variable-pitch propeller. The energy consumption of the climb-optimized propeller was less than both the constant- and variable-pitch propellers, by at-most 0.3%. The cruise-optimized propeller yielded a cruise energy consumption that is at-most 0.6% less than that of the optimal flexible constant-pitch propeller, and the optimal flexible variable-pitch propeller yielded a cruise energy consumption that is negligibly less than that of the cruise-optimized propeller. In descent, the descent-optimized blade was capable of recovering a negligibly larger amount of energy than the optimal flexible variable-pitch propeller, despite its significant differences in structural design. Conversely, the descent-optimized propeller is capable of recovering approximately 25% more energy in comparison to the ideal flexible constant-pitch propeller. This result illustrates the significance of the propulsive mode over the regenerative mode best, as even despite its apparently substantial decrease in regenerative performance, the flexible constant-pitch propeller noticeably outperforms both the rigid constant- and variable-pitch propellers at all cruise distances under consideration. This result is observed even though the rigid variable-pitch propeller yields a negligible difference in regenerative performance in comparison to the descent-optimized propeller blade. Thus, this result demonstrates that aeroelastic tailoring is most suitable for maximizing propeller performance in propulsive conditions, and its effects on performance come at a greater benefit than potential energy balance improvements that may be yielded through regeneration during descent.

(c) How do the optimal propeller blade designs perform over a range of operating conditions that may otherwise not be considered during the optimization studies? All propeller blades optimized for the full mission in addition to the blades optimized only for the climb and cruise segments feature an aerodynamic wash-out effect that broadens the range of advance ratio values corresponding to high-efficiency operation. This occurs in both propulsive and regenerative operating conditions. At on-design conditions corresponding to the descent segment, these blades yield performance that is only marginally degraded. As already stated, the performance improvements in climb and cruise significantly outweigh any decreases in performance during descent. The descent-optimized propeller yields a significantly different performance in comparison to the others due to its aerodynamic-wash in effect. In particular, it features an aerodynamic wash-in effect that yields a sharp decrease in efficiency at advance ratio values moving away from the operating point that characterizes the descent segment.

6.2. FUTURE RECOMMENDATIONS

Future recommendations have been identified to address limitations concerning the aeroelastic analysis routine and optimization procedure, the formulation of the optimization problem, and particularly the definition of the project scope. Potential extensions of this project have also been identified.

The aerodynamic model that was used during this project is an application of blade element momentum theory. The main limitations of this approach are that it is unable to take three-dimensional effects into consideration due to the lack of mutual interference between blade elements. Using a higher-fidelity aerodynamic model that is similar to the level of fidelity of the structural model, such as an application of either lifting-line or vortex-lattice methods, would enable finite-span effects and changes in blade axis geometry to be directly resolved. This may enhance the accuracy and precision of aerodynamic performance results. Additionally, the polar data for the propeller blade geometry that was considered during this project was evaluated numerically only and thus may be considerably different from reality. This is especially true for the drag coefficient data in the presence of at least moderate amounts of flow separation, as RFOIL is incapable of accurately modelling the effects of rotation on the drag coefficient [11]. It is therefore recommended to experimentally obtain lift and drag polar plots for the airfoils of the propeller, or to perform the same design study that was documented during this project on a propeller blade that features airfoil aerodynamic performance data that was obtained experimentally.

It was initially planned to complete the optimization studies for two mission profiles, one with relatively high speeds and another with relatively low speeds, to precisely investigate the effect of loading on the extent of performance increases or decreases obtained with aeroelastic tailoring. In this case, only the high-speed mission was performed due to timeline constraints, and thus it is recommended to perform the same investigation using lower flight speeds to identify how variations in performance depend on the amount of loading that the blade encounters. Like the work of van Neerven [33] or Scholtens [34], it could be interesting to consider a different reference aircraft that typically flies at lower airspeeds, such as an electric trainer aircraft like the Pipistrel Velis Electro (formerly the Alpha Electro) [71]. Additionally, during the optimization, it was initially planned to consider using multiple upper and lower surface laminates, spaced evenly along the span of the blade. Due to computing limitations and timing constraints, only one laminate (or design region) each for the upper and lower surfaces was eventually used to define the blade structure. It therefore may be possible to obtain even further enhancements in performance through the inclusion of multiple design regions, rather than just a single design region, and it is therefore recommended to perform further optimization studies with more than one design region over the propeller blade. Finally, the mission profile was approximated using one operating condition each for the climb, cruise, and descent to minimize computational cost. It would be more realistic to model the climb with at least two operating segments, as the climb operating conditions change with altitude.

As the number of design regions increases, the number of design variables will increase. Additionally, including more climb segments linearly scales the number of function evaluations. For the optimization studies performed during this project, the gradient was evaluated numerically using a central differencing scheme, and thus the objective function and constraints needed to be evaluated twice for each design variable, implying that the problem size increases as the number of mission segments or design variables increase. It is therefore recommended to modify the method of evaluating derivatives so that they are computed either analytically or through the method of automatic differentiation to significantly reduce the number of function evaluations, as this will ensure that the computational cost of the optimization procedure remains relatively low. It is also recommended to apply the method of aeroelastic tailoring for other laminate types, either by reducing the set of lamination parameters to symmetric-balanced, to directly investigate the influence of extension-shear coupling on potential performance improvements, or by increasing the set of lamination parameters to investigate any generic type of laminate. This extension is less practical than the others, as asymmetric laminates are difficult to manufacture.

Concerning the aeroelastic analysis and optimization, it would be interesting to validate the aeroelastic analysis procedure through comparisons to experimental data, as well as to investigate the optimal blade design in a wind tunnel to see its potential for enhanced performance. Experimental data that is suitable for validation studies was not found during this project, although it may be possible in future work to find a suitable case for comparison if further interest in aeroelastic tailoring for propeller blades is garnered. This work could also be extended through the implementation of a method of retrieving a realistic ply stacking sequence from the optimal set of lamination parameters. It would then be interesting to construct one of the optimal propeller blades that is yielded from the optimization studies completed during this work. This would enable the possibility for comparisons to be made between results obtained both experimentally and numerically, without any dependence on the collection of results from any external organization.

During this project, the effect of improvements in propeller performance through aeroelastic tailoring was evaluated independently of the blade's aerodynamic design. Furthermore, the aircraft configuration and mission profile were held constant and not included in the optimization. Thus, coupling between aircraft design, aircraft mission, and propeller performance was ignored during this thesis. It is therefore recommended in future work to consider also incorporating geometry changes to yield additional structural coupling through the blade geometry or to yield improvements in the aerodynamic design. This would offer greater design freedom as well as the potential for synergies between design characteristics to be exploited, which may enable even greater enhancements in performance to be reached. It would also be interesting to couple the aircraft design or mission strategy to the flexible propeller analysis and optimization, thus enabling the effect of aeroelastic tailoring on mission energy consumption to be determined more precisely. Lastly, multiple different mission profiles could be investigated to identify how the optimal blade structural design varies depending on the mission strategy under consideration.

A

Referenced Propellers

Blade geometry data for the TUD-XPROP propeller is provided in [13]. There are two composite propellers with the same blade geometry and either three or six blades (XPROP-3 and XPROP, respectively). The incidence angle of the blades can be manually adjusted, and the diameter of the propeller is 406.4 mm. The propeller represents a typical previous-generation turboprop propeller. It has negligible sweep and lean, making its geometry relatively simple, and the three rotors under consideration have been used extensively already for investigations into isolated propeller aerodynamics, propeller integration studies, and distributed propeller studies (i.e. [1, 10, 13]). Geometry data for this propeller is shown in Figure A.1 and Table A.1, and images of the propellers are shown in Figure A.2.

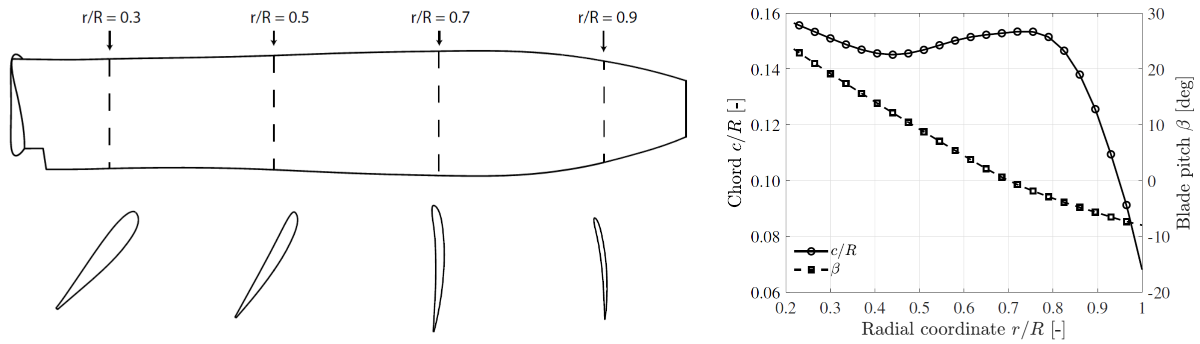

(a) Airfoils at varying spanwise locations.

(b) Chord and twist distributions.

Figure A.1: Geometric data for the TUD-XPROP propeller [13].

(a) TUD-XPROP [72].

(b) TUD-XPROP-3 [72].

Figure A.2: The propellers studied by Sinnige *et al.* [1], Goyal *et al.* [10], and Nederlof *et al.* [13].

Table A.1: Geometry data for the TUD-XPROP propeller.

Spanwise position, *r*/*R*	**Chord, *c*/*R***	**Twist angle, β**
0.160	0.1603	26.82
0.195	0.1580	24.83
0.230	0.1556	22.89
0.265	0.1533	20.99
0.300	0.1510	19.15
0.335	0.1488	17.38
0.370	0.1469	15.62
0.405	0.1456	13.87
0.440	0.1451	12.14
0.475	0.1456	10.43
0.510	0.1468	8.730
0.545	0.1485	7.050
0.580	0.1502	5.390
0.615	0.1515	3.750
0.650	0.1523	2.120
0.685	0.1528	0.600
0.720	0.1534	-0.730
0.755	0.1533	-1.870
0.790	0.1515	-2.910
0.825	0.1465	-3.900
0.860	0.1380	-4.800
0.895	0.1256	-5.670
0.930	0.1094	-6.530
0.965	0.0912	-7.370
1.000	0.0681	-8.000

During this project, the XPROP-3 was used exclusively because the reference aircraft configuration under consideration features a three-bladed propeller, and the pitch settings corresponding to optimal performance in climb, cruise, and descent are closer together for the XPROP-3 in comparison to the original six-bladed TUD-XPROP. Detailed airfoil geometries and polar plots have been made available for this project by researchers at the TU Delft.

B

Review of Applicable Disciplines

This chapter provides details on the review of literature concerning the applicable disciplines of this project. The purpose of this literature review is to provide a theoretical foundation that enables required decisions to be made on the scope, methodologies, formulations, and assumptions for this project. The main disciplines concerning this thesis include propeller aerodynamics, rotor blade static aeroelasticity, and aeroelastic tailoring. First, common aerodynamic modelling methods are reviewed in Appendix B.1 to identify an approach that would be most suitable for analysis and optimization of dual-role propellers. Engineering correction methods for aerodynamic models have subsequently been reviewed in Appendix B.2 to provide an indication of corrections to aerodynamic loads that must be applied during this work. Following this, a summary of open-source or otherwise available propeller aerodynamic analysis codes has been provided in Appendix B.3 to provide an indication of the modelling approaches and assumptions of other researchers, further motivating the selection of a suitable modelling method for this project. A discussion on main themes and overall conclusions obtained from the reviewed literature on aerodynamic models for propellers has then been provided in Appendix B.4. Static aeroelastic analysis methods for rotor blades are reviewed next in Appendix B.5, thus covering the second main discipline of this thesis. This section contains details on structural modelling methods for propellers, approaches towards the structural analysis with composite materials, and a list of material properties for common types of composite materials to identify a material type that would be suitable for this project. After reviewing suitable analysis methods for rotor blades, previous cases involving the structural or aerodynamic optimization of propeller blades were reviewed in Appendix B.6 to identify approaches that may be applicable to this project and to quantify the extent of performance improvements that were obtained by other researchers. Finally, all important conclusions from this literature study are summarized in Appendix B.7.

B.1. Propeller Aerodynamic Modelling

There are several methods to compute the aerodynamic loads that act on propellers with varying levels of complexity, precision, and computational cost. Within this section, various approaches with different levels of fidelity will be introduced and discussed within the context of their applicability towards the analysis of propeller aerodynamics. A trade-off study between the applicable aerodynamic models has been completed to identify the model that is most capable of addressing the important phenomena and challenges that were introduced in Section 1.1 while maintaining a low computational cost.

A detailed history of propeller aerodynamic model development is provided by Wald [41], and a summary of this information is provided here. Rankine [73] and Froude [74] first developed the momentum theory of propellers for marine applications. Applying this theory to aeronautics, Wilbur and Orville Wright were the first researchers to combine blade element and momentum theories to predict propeller aerodynamic load distributions [75]. Following this, the lifting-line model developed by Prandtl [76] provided more detail to the representation of propeller aerodynamics. Betz [77] later derived the condition that a minimum induced loss propeller has a wake that consists of vortex sheets that move axially downstream as rigid screw surfaces with a constant wake pitch. Goldstein [40] extended this formulation by presenting a closed-form solution for the circulation distribution over lightly loaded propeller blades. The work of Goldstein was extended by Theodorsen [78] to be applicable to highly loaded propellers by considering the vortex system far downstream of the propeller rather than directly behind the propeller. Tibery and Wrench Jr. [79] later provided accurate tabulated values to the Goldstein function over a wide range of tip-speed ratios. Larrabee [80] then developed a design procedure for propellers, which offers convenience, although it does not make use of the generalization made by Theodorsen and instead is limited to the assumption of light loading [41]. Finally, this design procedure was extended by Adkins and Liebeck [35], who dropped the small-angle approximation that Larrabee relied on.

According to Leishman [37] and Wald, blade element momentum (BEM) theory is most commonly used for modelling propellers in industrial applications, despite the clearer understanding that is offered by modelling the propeller with higher fidelity methods. Any textbook may be referenced for more information on this approach, including [36, 37, 39, 43, 81]. Nevertheless, other models have also been considered in previous works regarding the aeroelastic tailoring of propellers or wind turbines. For example, Hegberg [26] implemented a vortex lattice method to calculate aerodynamic loads, and MacNeill and Verstraete [82] implemented a three-dimensional free-wake panel method using a surface distribution of quadrilateral sources and doublets. In the latter case, comparisons were made with experimental data for a propeller in propulsive mode, for which excellent agreement was obtained. Yamamoto and August [18] also used a three-dimensional Euler method to calculate propeller aerodynamic loads, which also yielded reasonable agreement with experimental results. A review of propeller modelling techniques using Euler methods has been presented by Zondervan [83]. In these additional cases, however, the flow is assumed to be inviscid, and this assumption has already been shown to yield considerable inaccuracies for propellers operating in at least partially separated flow, such as in energy-harvesting conditions. Due to the high computational cost associated with CFD methods, applications involving this approach have not been reviewed during this project, although lifting-line and vortex-lattice methods may be of interest as they provide a medium level of fidelity and have been applied to similar problems such as in [26, 82, 84–86].

B.1.1. Blade Element Methods

Blade element models are commonly used in the design and optimization of propellers because they usually require a small amount of computational resources. A comparison between several blade element models for propellers has been provided by Gur and Rosen [87] for straight and swept blades in propulsive conditions, however no such comparison has been performed for propellers operating in energy-harvesting conditions. The paper identifies and describes three classifications of models to be combined with blade element models for the calculation of propeller aerodynamic properties: momentum, lifting-line, and vortex models. From this study, Gur and Rosen concluded that all models provide a similar level of precision, although BEM generally has the lowest computational cost. The low computational requirement of BEM makes it particularly useful for static aeroelastic analyses, with several researchers using it for application. For example, the blade element momentum theory has been applied towards the aeroelastic analysis and optimization of propeller blades by Dwyer and Rogers [17], Chattopadhyay *et al.* [19], Khan *et al.* [4, 24], and Ferede [25, 27]. In all examples, the reasons that the authors cite for choosing to use blade element momentum theory are twofold. First, the method provides results that correlate reasonably well with experimental data, while also yielding meaningful design trends when applied in a numerical optimization procedure. Second, the computational cost is very low in comparison to alternative methods, thus making it suitable for optimization. Within the following three sections, various applications of blade element models will be reviewed. The important difference between the three types of models presented is the way that induced velocities are calculated. For instance, the blade element momentum model calculates induced velocities using actuator disk theory, whereas the lifting-line method, formalized by Prandtl [76], effectively represents the propeller blade as a bound vortex filament at the quarter-chord line. Trailing vortices are created to form the wake as a result of the variations in circulation over the blade. The vortex-lattice method is an extension of the lifting-line method to allow for the detailed blade and wake geometry to be resolved directly. Lastly, vortex models, initially formulated by Betz [77] and later extended by Goldstein [40] and Theodorsen [78], refer to formulations that are based on the optimal distribution of circulation along the propeller blade.

Blade Element Momentum Theory

As the name suggests, the blade element momentum theory applies the previously discussed momentum theory with blade-element theory to compute the lift and drag distributions of the propeller. The theory was pioneered by Glauert [39], and it is commonly applied towards the aeroelastic analysis of wind turbines [88]. Indeed, wind turbines are generally stall-regulated and therefore large sections of the blades may be subject to flow separation, and the BEM method provides a simple approach to modelling separation that relies on lift and drag polar plots for each input airfoil section [88]. For these reasons (also for its low computational cost), several commercial or open-source wind turbine aeroelastic analysis codes apply the blade element momentum method, including *GH Bladed*, *HAWC*, *BHAWC*, *FAST*, and *Flex5* [88].

Several authors including McCormick [89], Leishman [37], and Burton *et al.* [43] have suggested that the propeller blade advance angle is small enough to apply the small angle approximation at all radial locations of the propeller blade and at all advance ratios while applying the blade element theory. This approximation requires the loss in propeller thrust resulting from the induced drag to be considered negligible, and has been shown to be inaccurate by Whitmore and Merrill, who proposed a solution method that drops this small-angle approximation in [90], although their method does not include the effect of rotational velocity in the propeller slipstream. Several years earlier, Adkins and Liebeck [35] developed a similar blade element momentum model that did include a conservation of angular momentum to include rotational velocities in the propeller slipstream. Adkins and Liebeck also applied their method towards an optimal propeller design procedure in [35], therefore improving upon the design procedure that was applied by Larrabee [80], which relied on the small-angle approximation.

As discussed previously, Gur and Rosen [87] performed a comparative study between the three different types of blade element models (momentum, lifting-line, and vortex). For their BEM code, Gur and Rosen included rotational velocities in the propeller slipstream and did not apply the small-angle approximation. Through their comparison, it was shown that evaluating propeller performance during propulsive operation using BEM theory compared well with experimental data. Moreover, the agreement obtained with BEM yielded similar differences in comparison to the other two modelling methods, as shown in Figure B.1.

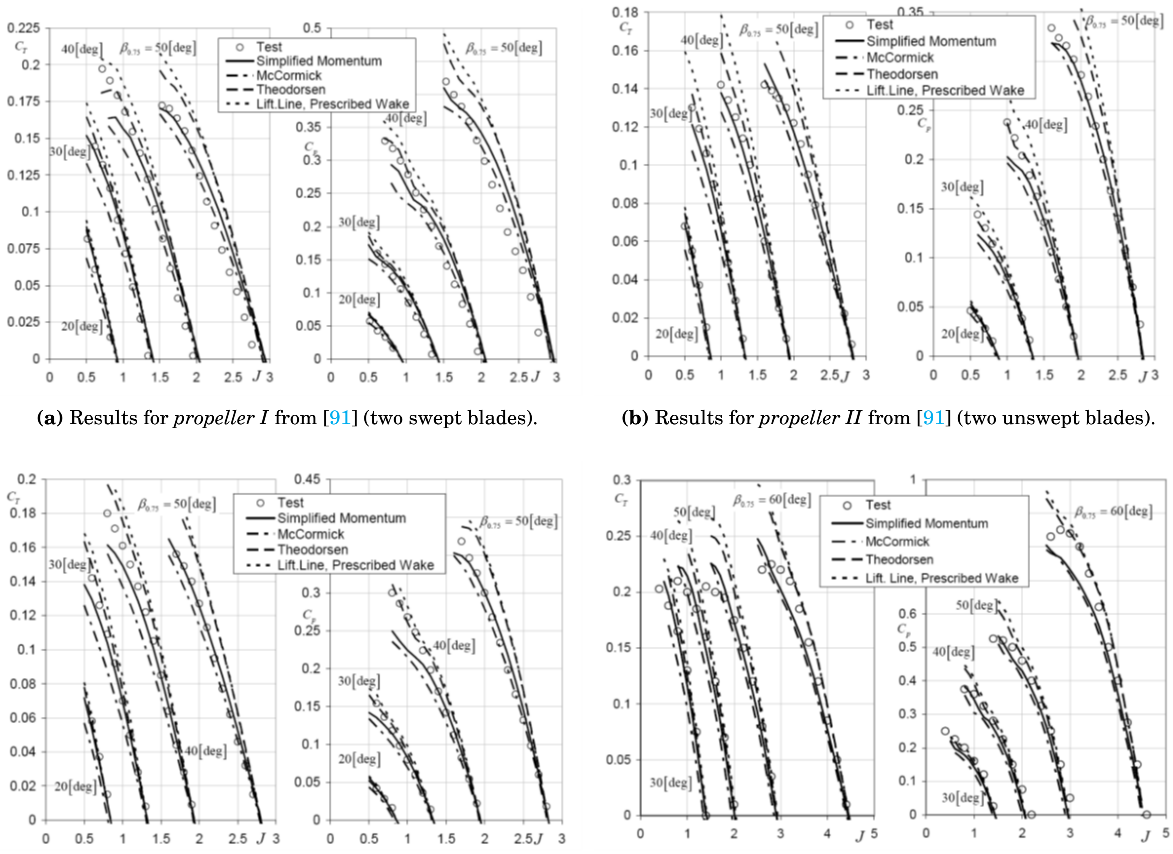

(a) Results for *propeller I* from [91] (two swept blades).

(b) Results for *propeller II* from [91] (two unswept blades).

(c) Results for *propeller III* from [91] (two unswept blades).

(d) Results for the propeller from [92] (four unswept blades).

Figure B.1: Comparison between C_T and C_P results from blade element models and experiments [87].

For applications in aeroelasticity, the effects of blade-axis deformations on aerodynamic loads have been identified as important to consider by Chattopadhyay *et al.* [19] and by Sodja *et al.* [3, 21]. Both authors applied the blade element momentum method of Adkins and Liebeck [35] and modified the procedure to allow for the loads to be affected by variations in sweep angle. The method that was applied by Chattopadhyay *et al.* [19] is not documented within their paper or within any derivatives of this work, although the method applied by Sodja *et al.* has been explained well in [3]. Sodja *et al.* expressed the BEM equations in vector form, therefore allowing a blade-axis of generic shape and orientation to be provided as an input and used to correct the calculated axial and tangential interference factors. Gur and Rosen also applied a different modification to the BEM equations (by adjusting the axial momentum theory) to account for the radial velocity component encountered by a propeller with a curved blade axis in [38]. Results presented in [3, 19, 21, 38, 93] all correlated well with results from high-fidelity simulations and physical tests, as shown for example in Figure B.2.

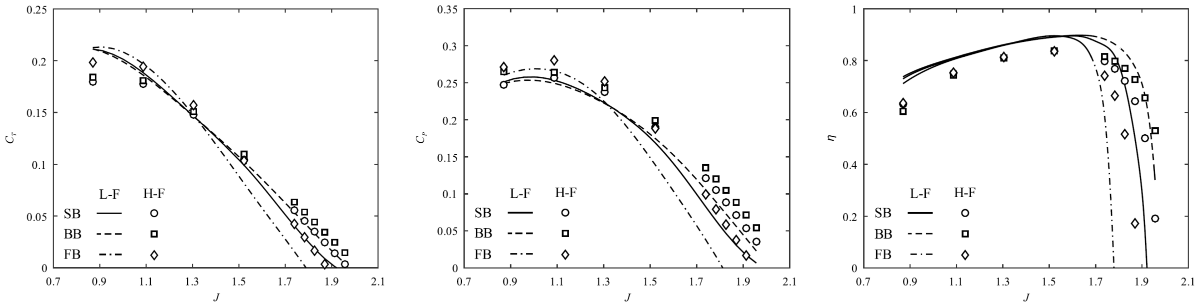

(a) C_T versus J. **(b)** C_P versus J. **(c)** η_P versus J.

Figure B.2: Results obtained using the extended BEM method of Sodja *et al.* within an iteratively coupled FSI model (L-F), and a previously validated high-fidelity FSI model (H-F) for flexible propeller blades that are either swept-forward (FB), swept-back (BB), or unswept (SB) [21].

The blade element momentum method has been found to yield results that are reasonable in comparison to experimental data and high-fidelity simulations in [43, 81, 87, 90, 93] among others, for propellers in propulsive conditions. However, for cases involving propellers operating in regenerative conditions, the accuracy of this method deteriorates as flow separation becomes more severe [10]. This has already been discussed within Section 1.1. Nevertheless, the general trends of the calculated distributive and integral properties appear to match the trends observed from other methods based on the results shown in Figure 1.2, Figure 1.3, Figure 1.8, Figure B.2, and Figure B.1 even if errors are present at exceedingly high or low advance ratios. It is likely that the errors present at these severe operating conditions cannot be mitigated by a different blade element model (such as lifting line or vortex theories), as the errors are likely caused by inaccuracies in the polar plots in the presence of partially or fully separated flow.

LIFTING-LINE AND VORTEX-LATTICE METHODS

The lifting-line method is another model that may be used to represent lifting bodies with a finite span. It is most effective for surfaces with high aspect ratios, and it was originally intended for fixed wings [36, 87]. The blade is discretized by a collection of vortex filaments with different strengths at the local aerodynamic centre. To satisfy the *Kelvin Helmholtz theorem*, these vortex lines bend and extend far downstream into the wake. The typical lifting-line model as applied to propeller aerodynamics is depicted within Figure B.3 to indicate this. Theory concerning the lifting-line model for fixed wings is provided by Anderson [94] for attached and separated flows, and by Drela [95]. In this way, the wake is explicitly resolved and therefore the empirical relations that the BEM model depends on to remain accurate do not need to be applied, such as the tip-loss factor [43]. The loads that are computed using this method therefore also depend on the shape of the wake, and three methods have been identified for modelling the wake Gur and Rosen:

a) A prescribed wake model

b) A semi-prescribed wake model

c) A free-wake model

In the *prescribed wake* model, the wake pitch is fixed and does not depend on the induced velocities; whereas in the *semi-prescribed wake* model, the wake shape is provided and its exact geometry depends mainly on the axial induced velocity. Finally, the *free-wake* model is the most complicated and the wake geometry is solved explicitly through the condition that trailing vortices have zero forces acting on them and the direction of the trailing vortices at any point in the wake is coincident with the direction of the local resultant velocity [87]. In their comparison between solutions obtained with the three approaches, Gur and Rosen [87] observed minimal differences in the solutions obtained, and aerodynamic loads were slightly overestimated in all cases, although the general trends in performance still matched.

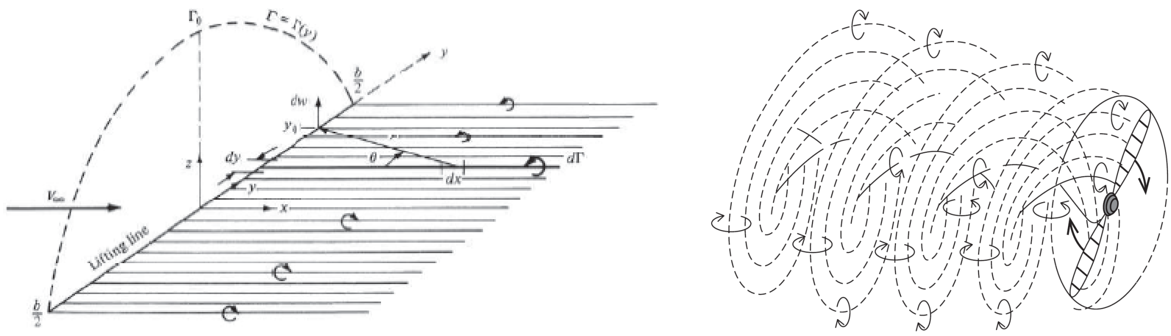

(a) The horseshoe vortex system of a fixed-wing [94]. **(b)** The vortex system of a propeller [43].

Figure B.3: Diagrams of the generic lifting-line model for a finite wing and a propeller.

To reduce computational cost, therefore enabling this method to be applied within an aeroelastic analysis and optimization procedure, it is desirable to use a prescribed wake model. Indeed, the free-wake method is generally reserved for performing unsteady analyses or evaluating complicated wake structures (such as a helicopter rotor in hover, where a significant amount of wake contraction would be present) [87, 88]. For the work of this thesis, evaluated loads are steady and the induced velocity components are relatively small in comparison to the freestream, and therefore it would be sufficient to use a prescribed helical wake model that neglects any wake contraction, similar to the work of Hegberg [26] or of Rand and Rosen [96], who respectively applied vortex-lattice and lifting-line rotor-blade aerodynamic models. To evaluate performance, lift polar data can also be supplied to obtain the circulation distribution using the *Kutta-Joukowski theorem*; the velocities induced by the wake may be obtained using the *Biot-Savart law* [94]. For a lifting-line propeller aerodynamic model with a prescribed helical wake that has a constant pitch and radius, Lerbs [97] derived solutions for the axial and tangential induced velocities in terms of potential functions under the assumption that the propeller hub is an infinite cylinder of zero circulation. Wrench Jr. [98] later improved upon this solution by providing expressions relating the axial and tangential induction factors directly to the wake pitch, yielding similar results to Lerbs. The closed-form approximations of Wrench Jr. are provided by Kerwin and Hadler [99]. The lifting-line method has been used within a few propeller or wind turbine aerodynamic analysis programs, such as in [85, 86]. Epps used the lifting-line method with a prescribed wake model for the calculation of aerodynamic loads acting on a marine propeller in [85, 100, 101]. More recently, Marten extended the lifting-line method in the development of an aeroelastic analysis program for modern wind turbine blades in [86]. The open-source code resulting from this work, *QBlade*, uses a lifting-line free vortex wake (LLFVW) that is largely based on the work of van Garrel [84], who developed a nonlinear steady wind turbine aerodynamic model using the LLFVW method. Both models apply the spacial discretization scheme from Figure B.4.

The LLFVW method is similar to the method that was applied by Hegberg [26], with the main difference being that Hegberg represented the wind turbine blades with vortex panels (using a prescribed wake model), which allowed the full blade geometry to be represented. The classical lifting-line theory was considered by Hegberg, although the vortex panel method was ultimately selected to enable a more detailed representation of the blade geometry, with a similar level of fidelity as the author's structural model, thus preserving the three-dimensional properties of each blade. Hegberg also used the panel method to obtain aerodynamic loads by evaluating the blade's bound vorticity distribution (thus not relying on the blade-element method for this, unlike the approach of van Garrel [84] and Marten [86]). The consequence of this is that Hegberg considered the flow to be inviscid, which implies that the flow is always fully attached over each blade [26]. The aerodynamic model that was applied by Hegberg is analogous to the aerodynamic model that was applied by Werter [30] and Dillinger [63] for aeroelastic tailoring of aircraft wings. It is suggested by Hansen *et al.* and in the list of future recommendations provided by Hegberg that the induced velocities that are calculated by the panel method at sections of the blade can be used to allow nonlinear aerodynamic loads to be evaluated using look-up tables within an iterative scheme, therefore allowing separated flow to be accounted for. This is effectively the same approach as applied by van Garrel [84] and Marten [86] (by evaluating the bound vorticity distribution using the lifting line method instead of the vortex lattice method), and it is already partially used by Hegberg to evaluate the parasitic drag encountered at each spanwise position of the wind turbine blade [26, 102].

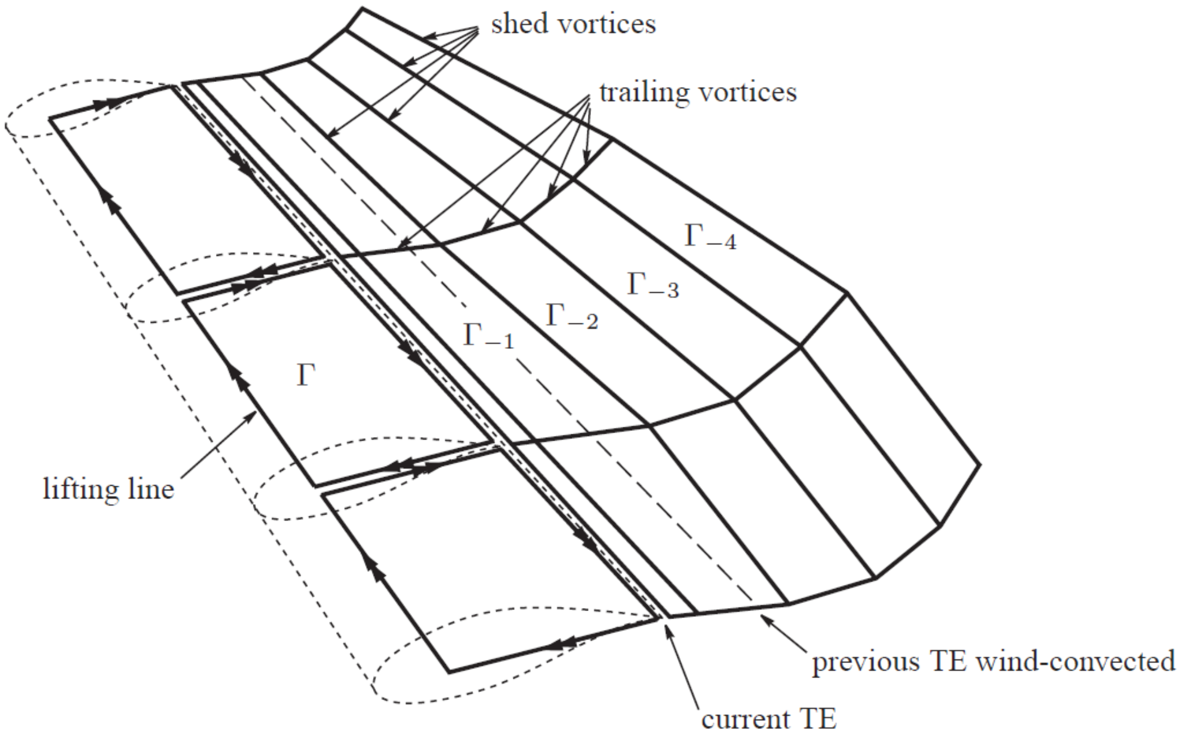

Figure B.4: The blade and wake spacial discretization method of van Garrel and Marten [84].

A review of lifting-line and vortex-lattice methods (VLM) for evaluating rotor-blade aerodynamics has been provided by Lee *et al.* in [103], although their discussion is primarily limited to free-vortex wake methods, which are not the main concern of this project. The authors do, however, provide a discussion on *nonlinear vortex-lattice methods* (NVLM), which combine the typical vortex-lattice method, as used within the work of Hegberg, with airfoil lookup tables, semi-empirical stall-delay models (see Appendix B.2.2), and vortex strength corrections [103]. The relevant aspects of this review include the discussion on vortex-lattice methods and the method of applying corrections with semi-empirical lift and drag polar data. Hegberg and Lee *et al.* both reference Katz and Plotkin [104] for a detailed description of the governing equations for the vortex-lattice method. According to Lee *et al.*, the sectional lift and drag forces evaluated with lookup tables may be used to correct the circulation distribution. A detailed iterative procedure has been provided and validated by Lee and Lee [105] to perform this calculation for a free-wake VLM code. It may be possible to adapt this procedure and implement it in the prescribed-wake code of Hegberg. This method facilitates the evaluation of nonlinear aerodynamic forces with a more precise method of evaluating induced velocities in comparison to BEM, due to the inclusion of three-dimensional effects.

One of the most important features differentiating the lifting-line and vortex-lattice methods in comparison to the blade element momentum theory model is that it intrinsically represents important aspects of the flow that the blade element momentum theory must rely on engineering approximations to capture. For instance, the VLM and lifting-line methods intrinsically represent three-dimensional effects, such as losses in circulation near the root and tip of each propeller blade [106]. However, because the selected aerodynamic model will be used to solve a somewhat large optimization problem, computational time is a crucial factor, and the lifting-line method is generally more computationally expensive in comparison to the BEM model. Regarding these concerns, comparisons were made between BEM and lifting-line or panel methods for wind turbines in [102, 106–109], and for propellers in [38]. Although the models used were different in each comparison, the general trends were roughly the same: The BEM and lifting-line models compared reasonably well in on-design conditions, although the induction factors evaluated by the BEM model were found to yield errors in cases of excessively high or low tip speed ratios. Gur and Rosen [87] observed that the lifting-line models outperformed the BEM models at low advance ratios, while Ismail and Okita [108] found that the BEM model noticeably over-predicted the wind turbine performance outside its normal operating conditions, and de Luna *et al.* [109] observed only marginal differences at off-design conditions. Moreover, Blondel *et al.* [107], Hauptmann *et al.* [106], and Perez-Becker *et al.* [102] did not observe any large differences between the two approaches within any of the operating conditions that would be of interest to this project. Lastly, the lifting-line models considered for comparisons all relied on a free-vortex wake representation and therefore the simulation time was between 6- and 34-times greater than that of the BEM codes according to Ismail and Okita, although Hegberg reported a relatively low computational time for evaluating aerodynamic loads using a prescribed-wake code despite not providing quantitative data on this. Thus, it is possible to conclude that the lifting-line or vortex-panel method should be considered if three-dimensional effects are important to model directly (such as in cases involving a large amount of wake contraction, non-uniform inflows, or complex blade geometries). For this project, it is anticipated that the required level of precision would be obtained by the more simple BEM model, as the geometry of the blade is expected to remain fixed, and BEM was found to at least replicate general trends at operating conditions of interest to this project.

VORTEX METHODS

Vortex theory was initially developed by Betz [77], who established a design criterion for minimizing the induced losses of a propeller. According to Betz, a minimum-induced-loss propeller creates a wake of helical vortex sheets with constant pitch along the radial axis, although the pitch may vary in the axial direction. This condition is only satisfied at one operating condition, which has maximum efficiency (excluding any viscous losses). A diagram depicting this condition is shown in Figure B.5.

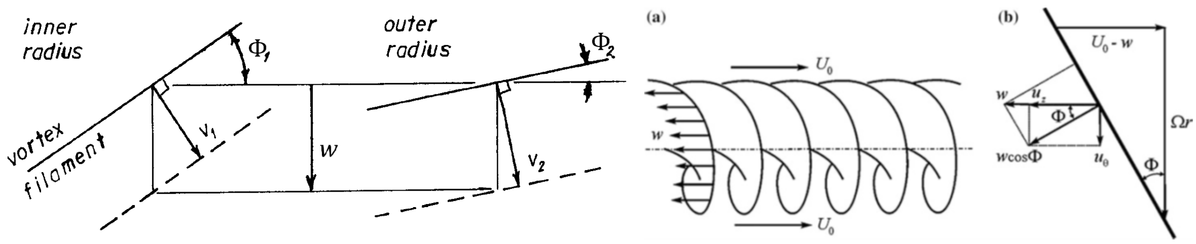

(a) Betz's rigid wake condition for minimum induced loss propellers, as indicated by the displacement velocity at two blade sections [80].

(b) A diagram of the wake behind an ideal wind turbine, showing a constant axial displacement velocity [81].

Figure B.5: Diagrams indicating that the wake of each blade section has an equal displacement velocity given by w, where $w\cos(\Phi)$ is the local vortex sheet velocity and Φ is the local helix angle of the vortex sheet, with the induced velocity always being orthogonal to the wake pitch.

A closed-form expression for the optimal circulation distribution over a lightly loaded propeller blade was first developed by Goldstein [40]. Theodorsen [78] subsequently extended this to heavily loaded propellers by identifying that the circulation distribution depends wholly on the configuration of vortex sheets in the wake, and that these vortex sheets do not need to have the same pitch as the blades of the propeller [41]. Another similar model was produced by McCormick [89] with the same assumptions as Theodorsen [87]. Vortex theory models rely on the assumption that the induced velocity in the propeller plane is orthogonal to the relative incoming flow velocity (as shown in Figure B.5), and that the axial displacement velocity of the vortex sheets produced by the propeller is half of its value in the far-wake. Gur and Rosen [87] compared results obtained with the vortex models of Theodorsen and McCormick to the results obtained with lifting-line and BEM models. Details on the calculation of the induced velocities are provided in [87] and Figure B.1 contains sample results of this comparison. As already mentioned, the simpler BEM model appears to provide an equal or more consistent approximation in comparison to the two vortex models. For this project, the advantages of using slightly more computationally expensive vortex models over the BEM models are not clear, although the vortex theory is helpful for explaining the *tip-loss factor*, which has been reviewed in Appendix B.2.1 and documented in Section 2.1.

B.2. CORRECTIONS FOR AERODYNAMIC MODELS

All three of the aerodynamic models discussed in the previous section require the use of blade element theory with nonlinear airfoil data to represent the effect on lift and drag due to flow separation and the transition from laminar to turbulent flow. Because the flow passing over each rotating blade is subjected to Coriolis and centrifugal forces, it will tend to travel outward, therefore causing the inboard sections to be more resistant to boundary layer growth, which affects the onset of both transition and separation. Several stall-delay models have been proposed to address this effect, and these models have been reviewed in Appendix B.2.2. Additionally, the BEM model is incapable of accounting for losses in circulation at the root and tip, and therefore root- and tip-loss corrections have been discussed briefly in Appendix B.2.1.

B.2.1. TIP LOSS FACTORS

For lifting-line and vortex methods, the root- and tip-loss factors are not required, since the solvers directly resolve losses in circulation at the root and tip of the blades. However, for the blade element momentum method, corrections for the root and tip losses are essential to ensure that loads are appropriately represented. Indeed, when the chord at the tip is finite, blade element momentum theory will produce a non-zero lift when it should instead be zero. This loss of lift at the tip of the rotor is important and if it is neglected, then the thrust for a given amount of power will be noticeably overestimated [36, 37]. A review of the methods used to account for these losses is provided by Shen *et al.* in [110]. The most well-known is the Prandtl tip-loss factor, which is provided in Equation (2.7) and documented in [41], among others.

The tip-loss factor provided by Glauert is the most widely used due to its ease of implementation [36, 37, 41, 43]. However, other tip loss factors have been provided by Wilson and Lissaman [111] and de Vries [112], although for the rotor that was analysed by Shen *et al.*, the differences in blade-loading distribution between the three methods were nearly indistinguishable. Plots to indicate this have not been included within this report for brevity. Shen *et al.* also suggests a modification to this tip-loss factor, which is recommended by Burton *et al.*, although this model depends on experimental data and is therefore not practical when propeller performance is not known *a priori*. For this project, it is only important that losses near the blade tips are represented with reasonable accuracy, and therefore the method of Glauert was selected over the method of Goldstein. This method has also been featured in most of the blade-element momentum models that were reviewed in this report (such as in [3, 19, 35, 42, 80, 87, 90, 113, 114]).

B.2.2. STALL-DELAY MODELS

3D effects on rotating blades near stall were investigated experimentally and with CFD methods by Himmelskamp [115], Dwyer and McCroskey [116], Young and Williams [117], Madsen and Christensen [118], Snel *et al.* [119], Narramore and Vermeland [120], and Robinson *et al.* [121]. The results of these investigations indicate that the sectional lift-curve slope may differ significantly from the otherwise 2D lift curve slope due to three-dimensional effects of rotation. This is directly due to the centrifugal and Coriolis forces that act on the boundary layer flow that passes over the propeller blades. In general, this effect tends to delay the onset of separation and transition, as the additional acceleration components tend to suppress the boundary layer growth [122]. At a given spanwise position, $\underset{\sim}{r}$, the Coriolis acceleration is given by Equation (B.1) and the centrifugal acceleration is given by Equation (B.2) [122]. Figure B.6 provides an indication of how the Coriolis and centrifugal forces will influence the trajectory of a fluid particle and the sectional lift coefficient curve. According to Leishman [37], a precise method that does not rely on high-fidelity simulations for modelling this effect on the boundary layer is still missing. Therefore, semi-empirical *stall-delay* models are generally used to account for this.

$$a_{\text{cor.}} = -2\underset{\sim}{\omega} \times \underset{\sim}{V} \tag{B.1}$$

$$a_{\text{cen.}} = -\underset{\sim}{\omega} \times (\underset{\sim}{\omega} \times \underset{\sim}{r}) \tag{B.2}$$

As shown in Figure B.6, the Coriolis acceleration vector will act tangentially to the blade rotation and towards the blade trailing edge, whereas the centrifugal acceleration vector will point outward in the radial direction. This suggests that the stall-delay effect is more pronounced near the hub, as fluid particles get transported outward from the blade root, which leads to a thinner and therefore more stall-resistant boundary layer near the root, as indicated by the more favourable C_l-α curve shown in Figure B.6b. Goyal *et al.* [10] confirmed this by studying angles of attack where rotational effects are most significant for the TUD-XPROP propeller and providing a plot of the difference in lift and drag coefficients between the calculations with and without effects of rotation. Results from this investigation are shown in Figure B.7. It is also apparent from this plot that the stall-delay effect affects the drag coefficient even at very low angles of attack near the root section of the blade. The propeller blade under consideration in this case is cambered and thus experiences separation at lower magnitudes of negative angles of attack. The stall-delay effect appears to have a more pronounced effect at negative angles of attack in this case, because the separation is less gradual in comparison to if it occurred at positive angles of attack.

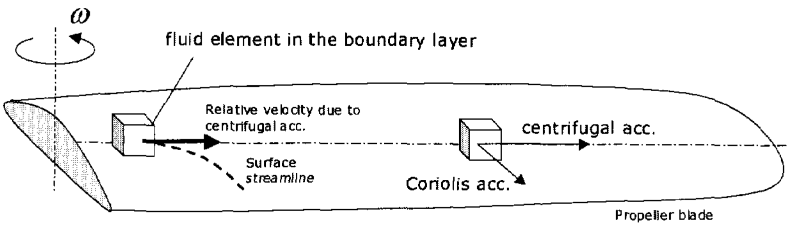

(a) A drawing demonstrating the effect of Coriolis and centrifugal forces on the trajectory of a fluid particle in the boundary layer [122]

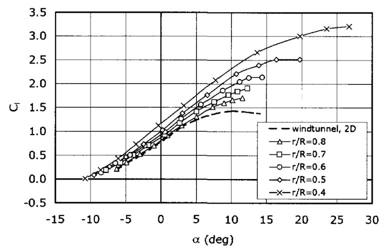

(b) An example of the effect of rotation on the spanwise 2D lift coefficients [115].

Figure B.6: Effects of rotation on sectional properties of a propeller blade (reproduced from [122]).

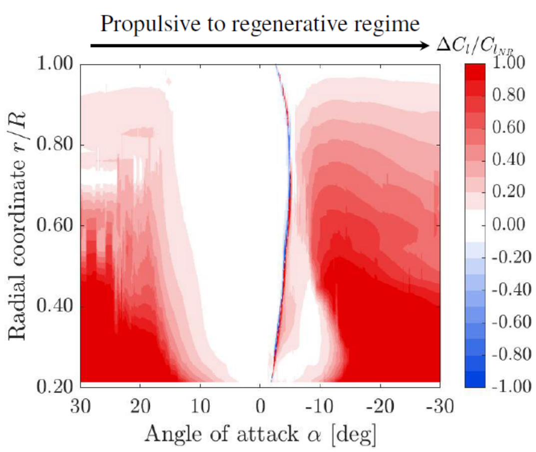

(a) Lift.

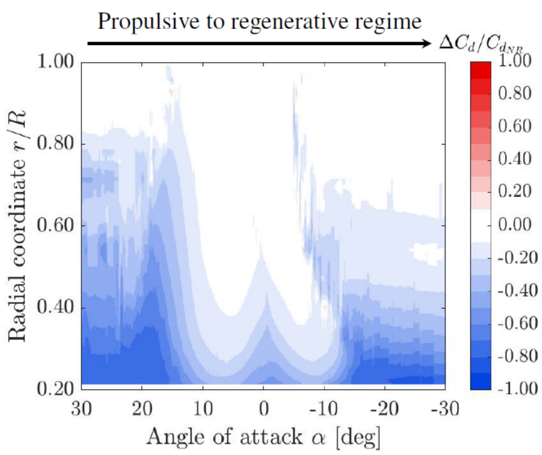

(b) Drag.

Figure B.7: Plots of the influence of effects due to rotation on the prediction of either lift or drag using blade element momentum theory for the TU Delft *XPROP* propeller [10].

Because the aerodynamic models that have been presented previously are either inviscid or rely on experimental data for the lift and drag coefficient information, stall-delay models should be included with any model that is capable of capturing nonlinear aerodynamic loads. A comparison between different stall delay corrections within a BEM model was completed by Morgado *et al.* [123] for propellers operating at low advance ratios. However, mistakes were present in the equations that they presented, and separation did not appear to occur for most of the operating conditions under consideration in their analysis. No other comparisons between stall-delay models appear to have been performed for propellers, although Breton *et al.* [124] performed a similar comparison for wind turbines using a prescribed-wake lifting-line model. Breton *et al.* did not modify any of the stall-delay model coefficients to match their experimental data, and therefore were unable to observe common trends between any of the results from different models. It is anticipated that the stall-delay effect is more pronounced during propulsive conditions in comparison to regenerative conditions, since the centrifugal force increases quadratically with rotational speed and the Coriolis force increases linearly with rotational speed. Hence, the acceptable model parameters may differ between the two modes of operation. Some applicable stall delay models have been reviewed within this report. Many of the developed models apply the expressions shown in Equation (B.3) and Equation (B.4) to respectively correct the lift and drag coefficients; including models of Snel *et al.* [119], Du and Selig [125], Chaviaropoulos and Hansen [126], Gur and Rosen [127], and Dumitrescu and Cardos [128]. Note that terms g_{C_l} and g_{C_d} correspond to model coefficients that are determined from empirical or numerical data.

$$C^{\text{visc}}_{l,\text{3D}} = C^{\text{visc}}_{l,\text{2D}} + g_{C_l}\left[C^{\text{inv}}_{l,\text{2D}} - C^{\text{visc}}_{l,\text{2D}}\right] \tag{B.3}$$

$$C^{\text{visc}}_{d,\text{3D}} = C^{\text{visc}}_{d,\text{2D}} + g_{C_d}\left[C^{\text{inv}}_{d,\text{2D}} - C_{d,0}\right] \tag{B.4}$$

Coefficients that have the subscript "3D" will always refer to values that include effects of rotation, and the subscript "2D" will always be used to denote values that do not include effects of rotation.

Modelling Stall-Delay Using the Method of Corrigan and Schillings

One of the oldest stall delay models for propellers or helicopter rotors was developed by Corrigan and Schillings [129], which correlates stall delay to the ratio between the local blade chord and radial position. This implies that the stall-delay phenomenon increases proportionally with local solidity. Corrigan and Schillings continued the work of Banks and Gadd [130], who analysed pressure gradients in the boundary layer to determine the location of laminar separation by assuming chordwise and radial boundary layer profiles. The model of Corrigan and Schillings also requires the assumption that the external flow on the suction surface has a constant adverse velocity gradient in the streamwise direction, given by K [124]. As shown in Figure B.8, the authors define an angle Θ, between two lines starting at the axis of rotation and extending respectively to the trailing edge and the location of separation, which is approximated by c/r. Equation (B.5) is then used to determine the 3D lift coefficient, and no relation is provided for the drag.

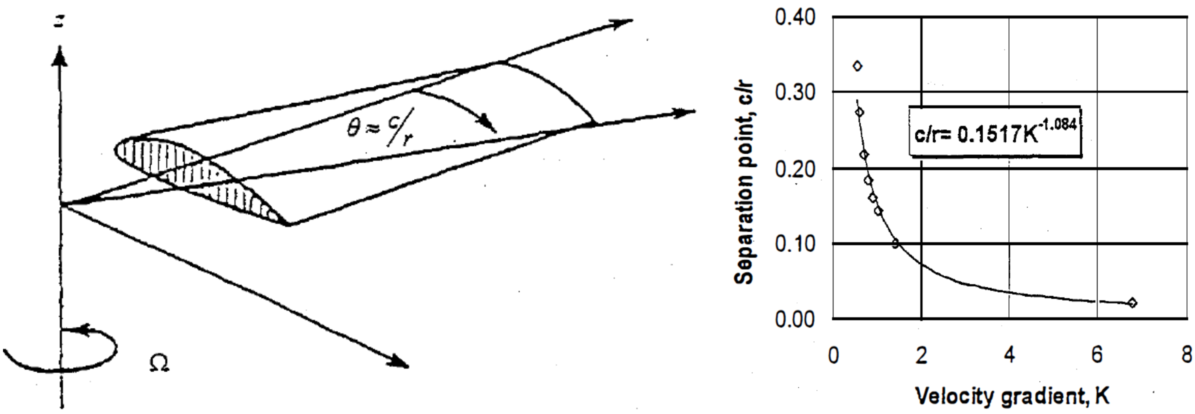

(a) A sketch of the coordinate system that was used.

(b) An approximation of the adverse velocity gradient using the separation location.

Figure B.8: Images corresponding to the stall-delay model of Corrigan and Schillings [131].

The model of Corrigan and Schillings effectively represents the delay of stall by a perturbation in angle of attack, and assumes that separation occurs near the leading edge [124, 131]. More information on this model and its assumptions may be found in [131] and has been left out for brevity. Contrary to most of the models, which were compared with data for wind turbines, Equation (B.6) was obtained largely through comparisons with empirical data for helicopters and propellers (a value of $n = 1$ is usually used) [131].

$$C^{\text{visc}}_{l,\text{3D}} = C^{\text{visc}}_{l,\text{2D}} + (\alpha + \Delta\alpha)C^{\text{inv}}_{l_\alpha} \tag{B.5}$$

$$\Delta\alpha = \left(\alpha_{C_{l,\max}} - \alpha_{C_l=0}\right)\left[\left(\frac{K(c/r)}{0.136}\right)^n - 1\right] \qquad n \in [0.8, 1.6] \tag{B.6}$$

Modelling Stall-Delay Using the Method of Snel

The seminal work of Snel *et al.* [119, 132] involves the development of 3D boundary layer equations on a rotating blade in cylindrical coordinates. The authors then implemented these equations into a 2D viscous-inviscid interaction program. Through comparisons with simulation and experimental results for a wind turbine, the following simple correction was applied, corresponding to Equation (B.3).

$$g_{C_l} = 3.1\left(\frac{c}{r}\right)^2 \tag{B.7}$$

Bosschers *et al.* used the modified 3D boundary layer equations that were proposed by Snel to include rotational effects, and implemented them within XFOIL to form the program RFOIL [11]. This is the program that was used by Goyal *et al.* within their BEM code for comparisons with experimental data and CFD in [10]. The general solution procedure is explained by Bosschers *et al.* in [11]. RFOIL is most applicable in high-lift conditions, where the separated flow is affected primarily by the Coriolis force, pressure force, and shear stress [122]. Nevertheless, this method is advantageous because it does not require empirical data and thus is less configuration-specific than the methods discussed previously.

Several stall-delay models were developed following the work of Snel [119], using either the boundary layer equations that were formulated or experimental data. For example, Du and Selig [125], Chaviaropoulos and Hansen [126], Eggers *et al.* [133], Lindenburg [134], and Dumitrescu and Cardos [128] developed stall-delay models using both calculated and experimental data for horizontal axis wind turbines. Models developed by these authors will not be discussed further within this report, as it is suggested that the stall-delay phenomenon is primarily dependent on the local chord (c/r), airfoil shape, and twist angle [88, 124, 126]. Furthermore, the results presented by Breton *et al.* [124] during their comparisons between six of the stall-delay models under consideration showed strong differences between model predictions for the power, lift, and drag. This indicates that empirically derived models are poorly representing the underlying physics and instead are highly dependent on the configuration being analysed. For these reasons, the only models considered were developed for propellers in particular.

MODIFICATIONS TO THE MODEL OF SNEL

Regarding the lift coefficient correction, Snel [132] and Gur and Rosen [127] both reason through physical arguments that $\lim_{(c/r)\to\infty} g_{C_l} = 1$ and $\lim_{(c/r)\to 0} g_{C_l} = 0$. Resulting from this, both authors suggested using a hyperbolic tangent function within g_{C_l}, as it possesses these properties and is mostly linear between 0 and 1 [127]. Gur and Rosen showed promising results when comparing the calculated performance of propellers with this correction to experimental data at low advance ratios. However, the drag coefficient correction, g_{C_d}, is less straightforward. Some researchers, including Du and Selig [125], suggest that the drag coefficient decreases with rotation through arguments that are motivated by results from CFD simulations. Whereas other researchers suggest that the drag coefficient will decrease due to a delayed separation point that reduces the size of the wake [135]. Several other researchers, including Lindenburg and Chaviaropoulos and Hansen, have also suggested that the drag force will increase [135]. For these reasons, it is tempting to not modify the drag coefficient, as suggested by Corrigan and Schillings, Snel *et al.*, Dumitrescu and Cardos, and Bosschers *et al.*.

Gur and Rosen [127] suggest using Equation (B.8) to correct the lift coefficient, which may be viewed as a potential generalization for the model of Snel [132], since the coefficient used in that case was just fit to experimental data. Veldhuis [122] suggests that $k_1 = 0$ and $k_2 = 3$ may yield interesting results, as it is similar to the model of Snel [132] and using a hyperbolic tangent function introduces the potentially favourable properties that were previously discussed. Nevertheless, this model has not been compared with experimental data.

$$g_{C_l} = \tanh\left(k_1(c/r) + k_2(c/r)^2\right) \tag{B.8}$$

B.3. AVAILABLE PROPELLER AERODYNAMIC ANALYSIS CODES

Some codes that are either open-source or available at the TU Delft have been explained in this section to identify the assumptions and methods that have been applied by other researchers. Table B.1 contains a tabulated summary of propeller aerodynamic analysis codes that would be suitable for optimization. Most of the codes contained within this list apply blade element momentum models. Brief summaries of each code have also been provided below. In general, all of these programs were largely developed from the same underlying theory, and are therefore expected to behave similarly, with differences in performance being largely due to minor variations in the assumptions considered.

Comparisons between results from physical tests, RANS simulations, and three of the aerodynamic analysis codes shown in Table B.1 are provided by Bergmann *et al.* in [137]. The authors provide a short review of JavaProp, JBLADE, and XROTOR. JBLADE and XROTOR appear to perform similarly, whereas JavaProp appears to consistently underperform. From this comparison, it was concluded that JavaProp is only suitable for preliminary analysis due to the large errors observed, whereas XROTOR provides a level of fidelity that is more suitable for blade design applications, and it especially provides a good thrust prediction. The errors observed when using JBLADE are primarily due to its poor performance in post-stall conditions. Thus, from the results obtained in [137], XROTOR appears to be most suitable for this project; the aerodynamic model within XROTOR is also closer to the level of fidelity that is provided by the structural model of PROTEUS. The other codes listed in Table B.1 were not directly compared in any studies, although CCBlade would be interesting to consider for applications related to optimization, since it was primarily developed for this purpose [42].

Table B.1: Information on open-source or otherwise available propeller aerodynamic models.

Model	Year	Type & Theory Reference	Author(s)
CCBlade	2020	BEM [42, 113]	Ning
JavaProp	1996	BEM [80, 138, 139]	Eppler and Hepperle
JBLADE	2014	BEM [140–142]	Morgado *et al.*
PROTEUS[a]	2019	VLM (prescribed wake) [26, 104]	Hegberg
QPROP	2007	BEM [143]	Drela
XROTOR	2003	BEM [35, 80, 143], lifting-line, or vortex [40]	Drela and Youngren
XFOIL	1986	Viscous airfoil analysis (no rotation) [145]	Drela
RFOIL	1996	Viscous airfoil analysis (with rotation) [11]	Bosschers *et al.*

[a] PROTEUS generally refers to the complete structural analysis and optimization program of Werter and De Breuker [29], although in this context, it only refers to the rotor aerodynamic analysis method that was applied by Hegberg in [26].

XROTOR and QPROP Both of these applications were developed by Drela [143], and feature very similar formulations for the BEM solvers. The BEM model uses the Prandtl tip-loss factor and is based on the classical theory of Goldstein [40] and Theodorsen [78], which was reformulated by Larrabee [80] and Adkins and Liebeck [35]. In both codes, the wake has zero contraction (the induced velocity vector is orthogonal to the resultant incoming flow velocity) and there is a notable difference in the application of the Prandtl tip-loss factor, which includes effects at the blade root, as shown in Equation (B.9). It is also expressed using the local wake advance ratio, λ_2^{w} (instead of the inflow ratio, λ_2). This is possibly more realistic for heavy disk loading, though it likely would not be noticeable for cases investigated in this project. Otherwise, the theory used is nearly identical to that of Adkins and Liebeck.

$$F_{\mathrm{tip}} = \frac{2}{\pi} \arccos\left[\exp\left(-\frac{N_{\mathrm{b}}}{2}\frac{1-\tilde{r}}{\lambda_2^{\mathrm{w}}}\right)\right]\sqrt{1+\left(4\lambda_2^{\mathrm{w}}/(\pi N_{\mathrm{b}}\tilde{r})\right)^2} \qquad \lambda_2^{\mathrm{w}} = \tilde{r}\tan\left(\varphi\right) \tag{B.9}$$

XROTOR was later modified to also feature a prescribed-wake lifting-line solver and a vortex solver based on the theory of Goldstein [40]. The lifting-line theory that is applied within XROTOR is not documented anywhere by the authors, and has a higher computational requirement than the other two approaches, though the prescribed wake appears to have a constant pitch with zero contraction.

PROTEUS This code has been discussed briefly within Appendix B.1.1, and it features the only aerodynamic model of the presented alternatives that does not rely on the blade element method. In this context, PROTEUS describes the prescribed-wake VLM model that was used by Hegberg [26] to evaluate wind turbine aerodynamic loads. The flow over the blades does not feature any viscous effects because it is evaluated using a linear aerodynamic theory. This code also may be modified to include viscous effects such as separation, for example, using the method of Lee and Lee [105]

JBLADE This program is slightly more recent, and largely based on the PhD research of Morgado [142]. Like the others, it is also based on the classical blade element momentum theory, which relies on 2D polar plots from XFOIL that are corrected by an empirical post-stall model. JBLADE includes a calculation for radial induced velocities, meaning that it could be suitable for more heavily loaded rotors, though it relies on the assumption of a constant axial induced velocity during the radial induced velocity calculation only (to apply the free-vortex condition), which is generally unrealistic for propellers and wind turbines [81].

JavaProp This program does not appear to contain any notable differences from the original method of Larrabee [138]. Additionally, tangential induced velocities are not included in its calculations. For these reasons, this code is expected to provide the least accurate prediction of propeller performance.

CCBlade This code was developed with the purpose of being applied within a numerical optimization procedure, and it is intended to be used for both the analysis of wind turbines and propellers. As such, a correction was applied for cases involving large negative induction factors ($a < -0.5$) that result in a non-physical flow reversal in the far-wake to be represented by the traditional momentum theory (this is not relevant for positive thrust conditions, although required during negative-thrust operation), and a modification to the solution procedure is applied to allow the formulation to be capable of handling cases with zero freestream velocity (such as for a hovering rotor) [42]. Lastly, the calculations applied by Ning [42] enable all induced velocities to be obtained by minimizing only one residual function that depends solely on the inflow angle, φ, thus making the method particularly reliable for optimization, where numerical difficulties can be encountered. Otherwise, it uses the conventional Prandtl tip loss factor and the theory of Adkins and Liebeck for the analysis of propellers.

B.4. CRITICAL DISCUSSIONS ON AERODYNAMIC MODELLING METHODS

Approaches to modelling the aerodynamics of propellers have been reviewed within this section, with the goal of identifying the most suitable method for use within an aeroelastic analysis and optimization procedure. Within this context, it has been identified that propeller performance is usually evaluated with blade-element models, as the use of higher fidelity approaches involving CFD is precluded by computational cost. Thus, two types of models were found to be suitable for this project: blade element momentum (such as the approach of Adkins and Liebeck [35] or Sodja *et al.* [3, 21]), and prescribed-wake VLM or lifting-line methods (like the model used by Hegberg [26]). With these classifications, Table B.2 groups and summarizes characteristics of each method to highlight their advantages and drawbacks.

Table B.2: Comparison between characteristics of BEM and VLM or lifting-line methods.

Characteristic	Blade Element Momentum	VLM or Lifting-Line
Intrinsic Effects	• Axial Induced Velocity • Tangential Induced Velocity	• Axial induced velocity • Tangential induced velocity • Radial induced velocity • Finite number of blades • Three-dimensional effects (including sensitivity to changes in blade-axis geometry)
Engineering Corrections	• Finite number of blades • Rotational effects on boundary layer flow	• Rotational effects on boundary layer flow
Simulation Time	• Minimal	• Prescribed wake: low • Free wake: high

Any nonlinear blade element method that is selected requires nonlinear static lift and drag polar plots to be used, which include effects of rotation due to the presence of powerful Coriolis and centrifugal forces. Additionally, while the airfoils of the TUD-XPROP propeller are known, experimental lift and drag polar plots for the airfoils of this propeller have not been collected. Therefore, the 2D lift and drag polar plots will need to be evaluated using a numerical procedure such as XFOIL. For representing the effects of rotation, only the nonlinear aerodynamic model that was proposed by Bosschers *et al.* [11] may be used for calculating sectional lift and drag coefficients. This decision was made despite the problems with RFOIL that were observed by Goyal *et al.* [10], as they report that it led to an overestimated prediction of stall near the tips of the propeller blade. The key advantage that RFOIL has over all other methods that were reviewed in this chapter is that it is not configuration-dependent, and therefore does not rely on any experimental data. Indeed, it was observed in Appendix B.2.2 that all other stall-delay models require empirical data for the selection of coefficient values. Because it has been shown by Breton *et al.* [124] that the applicability of these semi-empirical stall-delay models depends heavily on the choice of coefficient values, they have all not been considered appropriate for this project.

As identified in Appendix B.1.1, the main advantage of using a lifting-line or VLM code to calculate propeller aerodynamic loads is that it does not require an engineering correction model to be applied for considering root and tip losses. It also will likely provide a more precise result for the induced velocities at each blade element, as the 3D blade geometry will be accurately represented. Nevertheless, it is not clear whether this increase in fidelity will yield a noticeable improvement in the ability to quantify general design trends for improved regenerative performance (as is the primary purpose of this project). Indeed, the baseline propeller blade even has a simple geometry with zero sweep and lean. However, it has even been shown by Sodja *et al.* [3] and Chattopadhyay *et al.* [19] that it is possible to quantify the effect of changes in sweep or lean on aerodynamic loads using a BEM code. The effectiveness of using BEM for propeller aeroelastic analyses is further confirmed through the reasonable agreement that was obtained by Sodja *et al.* [21] when they compared their low-fidelity aeroelastic analysis approach, which relies on BEM, to high-fidelity FSI simulations, which rely on CFD solutions.

For this project, VLM is not expected to provide noticeable improvements in the ability to represent lift and drag coefficients during conditions involving flow separation. Indeed, the main source of the errors shown in Figure 1.3 according to Goyal *et al.* [10] concerns the calculation of lift and drag coefficients, and not necessarily the calculation of induced velocities. It is therefore likely that similar discrepancies will always be present at excessively high or low advance ratios, regardless of the type of model that is selected. This is because the lift and drag coefficients are calculated in the same way in all blade element models. Hence, an otherwise better approximation for the lift and drag coefficients in the presence of separated flow may be equivalently applied to either model. For these reasons, blade element momentum theory is sufficient for calculating blade loads and evaluating propeller performance during this research.

Lastly, because the relative flow velocity is expected to be significantly larger than the induced velocity in all cases under consideration for this project, only a small amount of wake contraction is expected. Resulting from this, it may be concluded that the momentum theory model proposed by Glauert [39] is sufficient for evaluating induced velocities. Moreover, because the propeller being analysed during this project will always be lightly loaded, the vortex model that was applied by Goldstein [40] could also be applicable. During this project, it was considered sufficient to approximate losses due to approximate losses in circulation at the root and tip of each blade with the *Prandtl tip-loss factor* instead of the potentially more precise circulation function developed by Goldstein. While the uncertainty that is associated with each approximation concerning the propeller aerodynamics may compound to provide a noticeable decrease in precision, it is expected that general trends will be reasonably represented. To confirm this, model verification and validation has been provided in comparison with results obtained by Goyal *et al.* [10] and Nederlof *et al.* [13] for aerodynamic loads and performance in propulsive and regenerative conditions.

B.5. Rotor Blade Structural Modelling and Aeroelasticity

B.5.1. Structural Analysis

In most cases, the propeller structure is represented as a cantilever beam, with aerodynamic loads acting as a distributed transverse force and torsional moment out the span of the blade, and centrifugal loads acting radially [146]. For both propellers and wind turbines, the loading and structural models that have been applied are fairly similar. For propellers that are not made from composite materials, structural models that are applied within an optimization program are usually mathematical models based on Euler-Bernoulli beam theory for bending and Saint-Venant theory for torsion. For example, Sodja *et al.* [3], Gur and Rosen [28], and Hoyos *et al.* [147] applied this principle during the optimization of propeller blades made from homogenous and isotropic elastic materials. For rotor blades that are made from composite materials, the finite element formulation is usually applied to enable a more detailed representation of each laminate. For example, Cornell and Rothman [146], Khan [4], and Yamamoto and August [18] used 2D shell elements within a finite element analysis program to compute deformations and stresses. For structural optimization and aeroelastic analyses of propeller blades, usually a beam model is used to minimize the number of degrees of freedom. For example, beam models were developed and applied by Möhren *et al.* [23, 148] and MacNeill and Verstraete [82] for performing aeroelastic analyses, and by Chattopadhyay *et al.* [19] for structural optimization.

When modelling rotor blades with 1D elements, Euler-Bernoulli beam theory [149] or Timoshenko beam theory [150] are most commonly applied in practice. More information on higher-order beam theories and comparisons between beam models are provided by Öchsner [151]. Euler-Bernoulli beam theory is only applicable to slender and straight beams, and fundamentally assumes that sections that are orthogonal to the neutral axis remain orthogonal even after deformations [149]. This assumption implies that deformations only occur in a single plane. The Timoshenko beam theory extends the Euler-Bernoulli beam theory by being applicable to shear-deformable curved beams or elements of relatively low aspect ratio [149]. This theory was applied by Hegberg [26], Werter [30], and Ferede [25] for aeroelastic tailoring, and by Möhren *et al.* [23, 148] for the aeroelastic analysis of a propeller blade.

To provide a compromise between the high level of fidelity that is provided by detailed 3D blade models, and the low computational cost of beam models, a cross-sectional modelling approach that is similar to the method that was applied by Möhren *et al.* [23, 148] for propeller blades has been applied during this work. The approach that has been applied is part of PROTEUS, this time referring to the aeroelastic analysis and optimization program that was developed at the TU Delft, which is documented by Werter and De Breuker in [29]. This structural modelling method has been applied by Hegberg [26] for the aeroelastic tailoring of wind turbine blades, and by Werter [30] for the aeroelastic tailoring of wing structures. Within PROTEUS, the so-called *cross-sectional modeller* program converts an input detailed 3D model of a rotor blade (or wing) structure into an approximately equivalent 1D beam model with a significantly reduced number of degrees of freedom. This so-called *cross-sectional modelling* approach is commonly applied towards the analysis of wind turbines or helicopter rotors because it is very computationally efficient due to the low number of degrees of freedom being included, whilst approximately preserving the level of precision that is simultaneously associated with high-fidelity 3D finite element models and required for aeroelastic tailoring [152, 153]. PROTEUS was chosen to be used during this project because it has been extensively verified and validated in [29, 30], and it has already been applied towards the optimization of wings and wind turbines in [29–31, 154].

B.5.2. Modelling Composite Structures

The cross-sectional modeller approach that is applied within PROTEUS was verified and validated by Werter [30] through comparisons with experimental data collected by Chandra *et al.* [155] for the response of an orthotropic composite box beam subjected to a torsional load. Deformations obtained by PROTEUS were compared to the result from VABS (Variable Asymptotic Beam Section analysis), which is a commercial cross-sectional modelling program that was developed by Hodges [156]. The result from PROTEUS was nearly identical to the result from VABS, while also being in reasonable agreement with the experimental data. This comparison demonstrates that the two solvers provide an approximately equivalent result for hollow composite beam structures. Moreover, VABS has been extensively verified and validated by its authors, and through the in-depth comparison between several cross-sectional modelling programs that was performed by Chen *et al.* [157], it was found that VABS consistently showed excellent agreement with higher-fidelity methods and experimental data in all benchmark cases that were used for comparison [157]. Therefore, further verification and validation of PROTEUS was found to not be necessary during this project unless substantial changes are required.

PROTEUS applies *Classical Laminated Plate theory* to represent the detailed 3D rotor blade structure. Detailed information on the relationship between loads, strains, and curvatures of each laminate is provided in most textbooks on composite materials, including [49, 50, 52]. PROTEUS then represents the $(\boldsymbol{A},\boldsymbol{B},\boldsymbol{D})$ stiffness tensors as a function of lamination parameters, ξ^i_j ($i \in \{\mathrm{A},\mathrm{B},\mathrm{D}\}$ and $j \in \{1,2,3,4\}$), and material stiffness invariants, U_k ($k \in \{1,2,3,4,5\}$), according to the method of Tsai and Hahn [54]. Note that each stiffness tensor is defined by four lamination parameters, and thus each laminate of a composite structure is made up of 12 lamination parameters. If symmetric laminates are used, then $\boldsymbol{B} = \mathbf{0}$ and thus only 8 lamination parameters are required. The governing equations for *classical laminated plate theory* are provided in Section 2.2.1 and have been documented in [25, 26, 30, 54, 57], among others. Lastly, a discussion on feasible regions for lamination parameters has been provided in this section for completeness, although research within this area is not entirely relevant to this thesis. Indeed, the incomplete set of nonlinear inequalities defining the feasible region of lamination parameters (see Equation (B.11)) have been applied without further investigation. The main drawback of using lamination parameters is that an additional post-processing step is required to convert a set of lamination parameters into a feasible stacking sequence with a corresponding set of ply orientations, and usually a decrease in performance is obtained through this process due to manufacturing limitations [30]. A review of work done towards mitigating this is provided by Albazzan *et al.* [56]. However, this is currently outside the scope of this thesis, as the structural design of the propeller has always been expressed using lamination parameters during this project, with the expectation that the conversion of lamination parameters into a sequence of plies and angles will be addressed during a future research project.

After evaluating the structural properties of each blade section using the lamination parameters and material stiffness invariants, PROTEUS discretizes the structure into linear Timoshenko beam elements that preserve the orthotropic material properties of each laminate, while applying a co-rotational framework that results in a geometrically nonlinear structural model [29]. This co-rotational approach was developed by De Breuker [48], who provides the following explanation for it: "...the elastic beam deformations are solved in a coordinate system which is connected to each beam element, and which moves rigidly with the deformations of the beam. This coordinate system is called the element frame, and is also referred to as the local frame." More information on this approach is provided in [26, 29, 30, 48, 63]. Each segment of the 1D and 3D structural models used by PROTEUS has a constant cross-section, and thus small sections may be required to precisely represent detailed geometries.

Feasible Regions for Lamination Parameters

Because there is no direct physical connection between lamination parameters and a feasible laminate design of plies with thicknesses, orientations, and materials, it is necessary to ensure that sets of lamination parameters being used to represent any laminate of the blade are contained within regions that guarantee the existence of a feasible structural design. A comprehensive review into the use of lamination parameters with feasible regions for the efficient design of laminated composites was performed by Albazzan *et al.* [56]. The main details of this review have been summarized here. Using lamination parameters allows the composite structure to be completely represented by continuous design variables over a convex domain, although the main drawback of this approach is that closed-form expressions for the feasible regions of lamination parameters are not known in general [30]. Moreover, the lamination parameters have values that are inter-related (i.e. the feasible regions of each lamination parameter are dependent on the values of the other lamination parameters) [57]. Some work has been done to address this. For example, Hammer *et al.* [158], Miki and Sugiyama [159], and Wu *et al.* [160, 161] derived expressions relating the in-plane, coupling, and out-of-plane lamination parameters to define the feasible region of orthotropic laminates with 19 nonlinear constraints. These equations (as listed in Equation (B.10)) are currently regarded as the most efficient expression of the boundary for orthotropic laminates. Modifications to these expressions were later suggested by Raju *et al.* [162] so that they may be applicable toward cases with non-zero bend-twist coupling, although the list of constraints for anisotropic plates is not expressed in a directly applicable way. Otherwise, Setoodeh *et al.* [163] developed a method for determining a set of constraints that completely defines the feasible region of lamination parameters, though it usually results in a huge number of constraints that is impractical for optimization. Bloomfield *et al.* [57] derived a potentially small set of constraints that should be satisfied to yield a feasible region. However, the authors restrict feasible ply orientations to a finite set, which may not be practical. Expressions defining feasible regions for lamination parameters that represent symmetric or symmetric-balanced laminates are shown below.

Symmetric-Balanced Laminates These laminates do not have extension-shear coupling, although they do have bend-twist coupling, and $\boldsymbol{B} = \mathbf{0}$. Thus, $\xi_2^A = \xi_4^A = 0$. Efficient feasible regions for these types of laminates were defined by Wu *et al.* [160], as shown in Equation (B.10). Note that to precisely represent the boundary, t must be defined by any value in the compact interval $[-1, 1]$, though the domain that is indicated in this set of equations has generally been found to provide a reasonable result.

$$\left.\begin{array}{c} 5\left(\xi_1^A - \xi_1^D\right)^2 - 2\left(1 + \xi_3^A - 2\left(\xi_1^A\right)^2\right) \leq 0 \\ \left(\xi_3^A - 4t\xi_1^A + 1 + 2t^2\right)^3 - 4\left(1 + 2|t| + t^2\right)^2\left(\xi_3^D - 4t\xi_1^D + 1 + 2t^2\right) \leq 0 \\ \left(4t\xi_1^A - \xi_3^A + 1 + 4|t|\right)^3 - 4\left(1 + 2|t| + t^2\right)^2\left(4t\xi_1^D - \xi_3^D + 1 + 4|t|\right) \leq 0 \\ t \in \{-1.00, -0.75, -0.50, -0.25, 0.00, 0.25, 0.50, 0.75, 1.00\} \end{array}\right\} \tag{B.10}$$

Symmetric Laminates For laminates that are symmetric and not necessarily balanced, the expressions shown in Equation (B.10) are too restrictive. The first two expressions of Equation (B.11) were derived by Fukunaga and Sekine [164] and Grenestedt and Gudmundson [165] by applying the *Cauchy-Schwarz* *inequality*. The same approach was applied by Raju *et al.* [162] to obtain the final equation in this set, which generalizes the first expression of Equation (B.10) for non-zero ξ_2^{A}, ξ_4^{A}, ξ_2^{D}, and ξ_4^{D}.

A generalization of the last two expressions within Equation (B.10) for monotropic plates was provided by Bloomfield *et al.* [57], and is repeated in [160–162]. This generalization allows the feasible region for each lamination parameter to be precisely constructed, and it was successfully applied in [162].

$$
\left.
\begin{aligned}
2\left(\xi_1^k\right)^2\left(1-\xi_3^k\right)+2\left(\xi_2^k\right)^2\left(1+\xi_3^k\right)+\left(\xi_3^k\right)^2+\left(\xi_4^k\right)^2-4\xi_1^k\xi_2^k\xi_4^k\leq 1 \\
\left(\xi_1^k\right)^2+\left(\xi_2^k\right)^2\leq 1 \\
-1\leq \xi_i^k\leq 1 \qquad i\in\{1,2,3,4\} \qquad k\in\{\mathrm{A},\mathrm{D}\} \\
-16+32\xi_3^{\mathrm{A}}+40\left(\xi_2^{\mathrm{D}}\right)^2+40\left(\xi_1^{\mathrm{D}}\right)^2+16\left(\xi_4^{\mathrm{A}}\right)^2-80\xi_2^{\mathrm{A}}\xi_2^{\mathrm{D}}+72\left(\xi_2^{\mathrm{A}}\right)^2-80\xi_1^{\mathrm{A}}\xi_1^{\mathrm{D}}+72\left(\xi_1^{\mathrm{A}}\right)^2 \\
-80\xi_4^{\mathrm{A}}\xi_1^{\mathrm{D}}\xi_2^{\mathrm{D}}+80\xi_2^{\mathrm{A}}\xi_4^{\mathrm{A}}\xi_1^{\mathrm{D}}-40\xi_3^{\mathrm{A}}\left(\xi_2^{\mathrm{D}}\right)^2-120\xi_3^{\mathrm{A}}\left(\xi_1^{\mathrm{D}}\right)^2-32\xi_3^{\mathrm{A}}\left(\xi_4^{\mathrm{A}}\right)^2+80\xi_3^{\mathrm{A}}\xi_2^{\mathrm{A}}\xi_2^{\mathrm{D}}-72\xi_3^{\mathrm{A}}\left(\xi_2^{\mathrm{A}}\right)^2 \\
-32\left(\xi_3^{\mathrm{A}}\right)^3+80\xi_1^{\mathrm{A}}\xi_4^{\mathrm{A}}\xi_2^{\mathrm{D}}-144\xi_1^{\mathrm{A}}\xi_2^{\mathrm{A}}\xi_4^{\mathrm{A}}+240\xi_1^{\mathrm{A}}\xi_3^{\mathrm{A}}\xi_1^{\mathrm{D}}-216\left(\xi_1^{\mathrm{A}}\right)^2\xi_3^{\mathrm{A}}-25\left(\xi_1^{\mathrm{D}}\right)^2\left(\xi_2^{\mathrm{D}}\right)^2 \\
+50\xi_2^{\mathrm{A}}\left(\xi_1^{\mathrm{D}}\right)^2\xi_2^{\mathrm{D}}-105\left(\xi_2^{\mathrm{A}}\right)^2\left(\xi_1^{\mathrm{D}}\right)^2+160\xi_3^{\mathrm{A}}\xi_4^{\mathrm{A}}\xi_1^{\mathrm{D}}\xi_2^{\mathrm{D}}-160\xi_3^{\mathrm{A}}\xi_2^{\mathrm{A}}\xi_4^{\mathrm{A}}\xi_1^{\mathrm{D}}-40\left(\xi_3^{\mathrm{A}}\right)^2\left(\xi_2^{\mathrm{D}}\right)^2 \\
+120\left(\xi_3^{\mathrm{A}}\right)^2\left(\xi_1^{\mathrm{D}}\right)^2+16\left(\xi_3^{\mathrm{A}}\right)^2\left(\xi_4^{\mathrm{A}}\right)^2+80\left(\xi_3^{\mathrm{A}}\right)^2\xi_2^{\mathrm{A}}\xi_2^{\mathrm{D}}-72\left(\xi_3^{\mathrm{A}}\right)^2\left(\xi_2^{\mathrm{A}}\right)^2+16\left(\xi_3^{\mathrm{A}}\right)^4 \\
+50\xi_1^{\mathrm{A}}\xi_1^{\mathrm{D}}\left(\xi_2^{\mathrm{D}}\right)^2+20\xi_1^{\mathrm{A}}\xi_2^{\mathrm{A}}\xi_1^{\mathrm{D}}\xi_2^{\mathrm{D}}+90\xi_1^{\mathrm{A}}\left(\xi_2^{\mathrm{A}}\right)^2\xi_1^{\mathrm{D}}-160\xi_1^{\mathrm{A}}\xi_3^{\mathrm{A}}\xi_4^{\mathrm{A}}\xi_2^{\mathrm{D}}+288\xi_1^{\mathrm{A}}\xi_3^{\mathrm{A}}\xi_2^{\mathrm{A}}\xi_4^{\mathrm{A}} \\
-240\xi_1^{\mathrm{A}}\left(\xi_3^{\mathrm{A}}\right)^2\xi_1^{\mathrm{D}}-105\left(\xi_1^{\mathrm{A}}\right)^2\left(\xi_2^{\mathrm{D}}\right)^2+90\left(\xi_1^{\mathrm{A}}\right)^2\xi_2^{\mathrm{A}}\xi_2^{\mathrm{D}}-81\left(\xi_1^{\mathrm{A}}\right)^2\left(\xi_2^{\mathrm{A}}\right)^2+216\left(\xi_1^{\mathrm{A}}\right)^2\left(\xi_3^{\mathrm{A}}\right)^2 \\
+50\xi_4^{\mathrm{A}}\xi_1^{\mathrm{D}}\left(\xi_2^{\mathrm{D}}\right)^3-150\xi_2^{\mathrm{A}}\xi_4^{\mathrm{A}}\xi_1^{\mathrm{D}}\left(\xi_2^{\mathrm{D}}\right)^2+190\left(\xi_2^{\mathrm{A}}\right)^2\xi_4^{\mathrm{A}}\xi_1^{\mathrm{D}}\xi_2^{\mathrm{D}}-90\left(\xi_2^{\mathrm{A}}\right)^3\xi_4^{\mathrm{A}}\xi_1^{\mathrm{D}}+50\xi_3^{\mathrm{A}}\left(\xi_1^{\mathrm{D}}\right)^2\left(\xi_2^{\mathrm{D}}\right)^2 \\
-100\xi_3^{\mathrm{A}}\xi_2^{\mathrm{A}}\left(\xi_1^{\mathrm{D}}\right)^2\xi_2^{\mathrm{D}}+210\xi_3^{\mathrm{A}}\left(\xi_2^{\mathrm{A}}\right)^2\left(\xi_1^{\mathrm{D}}\right)^2-80\left(\xi_3^{\mathrm{A}}\right)^2\xi_4^{\mathrm{A}}\xi_1^{\mathrm{D}}\xi_2^{\mathrm{D}}+80\left(\xi_3^{\mathrm{A}}\right)^2\xi_2^{\mathrm{A}}\xi_4^{\mathrm{A}}\xi_1^{\mathrm{D}} \\
+40\left(\xi_3^{\mathrm{A}}\right)^3\left(\xi_2^{\mathrm{D}}\right)^2-40\left(\xi_3^{\mathrm{A}}\right)^3\left(\xi_1^{\mathrm{D}}\right)^2-80\left(\xi_3^{\mathrm{A}}\right)^3\xi_2^{\mathrm{A}}\xi_2^{\mathrm{D}}+72\left(\xi_3^{\mathrm{A}}\right)^3\left(\xi_2^{\mathrm{A}}\right)^2-50\xi_1^{\mathrm{A}}\xi_4^{\mathrm{A}}\left(\xi_2^{\mathrm{D}}\right)^3 \\
+190\xi_1^{\mathrm{A}}\xi_2^{\mathrm{A}}\xi_4^{\mathrm{A}}\left(\xi_2^{\mathrm{D}}\right)^2-270\xi_1^{\mathrm{A}}\left(\xi_2^{\mathrm{A}}\right)^2\xi_4^{\mathrm{A}}\xi_2^{\mathrm{D}}+162\xi_1^{\mathrm{A}}\left(\xi_2^{\mathrm{A}}\right)^3\xi_4^{\mathrm{A}}-100\xi_1^{\mathrm{A}}\xi_3^{\mathrm{A}}\xi_1^{\mathrm{D}}\left(\xi_2^{\mathrm{D}}\right)^2 \\
-40\xi_1^{\mathrm{A}}\xi_3^{\mathrm{A}}\xi_2^{\mathrm{A}}\xi_1^{\mathrm{D}}\xi_2^{\mathrm{D}}-180\xi_1^{\mathrm{A}}\xi_3^{\mathrm{A}}\left(\xi_2^{\mathrm{A}}\right)^2\xi_1^{\mathrm{D}}+80\xi_1^{\mathrm{A}}\left(\xi_3^{\mathrm{A}}\right)^2\xi_4^{\mathrm{A}}\xi_2^{\mathrm{D}}-144\xi_1^{\mathrm{A}}\left(\xi_3^{\mathrm{A}}\right)^2\xi_2^{\mathrm{A}}\xi_4^{\mathrm{A}}+80\xi_1^{\mathrm{A}}\left(\xi_3^{\mathrm{A}}\right)^3\xi_1^{\mathrm{D}} \\
+210\left(\xi_1^{\mathrm{A}}\right)^2\xi_3^{\mathrm{A}}\left(\xi_2^{\mathrm{D}}\right)^2-180\left(\xi_1^{\mathrm{A}}\right)^2\xi_3^{\mathrm{A}}\xi_2^{\mathrm{A}}\xi_2^{\mathrm{D}}+162\left(\xi_1^{\mathrm{A}}\right)^2\xi_3^{\mathrm{A}}\left(\xi_2^{\mathrm{A}}\right)^2-72\left(\xi_1^{\mathrm{A}}\right)^2\left(\xi_3^{\mathrm{A}}\right)^3 \\
-25\left(\xi_4^{\mathrm{A}}\right)^2\left(\xi_2^{\mathrm{D}}\right)^4+100\xi_2^{\mathrm{A}}\left(\xi_4^{\mathrm{A}}\right)^2\left(\xi_2^{\mathrm{D}}\right)^3-190\left(\xi_2^{\mathrm{A}}\right)^2\left(\xi_4^{\mathrm{A}}\right)^2\left(\xi_2^{\mathrm{D}}\right)^2+180\left(\xi_2^{\mathrm{A}}\right)^3\left(\xi_4^{\mathrm{A}}\right)^2\xi_2^{\mathrm{D}} \\
-81\left(\xi_2^{\mathrm{A}}\right)^4\left(\xi_4^{\mathrm{A}}\right)^2-50\xi_3^{\mathrm{A}}\xi_4^{\mathrm{A}}\xi_1^{\mathrm{D}}\left(\xi_2^{\mathrm{D}}\right)^3+150\xi_3^{\mathrm{A}}\xi_2^{\mathrm{A}}\xi_4^{\mathrm{A}}\xi_1^{\mathrm{D}}\left(\xi_2^{\mathrm{D}}\right)^2-190\xi_3^{\mathrm{A}}\left(\xi_2^{\mathrm{A}}\right)^2\xi_4^{\mathrm{A}}\xi_1^{\mathrm{D}}\xi_2^{\mathrm{D}} \\
+90\xi_3^{\mathrm{A}}\left(\xi_2^{\mathrm{A}}\right)^3\xi_4^{\mathrm{A}}\xi_1^{\mathrm{D}}-25\left(\xi_3^{\mathrm{A}}\right)^2\left(\xi_1^{\mathrm{D}}\right)^2\left(\xi_2^{\mathrm{D}}\right)^2+50\left(\xi_3^{\mathrm{A}}\right)^2\xi_2^{\mathrm{A}}\left(\xi_1^{\mathrm{D}}\right)^2\xi_2^{\mathrm{D}}-105\left(\xi_3^{\mathrm{A}}\right)^2\left(\xi_2^{\mathrm{A}}\right)^2\left(\xi_1^{\mathrm{D}}\right)^2 \\
+50\xi_1^{\mathrm{A}}\xi_3^{\mathrm{A}}\xi_4^{\mathrm{A}}\left(\xi_2^{\mathrm{D}}\right)^3-190\xi_1^{\mathrm{A}}\xi_3^{\mathrm{A}}\xi_2^{\mathrm{A}}\xi_4^{\mathrm{A}}\left(\xi_2^{\mathrm{D}}\right)^2+270\xi_1^{\mathrm{A}}\xi_3^{\mathrm{A}}\left(\xi_2^{\mathrm{A}}\right)^2\xi_4^{\mathrm{A}}\xi_2^{\mathrm{D}}-162\xi_1^{\mathrm{A}}\xi_3^{\mathrm{A}}\left(\xi_2^{\mathrm{A}}\right)^3\xi_4^{\mathrm{A}} \\
+50\xi_1^{\mathrm{A}}\left(\xi_3^{\mathrm{A}}\right)^2\xi_1^{\mathrm{D}}\left(\xi_2^{\mathrm{D}}\right)^2+20\xi_1^{\mathrm{A}}\left(\xi_3^{\mathrm{A}}\right)^2\xi_2^{\mathrm{A}}\xi_1^{\mathrm{D}}\xi_2^{\mathrm{D}}+90\xi_1^{\mathrm{A}}\left(\xi_3^{\mathrm{A}}\right)^2\left(\xi_2^{\mathrm{A}}\right)^2\xi_1^{\mathrm{D}}-105\left(\xi_1^{\mathrm{A}}\right)^2\left(\xi_3^{\mathrm{A}}\right)^2\left(\xi_2^{\mathrm{D}}\right)^2 \\
+90\left(\xi_1^{\mathrm{A}}\right)^2\left(\xi_3^{\mathrm{A}}\right)^2\xi_2^{\mathrm{A}}\xi_2^{\mathrm{D}}-81\left(\xi_1^{\mathrm{A}}\right)^2\left(\xi_3^{\mathrm{A}}\right)^2\left(\xi_2^{\mathrm{A}}\right)^2\leq 0
\end{aligned}
\right\} \tag{B.11}
$$

COMPOSITE MATERIAL PROPERTIES

For this project, only symmetric laminates have been considered, as stated in Appendix B.5.2, to prevent any manufacturing difficulties that may be present due to the inclusion of coupling between strains and curvatures [49]. Despite the "rules of thumb" provided by Kassapoglou [49], coupling between degree of freedom deformations will be used to enhance performance and thus unbalanced laminates have been considered. To calculate deformations, it is necessary to know the material properties of the fibre composites being used. Table B.3 contains a summary of material properties for some commercial fibre composites. The composites listed in this table are split into groups. The first group is for carbon fibres, which generally exhibit a good combination of strength and stiffness [50]. Shown next are glass fibres, which typically have a high strength, though they also have a low stiffness and high density [50]. Glass fibres generally exhibit less coupling between degree of freedom deformations, as their directional stiffnesses are relatively similar in magnitude. Boron fibres have been shown next, although they are very brittle and sensitive to surface damage despite their high elastic modulus and tensile/compressive strength [50]. Lastly, aramid fibres, colloquially known as *Kevlar* or *Twaron*, are generally used in applications that require materials with a high elastic modulus and impact resistance, although aramid fibres generally have a very low compressive strength [50]. Only carbon fibres will be considered for this project, as they are commonly used for aerospace applications, and exhibit more balanced properties, while aramid and boron fibres may not be applicable due to their aforementioned limitations. To enable relatively significant structural deformations, the only carbon fibres that have been considered during this work have a relatively low modulus of elasticity (such as AS4/APC2, AS4/3501-6, and T300/934).

It would be interesting to also consider using sandwich panels with symmetric facing sheets during a future project, as the added thickness is generally used to prevent buckling [26]. Nevertheless, buckling is generally not a primary concern for propeller blade structures because they normally do not experience substantial compressive loads. A model was proposed by Dillinger [63] for calculating failure due to buckling of laminated plates that are idealized as having zero curvature. This model would be suitable for this project, though it has not been included because its use would not assist in addressing the research questions and objectives. Material properties for applicable sandwich core materials are provided in several textbooks on composite structures, including the book of Daniel and Ishai [51].

Table B.3: Material properties for common unidirectional fibre composites [50, 51].

Material[a,b]	ρ_S	E_{11}	E_{22}	G_{12}	ν_{12}	σ_{11}^{UT}	σ_{11}^{UC}	σ_{22}^{UT}	σ_{22}^{UC}	τ_{12}^{U}
AS4 / APC2	1.57	134	8.70	5.1	0.28	2060	1100	78	196	157
AS4 / 3501-6	1.60	147	10.3	7.0	0.27	2280	1725	57	228	76
IM6G / 3501-6	1.62	169	9.00	6.5	0.31	2240	1680	46	215	73
IM7 / 977-3	1.61	190	9.90	7.8	0.35	3250	1590	62	200	75
T300 / N5208	1.60	181	10.3	7.2	0.28	1500	1500	40	246	68
T300 / 934	1.50	148	9.65	4.6	0.30	1314	1220	43	168	48
E-Glass	1.97	41	10.4	4.3	0.28	1140	620	39	128	89
S-Glass	2.00	45	11.0	4.5	0.29	1725	690	49	158	70
B-4 / N5505	2.00	204	18.5	5.6	0.23	1260	2500	61	202	67
Kevlar 49	1.46	76	5.5	2.3	0.34	1400	235	12	53	34

[a] SI units are used for all dimensional quantities, with g/cm^3 for densities, GPa for elastic constants, and MPa for strengths.
[b] Fibre composite materials are conventionally named as follows: "fibre material" / "resin composition".

B.6. AEROELASTIC TAILORING AND OPTIMIZATION

Previous implementations of propeller optimization procedures have been divided into two groups: aeroelastic optimization in Appendix B.6.1 and aerodynamic optimization in Appendix B.6.2. The goal of this review is to motivate decisions made concerning the formulation of the optimization problem for this project, as well as to provide an indication of the extent of potential improvements in propeller performance that may be achieved during this project. Optimization algorithms have not been discussed directly within this chapter because a suitable gradient-based optimization algorithm already exists within PROTEUS. It is therefore only necessary to ensure that the optimization problem is correctly formulated and that outcomes from previous studies are understood.

B.6.1. AEROELASTIC OPTIMIZATION

The first example of a dedicated optimization algorithm being used to obtain an aeroelastically tailored rotor blade is that of Khan [4], which has already been discussed extensively. In this work, multiple single-objective optimization problems were formulated, for a structure that is composed of a single laminate of 5 plies. Design variables in this case were ply orientations that could vary continuously between -90 and 90 degrees. In this case, only on-design performance was evaluated. The most notable optimization problem that was formulated was to maximize the on-design efficiency, while maintaining an approximately constant thrust coefficient (through an equality constraint). In this way, the propeller is still capable of satisfying the same mission requirements even after optimization, though it may have been sufficient for a lower limit on the thrust to instead be provided using an inequality constraint. A maximum improvement in efficiency of around 8% was obtained at low-to-moderate advance ratios, and a negligible improvement was obtained at higher advance ratios. Unconstrained optimization procedures involving the improvement of either the thrust, power, or efficiency were also performed, for which the respective maximum improvements were approximately 47%, 14%, and 3% at low-to-moderate advance ratios, and 32%, 24%, and 7% at high advance ratios. The author did not specify changes in other performance metrics besides the targetted values, and thus it is possibly unlikely that any baseline performance requirements were maintained during the generation of these unconstrained optimization results.

A single objective optimization problem was also formulated by Sodja *et al.* [3], though in this case, both on- and off-design efficiency was targetted by minimizing the function shown in Equation (B.12), which is defined as the curvature of the efficiency vs. advance ratio curve. The authors defined advance ratios above and below the design point, and at each iteration they would evaluate the efficiency at the three points to numerically determine the derivative using a central finite differencing scheme.

$$\rho_\eta(J) = \frac{\eta''(J)}{\sqrt{\left(1+\left(\eta'(J)\right)^2\right)^3}} \tag{B.12}$$

By selecting the above type of objective function, Sodja *et al.* [3] observed more significant improvements at high advance ratios beyond the design point, with only marginal improvements at lower advance ratios. The authors were therefore able to mainly improve off-design performance by maximizing the range of advance ratios where the propeller operates with high efficiency. Before performing the aeroelastic optimization using this objective, Sodja *et al.* performed an allowable stress design procedure to ensure that the maximum von Mises stress never exceeds the yield strength of the material. An aerodynamic optimization procedure was also performed at the design point to find the chord and twist distribution that minimizes induced losses. This method is suitable for improving the entire characteristic of the efficiency curve, while the method of Khan [4] is suitable for improving performance at a single operating point.

A multi-objective optimization problem was formulated by Sandak and Rosen [20] (which was also discussed in Section 1.1) because the authors were trying to maximize propulsive efficiency at several operating conditions. Sandak and Rosen reformulated the optimization problem by defining a single objective function that is a weighted average of the objective at each of the N_{trim} trim points, as shown below. This approach is formally referred to as the *weighted sum* method from the textbook of Martins and Ning [64]. The weight factors are usually normalized so that the sum shown in Equation (B.13) forms a convex combination, though Sandak and Rosen just set all the weighting parameters equal to 1. The trim points are selected to represent various operating conditions of the propeller that would be encountered during a full mission.

$$f = \sum_{i=1}^{N_{\text{trim}}} \frac{\zeta_i}{\eta_i^2} \tag{B.13}$$

Sandak and Rosen also applied constraints that prevented the thrust coefficient from decreasing by more than 10% at every trim point. The power coefficient was also not able to decrease by more than 25% during takeoff and initial climb (to limit the increase in engine RPM during takeoff to at-most 10%), and the rotation speed was prevented from changing during cruise [20]. With this formulation, the optimizer tended to improve performance at very low advance ratios (representing take-off conditions), with either marginal or degraded performance at advance ratios representing cruise conditions. Nevertheless, the result is heavily dependent on the selection of weighting parameters.

B.6.2. AERODYNAMIC OPTIMIZATION

Without any examples of aeroelastic tailoring for propellers in energy-harvesting conditions, examples involving aerodynamic optimization were considered instead. Additionally, by clearly identifying the potential benefits of aerodynamic optimization, the extent that performance can be improved through aeroelastic tailoring may be realized. These works were also used to identify how optimization problems regarding improvements in energy-harvesting performance were formulated in previous research.

It has been made clear throughout this chapter that traditional propeller design methods generally consider an isolated propeller, which is consequentially evaluated independently of any aircraft configuration. However, Gur and Rosen [28], van Neerven [33], and Scholtens [34] considered the overall performance of an aircraft configuration during their propeller optimization studies. For example, van Neerven developed an optimization procedure that performs a full mission analysis of an electric trainer aircraft to directly minimize the total required mission energy. This objective guarantees that the optimal propeller design, which regenerates energy during descent, decreases the total energy required for a predetermined mission. The objective that is presented in Appendix B.6.1 may not necessarily guarantee this, especially if performance during propulsive conditions deteriorates by too much through the improvement of regenerative performance. Gur and Rosen optimized the overall design of a propeller-based propulsion system for an ultralight aircraft through either the minimization of fuel consumption, the maximization of flight speed, or both, while also being subjected to both acoustic or structural constraints. This design approach was ultimately selected by Gur and Rosen instead of the optimal propeller design strategy that is provided by Adkins and Liebeck [35] to enable the inclusion of structural or acoustic constraints. Additionally, when comparing results from the two methods (for an unconstrained optimization problem), the optimal designs were nearly identical [28]. Finally, like the work of van Neerven, Scholtens developed an aircraft mission analysis and sizing method that allows changes to the propeller blade design to affect overall performance metrics. This sizing method was used to investigate how allowing energy to be recuperated during descent affects total energy consumption, for different mission strategies. It appears to be necessary to quantify propeller performance through the consideration of its effect on total mission energy for an aircraft configuration with a generic mission profile, like the work of van Neerven and Scholtens. In this way, it is possible to directly quantify how the use of an aeroelastically tailored dual-role propeller influences total required mission energy. It would also be interesting to compare or constrain other characteristics, such as the rate of descent or the energy consumption during each segment.

Dorfling and Rokhsaz [65] applied a similar propeller optimization study to that of [28, 33, 34] for a typical commuter aircraft performing a mission with only high-speed dash and loiter segments. The authors first identified propeller operating conditions corresponding to each mission segment, and then completed two optimization studies to design the propeller either for the loiter segment or for the high-speed dash segment, with the objective being to maximize the thrust output, subject to a constant power constraint. Mission analyses of the aircraft and propeller configurations were performed afterwards to compare the effect that the propeller design has on the required power. Because the aircraft design and mission were considered fixed, the computational requirement for the optimization procedure used by Dorfling and Rokhsaz is likely reduced in comparison to the optimization that was performed by van Neerven, who resorted to using a genetic algorithm to avoid performing the several objective function evaluations that would be required at each iteration of a gradient-based method.

AERODYNAMIC OPTIMIZATION RESULTS FOR DUAL-ROLE PROPELLERS

The main objective of the work of van Neerven [33] was to study the extent of potential performance improvements that may be achieved through the use of variable pitch or variable rotor speed capabilities on total energy consumption of an electric trainer aircraft (like the *Pipistrel Alpha Electro*) for a given climb-cruise-descent mission profile. This was completed solely through aerodynamic optimization of a dual-role propeller, which operates in energy-harvesting mode during descent and propulsive mode during the other two mission segments. Two different optimization studies were performed. First, propellers were optimized for minimum energy consumption (or maximum regeneration) in each mission segment independently, and then propellers were optimized for minimum energy consumption over the entire mission. In all cases, it was naturally found that the variable-pitch-variable-RPM (VPVR) propeller outperformed the constant-pitch-variable-RPM (CPVR) and variable-pitch-constant-RPM (VPCR) propellers in all comparisons that were performed. Additionally, the CPVR propeller that was optimized for cruise had a maximum energy-harvesting efficiency of approximately 6.5%, while the propeller that was optimized for climb had a maximum energy-harvesting efficiency of approximately 11%, and the propeller that was optimized for descent had a maximum energy-harvesting efficiency of approximately 16.5%. All three propellers have 3 blades, and the propeller that is optimized for descent has a noticeably larger solidity. The CPVR and VPVR propellers optimized for descent generally maintain around the same maximum energy-harvesting efficiency, while the VPVR propellers optimized either for climb or for cruise have a larger energy-harvesting efficiency by approximately 3-5 percentage points in comparison to their CPVR counterparts (the VPCR propellers were permitted to have variable RPM during descent and thus their performance is equivalent to the VPVR propeller in this circumstance).

The propellers that were optimized for descent tended to consume noticeably more energy than the propellers that were optimized for other flight phases. The descent propeller's climb efficiency was generally found to be between 1 and 3 percentage points lower than the propeller that was optimized for climb, although all propellers usually had an efficiency between 79% and 83% during climb. The noticeable effect on overall energy consumption likely resulted from a significant deterioration in propulsive efficiency during cruise, where the descent CPVR propeller had a maximum efficiency in cruise conditions of approximately 81% while the other two CPVR propellers had maximum efficiencies over 90%. The VPVR descent propeller had a maximum efficiency in cruise conditions of approximately 86%, although the other two propellers remained at efficiencies over 90%. The propellers that were optimized for maximum climb performance generally outperformed the other propellers in all single-point optimization cases. For the optimization of a propeller for minimum energy consumption over the full mission, the maximum energy-harvesting efficiency varied from 6-16% for the CPVR propeller and from 10-18% for the VPVR propeller. The optimizer naturally tended to prioritize the energy-harvesting performance less with increasing range. In all results presented by van Neerven, the blade twist, chord distribution, and tip radius were varied by the optimizer (the sweep and lean angles were fixed), and the number of blades was set as either 2 or 3. The airfoils of each blade section were also fixed.

Both van Neerven and Scholtens [34] observed a significant increase in solidity with propellers designed for regeneration during descent, which adversely impacts propulsive efficiency. Additionally, Scholtens found that decreasing the camber of each section or using variable-pitch capabilities enables sufficient regeneration at a reduced solidity. The fixed-pitch propellers with differing amounts of camber usually had an energy-harvesting efficiency around 12.5%, while the variable-pitch propellers had energy-harvesting efficiencies between 18.5% and 22% in [34]. It was also shown by Scholtens that regeneration during descent is only effective when the aircraft must perform a steep descent, and for a fixed range without any constraints on the minimum rate of descent, a shallow descent (for which energy-harvesting is not possible) always yielded a lower total mission energy. A relatively high minimum descent rate will therefore be applied if a mission analysis is required for this project.

It is not likely that the energy-harvesting efficiency obtained during this project will exceed the values reported in [33, 34]. This is because the baseline propeller considered in this work exhibits a maximum energy-harvesting efficiency of approximately 10-12% and the aerodynamic design of the propeller will not be directly optimized for maximum regenerative performance. However, the results presented in [33] are useful because they provide an upper-limit on the energy-harvesting efficiency that may be attained, which can be used to evaluate the effectiveness of aeroelastic tailoring for improving regenerative performance. The selection of constraints on performance in propulsive conditions should also be motivated by the results shown in [33, 34] for the propulsive efficiency during cruise and climb.

B.7. CONCLUSIONS

The purpose of the literature survey that is documented in this chapter is to provide information on aerodynamics, structural, and aeroelastic analysis methods for rotor blades, as well as on relevant optimization strategies. Within these subjects, the applicability of common analysis methods for propellers was discussed based on the physical phenomena that were found to be relevant for dual-role propellers.

Blade element methods have been relied on in most previous examples involving the aerodynamic analysis of propellers, as they are computationally efficient and provide a reasonable level of precision, especially if the sectional airfoil aerodynamic data is obtained experimentally. By correcting aerodynamic loads using nonlinear airfoil polar plots, it is possible to account for viscous effects including transition and separation through the use of blade element methods. Three different types of blade element theories have been identified for analysing propellers. The first is blade element momentum theory, which intrinsically models the axial and tangential induced velocity. However, this method relies on engineering approximations for variations in blade-axis geometry and losses in circulation at the blade tips due to the finite number of blades. Usually, losses in circulation are approximated using the so-called *Prandtl tip loss factor*, although more precise mathematical representations of the circulation distribution over a propeller blade have been derived, and these methods do not require any sort of engineering correction for tip losses. Within this project, these models were termed *vortex models*, and the theory proposed by Goldstein for lightly loaded rotor blades was found to be sufficient for this project. It is not possible to represent effects on performance resulting from variations in blade axis geometry because both of the aforementioned methods treat each blade element as independent (therefore neglecting the mutual interference between blade elements). Lifting-line or vortex-lattice methods conversely feature a greater level of fidelity by intrinsically modelling some effects of the mutual interference between blade elements through the *Biot-Savart law*, though most previously implemented VLM codes generally rely on the linear *Kutta-Joukowski theorem* to evaluate the lift distribution, and therefore do not rely on blade element theory to provide the lift and drag distributions. It is still possible however to correct aerodynamic loads using blade element theory while applying vortex-lattice and lifting-line methods, and therefore they remain relevant to this discussion. With these methods, the wake must either be prescribed, in which case its shape is known *a priori*, or a computationally expensive free-wake model must be used to iteratively determine the shape of the wake and its effect on aerodynamic loads. Blade element momentum theory provides a sufficient level of precision, whilst having the lowest associated computational requirement.

For all blade element methods, engineering corrections are generally required to account for the effect of rotation on fluid particles in the boundary layer. Most of the models that have been developed require empirical data for the selection of coefficients and therefore do not intrinsically represent the physical phenomena. The 2D boundary layer equations for an airfoil section were modified however by researchers at ECN and NLR to include effects of rotation, and these equations were used to develop RFOIL, which is a modified version of XFOIL. This is the only stall-delay model that was identified which does not require any empirical data, and therefore it has been applied during this project.

The common structural design of a propeller features an outer shell made from a carbon or glass fibre material, a spar, and a foam or honeycomb fill material. However, the structural design has usually been idealized by other researchers either to feature only the outer shell with or without spar caps, or to be represented as a variable-thickness plate. For applications involving aeroelastic tailoring, only unidirectional fibre composites are used, and *classical laminated plate theory* is generally applied to evaluate structural deformations. Historically, the blade structure is parametrized by a combination of discrete and continuous variables, although recent developments have been made towards the derivation of so-called *lamination parameters*, which enable the entire design space to be represented by a fixed number of continuous design variables. This method enables the application of gradient-based optimization procedures (despite a somewhat less intuitive physical description) and thus it has been applied during this research. Cross-sectional modelling tools have been developed both commercially and in academia to represent complex 3D blade structures as 1D beams, thus dramatically reducing the number of degrees of freedom to be evaluated and ultimately providing a significant decrease in computational cost. This approach has therefore also been applied during this research. Lastly, a two-way coupled scheme is required to couple the fluid and structural models from different tools because the structural deformations must influence the aerodynamic loads to allow the optimization to proceed. For this, two approaches have been identified. The first involves the application of *Newton's method* to minimize a residual function that is defined as the difference between internal and external forces, and the second approach involves iteratively recalculating aerodynamic loads and structural deformations until negligible differences in deformations are observed. The latter method requires under-relaxation to guarantee numerical stability.

Propeller optimization problems are typically formulated as constrained multi-objective optimization problems involving the improvement of performance at several operating conditions, subject to several operational or design-related constraints. Some relevant constraints include maintaining a maximum allowable power, a constant rotor speed, a minimum or constant thrust, or a maximum allowable strain (among others). Objectives considered by other researchers include either the minimization of power or the maximization of efficiency. Some researchers considered the optimization of propellers by integrating propeller performance calculations into a mission analysis procedure for a suitable reference aircraft and minimizing required mission energy, subject to structural or operational constraints. This approach was commonly used for optimizing the propeller aerodynamic design when subjected to opposing requirements during different mission segments, and thus has been applied towards the optimization of dual-role propellers in previous research. Other researchers considered the optimization of the propeller independently of any reference aircraft, this approach is only suitable for the characterization of generic design trends.

C

Completed List of Derivatives for Aerodynamic Loads

The assumption applied during this project is that the derivatives of aerodynamic loads with respect to radial deformations are negligible. The resulting derivative matrix is shown in Equation (C.1).

$$\left(\frac{d}{d\underline{p}_{\mathrm{a}}}\begin{bmatrix}\underline{\tilde{f}}_{\mathrm{a}}\\ \underline{\tilde{m}}_{\mathrm{a}}\end{bmatrix}\right)=\begin{bmatrix}\underline{0} & \underline{0} & \underline{0} & \underline{0} & \frac{d}{d\beta}\underline{\tilde{f}}_{\mathrm{a}} & \underline{0}\\ \underline{0} & \underline{0} & \underline{0} & \underline{0} & \frac{d}{d\beta}\underline{\tilde{m}}_{\mathrm{a}} & \underline{0}\end{bmatrix} \tag{C.1}$$

This derivative matrix is sufficient for this project, as indeed the radial deformations of each blade section were always found to be relatively small, resulting in deformations in the radial direction having a relatively small effect on changes in aerodynamic loads. Nevertheless, aerodynamic loads are still sensitive to changes in radial deformations, as changes in radius result in a change in tangential velocity, which affects the incoming flow angle. Moreover, the change in radius also affects the area of the annular control volume considered by momentum theory. This accordingly results in a change in induced velocity, thrust, and torque. The following derivation enables these effects to be accounted for.

The derivative matrix of aerodynamic loads considered during this section is provided in Equation (C.2).

$$\left(\frac{d}{d\underline{p}_{\mathrm{a}}}\begin{bmatrix}\underline{\tilde{f}}_{\mathrm{a}}\\ \underline{\tilde{m}}_{\mathrm{a}}\end{bmatrix}\right)=\begin{bmatrix}\frac{d}{dx}\underline{\tilde{f}}_{\mathrm{a}} & \frac{d}{dy}\underline{\tilde{f}}_{\mathrm{a}} & \underline{0} & \underline{0} & \frac{d}{d\beta}\underline{\tilde{f}}_{\mathrm{a}} & \underline{0}\\ \frac{d}{dx}\underline{\tilde{m}}_{\mathrm{a}} & \frac{d}{dy}\underline{\tilde{m}}_{\mathrm{a}} & \underline{0} & \underline{0} & \frac{d}{d\beta}\underline{\tilde{m}}_{\mathrm{a}} & \underline{0}\end{bmatrix} \tag{C.2}$$

The derivatives with respect to radial deformations are expressed in terms of the linear degree of freedom displacements, x and y, according to the expressions shown in Equation (C.3).

$$r=\sqrt{x^2+y^2}\implies\begin{cases}\dfrac{dr}{dx}=\dfrac{x}{\sqrt{x^2+y^2}}=\dfrac{x}{r}\\[2ex] \dfrac{dr}{dy}=\dfrac{y}{\sqrt{x^2+y^2}}=\dfrac{y}{r}\end{cases} \tag{C.3}$$

Thus, the derivatives of aerodynamic loads with respect to degree of freedom deformations, x and y, are expressed respectively with Equation (C.4) and Equation (C.5), using Equation (2.79).

$$\frac{d}{dx}\begin{bmatrix}\underline{\tilde{f}}_{\mathrm{a}}\\ \underline{\tilde{m}}_{\mathrm{a}}\end{bmatrix}=\frac{q_\infty x\,\Delta S}{r}\left(\begin{bmatrix}\frac{dC_x}{dr} & 0 & \frac{dC_z}{dr} & 0 & \frac{dC_m}{dr}c & 0\end{bmatrix}^T+\begin{bmatrix}C_x & 0 & C_z & 0 & C_m c & 0\end{bmatrix}^T\left(\frac{2V}{V_\infty^2}\right)\left(\frac{dV}{dr}\right)\right) \tag{C.4}$$

$$\frac{d}{dy}\begin{bmatrix}\underline{\tilde{f}}_{\mathrm{a}}\\ \underline{\tilde{m}}_{\mathrm{a}}\end{bmatrix}=\frac{q_\infty y\,\Delta S}{r}\left(\begin{bmatrix}\frac{dC_x}{dr} & 0 & \frac{dC_z}{dr} & 0 & \frac{dC_m}{dr}c & 0\end{bmatrix}^T+\begin{bmatrix}C_x & 0 & C_z & 0 & C_m c & 0\end{bmatrix}^T\left(\frac{2V}{V_\infty^2}\right)\left(\frac{dV}{dr}\right)\right) \tag{C.5}$$

From the above expressions, it is clear that only derivatives with respect to radial deformations are necessary to be evaluated. With blade element theory, the thrust and torque coefficients are defined a shown respectively in the following expressions, which have been repeated from Section 2.1.2.

$$C_t^{\mathrm{BE}} = C_z\,\sigma(r)\left(\frac{V}{V_\infty}\right)^2$$
$$C_q^{\mathrm{BE}} = C_x\,\sigma(r)\left(\frac{V}{V_\infty}\right)^2$$

Using blade element theory, derivatives of the thrust and torque coefficients with respect to radial deformations are expressed respectively in Equation (C.6) and Equation (C.7).

$$\frac{d}{dr}C_t^{\mathrm{BE}} = \frac{dC_z}{dr}\,\sigma(r)\left(\frac{V}{V_\infty}\right)^2 + C_z\,\frac{d\sigma}{dr}\left(\frac{V}{V_\infty}\right)^2 + C_z\,\sigma(r)\left(\frac{2V}{V_\infty^2}\right)\frac{dV}{dr} \tag{C.6}$$
$$\frac{d}{dr}C_q^{\mathrm{BE}} = \frac{dC_x}{dr}\,\sigma(r)\left(\frac{V}{V_\infty}\right)^2 + C_x\,\frac{d\sigma}{dr}\left(\frac{V}{V_\infty}\right)^2 + C_x\,\sigma(r)\left(\frac{2V}{V_\infty^2}\right)\frac{dV}{dr} \tag{C.7}$$

Derivatives of the local force coefficients, C_x and C_z, are given by Equation (C.8), shown below.

$$\begin{bmatrix}\frac{dC_z}{dr}\\ \frac{dC_x}{dr}\end{bmatrix} = \begin{bmatrix}\cos(\varphi) & -\sin(\varphi)\\ \sin(\varphi) & \cos(\varphi)\end{bmatrix}\begin{bmatrix}C_{l_\alpha}(\alpha, Re, Ma)\\ C_{d_\alpha}(\alpha, Re, Ma)\end{bmatrix}\left(\frac{d\alpha}{dr}\right) + \begin{bmatrix}-\sin(\varphi) & -\cos(\varphi)\\ \cos(\varphi) & -\sin(\varphi)\end{bmatrix}\begin{bmatrix}C_l(\alpha, Re, Ma)\\ C_d(\alpha, Re, Ma)\end{bmatrix}\left(\frac{d\varphi}{dr}\right) \tag{C.8}$$

The derivative of the local solidity, $\sigma(r)$, is given in Equation (C.9). Additionally, the derivative of the local incoming flow velocity with respect to radial deformations is given in Equation (C.10).

$$\sigma(r) = \frac{N_b\,c}{2\pi r} \implies \frac{d\sigma}{dr} = \frac{-N_b\,c}{2\pi r^2} = \frac{-\sigma}{r} \tag{C.9}$$
$$V = \sqrt{(V_\infty(1+a))^2 + (\omega r(1-a'))^2} \implies \frac{dV}{dr} = \frac{V_\infty^2(1+a)\frac{da}{dr} + \omega^2 r(1-a')\left[(1-a') - r\frac{da'}{dr}\right]}{V} \tag{C.10}$$

Derivatives of the flow angles with respect to radial deformations are additionally provided below.

$$\frac{d\alpha}{dr} = \frac{d\beta}{dr} - \frac{d\varphi}{dr} = -\frac{d\varphi}{dr} \tag{C.11}$$
$$\frac{d\varphi}{dr} = \frac{d}{dr}\left(\arctan\left(\frac{V_\infty(1+a)}{\omega r(1-a')}\right)\right) = \frac{V_\infty}{V}\frac{\omega r}{V}\left(\frac{da}{dr}(1-a') + \frac{da'}{dr}(1+a)\right) - \frac{V_\infty}{V}(1+a)\omega(1-a') \tag{C.12}$$
$$\implies \frac{d\alpha}{dr} = -\frac{V_\infty}{V}\frac{\omega r}{V}\left(\frac{da}{dr}(1-a') + \frac{da'}{dr}(1+a)\right) + \frac{V_\infty}{V}(1+a)\omega(1-a') \tag{C.13}$$

Substituting Equation (C.9) and Equation (C.10) into Equation (C.6) and Equation (C.7) yields the expressions shown in Equation (C.14) and Equation (C.15), which define the derivatives of the thrust and torque coefficients with respect to radial deformations using blade element theory.

$$\frac{dC_t^{\mathrm{BE}}}{dr} = \frac{C_z\,\sigma(r)}{V_\infty^2}\left(2\left(V_\infty^2(1+a)\frac{da}{dr} + \omega^2 r(1-a')\left[(1-a') - r\frac{da'}{dr}\right]\right) - \frac{V^2}{r}\right) + \frac{dC_z}{dr}\,\sigma(r)\left(\frac{V}{V_\infty}\right)^2 \tag{C.14}$$
$$\frac{dC_q^{\mathrm{BE}}}{dr} = \frac{C_x\,\sigma(r)}{V_\infty^2}\left(2\left(V_\infty^2(1+a)\frac{da}{dr} + \omega^2 r(1-a')\left[(1-a') - r\frac{da'}{dr}\right]\right) - \frac{V^2}{r}\right) + \frac{dC_x}{dr}\,\sigma(r)\left(\frac{V}{V_\infty}\right)^2 \tag{C.15}$$

Using momentum theory, the derivation largely follows the derivation shown in Section 2.3.

$$\frac{dC_t^{\mathrm{M}}}{dr} = \begin{cases} 4\left((1+2a)F\frac{da}{dr} + a(1+a)\frac{dF}{dr}\right) & a \geq -0.326\\ 1.39F\frac{da}{dr} + (1.39(1+a) - 1.816)\frac{dF}{dr} & a < -0.326\end{cases} \tag{C.16}$$
$$\frac{dC_q^{\mathrm{M}}}{dr} = 4\frac{\omega r}{V_\infty}\left(F\left((1+a)\frac{da'}{dr} + a'\frac{da}{dr}\right) + a'(1+a)\frac{dF}{dr}\right) \tag{C.17}$$

The major difference between the derivation shown in this appendix and the derivation shown in Section 2.3, is how the root and tip losses are treated. In this case, they must be differentiated directly with respect to radial deformations, as the radius term appears directly in the expression for the root and tip losses. Thus, the expression for the root and tip losses must be differentiated directly with respect to radial deformations. Differentiating the root and tip losses with respect to r yields the following expressions. Derivatives of F_{root} and F_{tip} with respect to φ are shown in Equation (2.90) and Equation (2.91).

$$\frac{dF_{\text{root}}}{dr} = \frac{N_b e^{-f_{\text{root}}}}{\pi r_{\text{root}} \left|\sin(\varphi)\right| \sqrt{1-e^{-2f_{\text{root}}}}} + \frac{dF_{\text{root}}}{d\varphi}\frac{d\varphi}{dr}$$

$$\frac{dF_{\text{tip}}}{dr} = -\frac{N_b \left(r_{\text{tip}}-r\right) e^{-f_{\text{tip}}}}{\pi r^2 \left|\sin(\varphi)\right| \sqrt{1-e^{-2f_{\text{tip}}}}} + \frac{dF_{\text{tip}}}{d\varphi}\frac{d\varphi}{dr}$$

Expanding derivatives of F_{root} and F_{tip} with respect to φ yields Equation (C.18) and Equation (C.19).

$$\frac{dF_{\text{root}}}{dr} = \frac{N_b e^{-f_{\text{root}}}}{\pi r_{\text{root}} \left|\sin(\varphi)\right| \sqrt{1-e^{-2f_{\text{root}}}}} - \frac{N_{\text{b}}}{\pi}\left(\frac{r-r_{\text{root}}}{r\left|\sin(\varphi)\right|}\right)\frac{\cos(\varphi)}{\sin(\varphi)}\left(\frac{\exp\left[-\frac{N_{\text{b}}}{2}\left(\frac{r-r_{\text{root}}}{r\left|\sin(\varphi)\right|}\right)\right]}{\sqrt{1-\exp\left[-N_{\text{b}}\left(\frac{r-r_{\text{root}}}{r\left|\sin(\varphi)\right|}\right)\right]}}\right)\frac{d\varphi}{dr} \tag{C.18}$$

$$\frac{dF_{\text{tip}}}{dr} = -\frac{N_b \left(r_{\text{tip}}-r\right) e^{-f_{\text{tip}}}}{\pi r^2 \left|\sin(\varphi)\right| \sqrt{1-e^{-2f_{\text{tip}}}}} - \frac{N_{\text{b}}}{\pi}\left(\frac{r_{\text{tip}}-r}{r\left|\sin(\varphi)\right|}\right)\frac{\cos(\varphi)}{\sin(\varphi)}\left(\frac{\exp\left[-\frac{N_{\text{b}}}{2}\left(\frac{r_{\text{tip}}-r}{r\left|\sin(\varphi)\right|}\right)\right]}{\sqrt{1-\exp\left[-N_{\text{b}}\left(\frac{r_{\text{tip}}-r}{r\left|\sin(\varphi)\right|}\right)\right]}}\right)\frac{d\varphi}{dr} \tag{C.19}$$

The complete derivative of the Prandtl tip-loss factor, F, with respect to radial deformations is given by Equation (C.20), which follows directly from applying the chain rule.

$$\frac{dF}{dr} = \left[\frac{dF_{\text{root}}}{dr}F_{\text{tip}} + F_{\text{root}}\frac{dF_{\text{tip}}}{dr}\right] \tag{C.20}$$

With these expressions, the method of evaluating sensitivities with respect to radial deformations similarly follows the method that was applied to evaluate sensitivities with respect to the angular deformations. A residual function is constructed by taking the difference between the coefficient values obtained from blade element and momentum theory. This residual function is then used to solve for derivatives of the axial and azimuthal induction factors with respect to radial deformations, da/dr and da'/dr. The residual vector that is constructed to solve these equations is shown below in Equation (C.21). This expression is solved using Newton's method by iteratively evaluating Equation (C.22).

$$\underline{R} = \begin{bmatrix} \frac{dC_t^{\text{BE}}}{dr} - \frac{dC_t^{\text{M}}}{dr} & \frac{dC_q^{\text{BE}}}{dr} - \frac{dC_q^{\text{M}}}{dr} \end{bmatrix}^T := \underline{0} \tag{C.21}$$

$$\begin{bmatrix} \frac{da}{dr} \\ \frac{da'}{dr} \end{bmatrix}_{i+1} = \begin{bmatrix} \frac{da}{dr} \\ \frac{da'}{dr} \end{bmatrix}_{i} - \begin{bmatrix} \frac{\partial R_1}{\partial({}^{da}/_{dr})} & \frac{\partial R_1}{\partial({}^{da'}/_{dr})} \\ \frac{\partial R_2}{\partial({}^{da}/_{dr})} & \frac{\partial R_2}{\partial({}^{da'}/_{dr})} \end{bmatrix}_{i}^{-1} \cdot \underline{R} \tag{C.22}$$

After solving for derivatives of the axial and tangential induction factors with respect to radial deformations, the derivatives of the thrust and torque coefficients may be evaluated either with momentum theory (Equation (C.16) and Equation (C.17)) or with blade element theory (Equation (C.14) and Equation (C.15)). It is also now possible to directly evaluate the derivative of the local flow velocity with respect to radial deformations, Equation (C.10). Thus, all required terms in Equation (C.4) and Equation (C.5) are known.

Because the calculation shown above was not applied during this project, it was not necessary to verify whether it yields the correct solution. For this reason, comparisons between the sensitivities computed analytically have not been compared with sensitivities computed numerically. It is thus required to complete this verification study before implementing this derivative calculation into the aeroelastic analysis routine that was applied during this project.

D

ADDITIONAL SENSITIVITY STUDIES

Additional results from sensitivity studies have been provided in this chapter, corresponding to the inputs provided in Table 5.1, for the three-bladed TUD-XPROP at a fixed pitch setting of 15° and a rotor speed of 30 RPS. Only variations in a single ply orientation have been provided, corresponding to Equation (5.2) for symmetric-unbalanced laminates, and Equation (5.3) for symmetric-balanced laminates. It was considered redundant to perform additional variations over two independent ply orientations, as sufficient agreement was obtained for all variations in a single variable. Variations in propeller performance quantities have been shown in Appendix D.1, and variations in tip deformations have been shown in Appendix D.2, for comparison with results from Section 5.1.2 and Section 5.1.3, respectively.

D.1. PERFORMANCE RESULTS

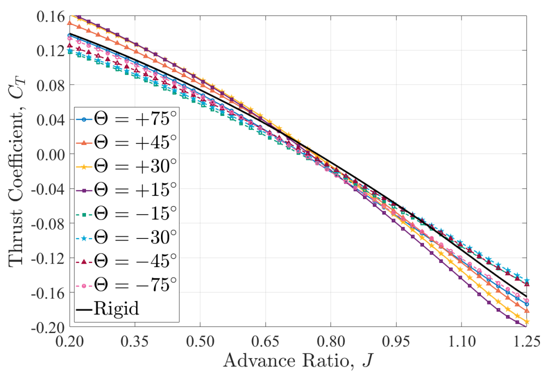

(a) Thrust coefficient (symmetric-unbalanced laminates).

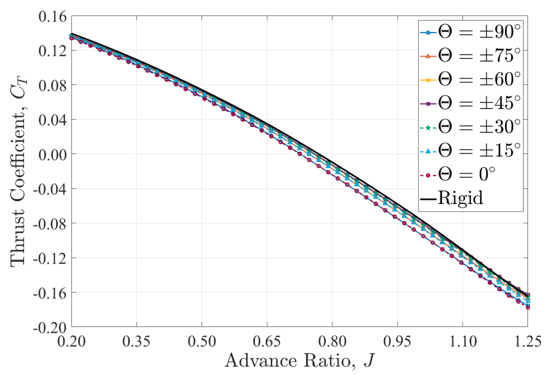

(b) Thrust coefficient (symmetric-balanced laminates).

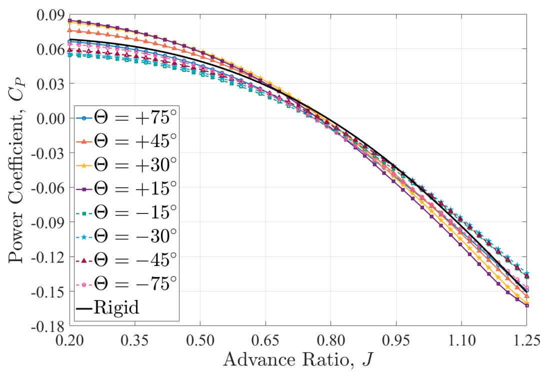

(c) Power coefficient (symmetric-unbalanced laminates).

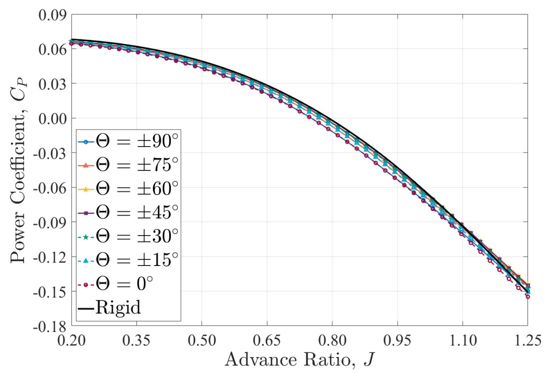

(d) Power coefficient (symmetric-balanced laminates).

Figure D.1: Thrust and power coefficient plots obtained from sensitivity studies ($\beta = 15°$).

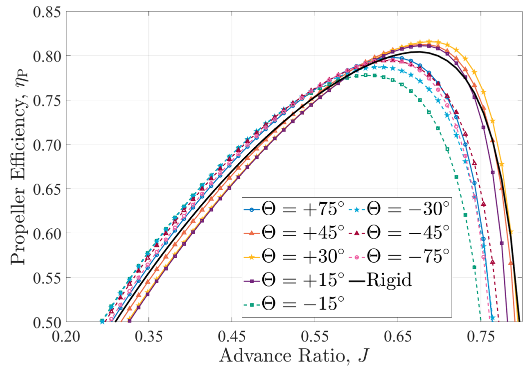

(a) Propeller efficiency (symmetric-unbalanced laminates).

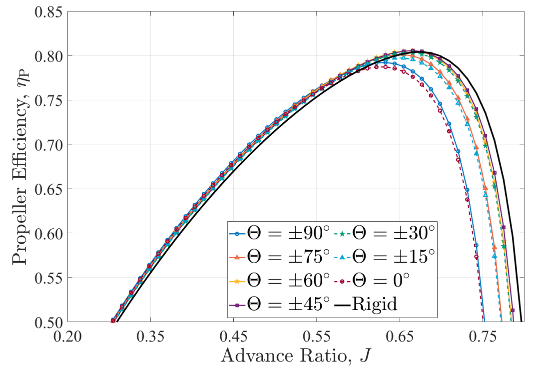

(b) Propeller efficiency (symmetric-balanced laminates).

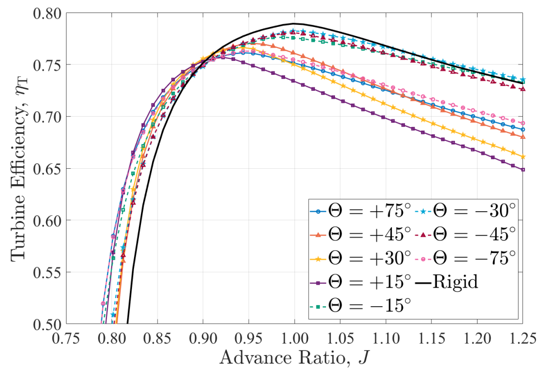

(c) Turbine efficiency (symmetric-unbalanced laminates).

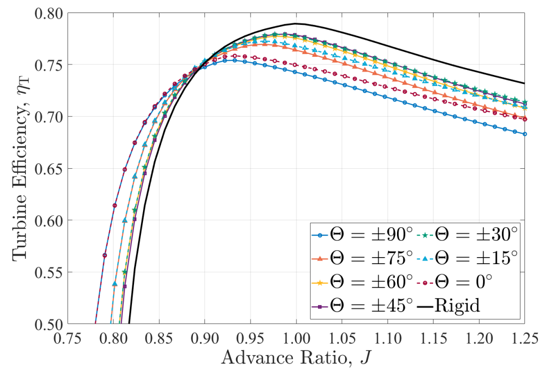

(d) Turbine efficiency (symmetric-balanced laminates).

Figure D.2: Propeller and turbine efficiency plots obtained from sensitivity studies ($\beta = 15°$).

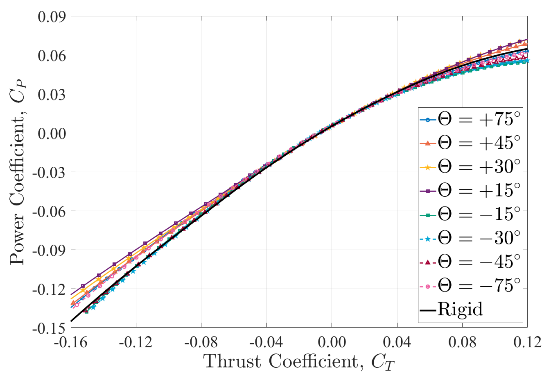

(a) C_P vs. C_T (symmetric-unbalanced laminates).

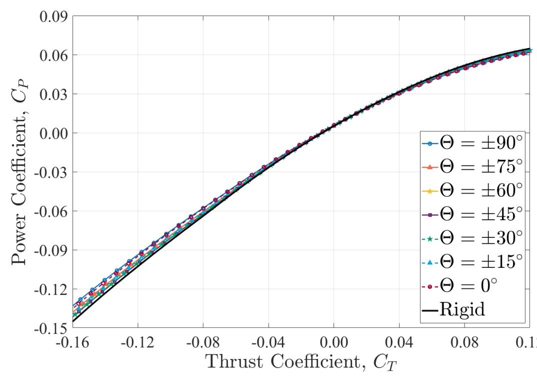

(b) C_P vs. C_T (symmetric-balanced laminates).

Figure D.3: Plots of power (C_P) as a function of thrust (C_T), obtained from sensitivity studies ($\beta = 15°$).

The results shown in this section indicate the same trends as observed in Section 5.1.2. The discussion of these results follows exactly from the discussion that was provided in Section 5.1.4, and thus has been omitted here. Not only did negative ply orientations show to yield less power consumption (or more power recovered) for a constant thrust requirement, but even the ply orientations yielding maximum performance increases or decreases appear to be approximately the same as for the case with a pitch setting of 25°. Small differences in the magnitudes of performance increases or decreases, or in the efficiency trends, were observed between the results obtained for the two different pitch settings and rotor speeds, although this is largely due to the differences in loading encountered by the propeller in each case. Moreover, due to the efficiency curves' dependence on advance ratio, which covers different ranges between the two pitch settings under investigation, minor differences in efficiency trends are expected.

D.2. DEFORMATION RESULTS

As expected, general trends also match the results shown in Section 5.1.3 for a pitch setting of 25°. Deformation plots under zero aerodynamic loads are shown first in Figure D.4 and Figure D.5, which indicate identical trends to the results shown in Figure 5.6 and Figure 5.7, except for the deformations being slightly larger due to the higher rotor speed setting. The remaining plots indicate deformations when subjected to aerodynamic loads, and the trends shown are nearly identical. All conclusions from Section 5.1.4 thus may also be drawn from the results presented at a pitch setting of 15° in this section.

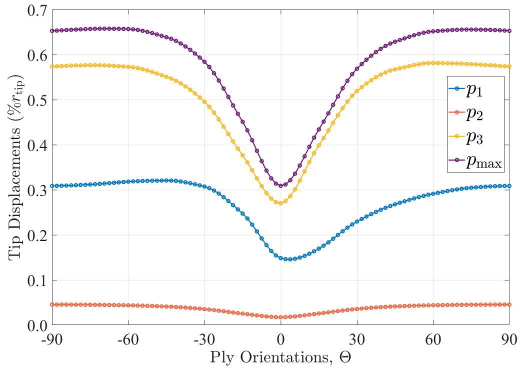

(a) Symmetric-unbalanced laminates ($\Theta_1 = \Theta_2$).

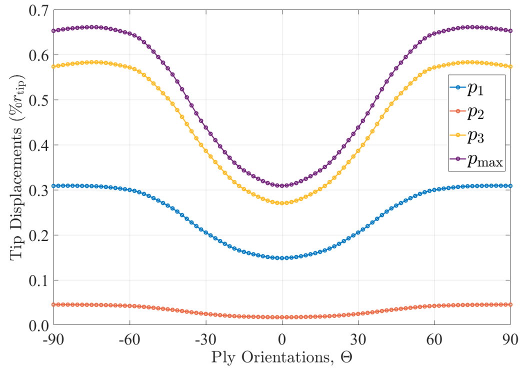

(b) Symmetric-balanced laminates ($\Theta_1 = -\Theta_2$).

Figure D.4: Blade tip displacements obtained from sensitivity studies of the TUD-XPROP, made from laminates defined by Equation (5.1) and subjected to zero aerodynamic loads ($\Omega = 30$ RPS, $\beta = 15°$).

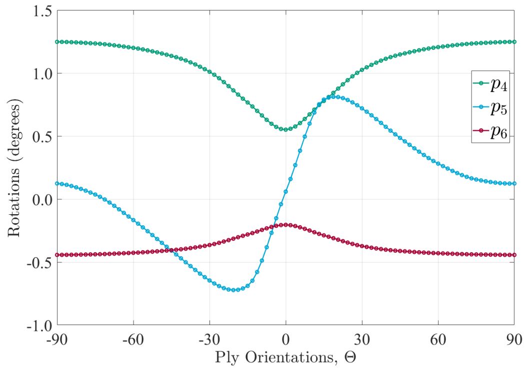

(a) Symmetric-unbalanced laminates ($\Theta_1 = \Theta_2$).

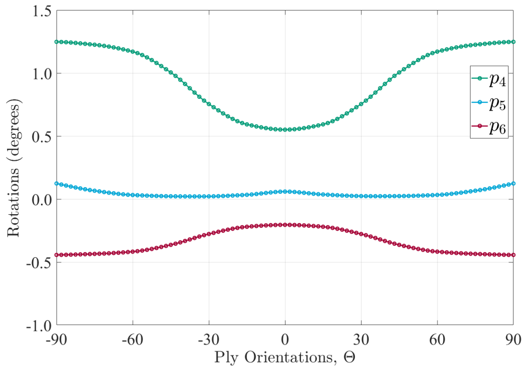

(b) Symmetric-balanced laminates ($\Theta_1 = -\Theta_2$).

Figure D.5: Blade tip rotations obtained from sensitivity studies of the TUD-XPROP, made from laminates defined by Equation (5.1) and subjected to zero aerodynamic loads ($\Omega = 30$ RPS, $\beta = 15°$).

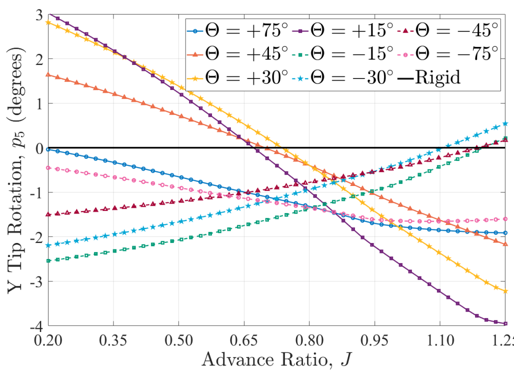

(a) Symmetric-unbalanced laminates ($\Theta_1 = \Theta_2$).

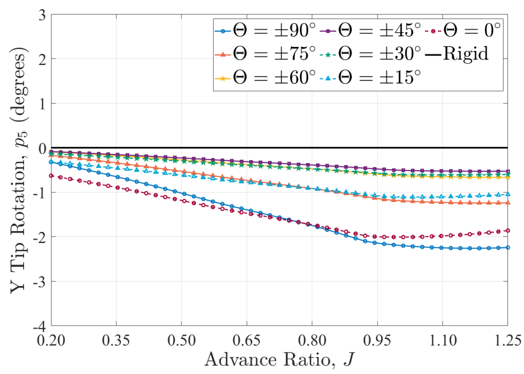

(b) Symmetric-balanced laminates ($\Theta_1 = -\Theta_2$).

Figure D.6: Blade tip torsional deformation plots from sensitivity studies ($\Omega = 30$ RPS, $\beta = 15°$).

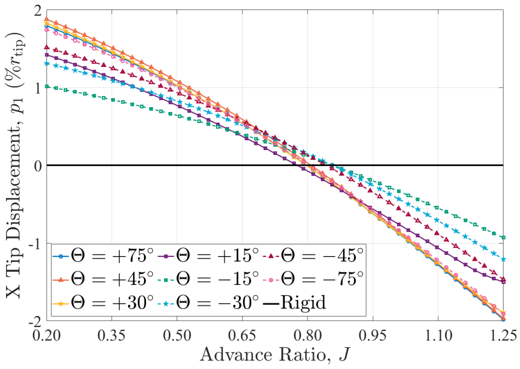

(a) Displacements along the x-axis (symmetric-unbalanced).

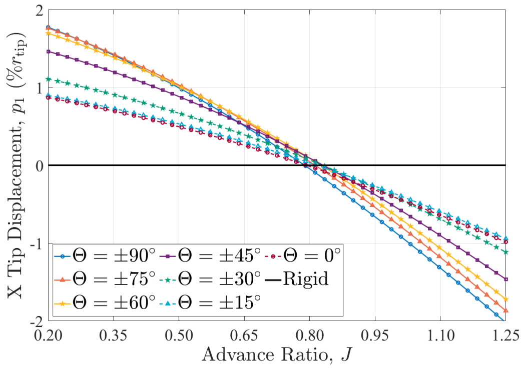

(b) Displacements along the x-axis (symmetric-balanced).

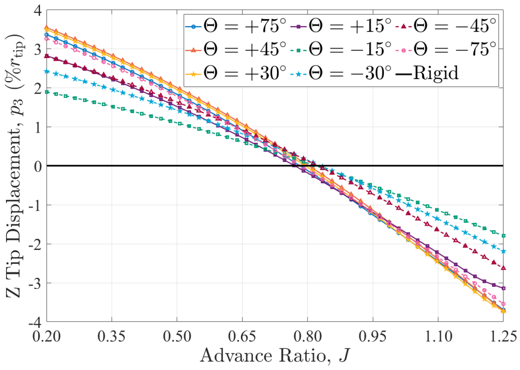

(c) Displacements along the z-axis (symmetric-unbalanced).

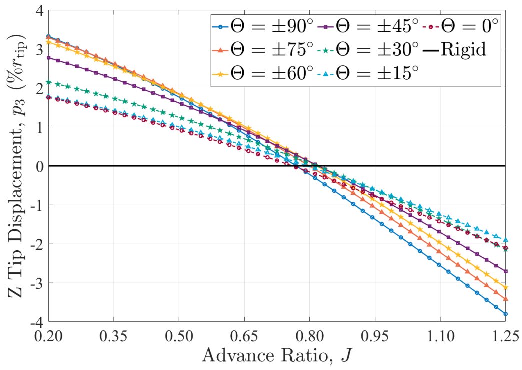

(d) Displacements along the z-axis (symmetric-balanced).

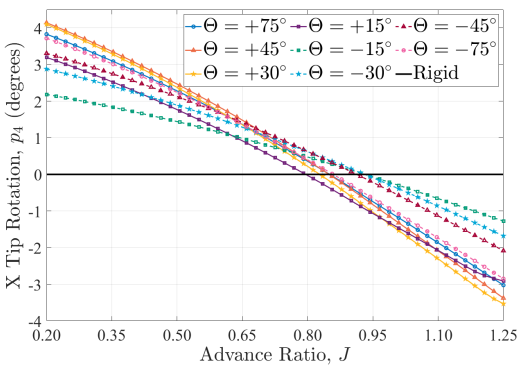

(e) Rotations about the x-axis (symmetric-unbalanced).

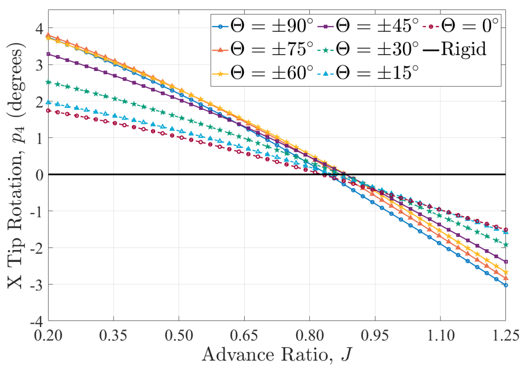

(f) Rotations about the x-axis (symmetric-balanced).

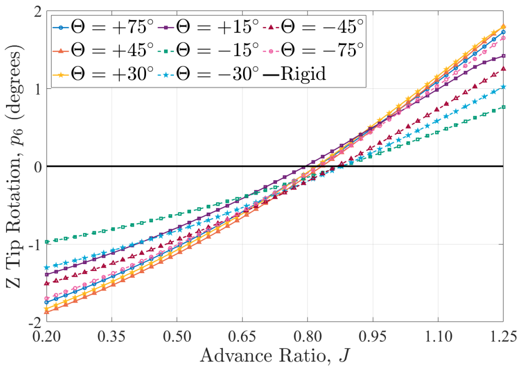

(g) Rotations about the z-axis (symmetric-unbalanced).

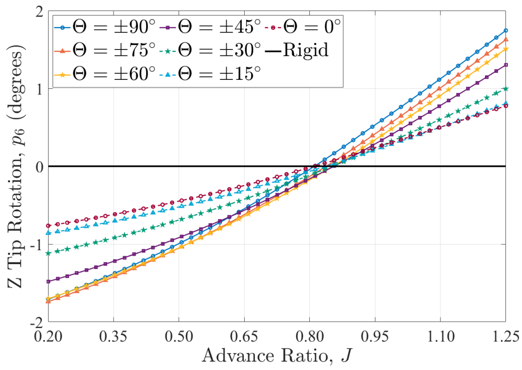

(h) Rotations about the z-axis (symmetric-balanced).

Figure D.7: Blade tip bending and shear deformation plots from sensitivity studies ($\Omega = 30$ RPS, $\beta = 15°$).

D.2.1. LAMINATION PARAMETER VARIATIONS AND STIFFNESS ROSETTES

Stiffness rosettes and lamination parameter values have been shown corresponding to the symmetric-balanced and symmetric-unbalanced laminates that were studied in Section 5.1 to provide an overview of stiffness properties corresponding to the ply orientations that were considered. Variations in lamination parameters are used to indicate the types of coupling that are present for each ply orientation. The discussions presented in this section correspond to Equation (5.2) for symmetric-unbalanced laminates, and Equation (5.3) for symmetric-balanced laminates.

STIFFNESS ROSETTES

Laminate stiffness rosettes have been shown at selected ply orientations, representing symmetric-unbalanced and symmetric-balanced laminates. Only six ply orientations of each type are shown. The in-plane stiffness represents the ability of the laminate to resist in-plane forces, whereas the out-of-plane stiffness represents the ability of the laminate to resist out-of-plane forces.

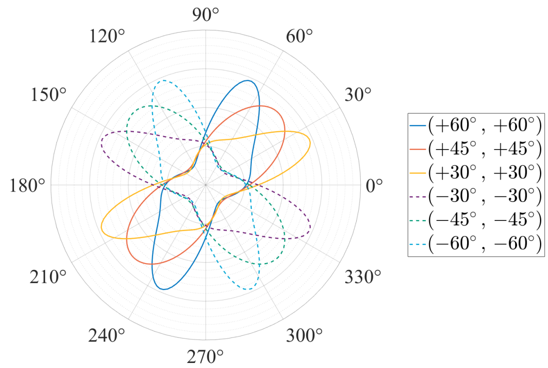

(a) In-plane stiffness (symmetric-unbalanced).

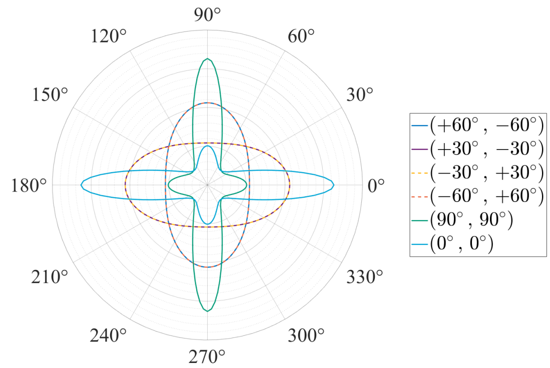

(b) In-plane stiffness (symmetric-balanced).

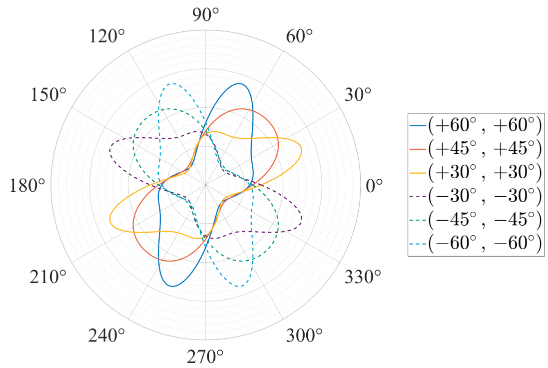

(c) Out-of-plane stiffness (symmetric-unbalanced).

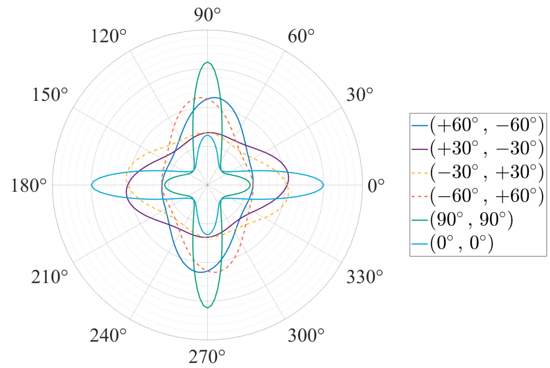

(d) Out-of-plane stiffness (symmetric-balanced).

Figure D.8: Plots of stiffness rosettes for ply orientations considered during sensitivity studies.

As expected from the stiffness rosettes for symmetric-unbalanced laminates, shown in Figure D.8a for in-plane stiffness and in Figure D.8c for out-of-plane stiffness, the direction of maximum stiffness is closely aligned with the angle that most of the plies are aligned with. This is immediately clear for laminates with $\Theta \in \{-45°, 45°\}$. The ply orientations of ±30° and ±60° are slightly skewed due to the constant presence of fibres with orientations of 0° and 90°. The in-plane stiffness of symmetric-balanced laminates appears to be independent of the stacking sequence, as Figure D.8b indicates that laminates corresponding to orientations of $(+\Theta, -\Theta)$ and $(-\Theta, +\Theta)$ have equal in-plane stiffness. The out-of-plane stiffness is skewed between laminates with equivalent ply angles of opposite sign, showing more stiffness towards the outermost plies and less stiffness towards the innermost plies. The difference observed between the out-of-plane stiffness corresponding to ply orientations of $(+\Theta, -\Theta)$ and $(-\Theta, +\Theta)$ would likely be greater if the laminate only consisted of fibres with these corresponding orientations, instead of also containing plies with angles of 0° and 90°. For symmetric-balanced laminates, the maximum stiffness is either aligned closely with 0° or 90°, depending on whether $\pm\Theta$ is closer to 0° or 90°. Without the outermost and innermost fibres that have constant angles of 0° and 90°, the stiffness rosettes would instead be more closely aligned with the angles given by $\pm\Theta$.

LAMINATION PARAMETER VARIATIONS IN A SINGLE VARIABLE

Figure D.9 contains plots of the lamination parameter values for symmetric-unbalanced and symmetric-balanced laminates. The only difference between the two plots are the curves for ξ_2^A and ξ_4^A, which indicate the presence of extension-shear coupling, and the curves for ξ_2^D and ξ_4^D, which indicate the presence of bend-twist coupling. For symmetric-balanced laminates, ξ_2^A and ξ_4^A are of course zero, meaning that there is zero extension-shear coupling. The small values for ξ_2^D and ξ_4^D indicate minimal amounts of bend-twist coupling. It is also useful to note that the stiffness properties are otherwise the same between symmetric-balanced and symmetric-unbalanced laminates that have the same ply orientations, which differ by a sign. Indeed, lamination parameters ξ_1^A, ξ_3^A, ξ_1^D, and ξ_3^D are all symmetric across the vertical line at 0°. The maximum amounts of torsional and shear stiffness appear to emerge at 45° for both laminate types, and the most amount of extension-shear and bend-twist coupling appears to emerge for unbalanced laminates with orientations between ±15° and ±45°. As the torsional stiffness decreases, the influence of coupling will tend to increase, which explains why the maximum variations in performance were observed for unbalanced laminates with ply orientations between ±15° and ±30°.

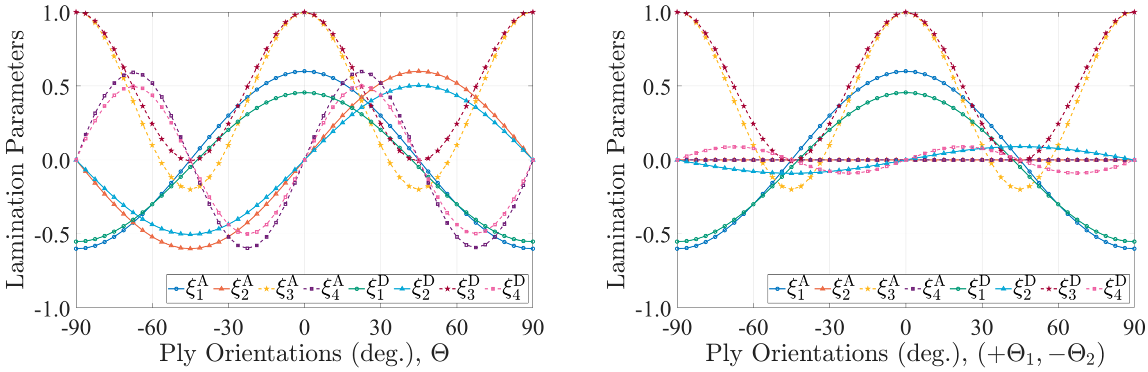

(a) Symmetric-unbalanced laminates. **(b)** Symmetric-balanced laminates.

Figure D.9: Plots of lamination parameters for ply orientations considered during sensitivity studies.

E

Optimization Output Details

Plots of the optimization progress for each case that was studied during this project are provided in this appendix. Figure E.1 through Figure E.3 contain plots for the individual mission segment optimization studies. For the full mission optimization studies, plots are shown in Figure E.4 through Figure E.9 for the variable-pitch propeller, and in Figure E.10 through Figure E.15 for the constant-pitch propeller. It is shown that the optimizer converged with a first-order optimality measure in the order of $1E-03$ or $1E-04$ in all cases. Additionally, a feasible design with a lower objective function value was found in every case, and convergence to a local optimum was obtained in at least two cases, as indicated by the first-order optimality measure decaying to exactly zero. To enable the optimizer to converge, a minimum step size of $1E-02$ was selected for the central finite differencing scheme that was used during the gradient evaluation. Thus, the truncation error associated with the finite differencing method is expected to be at least $\mathcal{O}(1E-04)$. Moreover, the cases that reached full convergence yielded similar values for the structural design, objective function, and inequalities in comparison to the remaining cases that appeared to have not fully converged. Thus, all cases yielded an adequate level of convergence.

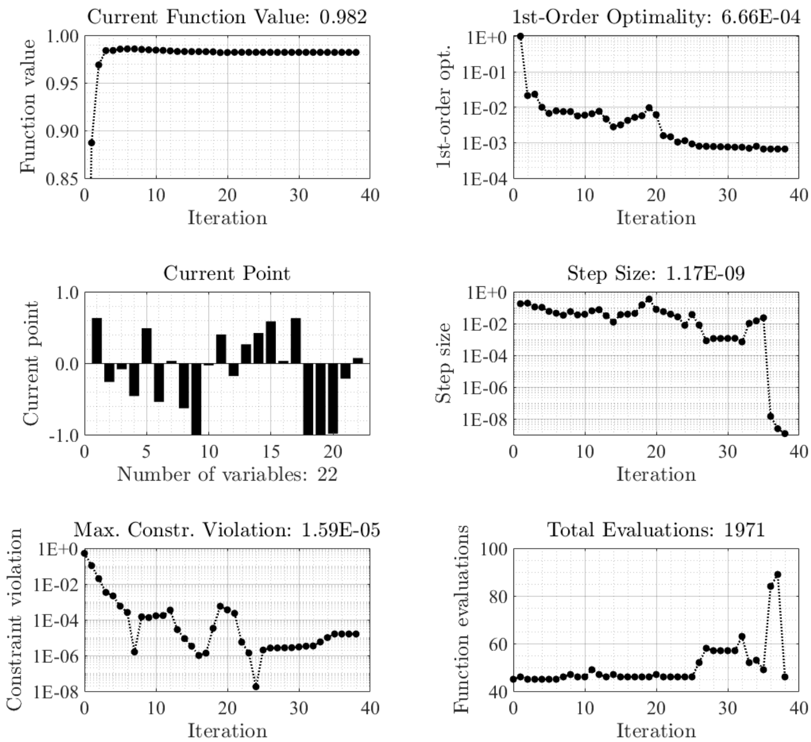

Figure E.1: Optimization progress history plots obtained from the climb-only case.

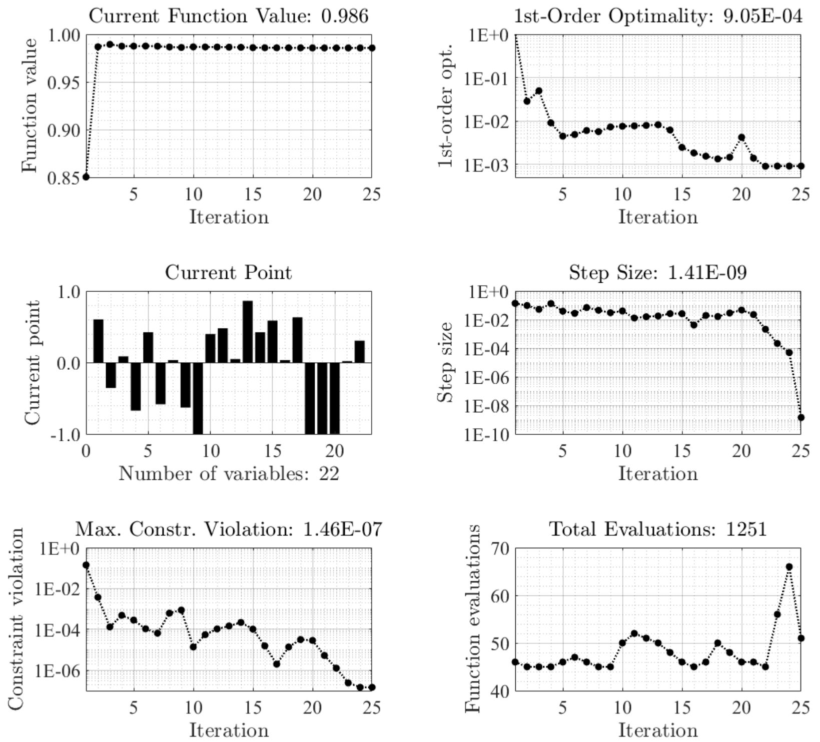

Figure E.2: Optimization progress history plots obtained from the cruise-only case.

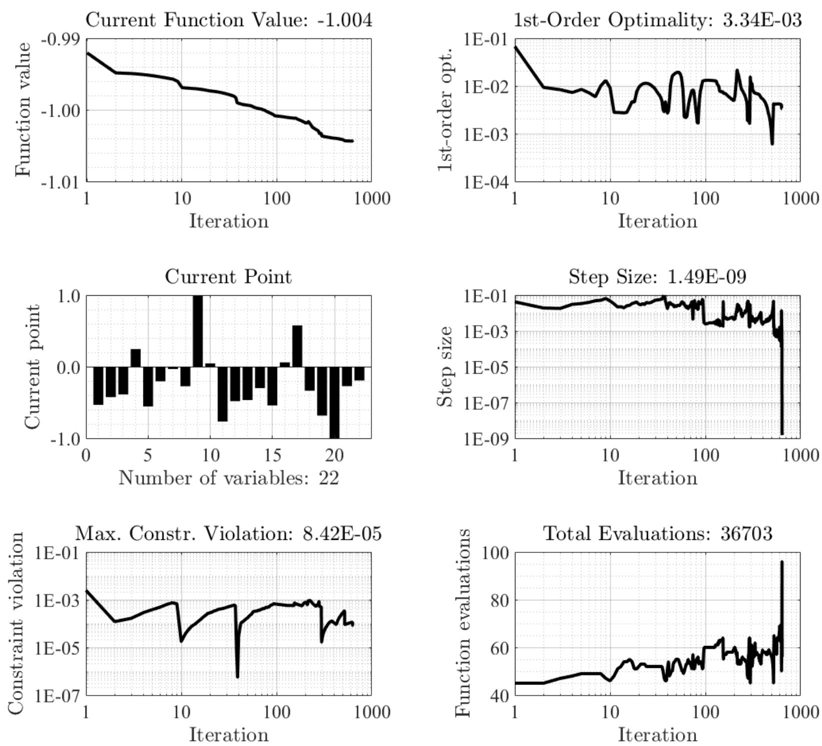

Figure E.3: Optimization progress history plots obtained from the descent-only case.

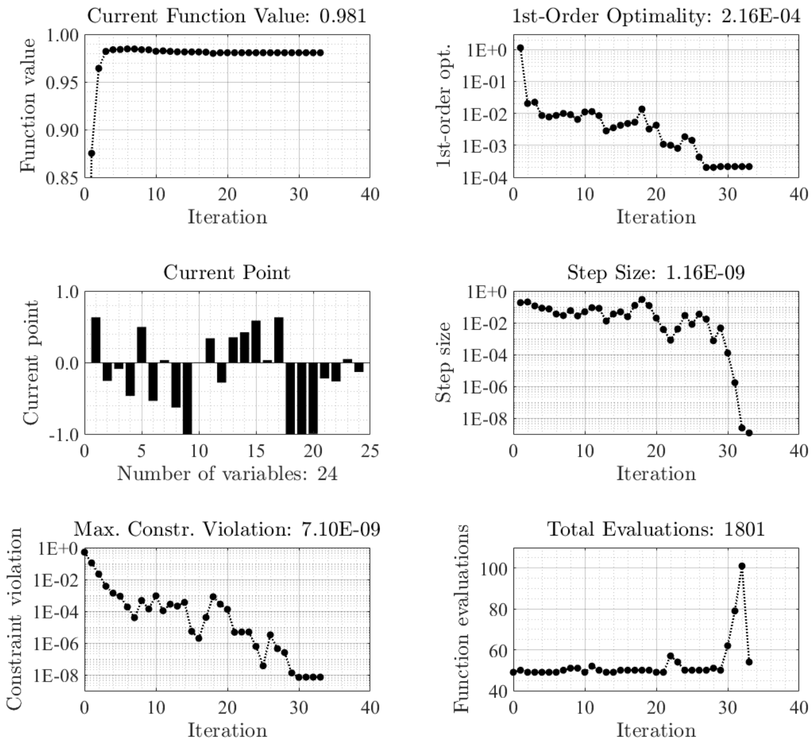

Figure E.4: Optimization progress history plots obtained from the variable-pitch 0 km mission case.

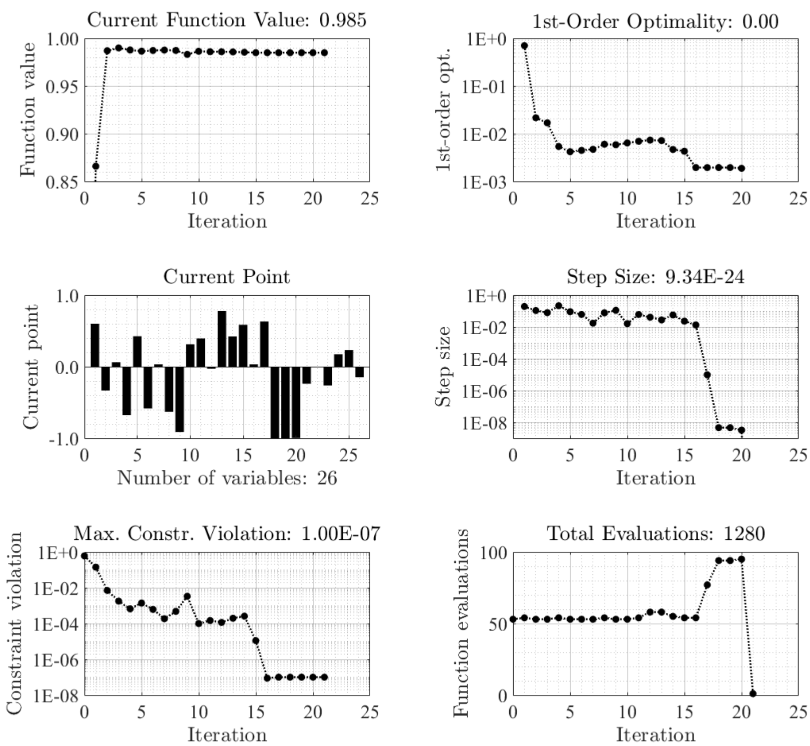

Figure E.5: Optimization progress history plots obtained from the variable-pitch 50 km mission case.

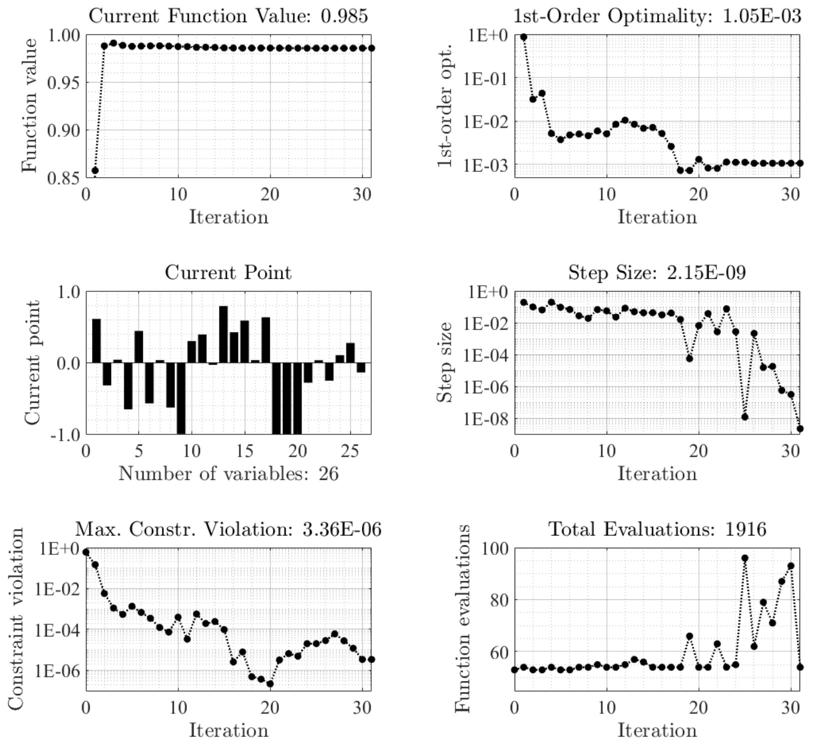

Figure E.6: Optimization progress history plots obtained from the variable-pitch 100 km mission case.

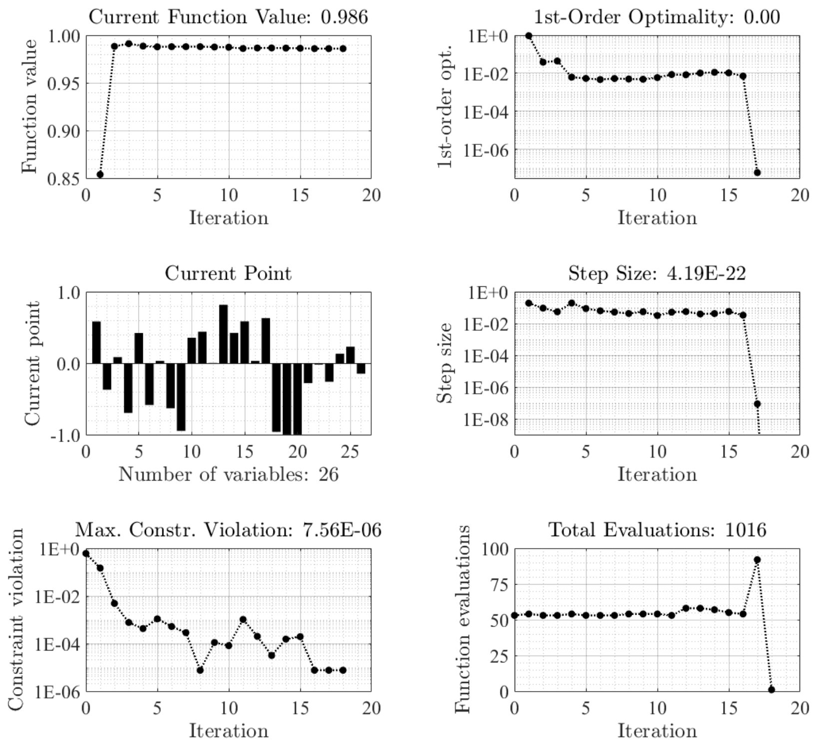

Figure E.7: Optimization progress history plots obtained from the variable-pitch 150 km mission case.

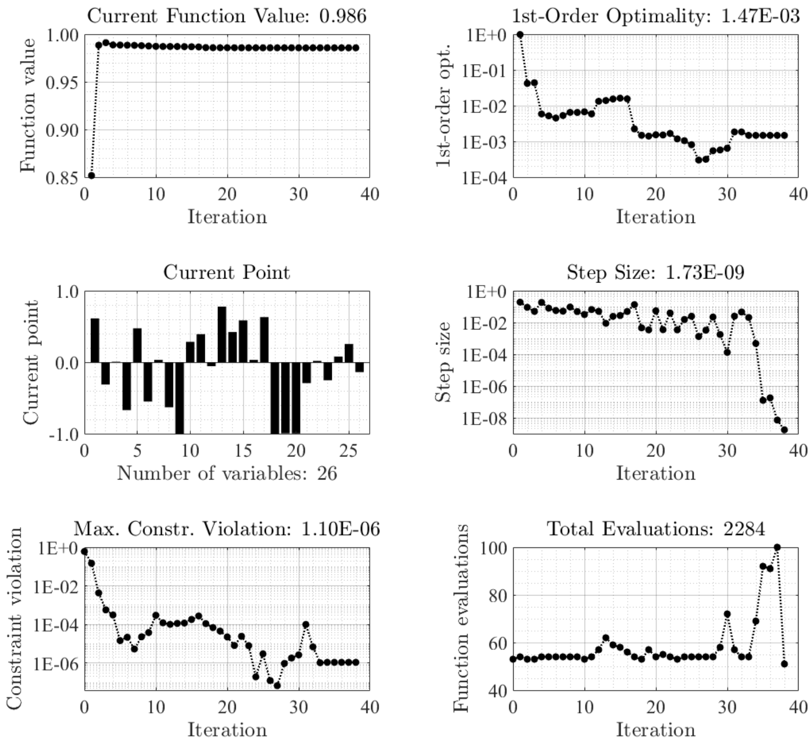

Figure E.8: Optimization progress history plots obtained from the variable-pitch 200 km mission case.

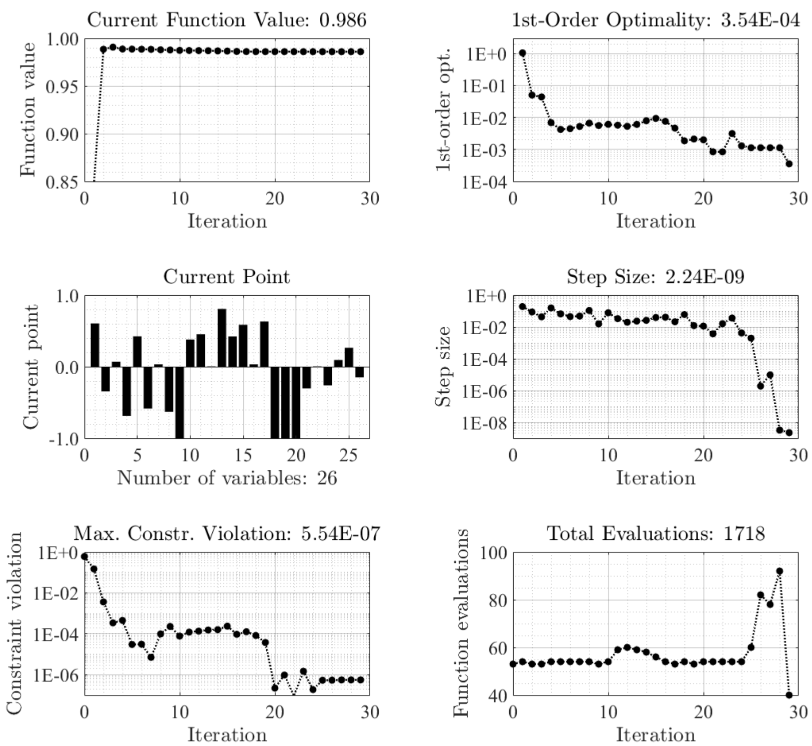

Figure E.9: Optimization progress history plots obtained from the variable-pitch 400 km mission case.

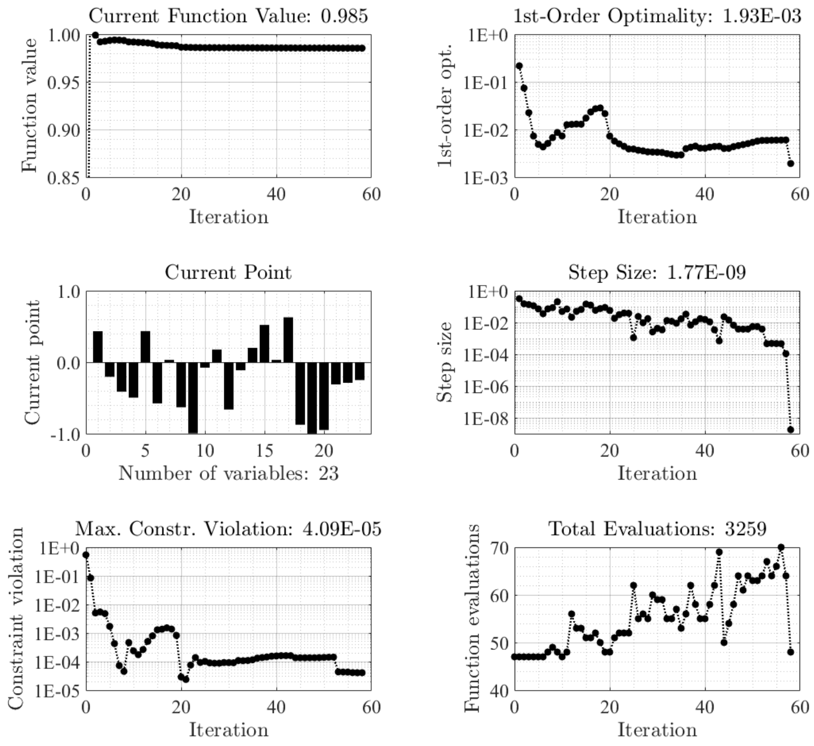

Figure E.10: Optimization progress history plots obtained from the constant-pitch 0 km mission case.

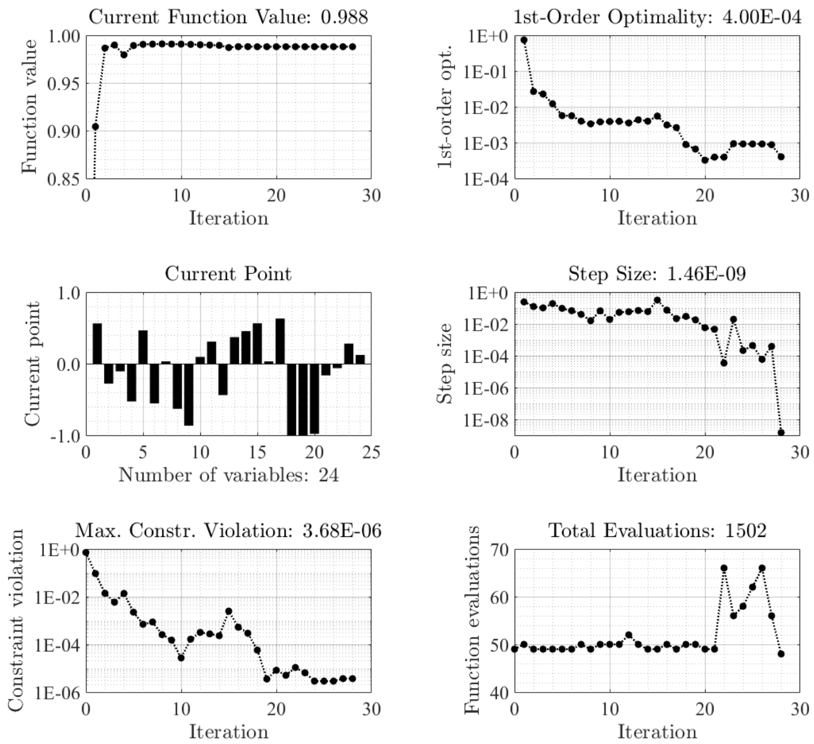

Figure E.11: Optimization progress history plots obtained from the constant-pitch 50 km mission case.

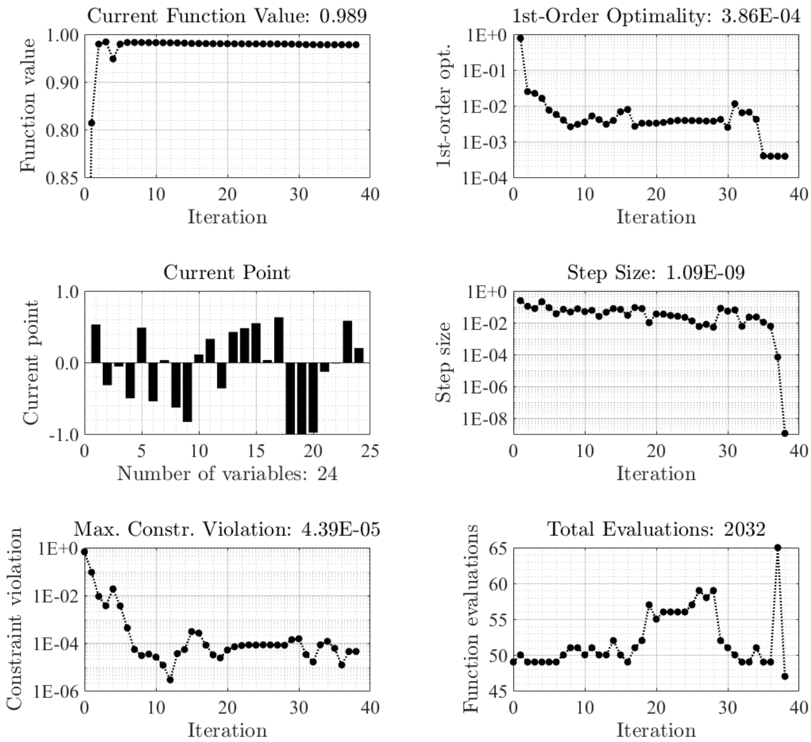

Figure E.12: Optimization progress history plots obtained from the constant-pitch 100 km mission case.

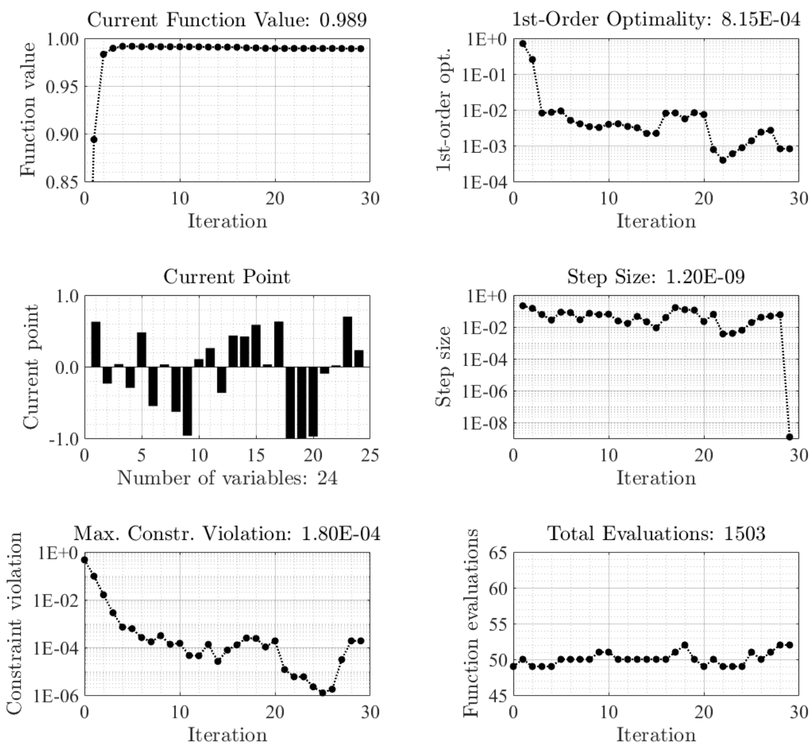

Figure E.13: Optimization progress history plots obtained from the constant-pitch 150 km mission case.

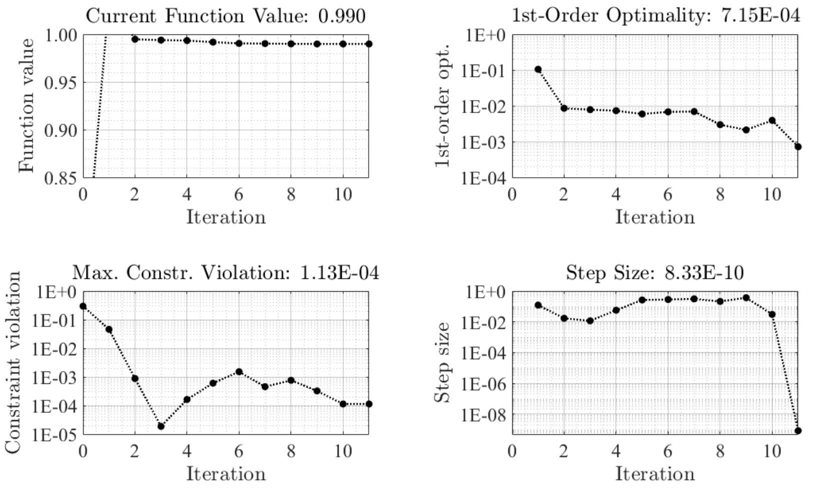

Figure E.14: Optimization progress history plots obtained from the constant-pitch 200 km mission case.

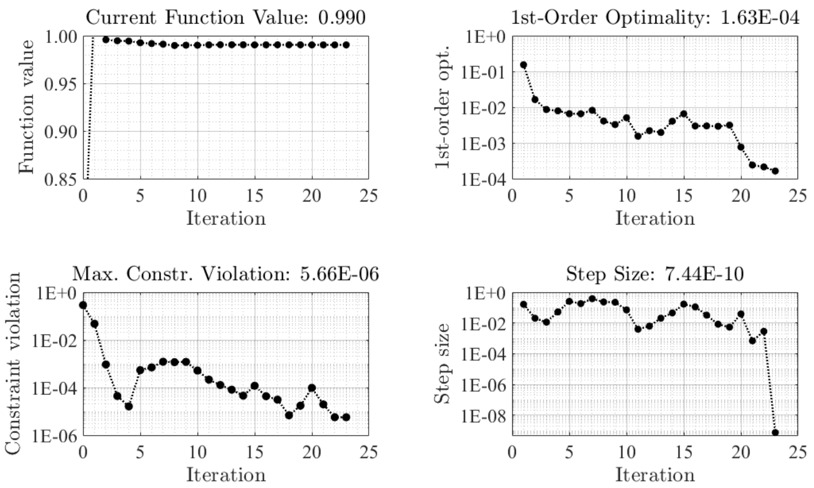

Figure E.15: Optimization progress history plots obtained from the constant-pitch 400 km mission case.

For the plots shown of the normalized design vector (labelled as *Current Point*), the first eight entries correspond to the upper surface lamination parameters, the ninth entry corresponds to the upper surface laminate thickness. Entries 10 through 17 correspond to the lower surface lamination parameters, with entry 18 corresponding to the lower surface laminate thickness. The remaining entries correspond to the advance ratio and pitch setting inputs at each mission segment. This plot was shown to indicate that the only design variables that are located on their upper or lower bounds correspond to the laminate thicknesses. In every case, the upper bound was set to 1.75 millimetres and the lower bound was set to 0.5 millimetres. The upper bound was selected as the largest value that could be selected without causing the upper and lower surfaces to interfere with each other. The lower bound value was selected to ensure that at least 10 plies could be used to construct any laminate returned by the optimizer. This assures that any structural configuration obtained by the optimizer is physically realizable.

For the final two cases investigated with the constant-pitch propeller, shown in Figure E.14 and Figure E.15, the optimizer did not plot the design variable values or the number of function evaluations. The optimization was not re-run to generate these plots due to time constraints. It is still clear that a reasonable level of convergence was reached, and values for the design vector may be inferred from results shown in Section 5.2.2, as well as from results shown in Figure E.11 through Figure E.13, as the design variable values are similar between all cases involving a mission with a non-zero cruise distance.

Bibliography

[1] T. Sinnige, T. Stokkermans, N. van Arnhem, and L. L. Veldhuis, *Aerodynamic performance of a wingtip-mounted tractor propeller configuration in windmilling and energy-harvesting conditions,* in *AIAA Aviation 2019 Forum*, AIAA Aviation Forum (American Institute of Aeronautics and Astronautics, 2019).

[2] D. Erzen, M. Andrejasic, and T. Kosel, *An optimal propeller design for in-flight power recuperation on an electric aircraft,* in *2018 Aviation Technology, Integration, and Operations Conference* (American Institute of Aeronautics and Astronautics, 2018).

[3] J. Sodja, R. Drazumeric, T. Kosel, and P. Marzocca, *Design of flexible propellers with optimized load-distribution characteristics,* Journal of Aircraft **51**, 117 (2014), publisher: American Institute of Aeronautics and Astronautics.

[4] A. M. Khan, *Flexible composite propeller design using constrained optimization techniques*, Ph.D. thesis, Iowa State University (1997).

[5] H. Glauert, *The Analysis of Experimental Results in the Windmill Brake and Vortex Ring States of an Airscrew* (Her Majesty's Stationery Office, 1926).

[6] P. MacCready, *Regenerative battery-augmented soaring,* Technical Soaring **23**, 28 (2022).

[7] J. P. Barnes, *Regenerative electric flight synergy and integration of dual role machines,* in *53rd AIAA Aerospace Sciences Meeting*, AIAA SciTech Forum (American Institute of Aeronautics and Astronautics, 2015).

[8] J. P. Barnes, *Math modeling of propeller geometry and aerodynamics,* (1999).

[9] J. P. Barnes, *Flight without fuel – regenerative soaring feasibility study,* (2006).

[10] J. Goyal, T. Sinnige, F. Avallone, and C. Ferreira, *Aerodynamic and aeroacoustic characteristics of an isolated propeller at positive and negative thrust,* in *AIAA Aviation 2021 Forum*, AIAA Aviation Forum (American Institute of Aeronautics and Astronautics, 2021) pp. 1–22.

[11] J. Bosschers, B. Montgomerie, A. J. Brand, and R. P. J. O. M. van Rooij, *Influence of blade rotation on the sectional aerodynamics of rotating blades,* in *European Rotorcraft Forum (22nd), Brighton, UK* (1996).

[12] N. Binder, S.-K. Courty-Audren, S. Duplaa, G. Dufour, and X. Carbonneau, *Theoretical analysis of the aerodynamics of low-speed fans in free and load-controlled windmilling operation,* Journal of Turbomachinery **137** (2015), 10.1115/1.4030308.

[13] R. Nederlof, D. Ragni, and T. Sinnige, *Experimental investigation of the aerodynamic performance of a propeller at positive and negative thrust and power,* in *AIAA Aviation 2022 Forum*, AIAA Aviation Forum (American Institute of Aeronautics and Astronautics, 2022).

[14] M. H. Shirk, T. J. Hertz, and T. A. Weisshaar, *Aeroelastic tailoring - theory, practice, and promise,* Journal of Aircraft **23**, 6 (1986), publisher: American Institute of Aeronautics and Astronautics.

[15] M. M. Munk, *Propeller Containing Diagonally Disposed Fibrous Material*, Tech. Rep. 2484308 (United States Patent Office, 1949).

[16] T. H. Wood and K. Ramakrishnan, *Aeroelastically Tailored Propellers for Noise Reduction and Improved Efficiency in a Turbomachine*, Tech. Rep. 20150344127 (US Patent Application, 2015).

[17] W. J. Dwyer and J. B. Rogers, *Aeroelastically Tailored Propellers*, SAE Technical Paper 770455 (SAE International, 1977).

[18] O. Yamamoto and R. August, *Structural and aerodynamic analysis of a large scale advanced propeller blade,* Journal of Propulsion and Power **8**, 367 (1992), publisher: American Institute of Aeronautics and Astronautics.

[19] A. Chattopadhyay, T. R. McCarthy, and C. E. Seeley, *Decomposition-based optimization procedure for high-speed prop-rotors using composite tailoring,* Journal of Aircraft **32**, 1026 (1995), publisher: American Institute of Aeronautics and Astronautics.

[20] Y. Sandak and A. Rosen, *Aeroelastically adaptive propeller using blades' root flexibility,* The Aeronautical Journal **108**, 411 (2004).

[21] J. Sodja, R. De Breuker, D. Nozak, R. Drazumeric, and P. Marzocca, *Assessment of low-fidelity fluid–structure interaction model for flexible propeller blades,* Aerospace Science and Technology **78**, 71 (2018).

[22] S. B. Heinzen, C. E. Hall, and A. Gopalarathnam, *Development and testing of a passive variable-pitch propeller,* Journal of Aircraft **52**, 748 (2015).

[23] F. Möhren, O. Bergmann, F. Janser, and C. Braun, *On the influence of elasticity on propeller performance: a parametric study,* CEAS Aeronautical Journal (2023), 10.1007/s13272-023-00649-y.

[24] A. M. Khan, V. Dayal, J. M. Vogel, and D. O. Adams, *Effects of bend–twist coupling on composite propeller performance,* Mechanics of Composite Materials and Structures **7**, 383 (2000).

[25] E. A. Ferede, *Static Aeroelastic Optimization of Composite Wind Turbine Blades Using Variable Stiffness Laminates: Exploring Twist Coupled Composite Blades in Stall Control*, Ph.D. thesis, Delft University of Technology (2016).

[26] T. Hegberg, *Fast Aeroelastic Analysis and Optimisation of Large Mixed Materials Wind Turbine Blades*, phdthesis, Delft University of Technology (2019).

[27] E. A. Ferede, M. M. Abdalla, F. Gandhi, G. van Bussel, and J. Dillinger, *Aeroelastic optimization of composite wind turbine blades using variable stiffness laminates,* in *AHS International - 73rd Annual Forum Proceedings*, Vol. 73 (AHS International, 2017) ISSN: 1552-2938.

[28] O. Gur and A. Rosen, *Optimization of propeller based propulsion system,* (American Institute of Aeronautics and Astronautics Inc., 2009) pp. 95–106.

[29] N. P. M. Werter and R. De Breuker, *A novel dynamic aeroelastic framework for aeroelastic tailoring and structural optimisation,* Composite Structures **158**, 369 (2016).

[30] N. P. M. Werter, *Aeroelastic Modelling and Design of Aeroelastically Tailored and Morphing Wings*, phdthesis, Delft University of Technology (2017).

[31] D. Rajpal, R. De Breuker, H. Timmermans, W. Lammen, and F. Torrigiani, *Including aeroelastic tailoring in the conceptual design process of a composite strut braced wing,* Proceedings of the 31st Congress of the International Council of the Aeronautical Sciences (2018).

[32] H. Glauert, *The Elements of Aerofoil and Airscrew Theory, Second Edition (Cambridge Science Classics)*, 2nd ed. (Cambridge University Press, 1983).

[33] J. M. F. van Neerven, *Design of a Variable Pitch, Energy-Harvesting Propeller for In-Flight Power Recuperation on Electric Aircraft*, Master's thesis, Delft University of Technology (2020).

[34] F. Scholtens, *Electric Aircraft Design Including an In-the-loop Propeller Design Model with Regenerative Mode*, Master's thesis, Delft University of Technology (2021).

[35] C. N. Adkins and R. H. Liebeck, *Design of optimum propellers,* Journal of Propulsion and Power **10**, 676 (1994), publisher: American Institute of Aeronautics and Astronautics.

[36] W. Johnson, *Rotorcraft Aeromechanics*, Cambridge Aerospace Series (Cambridge University Press, 2013).

[37] J. G. Leishman, *Principles of Helicopter Aerodynamics* (Cambridge University Press, 2006).

[38] O. Gur and A. Rosen, *Novel approach to axisymmetric actuator disk modeling,* AIAA Journal **46**, 2914 (2008).

[39] H. Glauert, *Airplane propellers,* in *Aerodynamic Theory: A General Review of Progress Under a Grant of the Guggenheim Fund for the Promotion of Aeronautics* (Springer Berlin Heidelberg, Berlin, Heidelberg, 1935) pp. 169–360.

[40] S. Goldstein, *On the vortex theory of screw propellers,* Proceedings of the Royal Society of London. Series A, Containing Papers of a Mathematical and Physical Character **123**, 440 (1929).

[41] Q. R. Wald, *The aerodynamics of propellers,* Progress in Aerospace Sciences **42**, 85 (2006).

[42] A. Ning, *Using blade element momentum methods with gradient-based design optimization,* Structural and Multidisciplinary Optimization **64**, 991 (2021).

[43] T. L. Burton, N. Jenkins, E. Bossanyi, D. Sharpe, and M. Graham, *Wind Energy Handbook*, 3rd ed. (Wiley, 2021).

[44] M. L. Buhl, *A New Empirical Relationship between Thrust Coefficient and Induction Factor for the Turbulent Windmill State*, Tech. Rep. TP-500-36834 (NREL - National Renewable Energy Laboratory, 2005).

[45] C. N. Lock, H. H. Bateman, and H. C. H. Townend, *An Extension of the Vortex Theory of Airscrews with Applications to Airscrews of Small Pitch Including Experimental Results* (Her Majesty's Stationery Office, 1926).

[46] A. Betz, *Introduction to the Theory of Flow Machines* (Pergamon, 1966).

[47] F. M. White, *Fluid Mechanics*, 9th ed. (McGraw-Hill, 2021).

[48] R. De Breuker, *Energy-based Aeroelastic Analysis and Optimisation of Morphing Wings*, Ph.D. thesis, Delft University of Technology (2011).

[49] C. Kassapoglou, *Design and Analysis of Composite Structures* (John Wiley & Sons, 2010).

[50] B. D. Agarwal, L. J. Broutman, and K. Chandrashekhara, *Analysis and Performance of Fiber Composites*, 4th ed. (John Wiley & Sons, 2017).

[51] I. M. Daniel and O. Ishai, *Engineering Mechanics of Composite Materials*, 2nd ed. (Oxford University Press, 2006).

[52] J. M. Whitney, *Structural Analysis Of Laminated Anisotropic Plates* (Routledge, 2017).

[53] R. M. Jones, *Mechanics Of Composite Materials*, 2nd ed. (CRC Press, 2018).

[54] S. W. Tsai and H. T. Hahn, *Introduction to Composite Materials*, 1st ed. (CRC Press, 1980).

[55] C. Mittelstedt, *Structural Mechanics in Lightweight Engineering* (Springer International Publishing, 2021).

[56] M. A. Albazzan, R. Harik, B. F. Tatting, and Z. Gürdal, *Efficient design optimization of nonconventional laminated composites using lamination parameters: A state of the art,* Composite Structures **209**, 362 (2019).

[57] M. W. Bloomfield, C. G. Diaconu, and P. M. Weaver, *On feasible regions of lamination parameters for lay-up optimization of laminated composites,* Proceedings of the Royal Society A: Mathematical, Physical and Engineering Sciences **465**, 1123 (2009).

[58] M. Lis, *Numerical analysis and optimization of motoglider's propeller structure,* Transactions of the Institute of Aviation **245**, 87 (2016).

[59] E. A. Ferede and M. M. Abdalla, *Cross-sectional modelling of thin-walled composite beams,* (2014).

[60] R. Guyan, *Reduction of stiffness and mass matrices,* AIAA Journal **3**, 380 (1965).

[61] J.-M. Battini and C. Pacoste, *Co-rotational beam elements with warping effects in instability problems,* Computer Methods in Applied Mechanics and Engineering **191**, 1755 (2002).

[62] A. Ibrahimbegovic, *On the choice of finite rotation parameters,* Computational Methods in Applied Mechanics and Engineering **149**, 49 (1997).

[63] J. K. S. Dillinger, *Static Aeroelastic Optimization of Composite Wings with Variable Stiffness Laminates*, phdthesis, Delft University of Technology (2014), ISBN: 9789462035898.

[64] J. R. R. A. Martins and S. A. S. A. Ning, *Engineering design optimization* (Cambridge University Press, 2021) p. 637.

[65] J. Dorfling and K. Rokhsaz, *Constrained and unconstrained propeller blade optimization,* (American Institute of Aeronautics and Astronautics, 2015) pp. 1179–1188.

[66] S. T. IJsselmuiden, M. M. Abdalla, and Z. Gürdal, *Implementation of strength-based failure criteria in the lamination parameter design space,* AIAA Journal **46**, 1826 (2008).

[67] A. Khani, S. T. Ijsselmuiden, M. M. Abdalla, and Z. Gürdal, *Design of variable stiffness panels for maximum strength using lamination parameters,* Composites Part B: Engineering **42**, 546 (2011).

[68] Pipistrel by Textron eAviation, *Panthera,* `https://www.pipistrel-aircraft.com/products/panthera/` (2023), accessed on July 18, 2023.

[69] S. Gudmundsson, *General Aviation Aircraft Design*, edited by S. Gudmundsson (Butterworth-Heinemann, Boston, Massachusetts, USA, 2014).

[70] M. Niţă and D. Scholz, *Estimating the Oswald factor from basic aircraft geometrical parameters* (Deutsche Gesellschaft für Luft-und Raumfahrt-Lilienthal-Oberth eV, 2012).

[71] Pipistrel by Textron eAviation, *Velis Electro,* `https://www.pipistrel-aircraft.com/products/velis-electro/` (2023), accessed on July 18, 2023.

[72] TU Delft: Faculty of Aerospace Engineering, *Propeller Models,* `https://www.tudelft.nl/lr/organisatie/afdelingen/flow-physics-and-technology/flight-performance-and-propulsion/flight-performance/propeller-aerodynamics/facilities/propeller-models` (2022), accessed on December 23, 2022.

[73] W. J. M. Rankine, *On the mechanical principles of the action of propellers,* Transaction of the Institute of Naval Architects **6**, 13 (1865).

[74] R. E. Froude, *On the part played in propulsion by difference in pressure,* Transaction of the Institute of Naval Architects **30** (1889).

[75] Q. Wald, *The wright brothers propeller theory and design,* 37th Joint Propulsion Conference and Exhibit Joint Propulsion Conferences (2001), 10.2514/6.2001-3386.

[76] L. Prandtl, *Applications of Modern Hydrodynamics to Aeronautics*, Research and Development NACA-TR-116 (National Advisory Committee for Aeronautics, 1923).

[77] A. Betz, *Schraubenpropeller mit geringstem energieverlust. mit einem zusatz von l. Prandtl,* Nachrichten von der Gesellschaft der Wissenschaften zu Göttingen, Mathematisch-Physikalische Klasse **1919**, 193 (1919).

[78] T. Theodorsen, *The theory of propellers,* The Aeronautical Journal **52**, 574 (1948).

[79] C. L. Tibery and J. W. Wrench Jr., *Tables of Goldstein Factors*, Research and Development AD0610171 (David Taylor Model Basin Washington DC, 1964).

[80] E. E. Larrabee, *Practical Design of Minimum Induced Loss Propellers*, SAE Technical Paper 790585 (SAE International, 1979) ISSN: 0148-7191, 2688-3627.

[81] J. N. Sørensen, *General Momentum Theory for Horizontal Axis Wind Turbines*, 1st ed., Research Topics in Wind Energy (Springer Cham, 2016).

[82] R. MacNeill and D. Verstraete, *Validation of an aeroelastic rotor analysis method,* in *2018 Joint Propulsion Conference*, AIAA Propulsion and Energy Forum (American Institute of Aeronautics and Astronautics, 2018).

[83] G. J. D. Zondervan, *A review of propeller modelling techniques based on Euler methods,* (Delft University Press, 1998).

[84] A. van Garrel, *Development of a Wind Turbine Aerodynamics Simulation Module*, Research and Development ECN-C–03-079 (Energy Research Centre of the Netherlands (ECN), 2003).

[85] B. P. Epps, *OpenProp v2.4 Theory Document*, Research and Development (Massachussetts Institute of Technology, 2010).

[86] D. Marten, *QBlade: A Modern Tool for the Aeroelastic Simulation of Wind Turbines*, Ph.D. thesis, Berlin Institute of Technology (2020).

[87] O. Gur and A. Rosen, *Comparison between blade-element models of propellers,* The Aeronautical Journal **112**, 689 (2008).

[88] M. O. L. Hansen, J. N. Sørensen, S. Voutsinas, N. Sørensen, and H. A. Madsen, *State of the art in wind turbine aerodynamics and aeroelasticity,* Progress in Aerospace Sciences **42**, 285 (2006).

[89] B. W. McCormick, *Aerodynamics, Aeronautics, and Flight Mechanics*, 2nd ed. (John Wiley & Sons, 1994).

[90] S. A. Whitmore and R. S. Merrill, *Nonlinear large angle solutions of the blade element momentum theory propeller equations,* Journal of Aircraft **49**, 1126 (2012).

[91] A. J. Evans and G. Liner, *A Wind-Tunnel Investigation of the Aerodynamic Characteristics of a Full-Scale Sweptback Propeller and Two Related Straight Propellers*, Research and Development (University of North Texas Libraries, UNT Digital Library, 1951).

[92] H. C. McLemore and M. D. Cannon, *Aerodynamic Investigation of a four-blade propeller operating through an angle-of-attack range from 0 to 180 degrees*, Tech. Rep. 3228 (NACA - National Advisory Committee for Aeronautics, 1954).

[93] J. Sodja, D. Stadler, and T. Kosel, *Computational fluid dynamics analysis of an optimized load-distribution propeller,* Journal of Aircraft **49**, 955 (2012).

[94] J. Anderson, *Fundamentals of Aerodynamics*, 6th ed. (McGraw-Hill Education, 2017).

[95] M. Drela, *Flight Vehicle Aerodynamics* (MIT Press, 2014).

[96] O. Rand and A. Rosen, *Efficient method for calculating the axial velocities induced along rotating blades by trailing helical vortices,* Journal of Aircraft **21**, 433 (1984).

[97] H. Lerbs, *Moderately Loaded Propellers with a Finite Number of Blades and an Arbitrary Distribution of Circulation*, Research and Development T1952-1 (The Society of Naval Architects and Marine Engineers, 1952).

[98] J. W. Wrench Jr., *The Calculation of Propeller Induction Factors AML Problem 69-54*, Research and Development AD0224732 (David Taylor Model Basin Washington DC, 1957).

[99] J. E. Kerwin and J. B. Hadler, *Principles of Naval Architecture Series - Propulsion* (Society of Naval Architects and Marine Engineers (SNAME), 2010).

[100] B. P. Epps and R. W. Kimball, *Unified rotor lifting line theory,* Journal of Ship Research **57**, 1 (2013).

[101] B. P. Epps, *On the rotor lifting line wake model,* Journal of Ship Production and Design **32**, 1 (2016).

[102] S. Perez-Becker, F. Papi, J. Saverin, D. Marten, A. Bianchini, and C. O. Paschereit, *Is the blade element momentum theory overestimating wind turbine loads? – an aeroelastic comparison between openfast's aerodyn and qblade's lifting-line free vortex wake method,* Wind Energy Science **5**, 721 (2020).

[103] H. Lee, B. Sengupta, M. S. Araghizadeh, and R. S. Myong, *Review of vortex methods for rotor aerodynamics and wake dynamics,* Advances in Aerodynamics **4**, 20 (2022).

[104] J. Katz and A. Plotkin, *Low-Speed Aerodynamics*, 2nd ed. (Cambridge University Press, 2012).

[105] H. Lee and D.-J. Lee, *Numerical investigation of the aerodynamics and wake structures of horizontal axis wind turbines by using nonlinear vortex lattice method,* Renewable Energy **132**, 1121 (2019).

[106] S. Hauptmann, M. Bülk, L. Schön, S. Erbslöh, K. Boorsma, F. Grasso, M. Kühn, and P. W. Cheng, *Comparison of the lifting-line free vortex wake method and the blade-element-momentum theory regarding the simulated loads of multi-mw wind turbines,* Journal of Physics: Conference Series **555**, 012050 (2014).

[107] F. Blondel, R. Boisard, M. Milekovic, G. Ferrer, C. Lienard, and D. Teixeira, *Validation and comparison of aerodynamic modelling approaches for wind turbines,* Journal of Physics: Conference Series **753**, 022029 (2016).

[108] K. A. R. Ismail and W. M. Okita, *A comprehensive comparative investigation of the lifting line theory and blade element momentum theory applied to small wind turbines,* Journal of Energy Resources Technology **144** (2022), 10.1115/1.4053066.

[109] R. B. de Luna, D. Marten, T. Barlas, S. G. Horcas, N. Ramos-García, A. Li, and C. O. Paschereit, *Comparison of different fidelity aerodynamic solvers on the iea 10 mw turbine including novel tip extension geometries,* Journal of Physics: Conference Series **2265**, 032002 (2022).

[110] W. Z. Shen, R. Mikkelsen, J. N. Sørensen, and C. Bak, *Tip loss corrections for wind turbine computations,* Wind Energy **8**, 457 (2005).

[111] R. E. Wilson and P. B. S. Lissaman, *Applied aerodynamics of wind power machines*, Tech. Rep. PB-238595 (Oregon State University, Corvallis (USA), 1974) OSTI Identifier: 7291582.

[112] O. de Vries, *Fluid Dynamic Aspects of Wind Energy Conversion*, Tech. Rep. AGARDograph 243 (Advisory Group for Aerospace Research and Development (AGARD), 1979).

[113] S. A. Ning, *A simple solution method for the blade element momentum equations with guaranteed convergence,* Wind Energy **17**, 1327 (2014).

[114] M. L. Ruh and J. T. Hwang, *Robust modeling and optimal design of rotors using blade element momentum theory,* in *AIAA Aviation 2021 Forum*, AIAA Aviation Forum (American Institute of Aeronautics and Astronautics, 2021) pp. 1–23.

[115] H. Himmelskamp, *Profile investigations on a rotating airscrew* (Ministry of Aircraft Production, 1947).

[116] H. A. Dwyer and W. J. McCroskey, *Crossflow and unsteady boundary-layer effects on rotating blades,* AIAA Journal **9**, 1498 (1971).

[117] W. H. Young and J. C. Williams, *Boundary-layer separation on rotating blades in forward flight,* AIAA Journal **10**, 1613 (1972).

[118] H. A. Madsen and H. F. Christensen, *On the relative importance of rotational, unsteady and three-dimensional effects on the hawt rotor aerodynamics,* Wind Engineering **14**, 405 (1990).

[119] H. Snel, R. Houwink, and W. J. Piers, *Sectional prediction of 3d effects for separated flow on rotating blades,* in *European Rotorcraft Forum (18th), Avignon, France* (1992).

[120] J. C. Narramore and R. Vermeland, *Navier-Stokes calculations of inboard stall delay due to rotation,* Journal of Aircraft **29**, 73 (1992).

[121] M. C. Robinson, M. M. Hand, D. A. Simms, and S. J. Schreck, *Horizontal axis wind turbine aerodynamics: Three-dimensional, unsteady, and separated flow influences,* in *ASME/JSME Joint Fluids Engineering Conference, San Francisco, CA* (1999).

[122] L. L. M. Veldhuis, *Propeller Wing Aerodynamic Interference*, Ph.D. thesis, Delft University of Technology (2005).

[123] J. Morgado, M. A. R. Silvestre, and J. C. Páscoa, *A comparison of post-stall models extended for propeller performance prediction,* Aircraft Engineering and Aerospace Technology **88**, 540 (2016).

[124] S.-P. Breton, F. N. Coton, and G. Moe, *A study on rotational effects and different stall delay models using a prescribed wake vortex scheme and nrel phase vi experiment data,* Wind Energy **11**, 459 (2008).

[125] Z. Du and M. Selig, *A 3-d stall-delay model for horizontal axis wind turbine performance prediction,* in *1998 ASME Wind Energy Symposium* (1998).

[126] P. K. Chaviaropoulos and M. O. L. Hansen, *Investigating three-dimensional and rotational effects on wind turbine blades by means of a quasi-3d navier-stokes solver,* Journal of Fluids Engineering **122**, 330 (2000).

[127] O. Gur and A. Rosen, *Propeller performance at low advance ratio,* Journal of Aircraft **42**, 435 (2005).

[128] H. Dumitrescu and V. Cardos, *Rotational effects on the boundary-layer flow in wind turbines,* AIAA Journal **42**, 408 (2004).

[129] J. J. Corrigan and J. J. Schillings, *Empirical model for stall delay due to rotation,* in *American Helicopter Society Aeromechanics Specialists Conference, San Francisco, CA*, Vol. 21 (1994).

[130] W. H. H. Banks and G. E. Gadd, *Delaying effect of rotation on laminar separation,* AIAA Journal **1**, 941 (1963).

[131] J. L. Tangler and M. S. Selig, *An evaluation of an empirical model for stall delay due to rotation for HAWTS*, Tech. Rep. NREL/CP-440-23258 (National Renewable Energy Lab. (NREL), 1997).

[132] H. Snel, *Sectional prediction of 3d effects for stalled flow on rotating blades and comparison with measurements,* in *1993 European Community Wind Energy Conference Proceedings*, ECN: X-serie (Netherlands Energy Research Foundation ECN, Germany, 1993) pp. 395–399.

[133] A. Eggers, K. Chaney, and R. Digumarthi, *An assessment of approximate modeling of aerodynamic loads on the uae rotor,* in *41st Aerospace Sciences Meeting and Exhibit* (2012).

[134] C. Lindenburg, *Investigation into Rotor Blade Aerodynamics*, Tech. Rep. ECN-C–03-025 (ECN Wind Energy, 2003).

[135] J. L. Dowler and S. Schmitz, *A solution-based stall delay model for horizontal-axis wind turbines,* Wind Energy **18**, 1793 (2015).

[136] C. Lindenburg, *Modelling of rotational augmentation based on engineering considerations and measurements,* (2004).

[137] O. Bergmann, F. Götten, C. Braun, and F. Janser, *Comparison and evaluation of blade element methods against rans simulations and test data,* CEAS Aeronautical Journal **13**, 535 (2022).

[138] R. Eppler and M. Hepperle, *A Procedure for Propeller Design by Inverse Methods*, Tech. Rep. (MH AeroTools, 2003).

[139] M. Hepperle, *Inverse aerodynamic design procedure for propellers having a prescribed chord-length distribution,* Journal of Aircraft **47**, 1867 (2010).

[140] M. A. Silvestre, J. Morgado, and J. C. Páscoa, *Jblade: A propeller design and analysis code,* (2013).

[141] J. Morgado, M. A. R. Silvestre, and J. C. Páscoa, *Validation of new formulations for propeller analysis,* Journal of Propulsion and Power **31**, 467 (2015).

[142] J. P. S. Morgado, *Development of an Open Source Software Tool for Propeller Design in the MAAT Project*, Ph.D. thesis, University of Beira Interior (2016).

[143] M. Drela, *QPROP Formulation*, Tech. Rep. (Massachusetts Institute of Technology, 2006).

[144] M. Drela and H. Youngren, *XROTOR Download Page,* `https://web.mit.edu/drela/Public/web/xrotor/` (2011), accessed on December 23, 2022.

[145] M. Drela, *XFOIL: An Analysis and Design System for Low Reynolds Number Airfoils*, Tech. Rep. (Massachusetts Institute of Technology, 1989).

[146] R. W. Cornell and E. A. Rothman, *Structural design and analysis of prop-fan blades.* (AIAA, 1979).

[147] J. D. Hoyos, J. H. Jiménez, C. Echavarría, J. P. Alvarado, and G. Urrea, *Aircraft propeller design through constrained aero-structural particle swarm optimization,* Aerospace **9** (2022), 10.3390/aerospace9030153.

[148] F. Möhren, O. Bergmann, C. Braun, and F. Janser, *Prediction and comparison of dynamic loads of propellers,* (American Institute of Aeronautics and Astronautics Inc, AIAA, 2022).

[149] A. Öchsner, *Euler–bernoulli beam theory,* in *Classical Beam Theories of Structural Mechanics* (Springer International Publishing, Cham, 2021) pp. 7–66.

[150] A. Öchsner, *Timoshenko beam theory,* in *Classical Beam Theories of Structural Mechanics* (Springer International Publishing, Cham, 2021) pp. 67–104.

[151] A. Öchsner, *Classical Beam Theories of Structural Mechanics* (Springer International Publishing, 2021).

[152] J. P. Blasques, *General rights User's Manual for BECAS: A cross section analysis tool for anisotropic and inhomogeneous beam sections of arbitrary geometry*, Tech. Rep. RISØ R 1785 (DTU – National Laboratory for Sustainable Energy, 2012).

[153] J. P. Blasques and R. D. Bitsche, *BECAS-an Open-Source Cross Section Analysis Tool Motivation & Overview*, Tech. Rep. RISØ R 1785 (DTU – National Laboratory for Sustainable Energy, 2012).

[154] F. Torrigiani, J. Bussemaker, P. D. Ciampa, M. Fioriti, F. Tomasella, B. Aigner, D. Rajpal, H. Timmermans, A. Savelyev, and D. Charbonnier, *Design of the strut braced wing aircraft in the AGILE collaborative MDO framework,* in *31st Congress of the International Council of the Aeronautical Sciences, ICAS 2018* (2018).

[155] R. Chandra, A. D. Stemple, and I. Chopra, *Thin-walled composite beams under bending, torsional, and extensional loads,* Journal of Aircraft **27**, 619 (1990), https://doi.org/10.2514/3.25331 .

[156] D. H. Hodges, *Nonlinear Composite Beam Theory* (American Institute of Aeronautics and Astronautics, 2006).

[157] H. Chen, W. Yu, and M. Capellaro, *A critical assessment of computer tools for calculating composite wind turbine blade properties,* Wind Energy **13**, 497 (2010).

[158] V. Hammer, M. Bendsøe, R. Lipton, and P. Pedersen, *Parametrization in laminate design for optimal compliance,* International Journal of Solids and Structures **34**, 415 (1997).

[159] M. Miki and Y. Sugiyama, *Optimum design of laminated composite plates using lamination parameters,* AIAA Journal **31**, 921 (1991).

[160] Z. Wu, G. Raju, and P. M. Weaverz, *Feasible region of lamination parameters for optimization of variable angle tow (vat) composite plates,* (American Institute of Aeronautics and Astronautics Inc, AIAA, 2013).

[161] Z. Wu, G. Raju, and P. M. Weaver, *Framework for the buckling optimization of variable-angle tow composite plates,* AIAA Journal **53**, 3788 (2015).

[162] G. Raju, Z. Wu, and P. M. Weaver, *On further developments of the feasible region of lamination parameters for composite laminates,* (American Institute of Aeronautics and Astronautics Inc, AIAA, 2014).

[163] S. Setoodeh, M. Abdalla, and Z. Gurdal, *Approximate feasible regions for lamination parameters,* (2006) https://arc.aiaa.org/doi/pdf/10.2514/6.2006-6973 .

[164] H. Fukunaga and H. Sekine, *Stiffness design method of symmetric laminates using lamination parameters,* AIAA Journal **30**, 2791 (1992).

[165] J. Grenestedt and P. Gudmundson, *Layup optimization of composite material structures,* Optimal Design with Advanced Materials , 311 (1993).